Ersatz

Internal Report
DESY F35D-97-11
November 1997

Measurement of Elastic ρ^0 Photoproduction at HERA

by

D. Westphal

Measurement of Elastic ρ^0 Photoproduction at HERA

Dissertation

zur Erlangung des Doktorgrades
des Fachbereichs Physik
der Universität Hamburg

vorgelegt von

Dirk Westphal
aus Wattenscheid

Hamburg
1997

Measurement of Elastic ρ^0 Photoproduction at HERA

Dissertation

zur Erlangung des Doktorgrades
des Fachbereichs Physik
der Universität Hamburg

vorgelegt von

Dirk Westphal
aus Wattenscheid

Hamburg
1997

Gutachter der Dissertation:	Prof. Dr. R. Klanner Prof. Dr. B. Naroska
Gutachter der Disputation:	Prof. Dr. R. Klanner Prof. Dr. G. Heinzelmann
Datum der Disputation:	15. Oktober 1997
Sprecher des Fachbereichs Physik und Vorsitzender des Promotionsausschusses:	Prof. Dr. B. Kramer

Abstract

The reaction $\gamma p \to \rho^0 p$ ($\rho^0 \to \pi^+\pi^-$) has been studied in ep interactions at HERA using the ZEUS detector for photon-proton center mass energies $W_{\gamma p}$ between 50 and 100 GeV and for $|t| < 0.5$ GeV^2, where t is the square of the four-momentum transfer at the proton vertex. The $\pi^+\pi^-$ invariant mass distribution has been investigated as a function of t. The asymmetry of the ρ^0 mass shape decreases as a function of $|t|$, as expected in models in which the asymmetry is ascribed to the interference of resonant and non-resonant $\pi^+\pi^-$ production. The resonant cross section has been measured as a function of $W_{\gamma p}$ and $|t|$. The reaction exhibits the features of a soft diffractive process, namely a weak energy dependence of the cross section and a differential cross section $d\sigma/d|t| \propto e^{-b|t|}$. The slope b of the t distribution was found to increase as $W_{\gamma p}$ increases. The angular distributions of the decay pions are analyzed as a function of the $\pi^+\pi^-$ invariant mass and the momentum transfer $|t|$ and found to be consistent with s-channel helicity conservation.

Zusammenfassung

Die Reaktion $\gamma p \to \rho^0 p$ ($\rho^0 \to \pi^+\pi^-$) wurde in ep Wechselwirkungen am HERA Speicherring mit dem ZEUS Detektor untersucht. Der kinematische Bereich der Messung erstreckt sich über eine Photon-Proton Schwerpunktsenergie $W_{\gamma p}$ zwischen 50 und 100 GeV und $|t| < 0.5$ GeV^2 im Betragsquadrat des am Protonvertex ausgetauschten Viererimpulses. Die invariante $\pi^+\pi^-$ Massenverteilung wurde als Funktion von t untersucht. Die Asymmetrie der ρ^0 Massenverteilung vermindert sich als Funktion von $|t|$, in Übereinstimmung mit Modellen in denen die Asymmetrie durch eine Interferenz von resonanter und nicht resonanter $\pi^+\pi^-$ Produktion beschrieben wird. Der Wirkungsquerschnitt für die resonante Produktion wurde als Funktion von $W_{\gamma p}$ und $|t|$ gemessen. Die Reaktion zeigt die Eigenschaften eines weichen diffraktiven Prozesses. Dies sind eine schwache Energieabhängigkeit des Wirkungsquerschnittes und ein differentieller Wirkungsquerschnitt $d\sigma/d|t|$ der exponentiell wie $e^{-b|t|}$ fällt. Ein Anwachsen der Steigung b als Funktion von $W_{\gamma p}$ wurde gemessen. Die Winkelverteilungen der Zerfallspionen wurden als Funktion der invarianten $\pi^+\pi^-$ Masse und des Impulsübertrages $|t|$ analysiert. Die Verteilungen sind mit s-Kanal-Helizitätserhaltung verträglich.

Contents

List of Figures

List of Tables

Chapter 1

Introduction

The hadron electron ring accelerator HERA, located at DESY in Hamburg provides colliding beams of electrons [1] with an energy of 27.5 GeV and protons with an energy of 820 GeV. A big fraction of the ep interactions, in which the exchanged four-momentum between the incoming and outgoing electron is small, have an interpretation as photon-proton (γp) interactions. Elastic photoproduction of vector mesons, $\gamma p \to Vp$, is a special kind of such photoproduction reactions. It has been studied in fixed target experiments at photon-proton center of mass energies up to $W_{\gamma p} \approx 20$ GeV and at HERA for $W_{\gamma p}$ up to approximately 200 GeV. Elastic photoproduction of ρ^0, ω and ϕ mesons at high energies exhibits the features of a soft diffractive process, namely a weak energy dependence of the cross section and a dependence on t, the squared four-momentum transferred at the proton vertex, which is approximately exponential at small $|t|$. Such an energy and t dependence, typical of elastic hadron-hadron interactions, are consistent with the expectations of the Vector Dominance Model (VDM) in which the photon is assumed to fluctuate into a vector meson before interacting with the proton.The vector meson is observed to retain the helicity of the photon (s-channel helicity conservation SCHC).

Elastic photoproduction of ρ^0 mesons has already been observed at HERA [110, 51], however many aspects of elastic ρ^0 photoproduction at large $W_{\gamma p}$ remain to be clarified. Among them, the $W_{\gamma p}$ dependence of the cross section, the $W_{\gamma p}$ dependence of the t slope, the origin of the asymmetry of the ρ^0 resonance shape and the extent to which the helicity of the photon is transferred to the ρ^0. In general, elastic photoproduction of ρ^0 mesons at HERA may offer a means of investigating the nature of the soft hadronic interaction as well as the hadronic features of the photon.

This thesis describes a measurement of elastic ρ^0 photoproduction using data collected in 1994 by the ZEUS experiment on the reaction $ep \to e\rho^0 p$ ($\rho^0 \to \pi^+\pi^-$) at small photon virtualities $Q^2 \lesssim 4$ GeV^2 (the median Q^2 is about 10^{-5} GeV^2). In this measurement the final state electron was not detected. The scattered proton was measured only for a subsample of the data. The relevant kinematic quantities were determined from the measured three-momenta of the ρ^0 decay products, assuming that they were pions. With respect to the published ZEUS data [110], the present results features larger statistics, a wider $W_{\gamma p}$ range and smaller systematic uncertainties. The kinematic range of the measurement was restricted to $50 < W_{\gamma p} < 100$ GeV and $|t| < 0.5$ GeV^2.

[1] Since 1994 positrons are stored in HERA instead of electrons. The term electron will be further used as a generic name for electrons and positrons.

The thesis is organized as follows. Those components of the ZEUS detector relevant for this analysis are introduced in chapter 2. Chapter 3 contains a short introduction to the physics of photon-proton reactions at HERA especially to elastic ρ^0 photoproduction. The online trigger and offline event selection as well as the reconstruction of the kinematic variables are presented in chapter 4. Chapter 5 contains a description of the Monte Carlo simulation programs used in this analysis. In chapter 6 the acceptance of the ZEUS detector for elastic ρ^0 photoproduction is presented, and the method used to determine the calorimeter trigger efficiency from the data is introduced. Chapter 7 is dedicated to the determination of the backgrounds to the elastic ρ^0 signal. The biggest background contribution is given by proton dissociative ρ^0 production, which was determined by a subsample of the data in which elastic events were unambiguously selected. In chapter 8 the response of the calorimeter for the ρ^0 decay pions is presented and chapter 9 summarizes the results obtained in this thesis. They cover a study of the ρ^0 mass asymmetry, a measurement of the energy dependence of the cross section and the t slope and a study of the ρ^0 decay angular distributions. Finally conclusions are given in chapter 10.

Chapter 2

The ZEUS Detector at HERA

2.1 HERA Accelerator

The **H**adron **E**lektron **R**ing **A**nlage HERA, located at DESY in Hamburg consists of two storage rings, 6.3 km in circumference in a tunnel 10-30 m underground (figure 2.1). In HERA electrons [1] of 27.5 GeV energy and protons of 820 GeV energy circulate in opposite direction. The beams collide at zero crossing angle in the two interaction regions north (N) and south (S), which are occupied by the ZEUS (S) and H1 (N) experiment. In these two experiments electron proton interactions at a center of mass energy $\sqrt{s} \approx 300$ GeV are studied

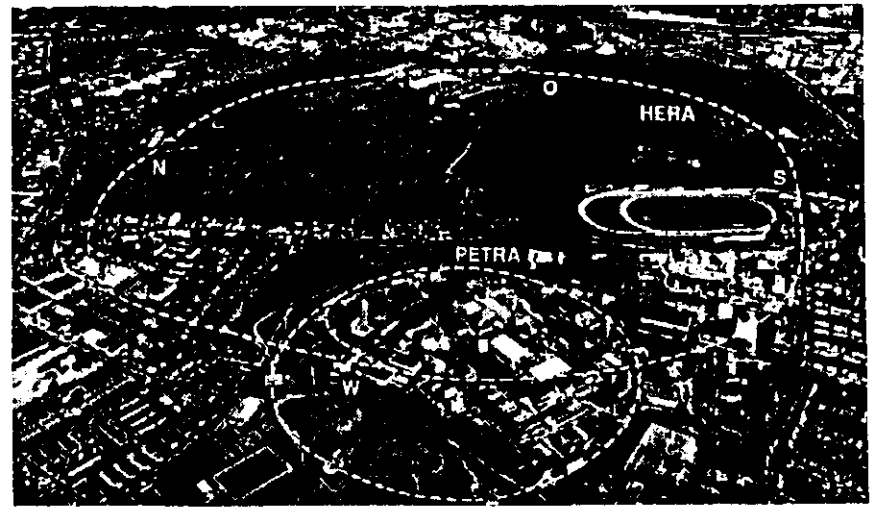

Figure 2.1: Bird eye's view of the DESY area in Hamburg. The dashed lines indicate the location of the PETRA and HERA storage rings.

[1] Since 1994 positrons are stored in HERA instead of electrons. The term electron will be further used as a generic name for electrons and positrons.

since 1992. The two remaining halls are used by the experiments HERMES (east hall O) and HERA-B (west hall W). These two experiments make use of the polarized electron beam (HERMES) or the proton beam (HERA-B) only. HERMES uses the longitudinally polarized electron beam in the east hall to study the spin structure of protons and neutrons. HERA is the world's first storage ring in which the natural transverse electron polarization caused by synchrotron radiation in the dipole magnets [105] is rotated to provide longitudinally polarized electrons. HERMES started operation in 1995. The B-physics experiment HERA-B is currently under installation.

Electrons and protons are accelerated in a chain of linear and circular accelerators located on the DESY site before they are injected at an energy of 12 GeV (electrons) and 40 GeV (protons) into HERA. In HERA both particle species are then accelerated to their collision energies. The maximal energy of protons in HERA is given by the maximal available magnetic field. To store protons at 820 GeV in the circumference of HERA, the super-conducting HERA magnets provide a magnetic field of 4.68 T. In contrast, the field required to store 30 GeV electrons can be accomplished by conventional magnets. The maximal electron energy is given by the available radio frequency power necessary to compensate for the losses due to synchrotron radiation.

The beams of protons and electrons are bunched and each of the HERA rings is capable of storing 220 bunches of particles. Thus electrons and protons meet every 96 ns in the experiments H1 and ZEUS. In 1994 the HERA rings were filled with 153 colliding bunches. The currents reached 30 mA in case of electrons (design 58 mA) and 50 mA for protons (design 163 mA). The highest observed luminosity was $5*10^{30}$ cm^{-2} s^{-1}.

2.2 ZEUS Detector

ZEUS is a multi purpose detector built and operated by a collaboration of 450 physicists from 50 institutes of 12 countries. An overview of the detector is given in figure 2.2 and figure 2.3. ZEUS is asymmetric in the proton direction because of the boost of the electron proton center of mass.

The coordinate system used throughout this thesis is the right handed ZEUS coordinate system defined as follows. The z-axis lies in the direction of the proton beam, the x-axis points horizontally towards the center of the HERA ring and the y-axis points upwards. The polar angle θ is measured with respect to the positive z direction and the azimuthal angle ϕ is measured around z relative to the positive x direction.

Charged particles are tracked in ZEUS by the inner tracking system comprising a vertex detector (VXD) and a central tracking detector (CTD). Both detectors are cylindrical drift chambers. The tracking system is completed by planar drift chambers in the forward (proton) and rear (electron) directions plus transition radiation detectors in the forward region. A thin super conducting solenoid surrounds the inner tracking detectors and produces a magnetic field of 1.43 T, allowing momentum measurements for charged particles. The tracking devices are surrounded by a high resolution calorimeter. The calorimeter consists of three parts covering different regions of the polar angle (forward (FCAL), barrel (BCAL) and rear (RCAL)). Each part is divided in depth into an electromagnetic and a hadronic component. The magnetized iron yoke surrounding the calorimeter is instrumented for the use as a backing calorimeter (BAC) and muon detector (BMUO/I, RMUO/I).

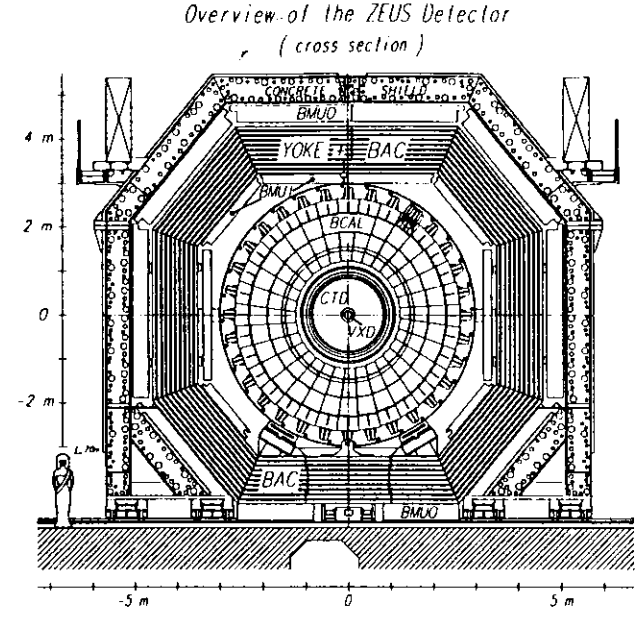

Figure 2.2: View of the ZEUS detector in cross section.

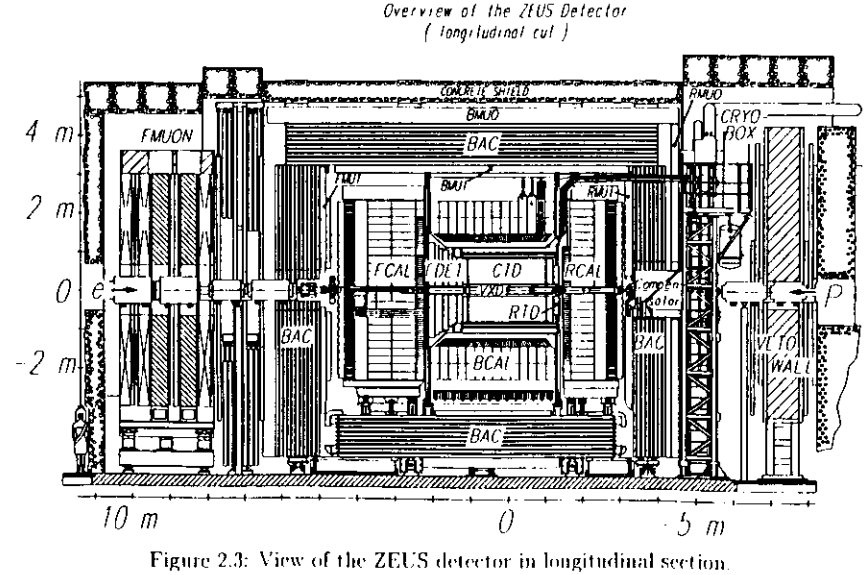

Figure 2.3: View of the ZEUS detector in longitudinal section.

In the forward direction, iron toroids and tracking chambers improve the muon detection (FMUON). The protons and neutrons emitted under very small angles in the forward direction are measured in the leading proton spectrometer (LPS) and the forward neutron calorimeter (FNC) installed in the HERA tunnel between 24 and 101 m. Slightly larger scattering angles are covered by the proton remnant tagger (PRT) installed behind the FCAL at z=5 m. In the backward direction photon and electron detectors close to the beampipe serve as a luminosity monitor (LUMI). In order to reduce the contamination of the data with proton beamgas events, ZEUS is equipped with background detectors in particular the veto wall (VETO), the C5 counter and the small angle rear tracking detector (SRTD).

In the following those detector components, which are used in this analysis are shortly introduced. A detailed description of all ZEUS detector components can be found elsewhere [107].

2.2.1 Tracking Detectors

The tracking devices relevant to this analysis are the vertex detector (VXD), the central tracking detector (CTD) and the rear tracking detector (RTD).

Vertex Detector VXD

The VXD is a cylindrical, high precision drift chamber [5] situated between the outer radius of the beam pipe and the inner wall of the CTD. It has an inner radius of 9.9 cm and an outer radius of 15.9 cm. The chamber is operated with Dimethyl-Ethan (DME) at atmospheric pressure. 6000 wires, 1.59 m in length, run parallel to the z-axis and are organized in 120 cells each containing 12 sense wires. The VXD covers the angular region $8.6° < \theta < 165°$. A spatial resolution in rϕ of 50 μm in the central region of a cell and 150 μm near the cell edges is achieved.

Central Tracking Detector CTD

The CTD [44] is a cylindrical drift chamber surrounding the VXD with a length of 240 cm, an inner diameter of 32.4 cm and an outer diameter of 164.8 cm. Its active length is 2 m corresponding to a angular coverage of $15° < \theta < 164°$. The chamber is filled with a gas mixture of Ar:CO_2:C_2H_6 (90:8:2). The CTD consists of 72 cylindrical drift layers arranged into 9 *superlayers* (figure 2.4). The wires within a superlayer are arranged azimuthally in cells, each containing 8 sense wires. In total the CTD is equipped with 4608 sense wires. The odd numbered superlayers have wires strung parallel to the z-axis (axial layers) while the four even numbered stereo layers are tilted by stereo angles between $-5.53°$ and $+5.62°$. The sense wires in superlayer 1 and alternate wires in superlayer 3 and 5 have an additional readout system which provides a fast determination of the track z coordinate by measuring the difference in arrival time of signals from both ends of the chamber. This information is used as input to the trigger and discriminates against events caused by upstream beamgas interactions. The CTD achieved in 1994 a spatial resolution in rϕ of 191 μm [76] and a z resolution of the z-by-timing system of 3.3 cm.

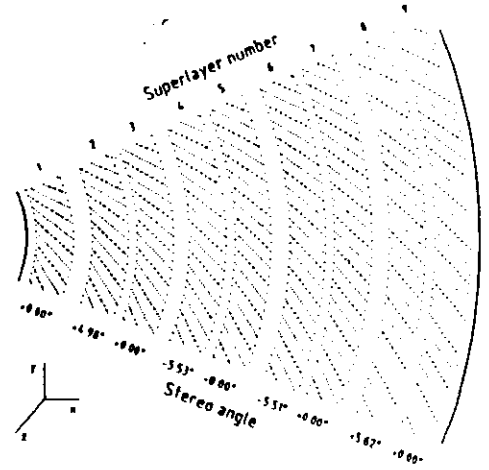

Figure 2.4: The arrangement of wires in one octant of the CTD. Sense wires are indicated by larger dots.

Rear Tracking Detectors RTD

The RTD [15] is a planar drift chamber extending the ZEUS inner tracking system in the rear direction. It consists of three layers of drift cells perpendicular to the beam axis with wire orientations at 0°, +60° and −60° with respect to the horizontal. The RTD covers polar angles between 160° and 170°. The six sense wires in each cell are separated by 7 mm and alternate wires are staggered by 300 μm with respect to the potential wires to resolve the left right ambiguity. During the 1994 data taking period the RTD was operated in ZEUS for the first time. It took data in 80% of the luminosity used in this analysis. The 20% luminosity taken without the RTD is accounted for in the Monte Carlo simulation (section 5) by excluding the RTD from the track reconstruction in 20% of the Monte Carlo events. For the 1994 data the RTD single wire efficiency was 91.5% and the single wire spatial resolution 240-300 μm [83]. The three RTD layers provide three independent stereo views of a track element. So the RTD information alone allows to reconstruct a three dimensional track element.

Track and Vertex Reconstruction

The VCTRAK [56] track finding program recognizes trajectories in the CTD, extends them into the VXD, fits them and then estimates the primary vertex. Track segments found in the RTD are used as an input to the program as well. The pattern recognition algorithm begins by looking for a track *seed* in an outer part of the CTD. A seed can either consist of three CTD hits from an axial superlayer or of a three dimensional track segment in the RTD plus a single axial CTD hit from superlayer 3 or 1. Given a track seed, the trajectory is extrapolated inward with increasing precision as more axial hits are assigned to the track.

The resulting trajectory forms a circle in the xy plane, which is used for the z-by-timing and stereo pattern recognition. The z-by-timing and stereo hits matching this trajectory are used to provide z information about the track. Eventually every track candidate must have three-dimensional information. An attempt is made to pick up hits in the VXD. The longest tracks are found first, then slightly shorter ones.

After correcting the drift distance for various systematic effects the track candidates are fitted to a five parameter helix model. A momentum is first estimated by using the slope and curvature provided by the pattern recognition. A trajectory is established by swimming through the magnetic field starting from the vicinity of the innermost used hit and proceeding outward as far as necessary. This swum trajectory is used to calculate the hit residuals as well as the derivatives of the residuals with respect to the helix parameter. Finally the trajectory and its covariance matrix are transported inward to the z-axis.

The primary event vertex is found in a three stage procedure. First trajectories incompatible with the beam-line are removed. The remaining tracks are used for an initial estimate of the vertex as the weighted center of gravity. Tracks with the maximum contribution to the χ^2 are discarded one by one until the fit quality is acceptable. In a final stage a full vertex fit is performed which not only solves the final vertex position but simultaneously re-evaluates the track parameters constrained to this vertex. The direction and curvature of the tracks at the vertex, rescaled to the curvature before the vertex fit, are used to determine the track momentum at the vertex.

The resolution in transverse momentum reached for full tracks in the CTD and VXD is $\sigma(P_T)/P_T \approx \sqrt{(0.005\ P_T)^2 + (0.016)^2}$ where P_T is in GeV.

2.2.2 Calorimeter CAL

The ZEUS calorimeter [6, 30, 14] is a high resolution sampling calorimeter. It consists of alternating layers of depleted uranium (3.3 mm thick) and plastic scintillator (2.6 mm thick) with one radiation length sampling. The light is collected via wavelength shifter plates and read out by photomultiplier tubes. The ZEUS calorimeter has equal response to electrons and hadrons, i.e. it is a compensating calorimeter. Compensation is achieved by choosing the correct fraction of absorber to readout material.

The calorimeter surrounds the inner tracking system and consists of three parts: the forward calorimeter (FCAL) in proton direction, the rear calorimeter (RCAL) in electron direction and the barrel calorimeter (BCAL) surrounding the central region (figure 2.5). The FCAL covers the range $2.2° < \theta < 39.9°$, the BCAL the range $36.7° < \theta < 129.1°$ and the RCAL the range $128.1° < \theta < 176.5°$. The forward and rear calorimeter are built out of 24 modules each, with maximum active dimensions of 4.6 m height, 0.2 m width and 1.52 m (FCAL) or 0.90 m (RCAL) depth. In the center of the FCAL and RCAL section an area of 20×20 cm^2 is left out for the beam pipe. The barrel calorimeter is build out of 32 wedge shaped modules with approximate dimensions of $3\times0.5\times1.7$ m^3.

The modules are subdivided transversely into towers and longitudinally into one electromagnetic section (EMC) and one (in RCAL) or two (in FCAL and BCAL) hadronic sections. The EMC sections have a depth of $\sim$25 radiation lengths, X_0, enough to fully contain electromagnetic showers. The depth of the EMC is equivalent to one nuclear interaction length λ_0 for hadrons. The HAC sections vary in depth from 6 λ_0, for hadrons in the forward direction to 3 λ_0 in the rear. All calorimeter towers are non projective except the BCAL towers,

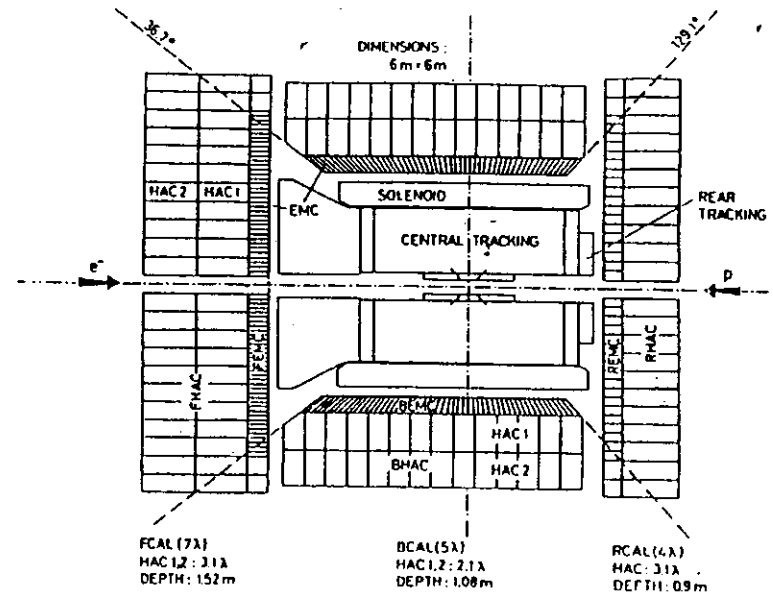

Figure 2.5: The different calorimeter sections and their division into EMC and HAC cells.

which are projective in azimuthal angle ϕ. The EMC towers of BCAL are also projective in polar angle θ. Each barrel calorimeter module is rotated by 2.5° clockwise in the azimuthal plane around an axis parallel to the z axis. This rotation assures that the wavelength shifter do not point to the beam axis.

A section of a tower is called a cell; each cell is viewed by two photomultiplier tubes. The cell size in the EMC sections are 5×20 cm^2 in FCAL and BCAL, 10×20 cm^2 in RCAL and 20×20 cm^2 in all HAC sections. In the region where FCAL and RCAL as seen from the nominal interaction point are hidden behind the barrel, the EMC segmentation is identical to the one in the HAC, namely 20×20 cm^2 (these cells are called HAC0 cells). Each HAC respectively EMC cell is read out by plastic wavelength shifter plates, attached on opposite sides of the cell, lightguides and attached photomultiplier tubes (PMT).

The pipelined calorimeter readout electronics covers a big dynamic range, allowing precise energy measurement from MIPS (300 MeV equivalent energy in EMC cells of FCAL) up to the highest expected signals ($\sim$400 GeV in individual cells of FCAL), by splitting the PMT signals in a high and low gain path. The fast response time of the plastic scintillator together with the readout electronics allows to measure the timing of a signal in a calorimeter cell with a resolution of less than 1 ns for energy deposits greater than 4.5 GeV. The energy resolution under test beam conditions without inactive material in front is $\sigma(E)/E = 0.18/\sqrt{E[\mathrm{GeV}]} \oplus 0.01$ for electrons and $\sigma(E)/E = 0.35/\sqrt{E[\mathrm{GeV}]} \oplus 0.02$ for hadrons.

The performance, energy and time calibration of the calorimeter are continuously monitored using pedestal triggers, charge and light injection as well as the uranium radioactivity. The uranium radioactivity can be used as a standard to calibrate the calorimeter with an accuracy of about 1%.

The noise of the calorimeter is approximately 15 MeV for electromagnetic and 25 MeV for hadronic cells, dominated by the uranium radioactivity.

Calorimeter First Level Trigger CFLT

The CFLT [100] provides trigger data for a global first level trigger (GFLT) decision 5 μs after each beam crossing, occurring every 96 ns. The charges from the 12864 photomultipliers of the CAL are summed in 1792 trigger tower pulseheights which are digitized by flash ADC's. The digital values are linearized, stored and used for sums and pattern tests. Energy sums are transfered to the GFLT for each crossing 2 μs after the crossing occured. The decisions are derived in a pipelined fashion every 96 ns.

Trigger towers consist of a block of four (FCAL and BCAL) or two (RCAL) EMC cells, and those HAC cells that lie most projective behind the EMC cells. Thus each trigger tower has a size of 20×20 cm^2 and is divided into an electromagnetic and a hadronic section. The energy sums corresponding to the 896 trigger towers are formed in trigger sum cards. Trigger towers are organized into sixteen 7×8 trigger regions; RCAL and FCAL consist of four trigger regions each and BCAL of eight. The analog signals from the trigger sum cards, are transfered to trigger encoder cards, which digitize the information every 96 ns by two 8 bit flash ADC's with high and low gain.

After digitization the trigger encoder cards linearize, pedestal correct and zero suppress the signals, making use of memory lookup tables. Calibration constants are reloaded into the lookup tables. The calibration is accomplished with the charge injection system of the CAL readout. The charge injectors are fired and the pulseheights for the trigger towers are individually compared against their expected values. The resolution of the digitized trigger energies is 49 MeV (high gain), 1.6 GeV (low gain FCAL) or 0.39 GeV (low gain RCAL and BCAL) giving a dynamic range up to 400 GeV. Energies below a low threshold, presently at 464 MeV are set to zero (zero suppression). The corrected energies are multiplied by geometric factors to calculate electromagnetic and hadronic total energy E_{total}, transverse energy E_T, E_x and E_y using again lookup tables. It is also tested whether the energy deposition in a trigger tower is consistent with an electron candidate, a minimum ionizing particle or a quiet tower and it is determined which of six threshold values (3 bit) is surpassed by the signal.

Adder cards combine the information (E_{total}, E_T, E_x and E_y) from the trigger encoder cards for a single trigger region. It also applies pattern recognition algorithms to identify isolated electrons and muons in a single trigger region and calculates the energy sums on a 3 bit scale. The adder cards send their information to the CFLT processor.

The CFLT processor calculates the total E_T, missing transverse energy E_T, electromagnetic and hadronic energy, compares region boundaries to calculate the number of isolated electrons and muons and computes regional EMC, HAC and total energies, particularly around the beam pipe region. The summary of this information is transmitted to the GFLT for each crossing. The quantities used in the trigger for elastic ρ^0 photoproduction are discussed in section 4.1.

2.2.3 Small Angle Detectors

Luminosity Detectors LUMI

The luminosity is measured by detecting Bremsstrahlung photons from the process $ep \rightarrow e\gamma p$. The cross section for this process is known to high accuracy from QED given by the Bethe-Heitler formula. Thus by accurately determining the rate of Bethe-Heitler photons above a given energy threshold a precise determination of the luminosity is possible.

Bremsstrahlung photons, scattered at an angle less than 0.5 mrad, are detected by a lead scintillator calorimeter [7, 84] positioned in electron beam direction at a distance of 107 m from the interaction point. The calorimeter is 23 radiation lengths (X_0) deep and has a position detector inserted after 4 X_0. The calorimeter is shielded against synchrotron radiation by a carbon filter (1.5 X_0) placed at z=-103 m and lead shielding (1 X_0). The calorimeter has a resolution of $\sigma(E)/E = 0.18/\sqrt{E[GeV]}$.

Bremsstrahlung of electrons on rest gas molecules has the same experimental signature as ep Bremsstrahlung. To subtract this background, the event rate for unpaired (pilot) electron bunches is also determined. This background rate is scaled by the current of particles in those bunches with respect to the bunches that participate in ep collisions and subtracted.

An additional calorimeter at a position of z=-35 m detects electrons scattered at small angles. Electrons from the interaction point that are below nominal beam energy are deflected by dipole and quadrupole magnets onto the electron calorimeter. The acceptance of the electron calorimeter in energy is therefore restricted to $E = 6.2 - 21.2$ GeV [73].

Leading Proton Spectrometer LPS

The LPS detects charged particles scattered at small angles and carrying a substantial fraction, x_L, of the incoming proton momentum. These particles remain in the beam pipe and their trajectories are measured by a system of position sensitive silicon micro-strip detectors very close to the proton beam. The track deflection induced by the magnets in the proton beam line is used for the momentum analysis of the scattered proton.

The LPS [114] consists of six detector stations, S1 to S6 of which in 1994 only S4 to S6 were equipped. Only these stations will be described in the following. The stations are placed along the beam line at z=63.0 m (S4), 81.2 m (S5) and 90.0 m (S6) respectively. Each of these stations consists of two halves, each half containing an assembly of six planes of silicon micro-strip detectors mounted on a mobile arm. Each assembly has two planes with vertical strips, two planes at +45° and two planes at -45° with respect to the vertical. Thus the particle trajectory is measured in three different projections in each assembly. The pitch is 115 μm for planes with vertical strips and 81 μm for the planes with ±45° strips. The distance in z between neighboring planes is $\approx$ 7 mm.

The detector planes are inserted in the beam pipe by means of a steel cylinder with on open end away from the beam and the other end closed (Roman pot). The silicon detectors are inserted from the open end and the whole cylinder is inserted into the beam pipe. The planes in the two halves of each station independently approach the beam from above and below. In the operation position the upper and lower halves partially overlap. Each detector plane

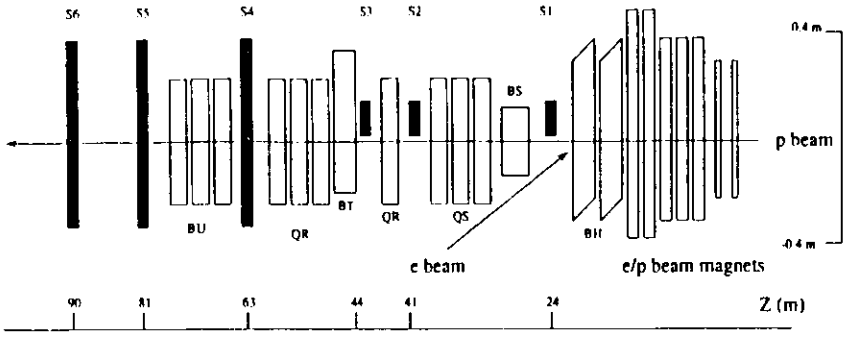

BU Vertical Dipole BT Horizontal Correction Dipole BH Horizontal Dipole
QR Quadrupoles QS Half Quadrupole BS Septum Magnet

Figure 2.6: Top view of the outgoing proton beam line together with the magnetic elements of the HERA proton beam line. The positions of the LPS stations S1 through S6 are also shown.

has an elliptical cutout which follows the profile of the 10 σ envelope of the beam.

Together with three HERA main dipole magnets (vertical bending) located between S4 and S5 the station S4, S5 and S6 form a spectrometer (figure 2.6). The insertion of the detectors into the operating positions typically is started soon after the beams are brought into collision. Since the insertion procedure took about fifty minutes and since the beam conditions did not always allow safe insertion of the detectors, only a reduced integrated luminosity is available for analyses using the LPS in 1994. The efficiency of the detector planes in 1994 after excluding noisy and malfunctioning channels (< 2%) was better than 99.8%.

Tracks are reconstructed in stages, proceeding from individual hits to full tracks. First clusters of adjacent hit strips are searched for in each detector plane. By combining pairs of clusters belonging to different projections, candidate local track segments are found independently in each detector assembly. All hits belonging to a candidate are used to find the transverse coordinate of the track at the value of z corresponding to the center of the station. The spatial resolution of these coordinates is about 30 μm. Coordinates reconstructed in pairs of different stations are combined into track candidates and the track momentum is determined using the average ep interaction vertex. Linear matrix equations relate the horizontal and vertical coordinates and slopes of the track at each station to the position and slope of the track at the interaction vertex. The matrix elements are known functions of x_L, the fraction of the incoming beam momentum carried by the outgoing proton. The functions describe the beam optics including the effects of quadrupoles and drift lengths. The two equations for the horizontal and vertical coordinates are independent apart from the common dependence on x_L and can be used to obtain two independent estimates of x_L. If the two values obtained are compatible, the pair of coordinates is retained as a candidate two station track.

As a final step of the pattern recognition, three station track candidates are searched for using pairs of two station candidates. If the two track candidates give compatible momenta, if the projection of the two tracks on the horizontal plane coincide and if they use the same hits in the common station, the two candidates are merged in a three-station track candidate. Two-station and three-station candidates are then passed to a conventional track fitting stage. A χ^2 is minimized with respect to five track parameters (the positions and slopes at the vertex and x_L) and the best track parameters, together with the error matrix are determined.

The alignment of the LPS relies on survey information for locating the detector planes along the beam trajectory and on high energy proton tracks for locating in the horizontal and vertical direction. The individual detector planes are first aligned within one station, then the relative alignment of the stations is determined, and finally the three stations are aligned relative to the ZEUS detector. Typical accuracies in the horizontal and vertical direction are better than 20 μm. The actual path of the proton beam is also determined. All the steps of the alignment procedure are described in detail in [114].

The LPS in it's 1994 setup accepts scattered protons in the range $x_L \gtrsim 0.4$ and with $0 \lesssim P_{Tp} \lesssim 1$ GeV, where P_{Tp} is the transverse momentum of the proton with respect to the incoming beam direction. With the configuration installed in 1994 the resolution in x_L is better than 0.4% at 820 GeV and the P_{Tp} resolution is about 5 MeV. The latter is less than the intrinsic transverse momentum spread in the proton beam at the interaction point (with rms of about 40 MeV horizontally and about 90 MeV vertically) due to the beam divergence of ≈ 50 μrad in the horizontal and ≈ 110 μrad in the vertical plane.

Proton Remnant Tagger PRT

The proton remnant tagger (PRT) [31] consists of two pairs of scintillation counters surrounding the beam pipe positioned at z=5.15 m. It is build out of two layers of scintillator separated by 1 mm thick lead and wrapped in lead (2 mm thick) and iron (0.5 mm thick) shielding foil. Each of the scintillator layers is split in two halves independently read out by two photomultiplier tubes. The geometrical layout of the PRT scintillation counters and the readout channel assignment are shown in figure 2.7. Two counters on one side of the beam pipe form a pair and cover the same area. Charged particles can be identified in the PRT by a coincidence of signals in the two counters of one pair. The PRT has an active area 30×26 cm^2 with a hole of 6.0×4.5 cm^2 at the center to accommodate the HERA beam pipe. The geometric acceptance of the PRT extends over the pseudo-rapidity ($\eta = -\ln\tan\theta/2$) range of $4.3 < \eta < 5.8$.

The PRT was operational for the first time in 1994. It took data with a proper voltage setting only for part of the luminosity range used in this analysis. The overall tagging efficiency for a coincidence signal, of at least 1 MIP in each counter of one pair, for the 1994 data taking period is 87 ± 3% [11].

Veto Wall

The veto wall (VW) is located at the exit of the beam pipe tunnel at z=-7.27 m. It consists of an 87 cm thick iron wall with overall dimensions of 5×6 m^2 which is sandwiched by two layers of scintillator. The VW shields the main detector against products of the interaction of beam protons with the rest gas (proton beamgas interaction) entering the interaction region. Particles which are not completely absorbed can be identified by the timing infor-

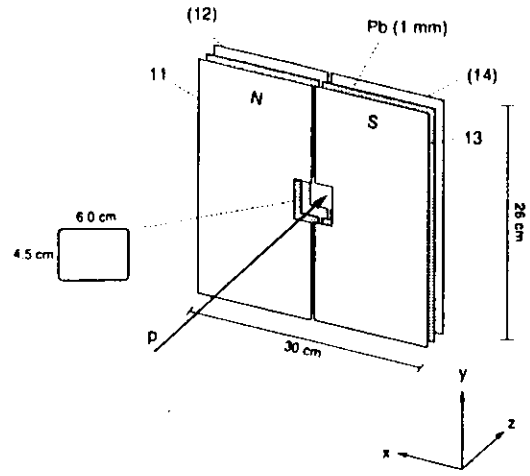

Figure 2.7: Layout of the PRT1 scintillation counters and the readout channel assignment.

mation from signals in the two layers of scintillator.

C5 Monitor

The C5 beam monitor is a small assembly of scintillators separated by lead sheets positioned orthogonal to the beam pipe. Two pairs of small scintillators (roughly 10×5 cm^2 of active area) are installed above and below the beam pipe behind the RCAL at z=-3.15 m. The C5 monitor allows to detect proton beamgas background occurring between the VW and C5 using the timing information of the scintillators. To reject noise and very low energetic particles, signals are accepted only if they occur in the scintillators on both sides of the lead sheet.

Small Angle Rear Tracking Detector SRTD

The SRTD consists of two planes of 1 cm wide and 0.5 cm thick scintillator strips which are attached to the front of the RCAL (z=-1.50 m). These planes are arranged in orthogonal directions and cover a region of 68×68 cm^2 around the beam pipe. The SRTD serves as a presampler for scattered electrons in order to correct for energy loss. The timing information is used to discriminate proton beamgas interactions close to the interaction point.

The VW, C5 and SRTD detectors discriminate between particles coming from a genuine ep collision at the nominal interaction point and from upstream proton beamgas interaction by precise measurement of the time of the hits in the scintillators relative to the bunch crossing time. Particles from proton beamgas background occur at times $2|z|/c$ before the arrival of particles from ep interactions at the ZEUS interaction point. The early timing is therefore a clear indication of the proton beamgas background. In case of a signal consistent with proton beamgas timing these detectors send a veto signal to the global first level trigger (GFLT).

2.2.4 Trigger and Data Acquisition System

The requirements on the ZEUS trigger and readout system are given by the HERA bunch crossing interval of 96 ns and the total number of 250000 ZEUS readout channels. The ZEUS data acquisition and trigger system has to reduce the raw input data stream of 5 TBytes/s to about 1 MBytes/s without rejecting too many important physics events. The system consists of the readout systems of the individual components and a three level trigger system, as shown in figure 2.8.

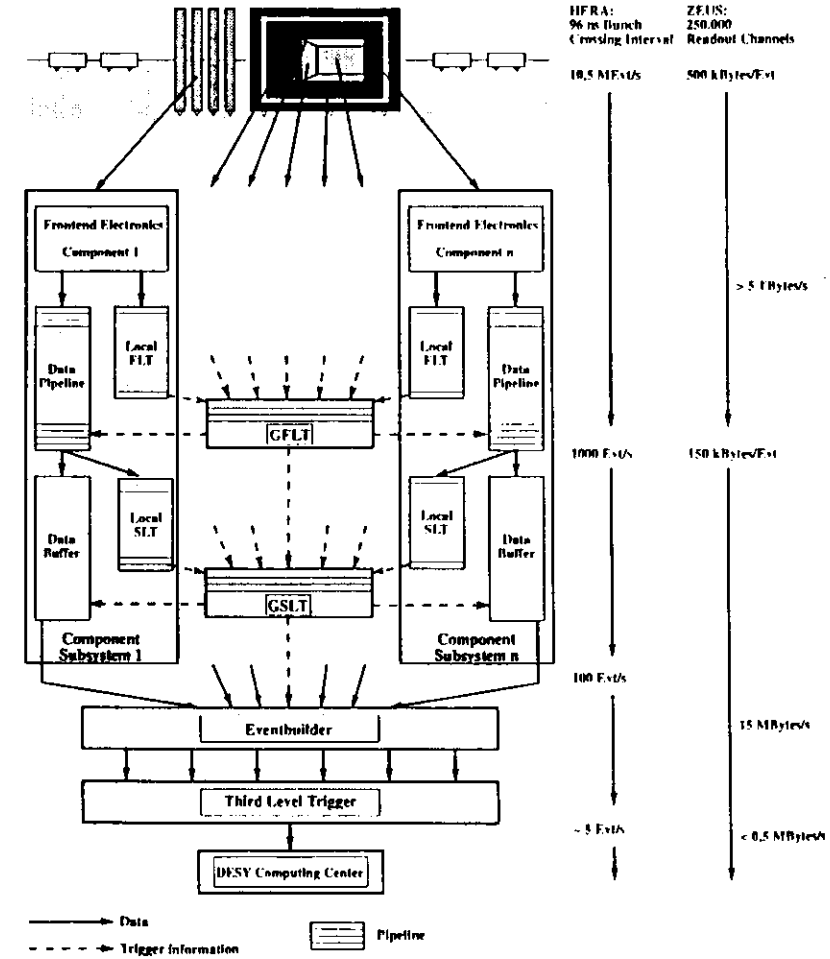

Figure 2.8: Layout of the ZEUS trigger and data acquisition system (from [79]). Numbers are design values.

Each ZEUS detector component is equipped with its own front-end electronics. Once a detector component has been read out, the data is stored in a 10.4 MHz pipeline and analyzed by a local first level trigger within the next 25 clock cycles. The results from the different components referring to the same beam crossing are input to the global first level trigger (GFLT). The GFLT calculation takes additional 20 bunch crossing (1.9 μs) and the overall decision is issued exactly 46 crossing (4.4 μs) after the bunch that produced it. The GFLT decision is send back to the components. The maximum rate of GFLT accept decisions is designed to be 1 kHz. Up to this stage both the trigger and readout are deadtime free.

On GFLT accept, data accepted for further analysis are copied to a second level trigger which is still local to the single component subsystem. A GFLT accept rate of 1 kHz and a copy time of 30 μs from the FLT to the SLT pipeline results in 3% deadtime. A local second level trigger computes the trigger information which is forwarded to the global second level trigger (GSLT). The GSLT computes the global second level trigger decision which is send back to the components. The GSLT is designed to veto approximately 90% of all GFLT triggers.

The component data accepted by the GSLT is given a GSLT decision number and transferred to the Eventbuilder. The Eventbuilder combines and formats all the component data carrying the same GSLT decision number into one data set, the so called event.

Once an event is complete it is handed over to the third level trigger (TLT). The TLT is a processor farm consisting of six branches of a total of 36 workstations. A single event is analyzed by an individual workstation. Based on the results a final filtering is done and the data is written to magnetic tape at a TLT output rate of about 5 events/s for reconstruction and offline analysis.

Reconstruction and Offline Analysis

Events from the detector are reconstructed by the program ZEPHYR. The calibration of each detector component is available and the raw data output as written to tape is converted into quantities useful for the physics analysis.

A subset of physical values in a reduced data structure, the so called MiniDST, is stored on 600 GByte of fast hard disks connected to a SGI Challenge DM machine acting as an I/O server to the farm of hard disks. The data is easily accessible from the analysis programs running on two SGI Challenge XL multiprocessor machines. This system is a central computing facility of the ZEUS experiment, the so called ZARAH.

Chapter 3

Photoproduction at High Energies

In this chapter the kinematic variables used to describe ep interactions are first introduced. It will be explained how ep interactions can be used to measure photoproduction (γp) cross sections. As then discussed, certain, photoproduction interactions can be described in the framework of the vector meson dominance model (VDM) and Regge phenomenology. The description includes the cross sections and decay angles.

3.1 ep Interactions

A diagram describing the scattering of electrons off protons in first order electromagnetic perturbation theory is shown in figure 3.1. The four momenta of the particles are given in brackets. The kinematics of an ep interaction can be described by the ep center of mass energy $\sqrt{s} \approx \sqrt{4E_eE_p}$, where E_e and E_p are the energy of the incoming electron and proton respectively, and any pair of the following variables:

$$Q^2 \equiv -\mathbf{q}^2 \equiv -(\mathbf{k}-\mathbf{k}')^2 \qquad \text{minimal } Q^2: Q^2_{min} \approx \frac{m_e^2 y^2}{1-y} \tag{3.1}$$

$$\nu \equiv \frac{\mathbf{qp}}{M_p} \tag{3.2}$$

$$y \equiv \frac{\mathbf{qp}}{\mathbf{kp}} \tag{3.3}$$

$$x \equiv \frac{Q^2}{2\mathbf{qp}} \tag{3.4}$$

$$W^2_{\gamma p} \equiv (\mathbf{q}+\mathbf{p})^2 \approx 4yE_eE_p \text{ for } W_{\gamma p} \gg M_p \tag{3.5}$$

In the electroweak theory the exchanged gauge boson in a neutral current interaction may be a photon (γ) or a neutral weak vector boson (Z^0). In the kinematic range of interest in this thesis ($Q^2 < 4GeV^2$) Z^0 exchange can be safely ignored.

The electromagnetic interaction between electrons and protons is given by [54]:

$$\frac{d\sigma}{dE'd\Omega} = \frac{\alpha^2}{Q^4}\frac{E'}{E}L^{\mu\nu}W_{\mu\nu} \tag{3.6}$$

where α is the electromagnetic coupling constant while E and E' are the energies of the incoming and outgoing electron in the proton rest frame respectively, $L^{\mu\nu}$ is the lepton

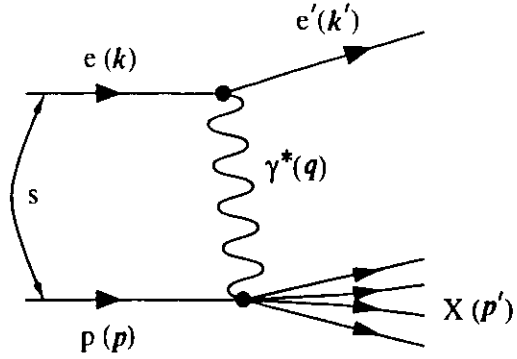

Figure 3.1: Schematic diagram of ep scattering in lowest order in α.

tensor:

$$L^{\mu\nu} = 2\left(k'^{\mu}k^{\nu} + k'^{\nu}k^{\mu} + \frac{\mathbf{q}^2}{2}g^{\mu\nu}\right) \tag{3.7}$$

and $W_{\mu\nu}$ the hadronic tensor:

$$W_{\mu\nu} = W_1\left(-g_{\mu\nu} + \frac{q_\mu q_\nu}{\mathbf{q}^2}\right) + W_2\frac{1}{M_p^2}\left(p_\mu - \frac{\mathbf{pq}}{\mathbf{q}^2}q_\mu\right)\left(p_\nu - \frac{\mathbf{pq}}{\mathbf{q}^2}q_\nu\right). \tag{3.8}$$

W_1 and W_2 are two independent inelastic structure functions. Alternatively the hadronic tensor can be written as

$$W_{\mu\nu} = \frac{1}{4\pi M_p}\sum_{\lambda,spins} < X \mid j_\mu \mid p >< p \mid j_\nu \mid X >^* (2\pi)^4\delta^{(4)}(\mathbf{p}' - \mathbf{p} - \mathbf{q}) \tag{3.9}$$

where the sum runs over all final states $\mid X >$ and spins of the incoming proton $\mid p >$ and j_μ denotes the electromagnetic current. The differential cross section 3.6 can also be expressed in terms of y and Q^2. Evaluating $L^{\mu\nu}W_{\mu\nu}$ using equations (3.7) and (3.8) the differential cross section reads:

$$\frac{d\sigma}{dydQ^2} = \frac{4\pi\alpha^2}{Q^4}\left[M_p W_1\left(1 - \frac{2M_e^2}{Q^2}\right)xy + \frac{s}{2M_p}W_2\left(1 - y + \frac{M_p^2 xy}{s}\right)\right] \tag{3.10}$$

3.2 Relating ep and γp Cross Sections

In the following we restrict ourselves to the proton rest frame, so the photon four momentum is given by $\mathbf{q} = (\nu, \vec{K})$. In this frame the total cross section for scattering of real photons of energy K and polarization ϵ_λ off unpolarized protons can be obtained from Feynman rules to be:

$$\sigma^{tot}(\gamma p \to X) = \frac{4\pi^2\alpha}{K}\epsilon_\lambda^{\mu *}\epsilon_\lambda^{\nu}W_{\mu\nu}. \tag{3.11}$$

The differential cross section for inelastic ep scattering (3.6) can be interpreted as a virtual photon proton cross section $\sigma^{\gamma^* p}$. But one has to keep in mind that real photons can occur in two transverse polarizations, whereas virtual photons can also occur in a longitudinal polarization state. Real photons have a flux factor $4M_pK$. For virtual photons the flux is not uniquely defined. The conventional approach due to Hand [55] requires the momentum K of the virtual photon to be equal to the energy of a real photon needed to give the same $W_{\gamma p}$:

$$K_{Hand} = \frac{2M_p\nu - Q^2}{2M_p} \tag{3.12}$$

where ν is the energy of the virtual photon. Defining the z axis along the virtual photon momentum $\vec{K}$, the polarization vector ϵ_λ^μ is given by:

$$\lambda = \pm 1: \qquad \epsilon_\pm = \mp\sqrt{\frac{1}{2}}(0, 1, \pm i, 0) \tag{3.13}$$

$$\lambda = 0: \qquad \epsilon_0 = \frac{1}{\sqrt{Q^2}}(\sqrt{\nu^2 + Q^2}, 0, 0, \nu) \tag{3.14}$$

Using the definition of $W_{\mu\nu}$ (3.8) together with the above polarization vector one finds the transverse and longitudinal cross section to be:

$$\sigma_T^{\gamma^* p} \equiv \frac{1}{2}(\sigma_+^{tot} + \sigma_-^{tot}) = \frac{4\pi^2\alpha}{K}W_1 \tag{3.15}$$

$$\sigma_L^{\gamma^* p} \equiv \sigma_0^{tot} = \frac{4\pi^2\alpha}{K}\left[\left(1 + \frac{\nu^2}{Q^2}\right)W_2 - W_1\right] \tag{3.16}$$

For $\gamma^* p$ scattering at small Q^2, Bjorken x is small and one can approximate $K \approx \nu$ and $1 + \nu^2/Q^2 \approx \nu^2/Q^2$. This yields:

$$\sigma_T^{\gamma^* p} = \frac{4\pi^2\alpha}{\nu}W_1 \tag{3.17}$$

$$\sigma_L^{\gamma^* p} = \frac{4\pi^2\alpha}{\nu}\left[\frac{\nu^2}{Q^2}W_2 - W_1\right] \tag{3.18}$$

Neglecting the term M_p^2/s in equation (3.10) and using the relation $Q^2_{min} \approx M_e^2 y^2/(1-y)$ yields the following differential ep cross section:

$$\frac{d\sigma}{dydQ^2} = \frac{\alpha}{2\pi}\frac{1}{Q^2}\left[\left(\frac{1 + (1-y)^2}{y} - 2\frac{1-y}{y}\frac{Q^2_{min}}{Q^2}\right)\sigma_T^{\gamma^* p}(y, Q^2) + 2\frac{1-y}{y}\sigma_L^{\gamma^* p}(y, Q^2)\right] \tag{3.19}$$

3.3 Photon-Proton Interactions

In the previous section it was shown that a ep cross section measured at HERA can be related to a virtual photon proton cross section. In this section a theoretical model used to describe γp interactions will be introduced.

3.3.1 Vector Meson Dominance Model

Photon hadron interactions at high energies exhibit similar properties as hadron hadron interactions. On a qualitative level this similarity can be understood as follows. The uncertainty principle allows fluctuations of the photon into a virtual $q\bar{q}$ state of the same quantum numbers as the photon ($J^{PC} = 1^{--}$; Q=S=B=0) namely vector mesons. In this subsection we restrict ourselves again to the proton rest frame so the photon four momentum is given by $\mathbf{q} = (\nu, \vec{K})$. The fluctuation time is given by

$$t_f \approx \frac{2\nu}{Q^2 + M_V^2} \tag{3.20}$$

If the distance that the virtual vector meson can travel is much larger than the nucleon radius $r_h \approx 1\,\mathrm{fm}$ the photon fluctuates long before it hits the hadron and the interaction occurs between the vector meson and the hadron.

Thus the physical photon $\mid \gamma >$ can be considered as a superposition of a bare photon $\mid \gamma_B >$ and a hadronic component $\sqrt{\alpha} \mid h >$

$$\mid \gamma >= \sqrt{Z_3} \mid \gamma_B > + \sqrt{\alpha} \mid h > \tag{3.21}$$

where Z_3 assures the proper normalization. Although the hadronic photon component is suppressed by $\sqrt{\alpha}$, it dominates low Q^2 photon proton interactions since hadronic cross section are very large. Photoproduction of the lightest vector mesons ρ^0, ω and ϕ suggests that they provide a very important contribution to $\mid h >$. Only considering these vector mesons as the hadronic component and neglecting the bare photon $\mid \gamma_B >$ contribution is the hypothesis of the vector dominance model (VDM). The inclusion of more constituents to $\mid h >$ is referred to as generalized vector dominance model (GVD). Reviews of these models are given in [10] and [32].

For the VDM the hadronic photon component can be written as:

$$\sqrt{\alpha} \mid h >= \sum_{V=\rho^0,\omega,\phi} \frac{M_V^2}{M_V^2 + Q^2} \frac{1}{f_V} \mid V > \tag{3.22}$$

where f_V is the $\gamma \leftrightarrow V$ coupling. The matrix element for photoproduction $(\gamma p \rightarrow X) < X \mid j \mid p >$ can therefore be related to the matrix element for vector meson photon scattering $(Vp \rightarrow X) < X \mid j^V \mid p >$ by

$$< X \mid j \mid p >= \sum_{V=\rho^0,\omega,\phi} \frac{M_V^2}{M_V^2 + Q^2} \frac{1}{f_V} < X \mid j^V \mid p > \tag{3.23}$$

where j denotes the electromagnetic current and j^V the current of the vector meson field. The currents j (j^V) can be separated in a transverse and longitudinal contribution, in which the currents are parallel $j_\parallel$ ($j_\parallel^V$) or perpendicular $j_\perp$ ($j_\perp^V$) to the three momentum of the virtual photon (vector meson) $\vec{K}$. Thus the virtual photon cross section can be calculated according to (3.11) in the Hand convention

$$\begin{aligned} \sigma_T^{\gamma p} &= \frac{4\pi^2\alpha}{K} \sum_{X,spin} |< X \mid j_\perp \mid p >|^2 \frac{1}{4\pi M_p} (2\pi)^4 \delta^{(4)}(\mathbf{p}' - \mathbf{p} - \mathbf{q}) \\ \sigma_L^{\gamma p} &= \frac{4\pi^2\alpha}{K} \frac{Q^2}{\nu^2} \sum_{X,spin} |< X \mid j_\parallel \mid p >|^2 \frac{1}{4\pi M_p} (2\pi)^4 \delta^{(4)}(\mathbf{p}' - \mathbf{p} - \mathbf{q}) \end{aligned} \tag{3.24}$$

The vector meson proton cross section (Vp) is accordingly given by

$$\begin{aligned} \sigma_T^{Vp} &= \frac{\pi}{K} \sum_{X,spin} |< X \mid j_\perp^V \mid p >|^2 \frac{1}{4\pi M_p} (2\pi)^4 \delta^{(4)}(\mathbf{p}' - \mathbf{p} - \mathbf{q}) \\ \sigma_L^{Vp} &= \frac{\pi}{K} \frac{M_V^2}{\nu^2} \sum_{X,spin} |< X \mid j_\parallel^V \mid p >|^2 \frac{1}{4\pi M_p} (2\pi)^4 \delta^{(4)}(\mathbf{p}' - \mathbf{p} - \mathbf{q}) \end{aligned} \tag{3.25}$$

Assuming that $\sum_{X,spin} |< X \mid j_{\parallel,\perp}^V \mid p >|^2 \, 1/(4\pi M_p)\delta^{(4)}(\mathbf{p}' - \mathbf{p} - \mathbf{q})$ varies very little with Q^2 the cross sections (3.24) and (3.25) can be related using equation (3.23). This yields the following Q^2 dependence of $\sigma_T^{\gamma p}$ and $\sigma_L^{\gamma p}$:

$$\sigma_T^{\gamma p}(W_{\gamma p}, Q^2) = \sum_{V=\rho^0,\omega,\phi} \frac{4\pi\alpha}{f_V^2} \left(\frac{M_V^2}{M_V^2 + Q^2} \right)^2 \sigma_T^{Vp}(W_{Vp}) \tag{3.26}$$

$$\begin{aligned} \sigma_L^{\gamma p}(W_{\gamma p}, Q^2) &= \sum_{V=\rho^0,\omega,\phi} \frac{4\pi\alpha}{f_V^2} \left(\frac{M_V^2}{M_V^2 + Q^2} \right)^2 \frac{Q^2}{\nu^2} \frac{\nu^2}{M_V^2} \sigma_L^{Vp}(W_{Vp}) \\ &= \sum_{V=\rho^0,\omega,\phi} \frac{4\pi\alpha}{f_V^2} \left(\frac{M_V^2}{M_V^2 + Q^2} \right)^2 \frac{Q^2}{M_V^2} \xi^2 \sigma_T^{Vp}(W_{Vp}) \end{aligned} \tag{3.27}$$

where $\xi^2 = \sigma_L^{Vp}/\sigma_T^{Vp}$ is the ratio of the longitudinal to transverse Vp cross section [91].

Since vector mesons are short lived particles it is impossible to study Vp scattering directly. The additive quark model [68, 69, 70] on the other hand allows to relate Vp cross sections to πp and Kp cross sections, since in this model the interaction between hadrons is determined by their valence quark constituents. This yields the following relations:

$$\sigma^{\omega p} = \sigma^{\rho^0 p} \approx \frac{1}{2} \left(\sigma^{\pi^+ p} + \sigma^{\pi^- p} \right) \tag{3.28}$$

$$\sigma^{\phi p} \approx \sigma^{K^+ p} + \sigma^{K^- p} - \sigma^{\pi^- p} \tag{3.29}$$

Photoproduction processes are classified similar to hadron hadron interactions. At high energies events with jet like structure, called hard photoproduction, are observed. The cross section for this process is very small and hard photoproduction is not important in the present analysis. The bulk of hadronic interactions is characterized by low transverse momenta and traditionally referred to as soft processes. Soft hadronic processes can be described phenomenologically by Regge theory (section 3.3.2). The following classification is commonly used for soft photoproduction.

- diffractive photoproduction
  The name of this event class originates from analogies to the diffraction of light by a circular aperture [48]. Diffractive photoproduction is classified as follows:
  - elastic diffraction ($\gamma p \rightarrow Vp$, $V : \rho^0, \omega, \phi$)
    In VDM this process is the analog to the elastic scattering process in hadron hadron collisions. The relative contribution of elastic diffraction to the total photoproduction cross section is similar to the relative contribution of elastic scattering in hadron hadron collisions. Elastic photoproduction of ρ^0 mesons accounts for ~ 80 % of the elastic diffractive cross section and is the interaction studied in this thesis.

- diffractive dissociation
  In this event class at least one of the incoming particles dissociates into a higher mass state (N or X with $M_X > M_i$, $M_N > M_p$). Diffractive dissociative events are classified as follows:
  - proton dissociation ($\gamma p \to XN$)
  - photon dissociation ($\gamma p \to Xp$)
  - double dissociation ($\gamma p \to XN$)

  The cross section of these processes has been found to approximately follow at a given $W_{\gamma p}$:

$$\frac{d^2\sigma}{dt dM^2_{X(N)}} \propto \frac{e^{bt}}{\left(M^2_{X(N)}\right)^a} \tag{3.30}$$

  with $a \approx 1$ [48]. The slope parameter b depends on the mass of the dissociative system $M_{N(X)}$. For single dissociation and masses above the resonance region, b is roughly half the value for elastic scattering.

- non diffractive photoproduction
  The remaining events are called non-diffractive. They are usually described by phenomenological models.

3.3.2 Regge Phenomenology

The high energy behavior of hadronic cross sections can presently not be determined from QCD, the microscopic theory of the strong interaction. Phenomenological models based on Regge's idea of scattering amplitudes analytically continued in the complex momentum plane are a possible approach to this data [23, 24, 16]. Those properties of Regge theory which are of interest for the analysis presented in this thesis are shortly summarized here.

The strong interaction between hadrons involve the exchange of quarks and gluons without net color exchange, thus objects like mesons and baryons are exchanged between strongly interacting hadrons.

Regge theory makes use of the so called crossing symmetry shown in figure 3.2. For the process $AB \to CD$ s is the square of the center of mass energy and t the squared four-momentum transfer. t is related to the scattering angle θ. In the crossed channel $A\bar{C} \to \bar{B}D$ the energy is given by t and the scattering angle related to s. Since the quantum numbers of the exchanged object in the s-channel reaction ($AB \to CD$) and the t-channel reaction ($A\bar{C} \to \bar{B}D$) are the same, both processes are assumed to be described by a common scattering amplitude, but in different regions of the variables s and t. The amplitude $A(s,t)$ can be expressed in the t-channel partial wave series by:

$$A(s,t) = \sum_{l=0}^{\infty} (2l+1) A_l(t) P_l(\cos\theta_t) \tag{3.31}$$

where P_l are the Legendre polynomials and $A_l(t)$ the l^{th}-partial wave amplitudes. The partial wave amplitude can be identified with a propagator-like term for the *exchanged* particles

$$A_l(t) = \frac{\Gamma_l(t)}{t - m_l^2} \tag{3.32}$$

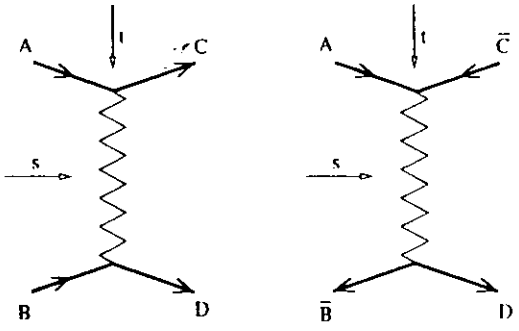

Figure 3.2: Diagrams of the s-channel ($AB \to CD$) and t-channel ($A\bar{C} \to \bar{B}D$) processes which are related by crossing symmetry.

where $\Gamma_l(t)$ is the partial decay width of a given particle of mass m_l. Now the scattering amplitude will be continued to complex angular momentum l. This enables to write the sum (3.31) as a Cauchy integral:

$$A(s,t) = \frac{1}{2i} \int_{path} dl \frac{e^{i\pi l} \pm 1}{2 \sin \pi l} (2l+1) \frac{\Gamma_l(t)}{t - m_l^2} P_l(\cos\theta_t) \tag{3.33}$$

Studying the t-channel reaction, it was experimentally found that the resonances which can be exchanged for a particular choice of the colliding particles lay on a straight line in the Chew-Frautschi plot (spin J versus mass m^2). This observation suggests, that for a given isospin and strangeness a function $l = \alpha(m_l^2)$, relating mass and angular momentum, exists. Expanding this function in a linear function ($\alpha(t) = \alpha(0) + \alpha' t$) around $m_l^2 = t$:

$$l = \alpha(m_l^2) \approx \alpha(t) + \frac{d\alpha(t)}{dt}(m_l^2 - t). \tag{3.34}$$

This can be used in equation (3.33):

$$A(s,t) = \frac{1}{2i} \int_{path} dl \frac{e^{i\pi l} \pm 1}{2 \sin \pi l} (2l+1) \frac{\Gamma_l(t)}{\alpha(t) - l} \frac{d\alpha(t)}{dt} P_l(\cos\theta_t). \tag{3.35}$$

Instead of an integral over many poles in equation (3.33), the amplitude is now given by an integration around just one pole $l = \alpha(t)$ in the complex l plane.

Assuming that the integral vanishes on a properly chosen path the integral reduces to the residue of the pole at $\alpha(t) = l$:

$$A(s,t) = -\pi \frac{e^{i\pi l} \pm 1}{2 \sin \pi l} (2\alpha(t)+1) \Gamma_{\alpha(t)} \frac{d\alpha(t)}{dt} P_{\alpha(t)}(\cos\theta_t). \tag{3.36}$$

The function $\alpha(t) = \alpha(0) + \alpha' t$ is usually called the Regge trajectory, representing a whole series of exchanged resonances of given isospin, strangeness and parity.

The asymptotic behavior of the amplitude for the reaction $AB \to CD$, in which t is negative and $|t| \ll s$ can now be written as

$$A(s,t) \overset{s\to\infty}{\sim} \beta(t) s^{\alpha(t)} \tag{3.37}$$

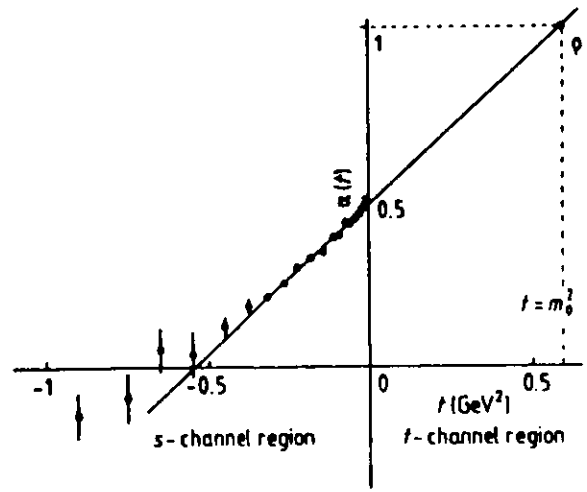

Figure 3.3: The values of $\alpha(t)$ (for $t \leq 0$) obtained by fitting to $\pi^- p \to \pi^0 n$ data together with the extrapolation of the linear ρ trajectory (from [24]).

since for $|t| \ll s$: $P_{\alpha(t)}(\cos\theta_t) \approx e^{-i\pi\alpha(t)}(s/s_0)^{\alpha(t)}$. The differential cross section in the two body process is therefore predicted to be:

$$\frac{d\sigma}{dt} \sim \frac{1}{s^2}|A(s,t)|^2 = |\beta(t)|^2 \left(\frac{s}{s_0}\right)^{2\alpha(t)-2} \tag{3.38}$$

The trajectory $\alpha(t)$ can be determined by plotting $\ln d\sigma/dt$ as a function of $\ln s$ at fixed t. Figure 3.3 shows the measured ρ trajectory for the s-channel reaction $\pi^- p \to \pi^0 n$. The points line up nicely with the resonances belonging to the ρ-trajectory (t-channel reaction $\pi^-\pi^0 \to \bar{p}n$).

The optical theorem relates the total cross section σ^{tot} to the imaginary part of the forward elastic scattering amplitude ($\sigma^{tot} = 1/s\Im(A)|_{t=0}$), so the forward differential cross section can be written as:

$$\left.\frac{d\sigma_{el}}{dt}\right|_{t=0} = \frac{1}{16\pi}(1+\eta^2)(\sigma^{tot})^2 \tag{3.39}$$

where η is the ratio of the forward real part to the forward imaginary part of the scattering amplitude. The optical theorem together with equation (3.37) leads to:

$$\sigma^{tot} \propto s^{\alpha(t=0)-1}. \tag{3.40}$$

So the high energy behavior of total hadron cross sections is determined by the highest lying trajectories, which in the Chew-Frautschi plot are the degenerated ω/f and ρ/a_2 trajectories ($\alpha_{\rho,\omega}(t=0) \approx 0.5$). They would lead to a total cross section $\sigma^{tot} \propto s^{-1/2}$. This behavior is not observed in hadron proton interactions at high energies. Instead total cross sections

above $\sqrt{s} = W \approx 10$ GeV are slowly rising. This implies, that if a Regge pole exchange is the dominant mechanism, there has to be a trajectory, called Pomeron $\mathbb{P}$ with $\alpha_{\mathbb{P}}(0) > 1$. It is generally supposed that the Pomeron represents gluon exchange [35, 67].

The slowly rising cross section can be explained by $\alpha_{\mathbb{P}}(0) > 1$, however such a power behavior should not continue indefinitely due to partial wave unitarity. The total cross section has to fulfill the Froissart-Martin bound:

$$\sigma^{tot} \leq \frac{c}{M_\pi^2}(\ln s)^2. \tag{3.41}$$

It is expected that the simultaneous exchange of many Pomerons will change the asymptotic behavior ($\sigma^{tot} \propto s^{\alpha_{\mathbb{P}}(0)-1}$) to at most a $(\ln s)^2$ behavior.

Total hadron proton cross sections can be successfully fitted by a sum of two terms, one due to the exchange of the highest lying Reggeon trajectory ($\rho/a_2, \omega/f$) and one due to the Pomeron trajectory. Such an ansatz has the form:

$$\sigma^{tot} = Xs^{\epsilon} + Ys^{-\eta} \tag{3.42}$$

where η and ϵ are effective exponents for Reggeon and Pomeron exchange. They are assumed to be the same for different interacting hadrons, while X and Y depend on the process under study. Donnachie and Landshoff [36] used pp and $p\bar{p}$ data with $\sqrt{s} > 10$ GeV and found:

$$\epsilon = 0.0808 \qquad \eta = 0.4525 \tag{3.43}$$

They used these powers also to fit the values for X and Y for various other hadron proton cross sections like $\pi^\pm p$, $K^\pm p$ and γp. Recently Cudell et al. [26] repeated the fits of Donnachie and Landshoff to pp and $p\bar{p}$ data. Using filtered data and non degenerated Reggeon trajectories ($\sigma^{tot} = Xs^{\epsilon} + Y_- s^{-\eta_-} + Y_+ s^{-\eta_+}$) their best estimate for the Pomeron intercept ($\alpha_{\mathbb{P}}(0) = 1-\epsilon$) is $\epsilon = 0.096^{+0.012}_{-0.009}$ but several models have a good χ^2 for values of ϵ in the range $[0.07, 0.11]$. In a very similar approach Covolan et al. [25] performed global fits to total cross section and η value data for $p^\pm p$, $\pi^\pm p$ and $K^\pm p$ with $\sqrt{s} \geq 6$ GeV. They obtained the secondary Reggeon trajectories from fits to the f/a and ω/ρ Chew-Frautschi plot and fixed the slope of the Pomeron trajectory ($\alpha'_{\mathbb{P}} = 0.25$ GeV^{-2}). A Born level simultaneous fit to the data yields a Pomeron intercept of $\alpha_{\mathbb{P}}(0) = 1.104 \pm 0.002$ and using an eikonalized amplitude they obtain $\alpha_{\mathbb{P}}(0) = 1.122 \pm 0.002$.

The exponents ϵ and η are effective exponents, where η accounts for four independent trajectories and a lower energy cut has to be introduced to exclude lower trajectories. The exponent ϵ is expected to show a (slow) dependence on s to assure the Froissart-Martin bound (3.41). For $\sqrt{s} > 10$ GeV and up to the highest available energy ($\sqrt{s} = 1.8$ TeV at the TEVATRON [40, 20]) the simple fit according to equation (3.42) is very successful.

In hadron hadron interactions it was found that for values $|t| \lesssim 0.3$ GeV^2 the elastic differential cross section $d\sigma/dt$ falls roughly exponentially with $|t|$:

$$\frac{d\sigma}{dt} \sim e^{bt} \tag{3.44}$$

The exponential behavior suggests that $\beta(t)$ in equation (3.38) can be written as $\beta(t) = \beta_0 e^{at}$ which, assuming a linear Pomeron trajectory, leads to:

$$\begin{aligned} \frac{d\sigma}{dt} &\sim \beta_0 \left(\frac{s}{s_0}\right)^{2\alpha_{\mathbb{P}}(t)-2} e^{at} \\ &= \beta_0 \left(\frac{s}{s_0}\right)^{2\alpha_{\mathbb{P}}(0)-2} e^{(a+2\alpha'_{\mathbb{P}}\ln\frac{s}{s_0})t} \end{aligned} \tag{3.45}$$

so that

$$b = a + 2\alpha'_{\mathbb{P}} \ln \frac{s}{s_0}. \tag{3.46}$$

Thus the forward peak sharpens as $\ln s$ increases. This effect is called shrinkage from which the slope of the Pomeron trajectory can be determined. Elastic pp and $p\bar{p}$ scattering yield a value of [33, 34]:

$$\alpha'_{\mathbb{P}} = 0.25 \text{ GeV}^{-2} \tag{3.47}$$

3.3.3 Elastic ρ^0 Photoproduction Cross Section

Elastic ρ^0 photoproduction can be measured at HERA in the reaction

$$e + p \rightarrow e + p + \rho^0. \tag{3.48}$$

The ρ^0 meson decays almost exclusively in a pair of charged pions. The analysis presented in this thesis is restricted to small values of Q^2. The upper limit on Q^2 is $Q^2_{max} \approx 4$ GeV^2 and the median Q^2 is about 10^{-5} GeV^2. Only events in which the outgoing electron was not detected in the ZEUS detector are accepted in this analysis. The kinematic variables used to describe the process are the invariant photon proton center of mass energy $W_{\gamma p} = \sqrt{4E_\gamma E_p}$ (or alternatively $y \approx E_\gamma/E_e$), where E_γ is the photon energy and the momentum transfer at the proton vertex $t = (\mathbf{p} - \mathbf{p}')^2$, where $\mathbf{p}$ and $\mathbf{p}'$ are the four momenta of the incoming and outgoing proton respectively.

For kinematical reasons a minimum momentum transfer is necessary for the transition $\gamma \rightarrow \rho^0$. So the following condition has to be fulfilled:

$$-t \geq |t_{min}| \approx M_p^2 \frac{(M_{\rho^0}^2 + Q^2)^2}{W_{\gamma p}^4} \tag{3.49}$$

In the kinematic range under study t_{min} is of order 10^{-8} GeV^2 and can be safely set to zero in the following.

As explained in section 3.2 ep scattering can be related to the scattering of virtual photons on protons (3.19). The VDM relates elastic γp to elastic Vp cross sections by the coupling f_V:

$$\sigma^{\gamma p \rightarrow Vp}(W_{\gamma p}) = \frac{4\pi\alpha}{f_V^2} \sigma^{Vp \rightarrow Vp}(W_{Vp}) \tag{3.50}$$

For elastic ρ^0 photoproduction equations (3.26) and (3.27) thus read:

$$\sigma_T^{\gamma^* p \rightarrow \rho^0 p}(W_{\gamma p}, Q^2) = \left(\frac{M_{\rho^0}^2}{M_{\rho^0}^2 + Q^2}\right)^2 \sigma^{\gamma p \rightarrow \rho^0 p}(W_{\gamma p}) \tag{3.51}$$

$$\sigma_L^{\gamma^* p \rightarrow \rho^0 p}(W_{\gamma p}, Q^2) = \left(\frac{M_{\rho^0}^2}{M_{\rho^0}^2 + Q^2}\right)^2 \xi^2 \frac{Q^2}{M_{\rho^0}^2} \sigma^{\gamma p \rightarrow \rho^0 p}(W_{\gamma p}) \tag{3.52}$$

Inserting these in equation (3.19) yields:

$$\frac{d^2\sigma^{ep \rightarrow ep\rho^0}}{dy dQ^2} = \varphi(y, Q^2) \sigma^{\gamma p \rightarrow \rho^0 p}(W_{\gamma p}) \tag{3.53}$$

where

$$\varphi(y, Q^2) = \frac{\alpha}{2\pi} \frac{1}{Q^2} \left[\frac{1 + (1-y)^2}{y} + 2\frac{1-y}{y} \left(\xi^2 \frac{Q^2}{M_{\rho^0}^2} - \frac{Q^2_{min}}{Q^2} \right) \right] \left(\frac{M_{\rho^0}^2}{M_{\rho^0}^2 + Q^2} \right)^2 \tag{3.54}$$

is the effective photon flux.

A measured ρ^0 electroproduction cross section ($ep \rightarrow ep\rho^0$) can thus be transformed into an elastic ρ^0 photoproduction cross section ($\gamma p \rightarrow \rho^0 p$) by dividing the electroproduction cross section by the effective photon flux integrated over the y and Q^2 range covered by the measurement.

Applying the optical theorem (3.39) to $\rho^0 p$ interactions yields:

$$\left.\frac{d\sigma^{\rho^0 p \rightarrow \rho^0 p}}{dt}\right|_{t=0} = \frac{1}{16\pi}(1+\eta^2)(\sigma^{tot}_{\rho^0 p})^2 \tag{3.55}$$

where η has been measured at high energies in hadron hadron interactions to be of the order 10% [61] and is set to 0 here. Since VDM relates γp to $\rho^0 p$ cross sections one can write:

$$\left.\frac{d\sigma^{\gamma p \rightarrow \rho^0 p}}{dt}\right|_{t=0} \approx \frac{4\pi\alpha}{f_{\rho^0}^2} \frac{1}{16\pi} (\sigma^{tot}_{\rho^0 p})^2 \tag{3.56}$$

Using the exponential behavior of elastic ρ^0 photoproduction one can write the cross section as:

$$\sigma^{\gamma p \rightarrow \rho^0 p} \approx \frac{4\pi\alpha}{f_{\rho^0}^2} \frac{1}{16\pi} \frac{(\sigma^{tot}_{\rho^0 p})^2}{b_{\gamma p \rightarrow \rho^0 p}} \tag{3.57}$$

The additive quark model relates $\sigma^{tot}_{\rho^0 p}$ to well measured hadronic cross sections by:

$$\sigma^{tot}_{\rho^0 p} \approx \frac{1}{2}(\sigma^{tot}_{\pi^+ p} + \sigma^{tot}_{\pi^- p}) \tag{3.58}$$

The slope $b_{\gamma p \rightarrow \rho^0 p}$ has to be fixed, too. Again, measurements of $\pi^+ p$ interactions could be used, assuming

$$b_{\gamma p \rightarrow \rho^0 p} \approx b_{\pi^+ p \rightarrow \pi^+ p}. \tag{3.59}$$

This approximation fits well to the data [10, 61].

The energy behavior of hadron hadron cross sections and energy behavior of the slope parameter b is described by Regge theory ((3.42) and (3.46)). Using these relations and equation (3.57) the elastic ρ^0 photoproduction cross section can be predicted, if the $\gamma\rho^0$ coupling f_{ρ^0} is known. Donnachie and Landshoff [37] and Schuler and Sjöstrand [97] used this procedure to predict the elastic ρ^0 photoproduction cross section. Their predictions are approximately 10%-20% higher than the measured values. This can be explained by the coupling constant f_{ρ^0} used by these authors. The coupling can be determined directly from the from e^+e^- collisions since the e^+e^- decay width of the ρ^0 is related to the coupling by $\Gamma(\rho^0 \rightarrow e^+e^-) = \alpha^2/3 \left(f^2_{\rho^0}/4\pi \big|_{e^+e^-} \right)^{-1} M_{\rho^0}$. The coupling $f^2_{\rho^0}/4\pi\big|_{e^+e^-}$ is smaller than the coupling determined from photoproduction data $f^2_{\rho^0}/4\pi$ [10] relevant in the analysis of elastic ρ^0 photoproduction. The difference in the coupling obtained from e^+e^- collisions and from photoproduction might be caused by intrinsic uncertainties in VDM and by the model dependence of the determination of the photoproduction results (assuming the additive quark

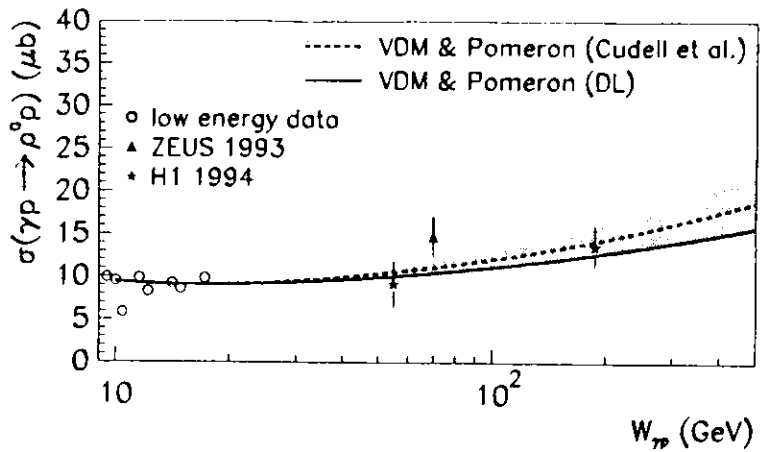

Figure 3.4: Measurements and predictions for the $\gamma p \to \rho^0 p$ cross section versus $W_{\gamma p}$ (from [49]).

model) [49]. To be consistent within photoproduction the coupling $f^2_{\rho^0}/4\pi$ was determined from elastic ρ^0 photoproduction cross section measurements with $W_{\gamma p} > 9$ GeV by inverting equation (3.57) ($f^2_{\rho^0}/4\pi = 2.69 \pm 0.27$ [49]).

Figure 3.4 shows predictions for the elastic ρ^0 photoproduction cross section [49] together with low energy data used to determine $f^2_{\rho^0}/4\pi$. The full line shows the prediction using the results of the parameters given by Donnachie and Landshoff (3.43). The dashed line indicates the prediction for the elastic ρ^0 photoproduction cross section using a value for ϵ of 0.096 as determined by Cudell et al. and the shaded area shows the effect on the predicted cross section by varying ϵ between 0.07 and 0.11. Details on the procedure used to derive the predictions in figure 3.4 are given in [49].

3.3.4 Decay Angular Distribution

The ρ^0 decay pions can be used as an analyzer of the spin states of the ρ^0. Analyzing the ρ^0 decay distribution allows to study the spin dependent properties of the production process. The relevant formalism has been developed in [96].

The angular distribution of the decay pion is studied in the ρ^0 rest frame. In this frame a right handed coordinate system is defined as follows. The $\vec{x} - \vec{z}$ plane is the production plane ($\gamma^* \rho^0$ plane in the hadronic center of mass system) and $\vec{y}$ the normal to this plane. The quantization axis can be chosen in different ways. A specific choice is the s-channel helicity system in which the $\vec{z}$ axis is opposite to the direction of the outgoing proton. This frame is the most convenient system for describing the ρ^0 decay in photoproduction [10]. Theoretical aspects of s-channel helicity conservation in diffractive scattering are discussed in [46].

The polar angle θ_h is defined as the angle between the π^+ and the $\vec{z}$ axis and the azimuthal

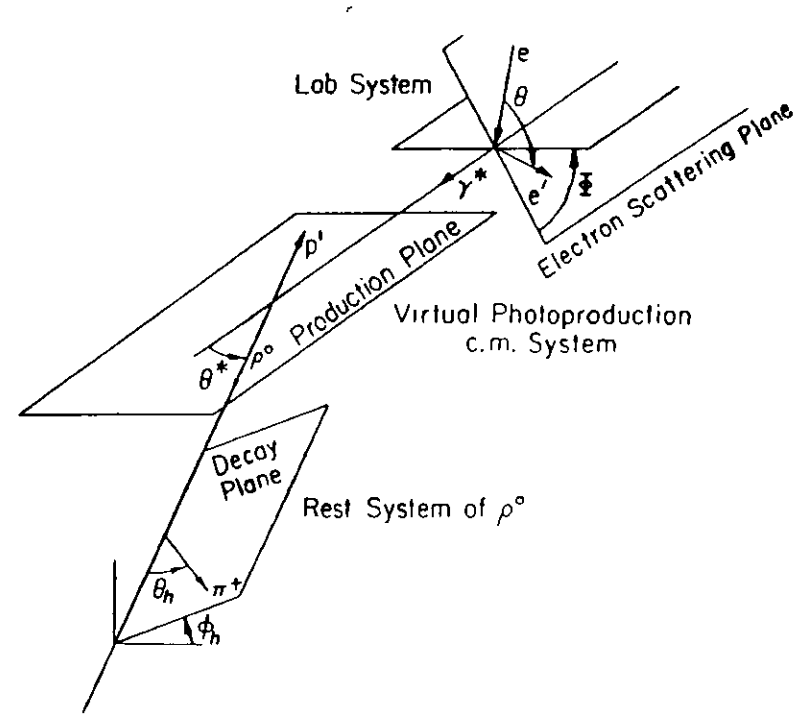

Figure 3.5: The ρ^0 decay angles in the s-channel helicity system.

angle ϕ_h is the angle between the production plane and the decay plane ($\pi^+\pi^-$ plane in the ρ^0 rest frame). A third angle Φ denotes the angle between the production plane and the electron scattering plane. All three angles are shown in figure 3.5.

The ρ^0 decay angular distribution $W(\cos\theta_h, \phi_h, \Phi)$ will be studied in terms of the ρ^0 spin density matrix [96]. The ρ^0 spin density matrix ρ in general can be decomposed into nine independent matrices ρ^α, where the matrices $\alpha = 0$ to 3 and 4 describe ρ^0 production by transverse and longitudinal photons respectively and the matrices $\alpha = 5$ to 8 measure interference between transverse and longitudinal photons.

In the analysis presented in this thesis the longitudinal and transverse photon flux (Γ_L, Γ_T) cannot be varied so the matrices ρ^0 and ρ^4 cannot be separated. The following combinations of matrix elements ρ^α_{ik} are therefore measured:

$$r^{04}_{ik} = \frac{\rho^0_{ik} + (\epsilon + \delta) R \rho^4_{ik}}{1 + (\epsilon + \delta) R} \qquad (3.60)$$

$$r^{\alpha}_{ik} = \begin{cases} \dfrac{\rho^{\alpha}_{ik}}{1+(\epsilon+\delta)R} & \alpha = 1-3 \\ \dfrac{\sqrt{R}\rho^{\alpha}_{ik}}{1+(\epsilon+\delta)R} & \alpha = 5-8 \end{cases} \quad (3.61)$$

with

$$R = \frac{\sigma_L}{\sigma_T} \quad (3.62)$$

$$\epsilon = \left[1 + \frac{y^2}{2(1-y)} \frac{1}{1-\frac{Q^2_{min}}{Q^2}}\right]^{-1} \quad (3.63)$$

$$\delta = \frac{2M_e^2}{Q^2}(1-\epsilon) = \frac{2Q^2_{min}}{Q^2}\frac{1-y}{y^2}(1-\epsilon) \quad (3.64)$$

$$\frac{\Gamma_L}{\Gamma_T} = \epsilon + \delta \quad (3.65)$$

R is the ratio of the cross sections for ρ^0 photoproduction by longitudinal and transverse photons. Usually in ρ^0 electroproduction experiments δ is neglected and $Q^2_{min}/Q^2 \approx 0$ so ϵ reduces to $\epsilon = (2(1-y))/(1+(1-y)^2)$. For the analysis presented in this thesis these approximations are not good since the whole Q^2 spectrum down to Q^2_{min} is measured. The y dependence of ϵ and δ in the range under study (50 GeV $< W_{\gamma p} <$ 100 GeV) is very small. Q^2 is not measured in this analysis, so in the following ϵ and δ are averaged over Q^2 and given for the mean y:

$$\langle\epsilon\rangle = 0.998 \quad (3.66)$$

$$\langle\delta\rangle = 0.052 \quad (3.67)$$

$$\frac{\Gamma_L}{\Gamma_T} = \langle\epsilon\rangle + \langle\delta\rangle = 1.05 \quad (3.68)$$

The normalized decay angular distribution of the π^+ with an unpolarized electron beam is given in terms of 15 spin density matrix elements:

$$\begin{aligned} W(\cos\theta_h, \phi_h, \Phi) = \frac{3}{4\pi}\Big[&\frac{1}{2}(1-r^{04}_{00}) + \frac{1}{2}(3r^{04}_{00}-1)\cos^2\theta_h - \sqrt{2}\Re r^{04}_{10}\sin 2\theta_h\cos\phi_h - \\ &r^{04}_{1-1}\sin^2\theta_h\cos 2\phi_h - \\ &\epsilon\cos 2\Phi(r^1_{11}\sin^2\theta_h + r^1_{00}\cos^2\theta_h - \sqrt{2}\Re r^1_{10}\sin 2\theta_h\cos\phi_h - \\ &r^1_{1-1}\sin^2\theta_h\cos 2\phi_h) - \\ &\epsilon\sin 2\Phi(\sqrt{2}\Im r^2_{10}\sin 2\theta_h\sin\phi_h + \Im r^2_{1-1}\sin^2\theta_h\sin 2\phi_h) + \\ &\sqrt{2\epsilon(1+\epsilon+\delta)}\cos\Phi(r^5_{11}\sin^2\theta_h + r^5_{00}\cos^2\theta_h - \sqrt{2}\Re r^5_{10}\sin 2\theta_h\cos\phi_h - \\ &r^5_{1-1}\sin^2\theta_h\cos 2\phi_h) + \\ &\sqrt{2\epsilon(1+\epsilon+\delta)}\sin\Phi(\sqrt{2}\Im r^6_{10}\sin 2\theta_h\sin\phi_h + \\ &r^6_{1-1}\sin^2\theta_h\sin 2\phi_h)\Big] \end{aligned} \quad (3.69)$$

where $\Re$ and $\Im$ stand for the real and imaginary part of the matrix element. If the electrons are transversely polarized, the following terms have to be added to equation (3.69):

$$\begin{aligned} W^{\text{tr pol}}(\cos\theta_h, \phi_h, \Phi) = \frac{3}{4\pi}(1-\epsilon)\frac{2m_e}{Q}P \times \\ \Big[\Big(\sqrt{\frac{1-\epsilon}{1+\epsilon}}\cos\alpha_l\cos\Phi + \sin\alpha_l\sin\Phi\Big)(\sqrt{2}\Im r^7_{10}\sin 2\theta_h\sin\phi_h + \\ \Im r^7_{1-1}\sin^2\theta_h\sin 2\phi_h) \\ \Big(\sqrt{\frac{1-\epsilon}{1+\epsilon}}\cos\alpha_l\sin\Phi - \sin\alpha_l\cos\Phi\Big)(r^8_{11}\sin^2\theta_h + r^8_{00}\cos^2\theta_h - \\ \sqrt{2}\Re r^8_{10}\sin 2\theta_h\cos\phi_h - \\ r^8_{1-1}\sin^2\theta_h\cos 2\phi_h)\Big] \end{aligned} \quad (3.70)$$

where α_l is the angle between the plane of polarization and the electron scattering plane and P is the degree of transverse polarization of the electron beam. $W^{\text{tr pol}}$ contains a factor m_e/Q and therefore the terms in equation (3.70) give a sizeable contribution to the decay angular distribution only for $Q \lesssim m_e$. Furthermore $W^{\text{tr pol}}$ contains a factor $1-\epsilon$. For the data presented in this thesis the average ϵ is 0.998 and therefore (3.70) can be neglected. So in the following the decay angular distribution is given by equation (3.69).

In the case of s-channel helicity conservation at the γp vertex all spin density matrix elements except r^{04}_{00}, r^1_{1-1}, $\Im r^2_{1-1}$, $\Re r^3_{10}$, $\Im r^6_{10}$, $\Im r^7_{10}$ and $\Re r^8_{10}$ are zero and $r^1_{1-1} = -\Im r^2_{1-1}$, $\Re r^5_{10} = -\Im r^6_{10}$, $\Im r^7_{10} = \Re r^8_{10}$. Furthermore for s-channel helicity r^{04}_{00} conservation the following relation holds:

$$R = \frac{1}{\epsilon+\delta}\frac{r^{04}_{00}}{1-r^{04}_{00}}. \quad (3.71)$$

Therefore by measuring the $\cos\theta_h$ distribution the ratio R can be determined.

Since in the analysis presented here the angle Φ is not measured the decay angular distribution reduces to:

$$\begin{aligned} W(\cos\theta_h, \phi_h) = \frac{3}{4\pi}\Big[&\frac{1}{2}(1-r^{04}_{00}) + \frac{1}{2}(3r^{04}_{00}-1)\cos^2\theta_h - \sqrt{2}\Re r^{04}_{10}\sin 2\theta_h\cos\phi_h - \\ &r^{04}_{1-1}\sin^2\theta_h\cos 2\phi_h\Big]. \end{aligned} \quad (3.72)$$

Chapter 4

Event Selection

In this chapter the trigger and the selection cuts for elastic ρ^0 photoproduction events will be discussed. ρ^0 mesons are measured in the decay channel $\rho^0 \to \pi^+\pi^-$. The branching ratio is ~100%. In the data presented, the scattered electron and proton escape undetected, so elastic ρ^0 photoproduction events are characterized by two oppositely charged tracks in the central tracking detector and no energy deposition in the calorimeter apart from that of the decay pions.

4.1 The Elastic ρ^0 Photoproduction Trigger

As mentioned in chapter 2.2.4 the ZEUS trigger has three levels. To trigger elastic ρ^0 photoproduction events a dedicated ρ trigger was developed. This trigger demands the following requirements:

- at the first level trigger (FLT) at least 464 MeV in the electromagnetic section of the rear calorimeter excluding the towers surrounding the beampipe ($REMC_{FLT}$), at least one good track candidate, less than 1250 MeV in the innermost ring surrounding the beam-pipe of the forward calorimeter ($FCAL\ BP_{FLT}$) and no veto signals from the ZEUS veto counters (section 2.2.3). The energies $REMC_{FLT}$ and $FCAL\ BP_{FLT}$ are measured by the CFLT (section 2.2.2).

- at the second level trigger (SLT) less than 5 GeV in the barrel and forward calorimeter ($BCAL_{SLT}$, $FCAL_{SLT}$) and no timing-veto signal from the calorimeter,

- at the third level trigger (TLT) the full event information of ZEUS is available. More stringent veto cuts are applied. To select ρ^0 photoproduction events two different TLT trigger streams are used. Both require at least one track pointing to the interaction region and an event vertex in z within 66 cm around the nominal vertex. The number of tracks has to be less than four (TLT ρ trigger) or six (TLT ω trigger) and the invariant mass of one 2 track pair smaller than 1.5 GeV (TLT ρ trigger) or the total invariant mass smaller than 2.5 GeV (TLT ω trigger). The mass calculation uses the momentum measurement from the CTD assuming that all particles are pions. In the 1994 running period both triggers were prescaled by a factor of six.

The efficiency of all the trigger cuts, except the $REMC_{FLT}$ requirement, is very high and can be determined from Monte Carlo events simulating ρ^0 photoproduction (section 5), which

are passed through the ZEUS detector simulation program MOZART, the trigger simulation program ZGANA and the reconstruction program ZEPHYR. The result derived from the Monte Carlo is correct, if the efficiencies in data are reproduced by the Monte Carlo. To make sure that this is the case all the trigger cuts are examined, except the $REMC_{FLT}$ requirement which will be discussed in section 6.1.1.

All the veto cuts are chosen to remove clear background events with a negligible loss of ep events. The veto cuts are not simulated in the trigger Monte Carlo program. An outline of all the veto cuts follows.

The veto cuts at the FLT are based on the timing in the veto counters upstream the proton beam direction. These timing cuts are chosen to remove obvious proton beamgas interactions. At SLT and TLT the calorimeter is used to provide a veto signal in case of a clear background event. Non ep events can be identified by the time of the event which is very precisely measured by the calorimeter. By the calibration, the mean calorimeter time for an event originating from the interaction point is zero. Upstream proton beamgas interactions, which are the most severe background at the SLT, have early RCAL times or big time differences between FCAL and RCAL. Similarly upstream electron beamgas interactions can be vetoed by an early FCAL time. At the SLT also events with an unphysically high value of $E - P_z$ are vetoed. Events triggered at FLT by noise in a photo multiplier are identified at SLT and TLT as having a cell with large energy imbalance, the difference in energy between the left and right photo multiplier, while the rest of the calorimeter is quiet. Cosmic muons are vetoed at the SLT by the time difference between the upper and lower half of BCAL. At the TLT, cosmic and halo muon events are rejected by making use of the time and position of the energy deposits in the calorimeter as well as the TLT track and vertex information. Details on the veto algorithms used at the SLT and TLT can be found in [22] and [12].

Highly prescaled control trigger streams, which use relaxed trigger cuts can be used to determine the efficiency of the trigger cuts in data. This efficiency has to be compared to the efficiency obtained from the Monte Carlo simulation. If necessary, cuts on offline quantities are introduced in data and Monte Carlo events to get good agreement in the trigger efficiencies. Data and Monte Carlo events are compared after selecting ρ^0 candidates by requiring exactly two, oppositely charged tracks from a vertex within three sigma around the mean vertex measured in the 1994 running period (section 4.3.1).

- The FLT trigger cuts are studied separately.
  - For the cut of at least one good track candidate, the vector meson control trigger streams can not be used to determine the efficiency in the data, since all triggers require this condition. So an independent control trigger, which does not require tracking is used, in this case the *tagged photoproduction trigger*. This trigger requires at the FLT a coincidence of an energy deposition in the rear calorimeter and a tag in the electron detector of the luminosity system. The efficiency of one good track candidate for the selected events in data is bigger than 95% and agrees with the Monte Carlo efficiency within 2% after applying cuts on the track quality, namely the pseudorapidity $|\eta| < 2.1$ and the transverse momentum $P_T > 150$ MeV of both tracks (section 5.3). The difference between data and Monte Carlo can be understood from the different η spectra of tagged and ρ^0 photoproduction events. By running the trigger simulation program ZGANA on data the correctness of the simulation program is checked as well. It turns out that the simulation is correct within 1%.
  - The cut on $FCAL\ BP_{FLT}$ does not affect elastic ρ^0 photoproduction events since the transverse momentum of the scattered proton is too small to reach the forward calorimeter and the calorimeter noise is much smaller than 1.2 GeV. But for proton dissociative ρ^0 photoproduction, in which the outgoing hadron is excited into a state M_N, energy can be deposited in the forward calorimeter. A control stream, which differs from the ρ trigger by the cut $FCAL\ BP_{FLT} < 5000$ MeV is used to compare data and Monte Carlo. Figure 4.1 shows the fraction of events fulfilling the cut $FCAL\ BP_{FLT} < 1250$ MeV for the control sample (full dots) and a proton dissociative Monte Carlo sample (open dots) as a function of the energy in the two innermost rings surrounding the beampipe $E_{FCAL\ BP2}$, measured offline. The fraction of events vetoed by the cut $FCAL\ BP_{FLT} < 1250$ MeV rises slowly and reaches $\approx 50\%$ for 3 GeV. To obtain a good agreement between data and Monte Carlo sample a cut on $E_{FCAL\ BP2}$ at 1.2 GeV is introduced. As already mentioned, this cut has no effect for elastic ρ^0 photoproduction events, but is important in the study of proton dissociative ρ^0 photoproduction (section 7.4).
- The efficiency of the SLT energy cuts is determined by using a control trigger stream, which is identical to the ρ trigger, but has no SLT energy cut. On top of the selection cuts mentioned above, elastic ρ^0 photoproduction events are selected by requiring that in the calorimeter no energy deposition above noise apart the one from the decay pions (section 4.3.2) is found. After applying this cut the SLT energy distribution for BCAL and FCAL peaks well below the 5 GeV. The maximum SLT energy in data and Monte Carlo is around 3 GeV. Also for proton dissociative events the SLT energy cut in FCAL has an efficiency of 100% since the FLT cut on $FCAL\ BP_{FLT}$ is already tighter. So the SLT energy cuts have an efficiency of 100% in data and Monte Carlo sample.

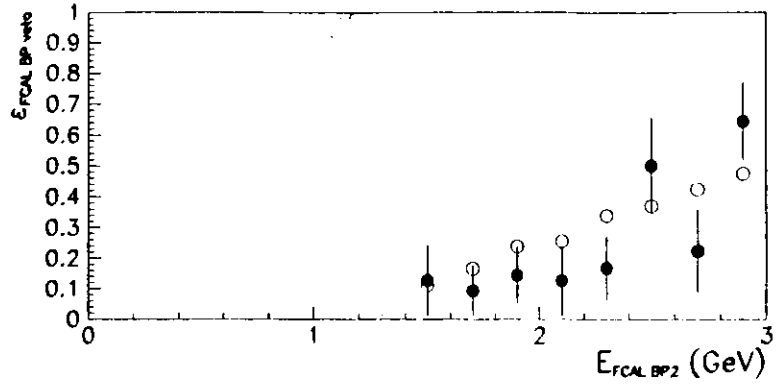

Figure 4.1: The fraction of events fulfilling the cut $FCAL\ BP_{FLT} < 1250$ MeV for the control sample (full dots) and a proton dissociative Monte Carlo sample (open dots) as a function of the energy in FCAL in the two innermost rings surrounding the beampipe.

- The TLT tracking cuts are studied with a control trigger stream which does not require any TLT tracking. For data and the Monte Carlo sample the number of tracks found at the TLT is lower than the number of tracks found offline. Since offline two tracks are required, the upper limit on the number of tracks at the TLT has an efficiency of 100%. Two prescaled trigger streams are used at the TLT which have different cuts on the invariant mass. To add up the events from both streams in one analysis it has to be assured that the two streams accept ρ^0 events with the same efficiency. So the fraction of events, which are triggered exclusively by one trigger stream, is determined. After applying a cut on the invariant two track mass, calculated offline, of $M_{\pi^+\pi^-} < 1.2$ GeV is introduced only less than 0.01% of the events taken by the ρ trigger are not triggered by the ω trigger and 0.27% of the events taken by the ω trigger are not triggered by the ρ trigger. The difference in the trigger efficiency between the two trigger streams increases with increasing mass and becomes sizeable above 1.2 GeV. So the analysis will be restricted to $M_{\pi^+\pi^-} < 1.2$ GeV. A vertex at the TLT is only reconstructed, if at least one track is pointing to the interaction region. The efficiency of the at least one TLT vertex track and a TLT event vertex in z within 66 cm around the nominal vertex is bigger than 98% for the selected events and well reproduced by the Monte Carlo.

As already mentioned the two TLT trigger streams used in this analysis are prescaled. For each physics run the prescale factor can be determined, since in the run summary the number of events fulfilling the trigger N_{trig} and the number of events taken by this trigger after prescale N_{take} are recorded. The prescale factor is given by $P = N_{trig}/N_{take}$. A correction factor for the prescale correction of two trigger streams can be defined as:

$$C = \frac{1}{P_{\rho\ trigger}} + \frac{1}{P_{\omega\ trigger}} - \frac{1}{P_{\rho\ trigger} P_{\omega\ trigger}} \tag{4.1}$$

To correct for the prescale factors the luminosity for each physics run is multiplied by its correction factor C.

In table 4.1 the efficiencies of the trigger requirements, for ρ^0 candidates (two oppositely charged tracks from a vertex), as determined from control samples and a Monte Carlo simulation are summarized. The efficiencies are close to 100% and agree very well between data and Monte Carlo after applying the extra selection criteria.

trigger requirement	efficiency from data	efficiency from MC	extra selection criteria
FLT: good track	95%	97%	$\|\eta\| < 2.1$ and $P_T > 150$ MeV
FLT: $FCAL\ BP_{FLT}$	100%	100%	$E_{FCAL\ BP2} < 1.2$ GeV
SLT: $BCAL_{SLT}$, $FCAL_{SLT}$	100%	100%	
TLT: multiplicity cut	100%	100%	
TLT: vertex cut	98%	99%	
TLT: mass cut	100%	100%	$M_{\pi^+\pi^-} < 1.2$ GeV

Table 4.1: Trigger efficiencies for ρ^0 candidates in data (control sample) and Monte Carlo. The extra selection criteria have to be applied to get a good agreement between data and Monte Carlo.

4.2 Reconstruction of Kinematic Variables

In section 3.1 the kinematics variables describing ρ^0 photoproduction are introduced. Since for this data sample only the decay pions of the ρ^0 are measured in the ZEUS detector, the kinematic variables have to be reconstructed from the momenta of the pions.

The selection cuts reject events in which the scattered electron hits the ZEUS calorimeter. This restricts Q^2 to be below $Q^2_{max} \approx 4$ GeV^2. The minimal Q^2 is given by $Q^2_{min} = M_e^2 y^2/(1-y)$. For $Q^2 = Q^2_{min}$ the virtual photon has zero transverse momentum and the longitudinal momentum $P_{z\gamma}$ can be approximated by $-E_\gamma$, since Q^2_{min} is of the order of 10^{-9} GeV^2 in the kinematic range under study. Energy and momentum conservation reads:

$$E_\gamma + E_p = E_{p'} + E_\rho \tag{4.2}$$
$$P_{z\gamma} + P_{zp} = P_{zp'} + P_{z\rho} \tag{4.3}$$

Subtracting equation (4.3) from (4.2) yields:

$$E_\gamma - P_{z\gamma} = 2E_\gamma \approx E_\rho - P_{z\rho} \tag{4.4}$$

since $E_p \approx P_{zp}$ and $E_{p'} \approx P_{zp'}$.

The photon-proton center of mass energy can now be expressed as:

$$W^2 \approx 4E_\gamma E_p \approx 2(E_\rho - P_{z\rho})E_p \tag{4.5}$$

The energy E_ρ is given by $E_{\pi^+} + E_{\pi^-}$ and $P_{z\rho}$ by $P_{z\pi^+} + P_{z\pi^-}$. The energies of the pions are calculated from the measured three momenta in the CTD assuming the tracks are pions.

The four-momentum transfer t at the proton vertex in the above approximation ($Q^2 \approx 0$, $P_{z\gamma} = -E_\gamma$) is given by:

$$\begin{aligned} t &= -Q^2 - 2qp_\rho + M_\rho^2 \\ &\approx -2E_\gamma(E_\rho + P_{z\rho}) + M_\rho^2 \\ &= -(E_\rho^2 - P_{z\rho}^2) + M_\rho^2 \\ &= -P_{T\rho}^2 \\ &= -P_T^2 = -(P_{x\pi^+} + P_{x\pi^-})^2 - (P_{y\pi^+} + P_{y\pi^-})^2 \end{aligned} \tag{4.6}$$

As can be seen from this derivation for non zero Q^2 the reconstructed P_T^2 will differ from $-t$. This effect will be discussed in more detail below.

The decay angles in the helicity frame, defined in section 3.3.4, are also reconstructed in the above approximation. A photon virtuality of $Q^2 \approx 0$ and no transverse momentum for the photon and the incoming proton are assumed. In this approximation only two angles can be measured, namely θ_h and ϕ_h. Φ defined as the angle between the lepton scattering and the production plane is not measurable, since the lepton scattering plane is undefined in this approximation.

The smearing in the kinematic variables and the decay angles, due to the detector resolution, is determined from a Monte Carlo simulation. Events simulating elastic ρ^0 photoproduction are passed through the ZEUS detector simulation program MOZART, the trigger simulation program ZGANA and the same reconstruction program ZEPHYR as the data. Radiation of

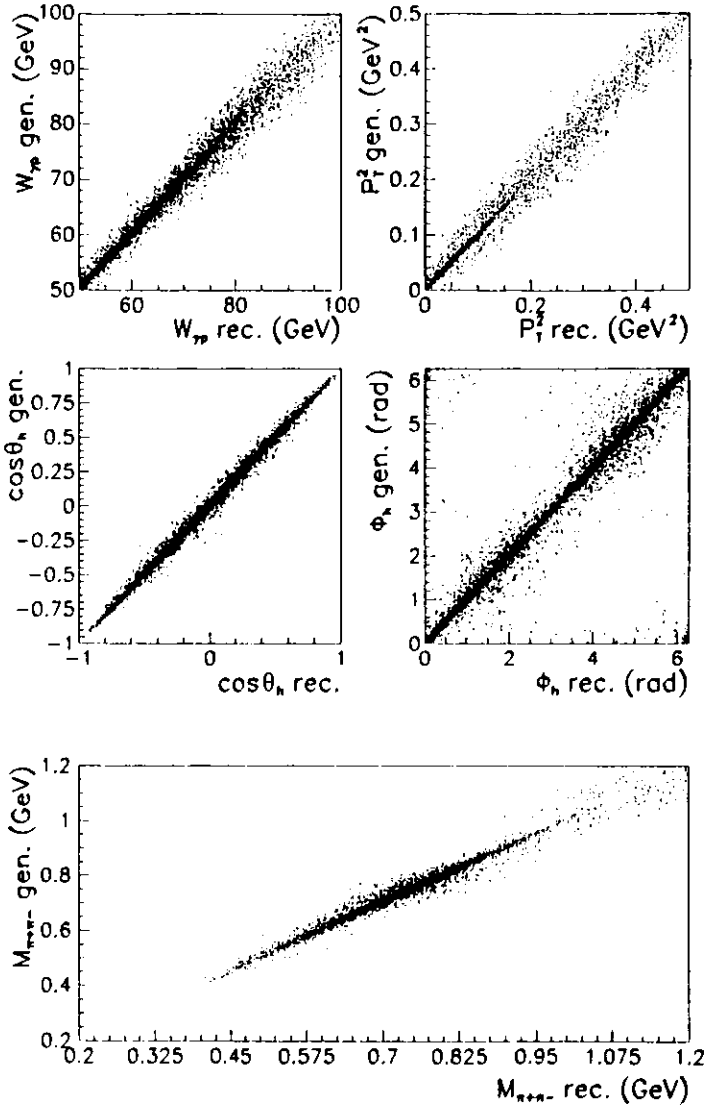

Figure 4.2: Correlation between the reconstructed and the generated values for the kinematic variables and the decay angles.

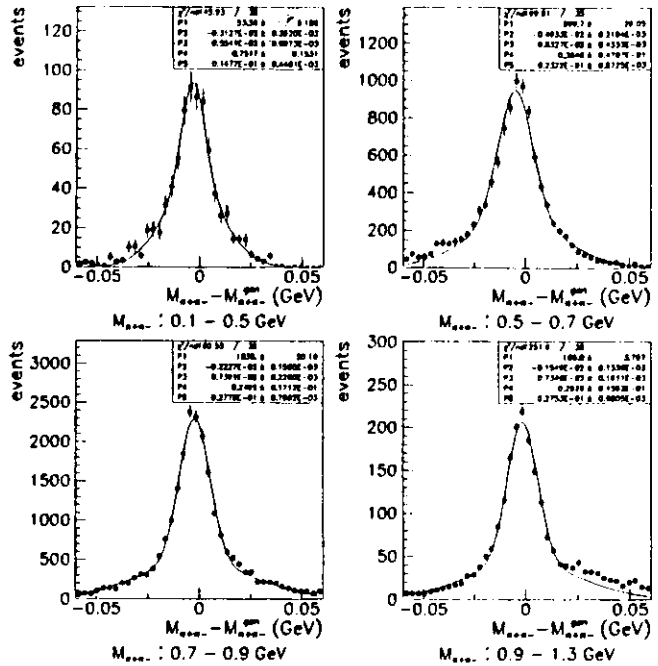

Figure 4.3: Difference between the reconstructed and generated mass for different mass bins. Superimposed is the result of a fit with a double Gaussian (4.7).

real photons from the incoming or outgoing electron is not included in the simulation (section 5). The smearing determined by comparing the generated and the reconstructed values of a kinematic variable includes the effects of the detector resolution and the approximation given above. In figure 4.2 the generated versus the reconstructed $W_{\gamma p}$, P_T^2, $\cos\theta_h$, ϕ_h and $M_{\pi^+\pi^-}$ are shown. A good correlation between the generated and the reconstructed values is seen. To look closer at the smearing, the resolution, defined as difference between reconstructed and generated values is studied. As an example figure 4.3 shows the resolution in mass ($M_{\pi^+\pi^-} - M_{\pi^+\pi^-}^{gen}$), for different bins in $M_{\pi^+\pi^-}$. The resolution can be well described by a double Gaussian of the form:

$$f(M_{\pi^+\pi^-} - M_{\pi^+\pi^-}^{gen}) = P_1 \left(e^{-\frac{1}{2}\left[\frac{(M_{\pi^+\pi^-} - M_{\pi^+\pi^-}^{gen}) - P_2}{P_3}\right]^2} + P_4\, e^{-\frac{1}{2}\left[\frac{(M_{\pi^+\pi^-} - M_{\pi^+\pi^-}^{gen}) - P_2}{P_5}\right]^2} \right). \quad (4.7)$$

$W_{\gamma p}$ bin (GeV)	P_2 (MeV)	P_3 (MeV)	P_4^1	P_4^2 (GeV^{-1})	P_5^1 (MeV)	P_5^2
50-100	-2.2	7.4	0.39	0.15	15.0	14.0
50-60	-2.7	6.4	0.34	0.27	4.0	21.0
60-70	-2.6	8.6	0.71	0.58	-6.0	38.0
70-80	-1.7	13.7	1.79	1.49	17.0	16.0
80-100	4.8	33.6	0.0	0.0	0.0	0.0

Table 4.2: The parameters describing the mass resolution in different $W_{\gamma p}$ bins according to equation (4.7).

As a result of a fit with this function it is found that the reconstructed mass is shifted versus the generated one by -2 MeV. The contribution of the second Gaussian P_4 is non negligible. The sigma of the dominating Gaussian $P_3 (= \sigma_{M_{\pi^+\pi^-}})$ is on the order 7 MeV. The parameter P_4 decreases as a function of $M_{\pi^+\pi^-}$ and P_5 increase as a function of $M_{\pi^+\pi^-}$. This dependence can be parameterized by linear functions $P_4 = P_4^1 - P_4^2 M_{\pi^+\pi^-}$[GeV]) and $P_5 = P_5^1 + P_5^2 M_{\pi^+\pi^-}$[GeV]). The mass resolution was also studied as function of $W_{\gamma p}$, P_T^2, $\cos\theta_h$ and ϕ_h. The mass resolution increases as a function of $W_{\gamma p}$ but no dependence is seen on P_T^2, $\cos\theta_h$ and ϕ_h. The parameters (P_2 to P_5) describing the mass resolution are summarized in table 4.2 for the $W_{\gamma p}$ bins, used in this analysis. These results will be used later in the analysis of the $M_{\pi^+\pi^-}$ distributions, when the corrected mass distribution is fitted by a convolution of the theoretical model and equation (4.7). The increase of the mass resolution for increasing $W_{\gamma p}$ can be understood from the fact that at low $W_{\gamma p}$ the tracks are well measured in the tracking chambers and for big $W_{\gamma p}$ the tracks are short, so the resolution is worse. A similar effect is seen in $\sigma_{P_T^2}$, which also increases as a function of $W_{\gamma p}$.

The decay angular distributions $\cos\theta_h$ and ϕ_h will be studied in this analysis as function of $M_{\pi^+\pi^-}$ and P_T^2. The resolution in $\cos\theta_h$ and ϕ_h decreases as $M_{\pi^+\pi^-}$ increases. On the other hand $\sigma_{\cos\theta_h}$ shows no dependence on P_T^2, but σ_{ϕ_h} increases for decreasing P_T^2. This is expected since for small $|t|$ the production plane is badly measured and for $t = t_{min}$ the photon and the ρ^0 are collinear, so ϕ_h is undefined.

The resolution in P_T^2 and $W_{\gamma p}$ is studied as well, but for the results presented in chapter 9 only corrected $M_{\pi^+\pi^-}$, $\cos\theta_h$ and ϕ_h are needed, so the focus is put on these variables. No systematic shifts between the generated and the reconstructed variables are seen for P_T^2, $W_{\gamma p}$, $\cos\theta_h$ and ϕ_h. In table 4.3 the typical sigma P_3 of the dominating Gaussian in all variables is listed together with the bin width chosen for these variable in the further analysis. The bin width is always chosen to be bigger than the resolution in the all regions, of the kinematic

quantity	sigma of the Gaussian	bin width in the analysis
$M_{\pi^+\pi^-}$	7 MeV	25 MeV
$\cos\theta_h$	0.04	0.08
ϕ_h	0.20 rad	$\pi/10$ rad
P_T^2	0.004 GeV^2	$\geq$ 0.00625 GeV^2
$W_{\gamma p}$	0.3 GeV	2.0 GeV

Table 4.3: The resolution, defined as the sigma of the dominating Gaussian and the chosen bin widths for the kinematic variables and the decay angles.

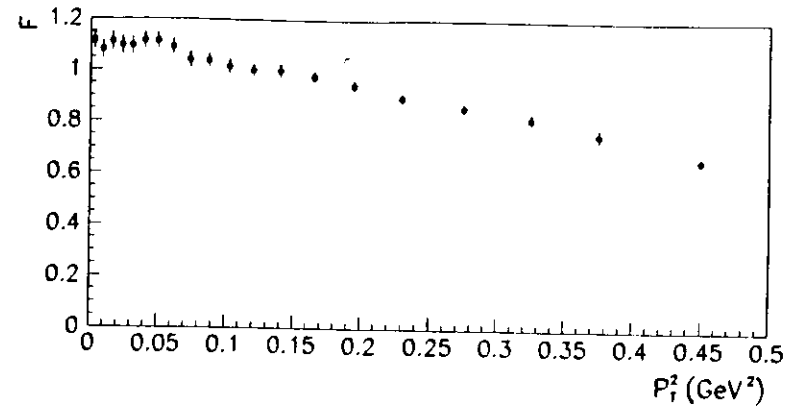

Figure 4.4: The correction function used to convert the measured P_T^2 distribution to a $|t|$ distribution. The correction increases for increasing P_T^2.

variables, under study.

As already mentioned above, $-P_T^2$ is used as a measure of t. For non zero Q^2 this approximation will become worse for increasing P_T^2, because big P_T^2 can be caused by $|t|$ or Q^2. The mean difference between P_T^2 and $|t|$ can be translated in a correction function F which has to be applied to the P_T^2 distribution to get the $|t|$ distribution. This correction function is defined as

$$F = \frac{\text{generated events in } P_T^2}{\text{generated events in } |t|} \tag{4.8}$$

and is evaluated from the Monte Carlo, assuming the Q^2 distribution given by (3.53). In figure 4.4 the function F is shown versus P_T^2. The correction starts to become big above 0.5 GeV^2 so this analysis is restricted to $P_T^2 < 0.5$ GeV^2. The correction function F is determined for each selected region of kinematic variables under study separately.

4.3 Selection Cuts for Elastic ρ^0 Events

Elastic ρ^0 photoproduction events are characterized in the ZEUS detector by two charged pions in the central tracking chamber (CTD) and no energy deposition in the calorimeter (CAL) apart from the one from the pions. The selection cuts make use of this characteristic.

4.3.1 Tracking Cuts

The efficiency for selecting events with exactly two tracks of opposite charge pointing to the vertex is calculated from the Monte Carlo sample. To get an idea of the inefficiency of this cut the following four classes of events in a control data sample are considered:

- (1) ρ^0 candidates, namely exactly two tracks of opposite charge pointing to the vertex,
- (2) two tracks but only one track is pointing to the vertex,

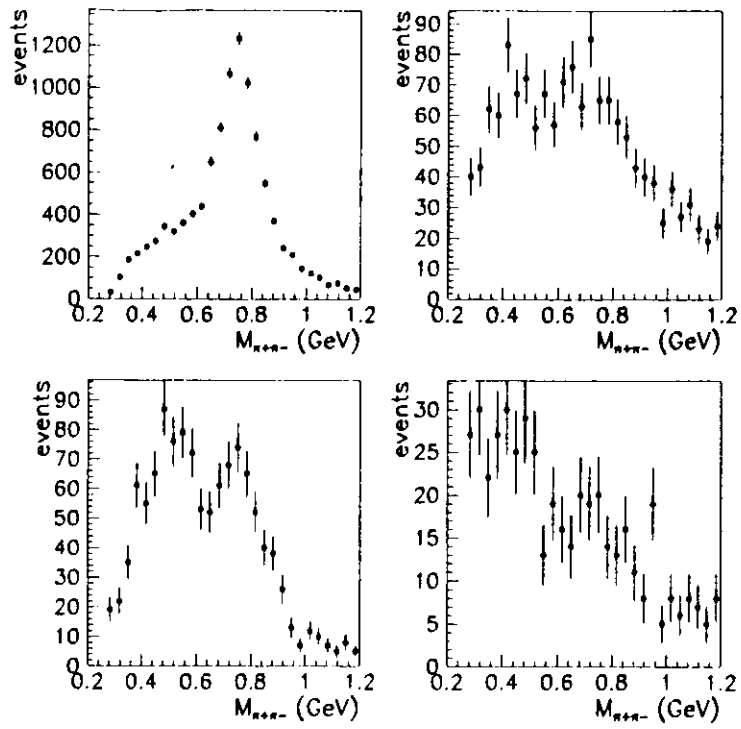

Figure 4.5: Invariant mass distributions for ρ^0 candidates (upper left plot) and event classes (2) to (4) defined in the text (upper right to lower right plot). For ρ^0 candidates a clear mass peak is seen.

- (3) additional to the two vertex tracks a third track is found,
- (4) exactly two tracks from the vertex but of the same charge.

In figure 4.5 the invariant mass distribution for the control sample is shown for the four event classes. For class (3) the mass is calculated from the two vertex tracks. No clear ρ^0 signal is seen for the events which fail the ρ^0 selection cuts slightly, but a clear peak at the proper mass is seen for the ρ^0 candidates. From the number of events in each figure it is obvious that the probability for a ρ^0 event to fail the tracking cuts is small. In table 4.4 the number of events in the classes (2), (3) and (4) divided by the number of events in class (1) is given for data and Monte Carlo sample. The ratios are given for a selection based on the track multiplicities (track selection) as explained above and for an elastic selection, where on top of the track selection no significant energy deposition in the calorimeter outside the tracks is allowed (section 4.3.2). For the track selection mainly background events are selected in

	data from a control sample		elastic ρ^0 Monte Carlo	
	track selection	elastic selection	track selection	elastic selection
class(2)	0.139 ± 0.003	0.008 ± 0.002	0.081 ± 0.008	0.016 ± 0.004
class(3)	0.100 ± 0.005	0.040 ± 0.004	0.026 ± 0.005	0.019 ± 0.004
class(4)	0.054 ± 0.004	0.011 ± 0.002	0.008 ± 0.002	0.005 ± 0.002

Table 4.4: The ratio of the number of events in classes (2),(3) and (4) over the number of events in class (1) for data (control sample) and elastic ρ^0 Monte Carlo for the track selection only and for track plus elastic event selection.

data, as is shown by the invariant mass distribution, which are not simulated by the elastic ρ^0 Monte Carlo sample. Therefore the ratios in data are much bigger than in the Monte Carlo. After applying the elastic selection the remaining events in classes (2), (3) and (4) in data are likely to be elastic ρ^0 events, which fail the selection (1). The ratios in data and Monte Carlo sample after the elastic selection are therefore much closer. From table 4.4 it can be concluded that the probability for an elastic ρ^0 event to fail the tracking cuts is small and the inefficiency is sufficiently well reproduced by the Monte Carlo.

As already mentioned previously a cut on the reconstructed vertex is applied. Figure 4.6

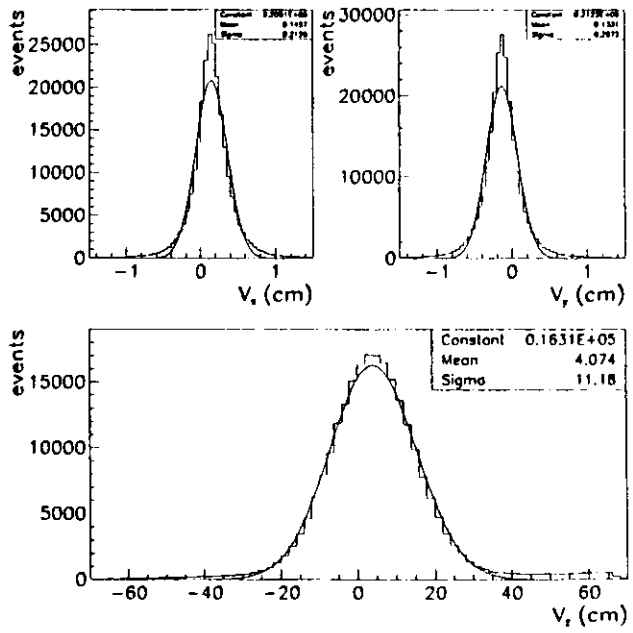

Figure 4.6: Vertex distributions in x (upper left plot), y (upper right plot) and z (lower plot) in data for all ρ^0 candidates. The result of a fit with a Gaussian is superimposed

shows the measured vertex distributions in x, y and z for all selected ρ^0 candidates in the selected runs (section 4.4). A Gaussian is fitted to this distributions and the mean vertex position found to be displaced, for example in z by 4.1 cm. Events with a vertex inside three sigma are selected, so the vertex cut reads:

$$\begin{aligned} |V_x - 4.07\,\text{cm}| &< 3 \cdot 11.18\,\text{cm} \\ |V_z - 0.15\,\text{cm}| &< 3 \cdot 0.21\,\text{cm} \\ |V_y + 0.13\,\text{cm}| &< 3 \cdot 0.21\,\text{cm}. \end{aligned}$$

The cuts on the vertex distributions in x and y reduce the data sample by ~2.5%. In the Monte Carlo simulation, vertex distributions in x, y and z are used at generator level, which was derived from an unbiased 1994 data sample.

4.3.2 Selection of Elastic Events

Elastic events are selected by requiring that the energy in the most energetic calorimeter cell not assigned to the tracks is below an energy which is given by the maximal noise in the calorimeter. All calorimeter cells in the electromagnetic and hadronic section of the calorimeter inside a circle around the track impact points are assigned to the tracks. The most energetic cell in each calorimeter section among those, which are not assigned is used in the selection cut. To select elastic events with a high purity and and high efficiency the radius of the circle and the noise in the calorimeter have to be determined. The noise in the calorimeter can be studied by using random triggered events. These events are taken during the usual data taking with a rate of 0.03 Hz. They are passed through all trigger levels without any trigger cuts and reconstructed like usual events. Since the probability of having a physics event in a randomly triggered event is almost zero, these events can be used to study the noise in the detector during data taking. The noise in the calorimeter is studied separately for the three different calorimeter parts (RCAL, BCAL, FCAL) and the electromagnetic (EMC) and hadronic section (HAC). Figure 4.7 shows the energy distribution of the most energetic calorimeter cell in randomly triggered events.

During the reconstruction an energy threshold is applied to the energy in each calorimeter cell. So energies below 60 MeV (EMC), 100 MeV (HAC0) or 110 MeV (HAC) are set to zero. This cuts out the very low energetic part of the noise spectra. Nevertheless it is obvious that the noise spectra fall off very fast. This is expected since the dominant source for noise are radioactive decays of the depleted uranium and electronic noise. From these plots the cut values for the most energetic cell apart from the tracks are determined as listed in table 4.5.

calorimeter section	most energetic cell cut (MeV)	inefficiency of the cut (%)
REMC	< 160	0.04
RHAC	< 200	0.11
BEMC	< 240	0.05
FEMC	< 200	0.15
FHAC	< 240	0.30

Table 4.5: The most energetic cell cut determined from randomly triggered events in the three calorimeter parts. The inefficiency is determined from data.

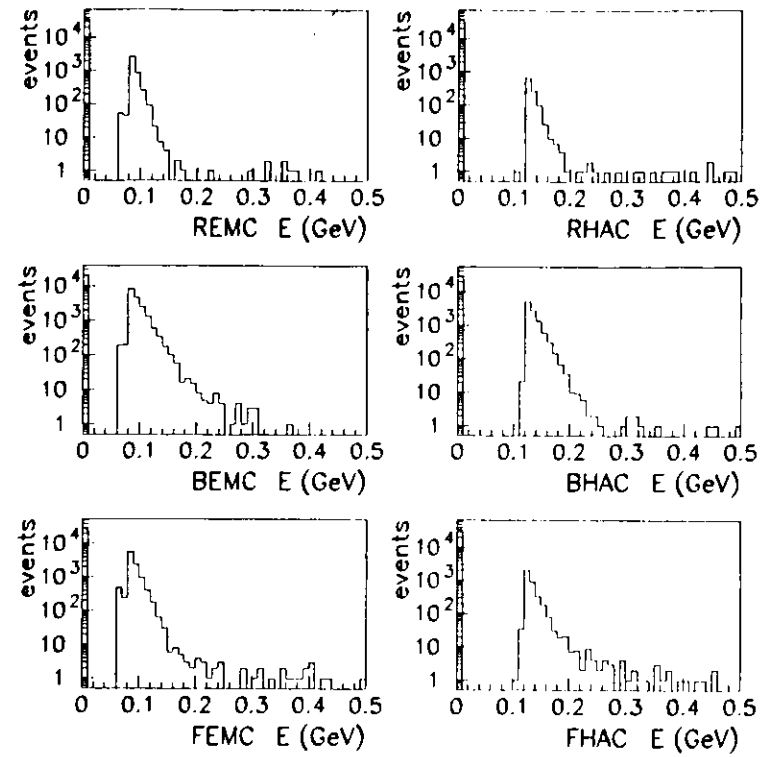

Figure 4.7: Energy of the most energetic cell in random triggered events, in the electromagnetic (left plots) and the hadronic sections (right plots) of the calorimeter.

The inefficiency of the cut is given by the number of events in random triggered events above the cut over all events. A cut on the hadronic section of the barrel calorimeter (BHAC) is not applied in this analysis since all neutral particles coming from the interaction region have to pass through the electromagnetic section (BEMC) first and therefore a cut on the most energetic cell in BEMC is sufficient to select elastic ρ^0 events. In the 1994 data taking period some calorimeter channels showed additional noise visible as tails in the noise spectra. Figure 4.7 shows the noise spectra after correcting for this extra noise. It turns out that this additional noise shows up only in a small number of cells. Some of these extra noisy cells are removed by cutting on the absolute value of the relative imbalance (< 0.7), the absolute value of the difference in the energy measurement form the left and right photo multiplier divided by the sum of these energies for a cell. This cut is applied to isolated cells with an energy below 0.7 GeV only. Those noisy cells, which fulfill the imbalance criterion are well identified by their occupancy as most energetic cells in random triggered events. It turns

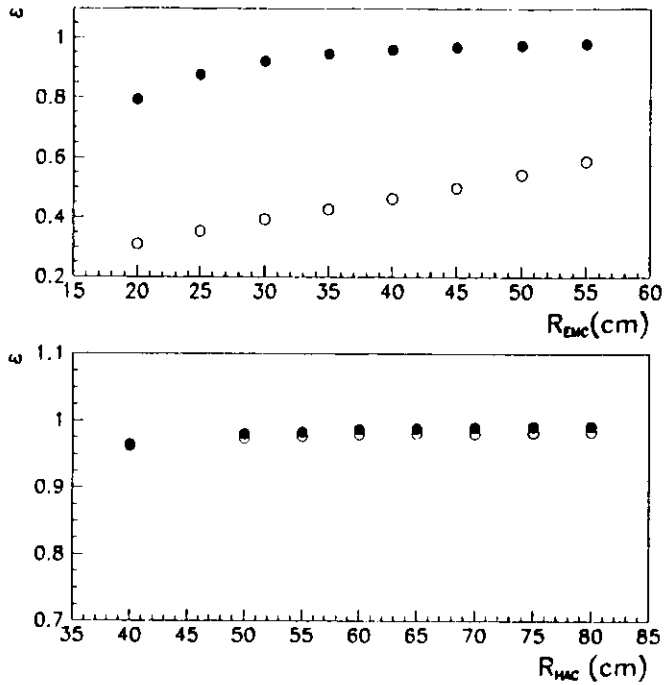

Figure 4.8: Efficiency of the cut on the most energetic cell away from the tracks, as a function of the radius around the track impact points, for ρ^0 Monte Carlo (full dots) and ω Monte Carlo (open dots) events. The upper plot shows the efficiency for different radii in the electromagnetic section and the lower plot for different radii in the hadronic section. In the lower plot a cut at $R_{EMC} = 40$ cm is already applied.

out that these extra noisy cells or *hot* cells only show up in parts of the running period. The energy for these cells in the affected run range is set to zero, if it is below a certain threshold. This threshold minimizes the loss of physics and is given by the highest energy deposit in randomly triggered events for each *hot* cell. A list of all *hot* cells with the corresponding upper energy cut and the affected run range is given in Appendix A. Since in the detector simulation only a parameterization of the radioactive decays of the uranium is used and *hot* cells are not simulated, the inefficiency of the cut on the most energetic cell is below the inefficiency estimated from data given above, but the effect is small.

Now the size of the circle around the track impact point has to be fixed. A different size is used in the electromagnetic and hadronic section of the calorimeter taking into account the different radial size of the shower at different depth in the calorimeter. For the study of the size of the circle Monte Carlo events simulating elastic ρ^0 photoproduction events as well as elastic ω photoproduction events (in the decay mode $\omega \to \pi^+\pi^-\pi^0$) are used.

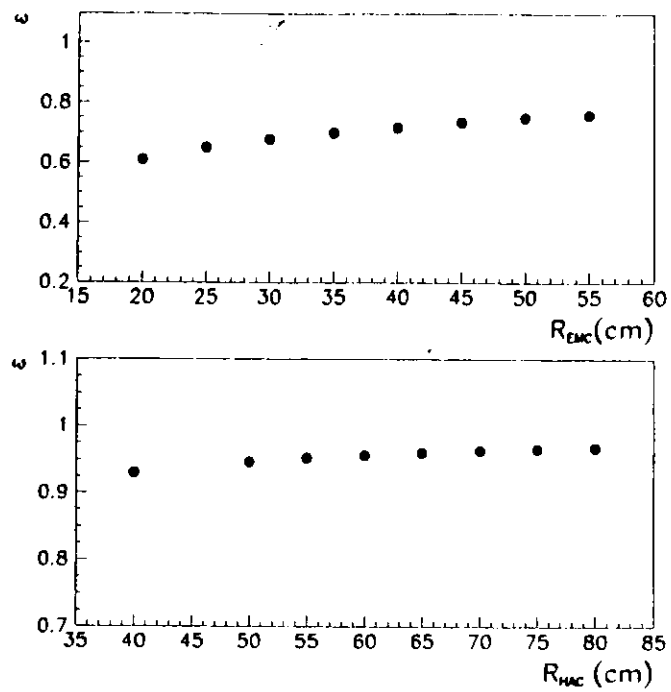

Figure 4.9: Like figure 4.8 but for data.

After selecting two track events the radii of the circles around the track impact points are varied for the electromagnetic and the hadronic section separately. Figure 4.8 shows the efficiency of the cut for different radii in the electromagnetic and the hadronic section for ρ^0 and ω events separately. The efficiency of the cut in the electromagnetic section (upper plot) for selecting ρ^0 events depends for small radii strongly on the radii but for radii above 40 cm the efficiency is almost constant. A high efficiency for selecting elastic ρ^0 photoproduction events together with an acceptable rejection against background from elastic ω photoproduction is therefore found at a radius of 40 cm in EMC. After applying the cut on the electromagnetic section, the efficiency for selecting elastic events is almost independent of the size of the circle in the hadronic section (lower plot in figure 4.8). The size of the circle in the hadronic section is chosen to be 55 cm to get an efficiency bigger than 98% for the ρ^0 Monte Carlo. Figure 4.9 shows the efficiency of the cut for different radii of the circles in the data. It is obvious that for bigger radii the amount of background in data becomes bigger since the efficiency does not flatten like in the case for the elastic ρ^0 Monte Carlo. On the other hand the increase in data is similar to the increase in the elastic ω Monte Carlo. So Monte Carlo samples can be used to estimate the amount of background in the measured ρ^0 signal (chapter 7).

4.4 Selection of the Run Range

For the analysis presented here only those runs, from the 1994 data taking period, with nominal vertex and positron beam are used. Runs from the electron running period in 1994 are not used since the CFLT was not calibrated for these runs, which results in a lower efficiency of the $REMC_{FLT}$ cut. Runs taken after the shifted vertex runs are also rejected, because in these runs extra noise in the forward calorimeter showed up.

Two selection criteria are imposed on the remaining runs. A run summary must have been created and the luminosity of the run has to be bigger than 500 μb^{-1}. The second selection makes sure that each run has a reasonable statistics for the study described below.

To select those runs for which the ZEUS detector was running stably the mean and RMS values for each run for the following distributions are determined: energies in REMC, RHAC, BCAL and FCAL and number of hits in the CTD for each track in the axial layers, stereo layers and z by timing layers. A run I is rejected, if the following criterion is fulfilled for the distribution in variable A:

$$|\langle\langle A\rangle\rangle_{all\ runs} - \langle A\rangle_{run\ I}| > \frac{3\langle RMS(A)\rangle_{all\ runs}}{\sqrt{N_{run\ I}}}, \tag{4.9}$$

where $\langle A\rangle$ is the mean value of the distribution. The mean values over all runs ($\langle\langle A\rangle\rangle_{all\ runs}$ and $\langle RMS(A)\rangle_{all\ runs}$) are determined by fits with a Gaussian to the distribution of the mean and RMS values of all runs. Two independent TLT trigger streams are used, so two lists of *bad* runs are created. Comparing these lists, it turns out that most *bad* runs show up for both trigger streams and that the *bad* runs are grouped. So always all runs in a single HERA electron fill are excluded, if one of the runs in the fill is identified as a *bad* run. The complete list of all runs excluded from the analysis can be found in Appendix B.

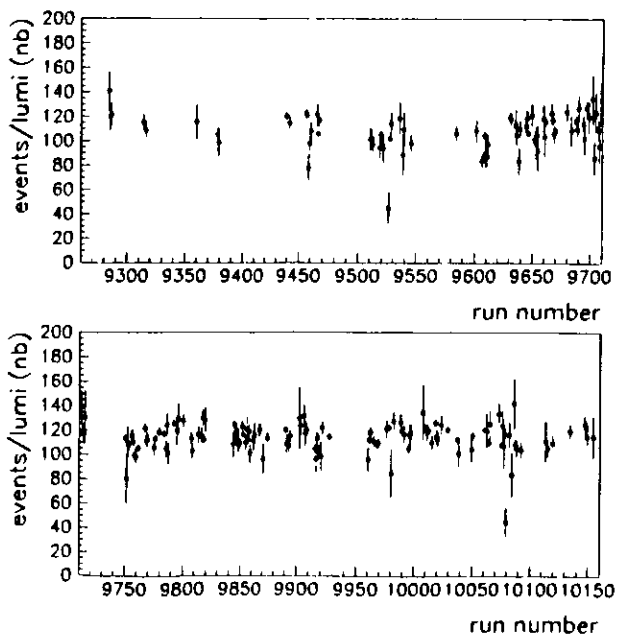

Figure 4.10: Number of events per luminosity after all selection cuts for the selected runs.

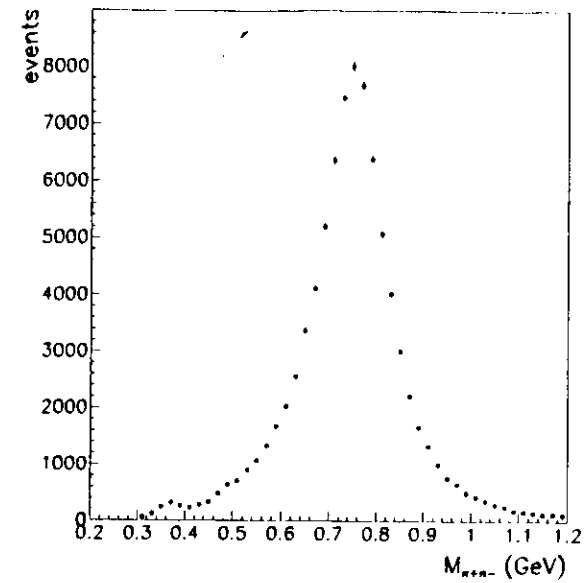

Figure 4.11: The ρ^0 signal in the 1994 data, after all selection cuts, for $W_{\gamma p}$ between 50 and 100 GeV. At low mass ϕ mesons in the decay channel K^+K^- are observed.

In figure 4.10 the number of events per luminosity versus run number is shown for the selected runs. The number of events per luminosity is flat over the selected runs.

The effective integrated luminosity of the selected sample, corrected for the trigger prescale factors (4.1), is $\mathcal{L} = 691 \pm 10\ nb^{-1}$.

Figure 4.11 shows the elastic ρ^0 photoproduction signal in the 1994 in the $W_{\gamma p}$ range between 50 and 100 GeV. Since the two tracks are assumed to be pions, background from elastic ϕ photoproduction with a decay of the ϕ in a K^+K^- pair can be seen in the data at low $M_{\pi^+\pi^-}$ (section 7.2). To reduce this background a cut of $M_{K^+K^-} > 1.038$ GeV is introduced. As will be shown in section 6.2 the acceptance is very small for low invariant masses $M_{\pi^+\pi^-}$ so the analysis of ρ^0 photoproduction is restricted to $M_{\pi^+\pi^-} > 0.55$ GeV. In total 79010 events are left after these cuts.

Chapter 5

Monte Carlo Simulation

The resolution and the acceptance of the ZEUS detector for elastic ρ^0 photoproduction and the for background processes to the elastic ρ^0 signal were studied by means of a Monte Carlo simulation. Events simulating the process under study were generated using the Monte Carlo generator DIPSI, PYTHIA or EPSOFT (table 5.1).

The generated events were passed through a detailed simulation of the ZEUS detector and trigger. All particles generated at the ep vertex are tracked through the apparatus, simulating the processes associated with the passage of particles through matter, using the program MOZART. The ZEUS trigger is simulated by the program ZGANA. The output format of MOZART and ZGANA is very similar to that of the data, so Monte Carlo events can be passed through the same reconstruction program (ZEPHYR) and analysis program as the data.

Monte Carlo events were generated over the whole Q^2 range covered by this measurement namely from $Q^2_{min} = m_e^2 y^2/(1-y)$ to $Q^2_{max} = 4$ GeV^2 and in $W_{\gamma p}$ from 40 GeV to 110 GeV, except for γ- and double dissociative background events, which cover a bigger $W_{\gamma p}$ region (40 GeV $\leq W_{\gamma p} \leq$ 300 GeV). Elastic and proton dissociative ρ^0 events were generated in the invariant mass $M_{\pi^+\pi^-}$ range $2M_\pi \leq M_{\pi^+\pi^-} \leq 1.3$ GeV.

In the following the three Monte Carlo generators will be shortly introduced. Neither generator simulates radiation of real photons from the incoming or outgoing electron, nor vacuum polarization loops in the virtual photon. Their effect on the cross section was estimated to be smaller than 2% [66] and their effect on the shape of the $M_{\pi^+\pi^-}$, $|t|$ and angular distributions are expected to be negligible.

process	Monte Carlo generator
$ep \to ep\rho^0$	EPSOFT, DIPSI
$ep \to eN\rho^0$	PYTHIA,EPSOFT
$ep \to ep\omega$	PYTHIA
$ep \to ep\phi$	PYTHIA
$ep \to epX$	PYTHIA,EPSOFT
$ep \to eNX$	PYTHIA

Table 5.1: The Monte Carlo generators used for the different processes.

5.1 DIPSI

The Monte Carlo generator DIPSI [8] is a generator for elastic vector meson production. It is based on a QCD leading logarithm model calculation by Ryskin. The model assumes that the exchanged virtual photon fluctuates into a $q\bar{q}$ pair which then interacts with a gluon ladder emitted by the incident proton. The parameters of the model are the strong coupling constant α_S, the two-gluon form factor of the proton and the gluon momentum density in the proton $\bar{x}g(\bar{x},\bar{q}^2)$ ($\bar{x} = (M_V^2 + Q^2 + P_T^2)/W^2$, $\bar{q}^2 = (M_V^2 + Q^2 + P_T^2)/4$). The model can be used at the small values of $\bar{q}^2$ involved in ρ^0 photoproduction, if the parameterization for $\bar{x}g(\bar{x},\bar{q}^2)$ is chosen to reproduce the experimental data. In this region of small $\bar{q}^2$ however it is doubtful whether the function $\bar{x}g(\bar{x},\bar{q}^2)$ can still be interpreted as the gluon momentum density in the proton.

For the events used in this analysis the effective $W_{\gamma p}$ dependence of the cross section was of the type $W_{\gamma p}^{0.2}$, the t dependence was approximately exponential with a slope of 9.5 GeV^{-2}. The invariant mass $M_{\pi^+\pi^-}$ was generated as to reproduce, after reconstruction, the measured distribution. The decay angular distribution of the decay pions was generated according to s-channel helicity conservation.

In this analysis DIPSI was used as a cross check of the results obtained with EPSOFT and for the calculation of the acceptance of the LPS (section 7.4).

5.2 PYTHIA

The Monte Carlo generator PYTHIA [98, 99] simulates γp interactions based on VDM and Regge theory (section 3.3.1 and section 3.3.2). The Q^2 and y spectra are generated using the ALLM parameterization [3] of the ep cross section. The ALLM parameterization relies on a Regge type relation similar to equation (3.42) with Pomeron and Reggeon intercepts that depend on Q^2. It was fitted to a large number of photoproduction and DIS data and provides a smooth transition between the two kinematical regions.

Elastic ω and ϕ photoproduction events were generated according to an exponential t distribution and s-channel helicity conservation. The slopes of the t distributions are those measured at ZEUS [111, 112].

PYTHIA was also used to study single (proton and photon) and double dissociative photoproduction. The dissociative cross sections are given by:

$$\frac{d^2\sigma_{SD}}{dtdM^2} \propto \frac{1}{M^2} e^{b_{SD}t} F_{SD} \tag{5.1}$$

$$\frac{d^3\sigma_{DD}}{dtdM_1^2 dM_2^2} \propto \frac{1}{M_1^2}\frac{1}{M_2^2} e^{b_{DD}t} F_{DD} \tag{5.2}$$

where the slope decreases with the mass like $b_{SD} = 2b + 2\alpha'_{I\!P} \ln W_{\gamma p}^2/M^2$. The effective exponential slope of the t distribution is 5.0 GeV^{-2} for proton dissociation, 6.8 GeV^{-2} for γ dissociation and 2.2 GeV^{-2} for double dissociation. The spectrum of diffractive masses M is taken to begin $2M_\pi$ above the mass of the respective incoming particle (e.g. $2M_\pi + M_p$ for $ep \to eN\rho^0$ and $2M_\pi + M_{\rho^0}$ for $ep \to epX$) and extends to $\sqrt{0.1}\, W_{\gamma p}$. The factors F_{SD} and F_{DD} are introduced in the Regge formula to suppress production close to the kinematic limit and to give an enhancement of the low mass region, where a resonance structure is observed in the data. So the resonance structure is modeled by an averaging procedure. The parameters in the factors are obtained from a fit to $pp/p\bar{p}$ data [98].

Light dissociative systems with masses M less than 1 GeV above the mass of the incoming particle are simulated to decay isotropically into a two body state. For more massive dissociative systems the hadronization processes are simulated according to the string hadronization model as implemented in JETSET [98].

5.3 EPSOFT

Similar to PYTHIA the generator EPSOFT [62] simulates γp interactions based on VDM and Regge theory. The EPSOFT program was developed within the framework of HERWIG [74] and was tuned to reproduce the properties of photoproduction collisions observed in the ZEUS detector [62]. Like in PYTHIA, the kinematics of the electron vertex in the ep interactions was generated according to the ALLM parameterization.

EPSOFT was used to generate single (proton and photon) dissociative and elastic ρ^0 photoproduction. The latter will be discussed in detail below.

Photon dissociation ($\gamma p \to Xp$) is generated from the following formula:

$$\frac{d^2\sigma^{\gamma p\to Xp}}{dtdM_X^2} = C\sigma_{ALLM}^{\gamma p}\frac{e^{b_{SD}t}}{(M_X^2 + Q^2 - M_V^2)^{\alpha_{I\!P}(0)}} \tag{5.3}$$

where the constant C=0.14 gives the ratio between the single dissociative cross section and the total one. The Pomeron intercept is chosen to be $\alpha_{I\!P}(0) = 1.1$ and the effective slope is set to be $b_{SD} = 6.0$ GeV^{-2}. The dissociative mass M_X is generated between $M_V + 2M_\pi$, where M_V is the mass of the vector mesons (M_{ρ^0} in 80% and M_ω, M_ϕ in 10 % of the events) and M_π the pion mass, and $\sqrt{0.1}\, W_{\gamma p}$.

The proton dissociative cross section is calculated in relation to the elastic reaction:

$$\frac{d^2\sigma^{\gamma p\to \rho^0 N}}{dtdM_N^2} = \frac{d\sigma^{\gamma p\to \rho^0 p}}{dt}0.3\frac{d^2\sigma^{pp\to pN}/dtdM_N^2}{d\sigma^{pp\to pN}/dt}. \tag{5.4}$$

The second term defines the ratio of probabilities that the proton dissociates into the nucleonic system N to that in which it emerges intact. It is derived from a parameterization of $pp \to pp$ and $pp \to pN$ cross sections [62]. The nucleonic mass M_N is generated in the range $(1.25\text{GeV})^2 < M_N^2 < 0.1\, W_{\gamma p}^2$. The t distribution follows an exponential and was generated with an effective slope of 5.0 GeV^{-2}.

The hadronization of the hadronic systems X and N is simulated using an algorithm similar to that used in HERWIG. The particle multiplicities and the momenta of the hadrons transverse to the photon-Pomeron collision axis are simulated using parameterizations of existing data, while the longitudinal momenta are generated uniformly in phase space. This algorithm was tuned to ZEUS data using non diffractive events [62]. In single dissociative events, instead of generating the γp collision at an energy $W_{\gamma p}$, a collision of the photon (or proton) with the Pomeron at an energy M_X (or M_N) is simulated.

EPSOFT was used to calculate the acceptance corrections for elastic ρ^0 photoproduction. The Monte Carlo efficiencies are reliable only, if the generator describes the physics of the

process under study correctly. The variables Q^2, $W_{\gamma p}$, t, $M_{\pi^+\pi^-}$ and the decay angles in the helicity system $\cos\theta_h$, ϕ_h and Φ are used to describe ρ^0 photoproduction. Since the outgoing electron is not measured in this analysis Q^2 and Φ can not be measured. The generated Q^2 distribution was reweighted according to equation (3.53), where the parameter ξ^2 is determined, under the assumption of s-channel helicity conservation, from the ρ^0 spin density matrix element r^{04}_{00} (3.71) by

$$\xi^2 = \frac{M^2_{\rho^0}}{\langle Q^2\rangle}\frac{1}{\langle\epsilon\rangle+\langle\delta\rangle}\frac{r^{04}_{00}}{1-r^{04}_{00}}. \tag{5.5}$$

$\langle Q^2\rangle$ is the average Q^2 of the data, assuming the Q^2 dependence given by equation (3.53). The average Q^2 depends on the maximal Q^2 accessible by the measurement, Q^2_{max} and on ξ^2. The ξ^2 dependence of $\langle Q^2\rangle$ was approximated by a linear function according to $\langle Q^2\rangle = Q_1 + Q_2\xi^2$. Inserting this equation into (5.5) yields:

$$\xi^2 = \sqrt{\frac{1}{Q_2}\frac{M^2_{\rho^0}}{\langle\epsilon\rangle+\langle\delta\rangle}\frac{r^{04}_{00}}{1-r^{04}_{00}}+\left(\frac{Q_1}{2Q_2}\right)^2}-\frac{Q_1}{2Q_2} \tag{5.6}$$

Q_1 and Q_2 are determined and parameterized as a function of Q^2_{max}. So for a given Q^2_{max} the values Q_1 and Q_2 are determined and inserted in equation (5.6). The values for $\langle\epsilon\rangle$ and $\langle\delta\rangle$ are given by (3.66) and (3.67). ξ^2 to be used for the Q^2 reweighting is thus given in terms of r^{04}_{00}. The optimal value of $r^{04}_{00} = 0.013$, as determined below, yields $\xi^2 = 0.2$.

Since Φ can not be measured, the decay angular distribution was reweighted according to equation (3.69), where the spin density matrix elements r^{04}_{00}, r^{04}_{1-1} and $\Re r^{04}_{10}$ are discussed below and all other spin density matrix elements are chosen according to s-channel helicity conservation and under the assumption of natural parity exchange. All elements are zero, except $r^1_{1-1} = -\Im r^2_{1-1} = 1/2(1-r^{04}_{00})$ and $\Re r^5_{10} = -\Im r^6_{10} = 0$ [60].

To improve the agreement between data and Monte Carlo in the reconstructed $W_{\gamma p}$, P^2_t, $M_{\pi^+\pi^-}$ and decay angular distributions, the Monte Carlo was reweighted in an iterative procedure. The reconstructed data distributions are compared to the reconstructed Monte Carlo distributions after statistical subtraction of the proton dissociative background (section 7.4) and after reweighting for the calorimeter trigger efficiency (section 6.1.1). As the first step of this procedure, the acceptance corrections were calculated using the Monte Carlo

parameter	optimal value	range corresponding to one standard deviation	
M_{ρ^0}	771 MeV		
Γ_0	138 MeV		
n_1	6.08	6.16	6.00
n_2	8.63 GeV^{-2}	8.01 GeV^{-2}	9.25 GeV^{-2}
r^{04}_{00}	0.013	0.020	0.006
$\Re r^{04}_{10}$	0.010	0.014	0.006
r^{04}_{1-1}	-0.008	-0.014	-0.002
a	1.17	1.23	1.11
b	11.54 GeV^{-2}	11.63 GeV^{-2}	11.46 GeV^{-2}
c	3.98 GeV^{-4}	4.22 GeV^{-4}	3.74 GeV^{-4}

Table 5.2: The final reweighting parameters and the change corresponding to one standard deviation.

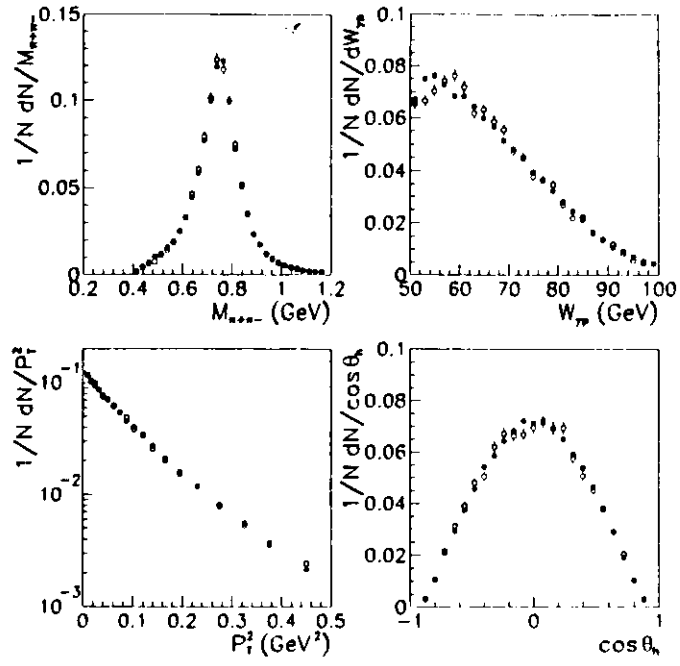

Figure 5.1: Reconstructed distributions in $M_{\pi^+\pi^-}$, $W_{\gamma p}$, P^2_t and $\cos\theta_h$ for data (full dots) and the Monte Carlo simulation (open dots) after reweighting.

events reweighted to the distributions as measured with the ZEUS 1993 data [110].

Since the ρ^0 mass shape is skewed and since this skewing changes with t, the corrected $M_{\pi^+\pi^-}$ distribution was fitted in t bins by the Ross Stodolsky parameterization (9.10). In this model the skewing is described by a skewing factor $(M_{\pi^+\pi^-}/M_{\rho^0})^n$. The parameter n is treated as a free parameter, which depends on t. Using a linear function $(n(|t|) = n_1 - n_2|t|)$ the parameter n_1 and n_2 describe the ρ^0 shape as a function of t. Similarly to the ρ^0 shape the spin density matrix elements r^{04}_{00}, r^{04}_{1-1} and $\Re r^{04}_{10}$ are determined from a fit of (3.72) to the corrected two dimensional $\cos\theta_h$, ϕ_h distribution.

The generated t distribution is parameterized by an exponential ($\sim e^{bt+ct^2}$) and the generated $W_{\gamma p}$ distribution by a power like dependence ($\sim W^{-a}_{\gamma p}$). The parameters b, c and a are determined as follows. The difference of the reconstructed P^2_t values (for the parameter b and c) or the reconstructed $W_{\gamma p}$ values (for the parameter a) between data and Monte Carlo was determined as a χ^2 function of the parameter λ. The χ^2 was defined as ([106]):

$$\chi^2(\lambda) = \sum_\mu \frac{(d_\mu - c_N m_\mu(\lambda))^2}{\sigma^2_\mu(\lambda)} \tag{5.7}$$

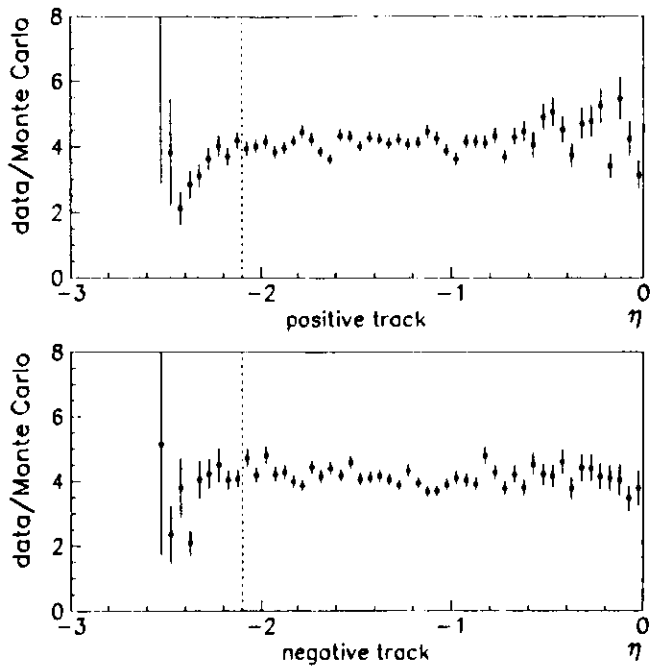

Figure 5.2: Ratio data over Monte Carlo versus η for positive (upper plot) and negative (lower plot) tracks. The dashed vertical line indicates the cut used in the analysis.

where d_μ is the number of data events in a bin μ, $m_\mu(\lambda)$ the number of Monte Carlo events determined with parameter λ in the corresponding bin and c_N is a normalization factor defined by $\sum_\mu d_\mu = c_N \sum_\mu m_\mu(\lambda)$. The error σ_μ is given by $\sigma_\mu^2 = \dot{d}_\mu^2/\dot{d}_\mu + c_N^2 m_\mu^2/\dot{m}_\mu$, where $\dot{d}_\mu$ and $\dot{m}_\mu$ are the equivalent event numbers. The values for a, b and c describing the data best are given by the minima in χ^2 and the error of these parameters by the change in χ^2 by one unit.

The parameters determined are used to reweight the Monte Carlo events and the acceptance corrections are recalculated. The whole procedure was repeated. After three iterations the parameters converged. In table 5.2 the final reweighting parameters are listed together with the error, corresponding to a change by one standard deviation. These errors are used later to determine the systematic error due to changes in the Monte Carlo simulation.

As an example of the agreement between data and Monte Carlo reached, after reweighting the Monte Carlo, various distributions are shown in figures 5.1 and 5.2. Figure 5.1 shows the reconstructed $M_{\pi^+\pi^-}$, $W_{\gamma p}$, P_T^2 and $\cos\theta_h$ distributions for data (full dots) and the Monte Carlo simulation (open dots). Good agreement is reached in all these distributions. The same kind of agreement is reached in bins of $W_{\gamma p}$, P_T^2 and $M_{\pi^+\pi^-}$. Figure 5.2 shows the ratio

data over Monte Carlo of the η spectra for positive (upper plot) and negative (lower plot) tracks respectively. The ratio if flat in the range under study, namely for $|\eta| < 2.1$. Similarly the Monte Carlo describes the data in the track transverse momentum spectra for $P_T > 150$ MeV.

Chapter 6

The Acceptance

The acceptance of elastic ρ^0 photoproduction events is given by the acceptance of the elastic ρ trigger and the efficiency of the selection cuts. For the efficiency calculation of the selection cuts Monte Carlo methods are used (section 6.2). The method used to determine the acceptance of the ρ trigger uses the data and will be explained in the next section.

6.1 Trigger Acceptance

As already described in chapter 4 the dedicated ρ trigger is using information of the tracking chamber and the calorimeter at the different trigger levels. Since the selection cuts on the tracks for elastic ρ^0 events are tighter than the trigger cuts based on tracking, the efficiency of these cuts is very high and well simulated by the ZEUS detector Monte Carlo simulation. The efficiency of the energy requirement in the electromagnetic section of the rear calorimeter at the FLT ($REMC_{FLT} > 161$ MeV) on the other hand is difficult to determine from

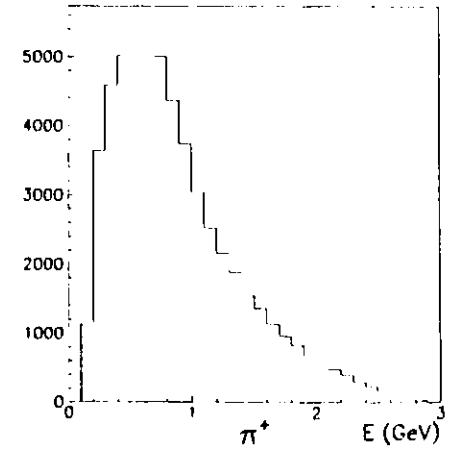

Figure 6.1: Monte Carlo energy spectrum of the π^+ from ρ^0 decays.

the detector simulation alone. The typical energy of a decay pion from a ρ^0 decay (figure 6.1) is close to the nominal trigger threshold of 464 MeV. Inactive material in front of the calorimeter and the calibration of the energies in the calorimeter first level trigger CFLT (section 2.2.2) have a big impact on the trigger acceptance. Pions are hadrons but the trigger uses only the energy deposition in the electromagnetic section of the calorimeter so the details of the interaction of the low energetic pions with the calorimeter are important. These effects must be well understood and simulated to rely on a Monte Carlo simulation of the ZEUS detector for the acceptance determination. To reduce the uncertainty in the measurement coming from these effects a method to determine the $REMC_{FLT}$ trigger acceptance from data was developed. This measured acceptance is used to correct the data for the $REMC_{FLT}$ trigger acceptance.

6.1.1 Correcting for the CFLT Acceptance Using Data

A ρ^0 decays in a $\pi^+\pi^-$ pair and the signature of such events in the ZEUS detector are two oppositely charged tracks in the CTD and no energy deposition in the CAL apart from the tracks. So only the pions can cause a trigger. If now one of the pions causes a trigger in the rear calorimeter the other pion can be used as an independent test pion to measure at which momentum this pion can trigger an event as well.

For the acceptance determination only events which fulfill the requirements of an elastic ρ^0 photoproduction event are used (chapter 4). The selection cuts make sure that also events are accepted in which only one of the decay pions has caused a trigger, in case the energy in a single CFLT trigger tower not matched to a track is below its zero suppression of 464 MeV. In the kinematic range under study the opening angle of the two tracks is too big to have both pions in the same CFLT trigger tower. So the two pions can independently

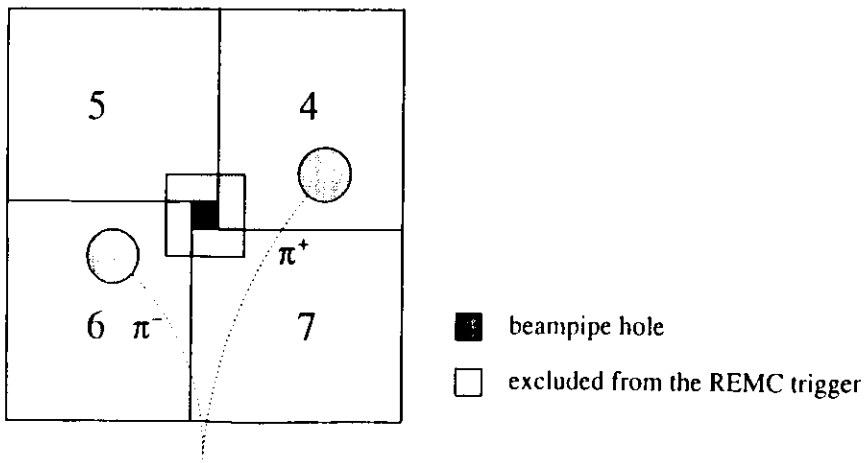

Figure 6.2: The four trigger regions in RCAL and a schematic picture of an ρ^0 elastic photoproduction events used for the acceptance calculation. The circles around the impact points of the tracks on the calorimeter indicate the energy deposition of the two pions.

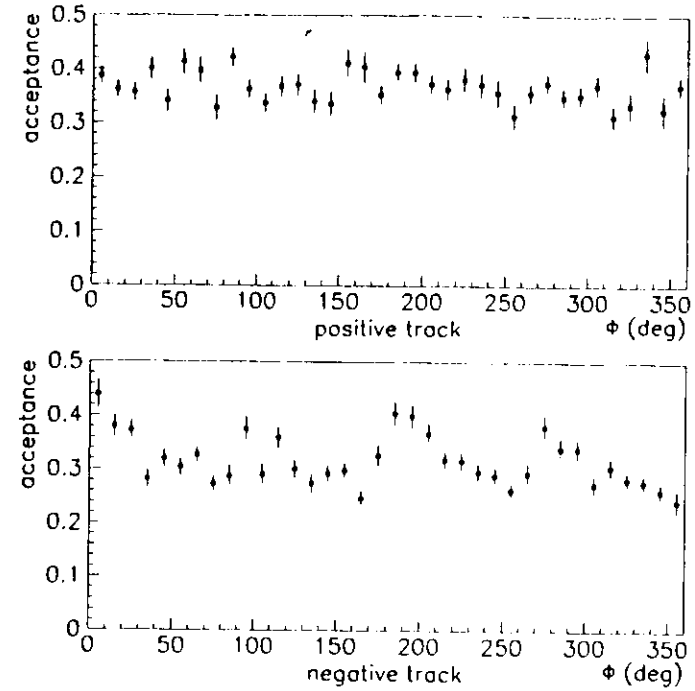

Figure 6.3: $REMC_{FLT}$ trigger acceptance as a function of the azimuthal angle ϕ, calculated from the track impact point on the calorimeter, for positive and negative tracks.

cause a trigger. Since the CFLT energy measurement of each of the four independent trigger regions in RCAL is stored in the ZEUS data stream for each event, it is possible to relate a trigger in one of the trigger region to one pion. This is done by extrapolating the tracks to the calorimeter and thereby determining which trigger region is hit by each pion. For the trigger acceptance determination events are used in which the two pions hit opposite trigger regions. In the 1994 data sample $\sim$ 20000 events fulfill this condition. An event of this type is illustrated in figure 6.2. The positive pion hits trigger region four and the negative pion trigger region six. If trigger region four causes a trigger one can use the pion hitting trigger region six as an independent test pion to measure the trigger acceptance. Since the energy deposition belonging to a pion has a lateral spread and the track extrapolation is not perfect, for events in which the second pion hits the calorimeter close to a border between two trigger regions (within 20 cm) also the adjacent trigger region is used to decide whether the second pion causes a trigger.

The $REMC_{FLT}$ trigger acceptance is determined for positive and negative pions separately. The acceptance is measured as a function of the pion momentum, its azimuthal angle ϕ, determined from the track impact point on the rear calorimeter, and the distance R of the

impact point to the center of the beam pipe. Figure 6.3 shows that there is no significant dependence of the trigger acceptance on ϕ, so in the further analysis the trigger acceptance is integrated over ϕ. A strong decrease of the acceptance can be seen as a function of R (figure 6.4). This can be understood from the kinematics of ρ^0 photoproduction. The bigger R the smaller the polar angle of the pions and the smaller the photon-proton center of mass energy $W_{\gamma p}$. Small $W_{\gamma p}$ mean small pion energies and result in a small the trigger acceptance.

It is know that the amount of inactive material in front on the calorimeter depends on the polar angle. Therefore the $REMC_{FLT}$ trigger acceptance is measured in six regions in R, indicated in figure 6.4. These regions are defined to take the most striking non-uniformities in inactive material distribution into account .

In figure 6.5 the trigger acceptance for negative and positive pions versus the particle momentum is shown. The acceptance curve starts at around 450 MeV and increases slowly. A plateau of ~ 0.55 to ~ 0.6 is reached above 1.5 GeV. The probability of a hadron shower to

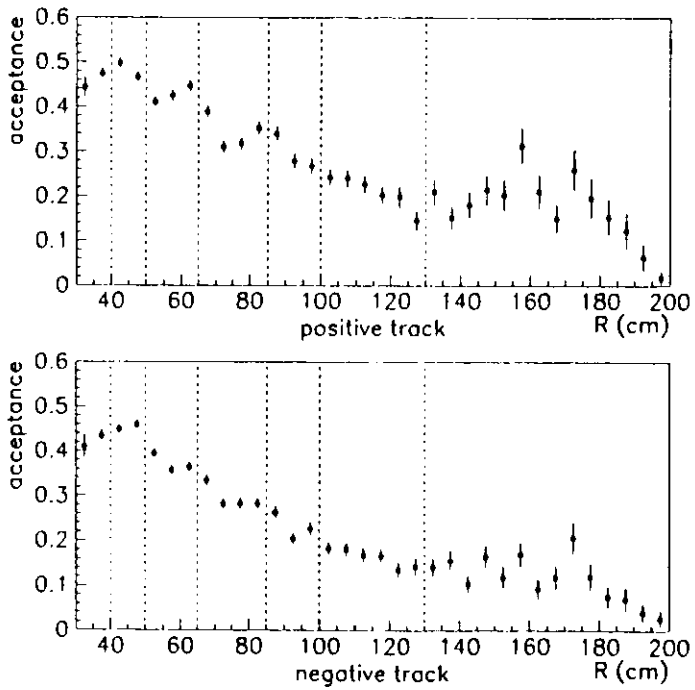

Figure 6.4: The $REMC_{FLT}$ trigger acceptance as a function of the distance of the track impact point on the calorimeter and the center of the beam pipe R for positive and negative tracks. The dashed vertical line indicate the seven bins which are used in the correction procedure.

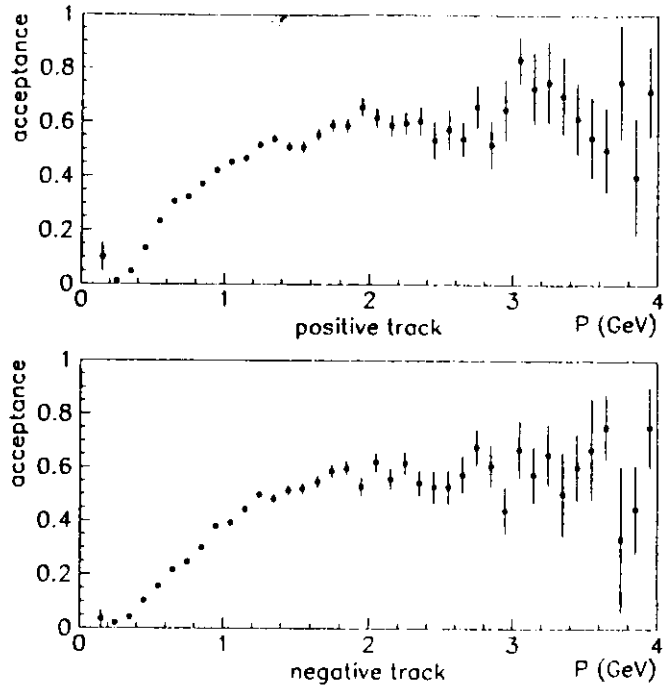

Figure 6.5: The $REMC_{FLT}$ trigger acceptance as a function of the track momentum $|\vec{P}|$ for positive and negative tracks.

start at a depth x in the calorimeter is approximately given by:

$$P(x) = \frac{1}{1.22\lambda_0} e^{-x/1.22\lambda_0},$$

where λ_0 is the interaction length. So the probability for the hadronic shower of one of the ρ^0 decay pions to start in the electromagnetic section of RCAL is:

$$P = \int_0^{0.9\lambda_0} P(x)\, dx = 1 - e^{-0.9/1.22} = 0.52.$$

This number is in rough agreement with the probability in figure 6.5 for momenta above the trigger threshold. Another observation is that the slope for π^- is smaller than for π^+ so the probability to trigger an event with a π^- is smaller than the probability for a π^+ of the same momentum. This can be translated to the observation that π^- and π^+ of the same momentum deposit different amounts of energy in the ZEUS calorimeter (chapter 8.1).

The measured acceptance curves are used to correct the data for the CFLT trigger acceptance.

6.1.2 The Acceptance Correction Method

As explained in the previous section for the $REMC_{FLT}$ trigger acceptance determination six bins in the radial distance R are used. For each of these bins the acceptance is measured as a function of the momentum $|\vec{P}|$ separately for positive and negative pions. The measured acceptances are fitted by:

$$\epsilon(|\vec{P}|) = P_1(1 - e^{(|\vec{P}|-P_2)\cdot P_3}) \tag{6.1}$$

P_2 and P_3 are free parameter in the fits. The parameter P_1 is only varied inside a given range. The range is determined by fitting the measured acceptances integrated over all R with a constant. This fit is performed in different ranges and the upper and lower bound represent the fluctuations in the result of the fit. Limiting the allowed value for P_1 is necessary, because in the bins of high R the statistics above 1 GeV is very small and a fit of equation (6.1) results in unreasonable values for P_1. The resulting parameters from the fits of equation (6.1) for all R bins are shown in figure 6.6 and table 6.1. The parameter P_2 which is a measure

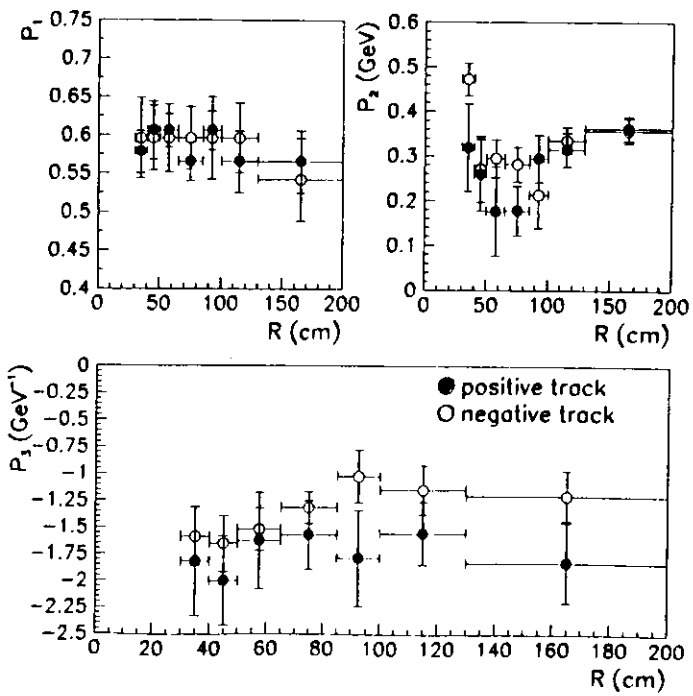

Figure 6.6: Parameters P_1, P_2 and P_3 of the fits according to equation (6.1) in R bin. Full circles show the result for positive tracks and open circles for negative tracks. The vertical error bars represent the statistical error of the fit and the horizontal error bar indicates the size of the R bin.

R bin (cm)	P_1^{pos}	P_1^{neg}	P_2^{pos} (GeV)	P_2^{neg} (GeV)
30-40	0.58 ± 0.03	0.60 ± 0.05	0.32 ± 0.09	0.47 ± 0.04
40-50	0.61 ± 0.04	0.60 ± 0.04	0.26 ± 0.08	0.27 ± 0.07
50-65	0.61 ± 0.02	0.60 ± 0.04	0.18 ± 0.10	0.29 ± 0.01
65-85	0.57 ± 0.03	0.60 ± 0.04	0.18 ± 0.06	0.28 ± 0.01
85-100	0.61 ± 0.03	0.60 ± 0.05	0.29 ± 0.05	0.21 ± 0.07
100-130	0.57 ± 0.04	0.60 ± 0.05	0.31 ± 0.04	0.33 ± 0.03
130-200	0.57 ± 0.04	0.54 ± 0.05	0.36 ± 0.03	0.36 ± 0.03

R bin (cm)	P_3^{pos} (GeV^{-1})	P_3^{neg} (GeV^{-1})
30-40	-1.82 ± 0.51	-1.58 ± 0.27
40-50	-2.00 ± 0.42	-1.65 ± 0.26
50-65	-1.62 ± 0.45	-1.52 ± 0.20
65-85	-1.57 ± 0.32	-1.32 ± 0.15
85-100	-1.79 ± 0.45	-1.02 ± 0.24
100-130	-1.56 ± 0.29	-1.15 ± 0.23
130-200	-1.83 ± 0.38	-1.20 ± 0.24

Table 6.1: Parameters P_1, P_2 and P_3 of the fits according to equation (6.1) for the R bins. The results are given separately for positive and negative tracks.

of the turn on point of the trigger and the parameter P_1 does not show a dependence on the charge. The parameter P_3 describing the slope on the acceptance is bigger in all R bins for negative pions and some dependence on R can be seen as well, reflecting the different amounts of inactive material in front of the calorimeter.

To correct the data for the trigger acceptance all events are reweighted. The reweighting factor for each event is the inverse of the trigger acceptance for this event. Taking the probability that both pions trigger an event into account, the weight W_{evt} is given by:

$$W_{evt} = \frac{1}{\epsilon(|\vec{P}|)_{\pi^+} + \epsilon(|\vec{P}|)_{\pi^-} - \epsilon(|\vec{P}|)_{\pi^+} \cdot \epsilon(|\vec{P}|)_{\pi^-}} \tag{6.2}$$

$$W_{evt} = 0 \qquad \text{for} \quad \epsilon(|\vec{P}|)_{\pi} = \epsilon(|\vec{P}|)_{\pi^+} = 0 \tag{6.3}$$

For $\epsilon(|\vec{P}|)_{\pi^+}$ and $\epsilon(|\vec{P}|)_{\pi^-}$ the results of the fits are used. To avoid big weights a cut on $|\vec{P}|$ is introduced. So the calculation of the CFLT acceptance consists of the following steps:

- extrapolate the tracks to the calorimeter surface,
- calculate the acceptance $\epsilon(|\vec{P}|)$ for each track, if the track hits one of the RCAL trigger regions. This condition is fulfilled if $R < 200$ cm. A lower cut on R is not necessary since a track in the CTD has a minimal polar angle which is big enough to hit a trigger region.
- set $\epsilon(|\vec{P}|)$ to zero if the track momentum is below a given minimal momentum to avoid very small values of ϵ resulting in very big weights. The value for the minimal momentum is chosen to be 450 MeV.

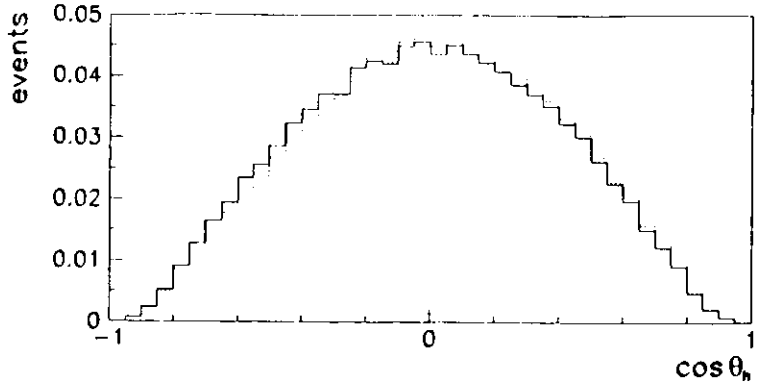

Figure 6.7: The measured $\cos\theta_h$ distribution before (dotted histogram) and after (full histogram) correcting for the $REMC_{FLT}$ trigger acceptance.

The correction method can be checked by applying it to simulated ρ^0 events which are passed through the ZEUS detector simulation. Calculating the correction functions $\epsilon(|\vec{P}|)$ by using the Monte Carlo, the previously described method reproduces very well the $REMC_{FLT}$ trigger acceptance put in the Monte Carlo.

As an example for the correction procedure figure 6.7 shows the measured $\cos\theta_h$ distribution, the helicity angle defined in section 3.3.4 before and after applying the correction method. The distribution is asymmetric with respect to zero before the correction. After correcting for the $REMC_{FLT}$ trigger acceptance, the distribution is symmetric. The asymmetry can be understood from the fact that positive and negative pions of the same momentum deposit different amount of energy in the calorimeter and therefore it is more likely to trigger a ρ^0 event by a positive pion. The decay angular distribution is discussed in more detail in section 9.6.

To determine the efficiency of the elastic ρ trigger Monte Carlo, events simulating elastic ρ^0 photoproduction are used. These events are passed through the ZEUS detector simulation program MOZART, the trigger simulation program ZGANA and the reconstruction program ZEPHYR. The efficiency of all trigger cuts except the $REMC_{FLT}$ requirement is determined from the Monte Carlo simulation. As explained the efficiency of the $REMC_{FLT}$ cut is corrected by reweighting the data and for the Monte Carlo events the same steps as for data are applied but the event weight W_{cut}^{MC} (equation (6.2)) is set to one.

6.2 Efficiency of the Selection Cuts

As already described in chapter 4 the following cuts are used to select elastic ρ^0 photoproduction events:

- runs inside the selected run ranges,
- exactly two tracks of opposite charge form a common vertex,

- the event vertex has to be within three standard deviations of the mean vertex position,
- the energy of the most energetic cell not assigned to the tracks has to be consistent with noise in the calorimeter,
- quality cuts on the tracks, namely $|\eta| < 2.1$, $P_T > 150$ MeV for each track,
- invariant mass assuming the tracks are pions $M_{\pi^+\pi^-} < 1.2$ GeV,
- squared momentum of the ρ^0 $P_T^2 < 0.5$ GeV^2,
- invariant mass assuming the tracks are kaons $M_{K^+K^-} > 1.038$ GeV.

The efficiency of all these cuts is determined using Monte Carlo events. Events simulating elastic ρ^0 photoproduction are passed through the ZEUS detector simulation program MOZART, the trigger simulation program ZGANA and the same reconstruction program ZEPHYR as the data. By the use of the Monte Carlo events the acceptance for elastic ρ^0 events as well as the smearing in the kinematic variables are evaluated. The acceptance includes the efficiency of the trigger cuts, except the $REMC_{FLT}$ requirement, and the efficiency of the selection cuts. In figure 6.8 and 6.9 ϵ_g, defined as the number of events triggered and selected in the generated variables over the generated events is shown as a function of the ρ^0 mass, the photon-proton center of mass energy $W_{\gamma p}$, the transverse momentum square P_T^2 of the ρ^0, ϕ_h and $\cos\theta_h$ the helicity angles defined in section 3.3.4. The statistical error shown in the plots was calculated by error propagation from the statistical error on the number of generated events and the statistical error on the number of triggered and selected events. The Monte Carlo program EPSOFT is used for the simulation of the process $\gamma p \longrightarrow \rho^0 p$. The acceptance increases for increasing $M_{\pi^+\pi^-}$ and reaches a plateau around 800 MeV. This acceptance decrease at small masses is due to the fact that for small $M_{\pi^+\pi^-}$ the polar angle

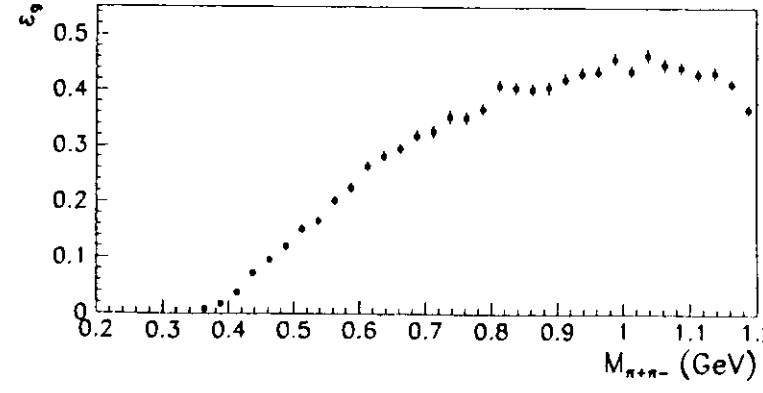

Figure 6.8: Acceptance of the trigger and the selection cuts for elastic ρ^0 photoproduction events as a function of the $M_{\pi^+\pi^-}$.

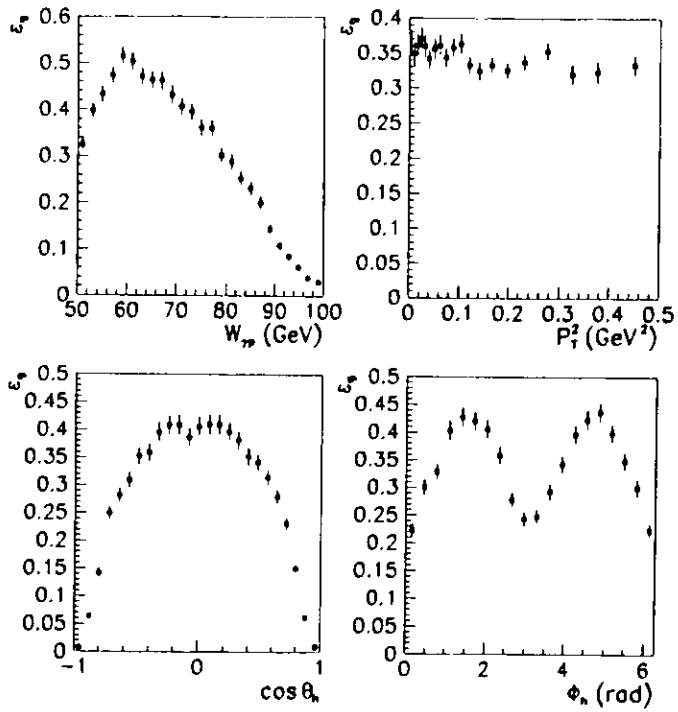

Figure 6.9: Acceptance of the trigger and the selection cuts for elastic ρ^0 photoproduction events as function of the kinematic variables.

of the decay pions is big so one of the pions or even both pions (for $M_{\pi^+\pi^-} \leq 500$ MeV) don't enter the CTD. The cut on $M_{K^+K^-}$ causes the acceptance to be very small below 400 MeV in $M_{\pi^+\pi^-}$, so the region below 550 MeV is excluded for most of the results presented in chapter 9. As can be seen in figure 6.9 the maximum in the acceptance in $W_{\gamma p}$ is around 60 GeV. For $W_{\gamma p}$ smaller than 50 GeV the energy of the decay pions is too small to cause a trigger in the $REMC_{FLT}$ and the pions start to hit the barrel calorimeter BCAL. On the other hand for big $W_{\gamma p}$ the polar angle of the decay pions is too big to reconstruct the pions in the tracking chambers. Therefore the analysis is limited to the range $50 < W_{\gamma p} < 100$ GeV. The acceptance is almost flat as a function of P_T^2 but shows a strong dependence on $\cos\theta_h$ and on ϕ_h. For big values of $|\cos\theta_h|$ and $\phi_h \sim 0$, π or 2π again one of the pions is outside the CTD. The kinematic variables are correlated. For example the acceptance is nearly zero for small masses and big $|\cos\theta_h|$. The Monte Carlo used to calculate the acceptance only gives a reliable results, if the generator describes the underlying physics well. To make sure that this is the case the ratio of data over Monte Carlo has to be flat in the measured range (section 5.3).

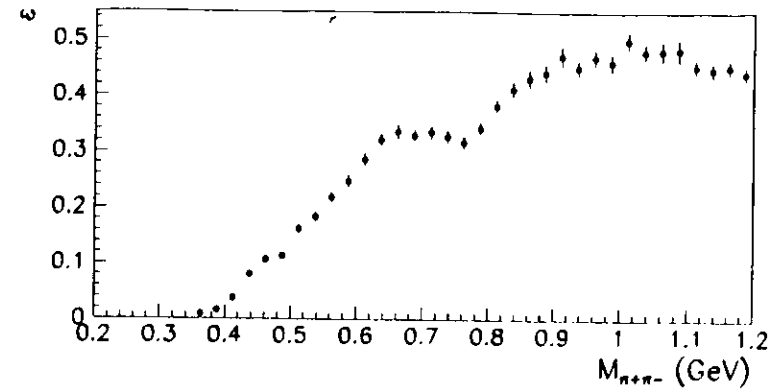

Figure 6.10: Acceptance ϵ, which includes the smearing corrections as a function of the invariant mass $M_{\pi^+\pi^-}$.

The smearing in the kinematic variables was already discussed in section 4.2. There are two methods to take the finite resolution in the correction procedure into account. The first one is to correct the measured distributions by ϵ_g and fit the corrected distributions with a convolution of the resolution function R and the function describing the physics F. So the function used in such a fit reads like:

$$f(x) = \int_{-\infty}^{\infty} R(x,x')F(x')dx'. \tag{6.4}$$

This integral can only be solved in general for special cases of the functions R and F. The correction procedure using the convoluted function f is applied in the study of the invariant mass distributions (section 9.3), where the convolution integral is solved numerically.

A second method to take the resolution into account is to redefine the acceptance, by the ratio of the number of triggered and selected events in the reconstructed variable over the generated events in the generated variable. This acceptance ϵ includes the effect of event losses and resolution. The statistical error of ϵ was again calculated by error propagation from the statistical error on the number of generated events and the statistical error on the number of triggered and selected events. Distributions corrected with ϵ can be directly compared to the physics expectation $F(x)$.

The second correction method is used in most cases in this analysis. Figure 6.10 shows as an example ϵ for the invariant mass. In contrast to figure 6.8 ϵ shows a dip around the ρ^0 mass. This is due to the fact that it is more likely for an event to migrate out of of the ρ^0 peak than to migrate into the peak. The second correction method is simpler but has disadvantages. If the Monte Carlo simulation gives a wrong resolution it is difficult to determine the effect on the final result, whereas in the first method only R has to be changed. A special case of a wrong resolution can occur when the Monte Carlo program simulating the physics process (in this case ρ^0 photoproduction) is not describing the underlying physics well. To make sure that this is not the case the ratio of data over Monte Carlo events in all reconstructed

variables has to be flat. In this analysis the EPSOFT Monte Carlo events are reweighted until the ratios of data and Monte Carlo are flat. In this way the Monte Carlo is tuned to the data.

Chapter 7

Backgrounds to the Elastic ρ^0 Signal

In this chapter different sources of background which contribute to the elastic ρ^0 signal will be studied. Background events originate from ep interactions, from beamgas interactions and cosmic events. The contribution from beamgas interactions and cosmics to the elastic ρ^0 signal turned out to be negligible. The background from elastic photoproduction of ω and ϕ mesons and γ and double dissociative photoproduction is small. On the other hand proton dissociative ρ^0 photoproduction accounts for 20% of the selected events and is subtracted statistically.

7.1 Proton and Electron Beamgas Background

Beamgas events cannot be distinguished from ep events, if they occur close to the interaction point. Therefore they were subtracted statistically using pilot bunches. Pilot bunches are unpaired electron or proton bunches, where the RF-bucket of the other particle species is not filled. In 1994 HERA operated typically with the following bunch configuration:

153 electron-proton bunches (ep bunches)

15 electron pilot bunches

17 proton pilot bunches

35 empty bunches

For the statistical subtraction, the selected events which originated from the pilot bunches were added to the data sample with a negative weight. This weight is given by the probability to get a beamgas event while filled electron and proton bunches collided in ZEUS. Since the number of beamgas events is proportional to the current in the corresponding bunches, the weight is given by the ratio of the current in all pilot bunches over the current contained in all colliding bunches for each particle type:

$$W_{e^+}^{\text{pilot}} = -\frac{I_{e^+} \text{ in all } ep \text{ bunches}}{I_{e^+} \text{ in all } e^+ \text{ pilot bunches}}$$

$$W_{p}^{\text{pilot}} = -\frac{I_{p} \text{ in all } ep \text{ bunches}}{I_{p} \text{ in all p pilot bunches}}$$

Assuming the same e^+ and p lifetimes of pilot and ep bunches, the weights are constant within one HERA fill. In this analysis the weights were calculated for each physics run separately.

Similarly to beamgas events, cosmic events could be subtracted from the sample statistically using the empty bunches. In the final sample 49 events were found in the electron pilot bunches, but none in the proton pilot bunches. The mean weights $\langle W_{e^+}^{pilot} \rangle = -10.2$ and $\langle W_p^{pilot} \rangle = -9.7$ and an upper bound of 1 event in proton pilot bunches resulted in a contribution of 0.6±0.1% electron and <0.01±0.01% proton beamgas events in the final sample. No event was found in empty bunches. The electron beamgas contribution was subtracted statistically in all corrected distributions in chapter 9, whereas contribution from proton beamgas and cosmic events were neglected.

7.2 Photoproduction of ω and ϕ Mesons

In these processes a ω or ϕ meson is produced instead of a ρ^0 meson in the final state. These background reactions were studied using Monte Carlo events from the PYTHIA generator, which were passed through the ZEUS detector simulation program MOZART, the trigger simulation program ZGANA and the reconstruction program ZEPHYR. The most important decay channels of these mesons are:

ω	$\rightarrow \pi^+\pi^-\pi^0(\rightarrow \gamma\gamma)$	BR: 87.7%
ω	$\rightarrow \gamma\pi^0(\rightarrow \gamma\gamma)$	BR: 8.4%
ϕ	$\rightarrow K^+K^-$	BR: 49.1%
ϕ	$\rightarrow K_S^0K_L^0$	BR: 34.3%
ϕ	$\rightarrow \rho\pi \rightarrow \pi^+\pi^-\pi^0$	BR: 12.9%
ϕ	$\rightarrow \pi^+\pi^-\pi^0(\rightarrow \gamma\gamma)$	BR: 2.5%

From these channels only those which could leave the same signature as the $\rho^0 \rightarrow \pi^+\pi^-$ in the ZEUS detector were considered. These were the decay channels ω or $\phi \rightarrow \pi^+\pi^-\pi^0$, if the events were not rejected by the energy deposition caused by the decay of the π^0, and $\phi \rightarrow K^+K^-$ since no particle identification was used in the analysis. Since the P_T of the vector meson is very small, the final state pions in the ϕ decay channel $K_S^0K_L^0$ escape undetected through the beampipe, so this channel does not contribute to the ρ^0 signal. Decays of the ϕ meson in two kaons were identified easily, since the mass difference between the ϕ and the two kaons is very small. As a result these events show up in the invariant mass distribution close to threshold. Indeed in figure 4.11 a small peak is seen at $M_{\pi^+\pi^-} < 400$ MeV. This background was thus rejected completely by a cut on the invariant mass of $M_{K^+K^-} > 1.038$ GeV, calculated from the track momenta assuming kaon mass.

Figure 7.1 shows the invariant mass distribution $M_{\pi^+\pi^-}$ after all ρ^0 selection cuts for ω (upper plot) and ϕ (lower plot) mesons decaying in three pions. ω events peak well below the ρ^0 peak, whereas ϕ mesons show up under the ρ^0 resonance as well. This can be explained from the fact that ϕ mesons can decay via the chain $\phi \rightarrow \rho^0\pi^0 \rightarrow \pi^+\pi^-\pi^0$. Using the measured cross sections of elastic ϕ and ω photoproduction [111, 112] and the branching ratios [82] the following contributions were determined:

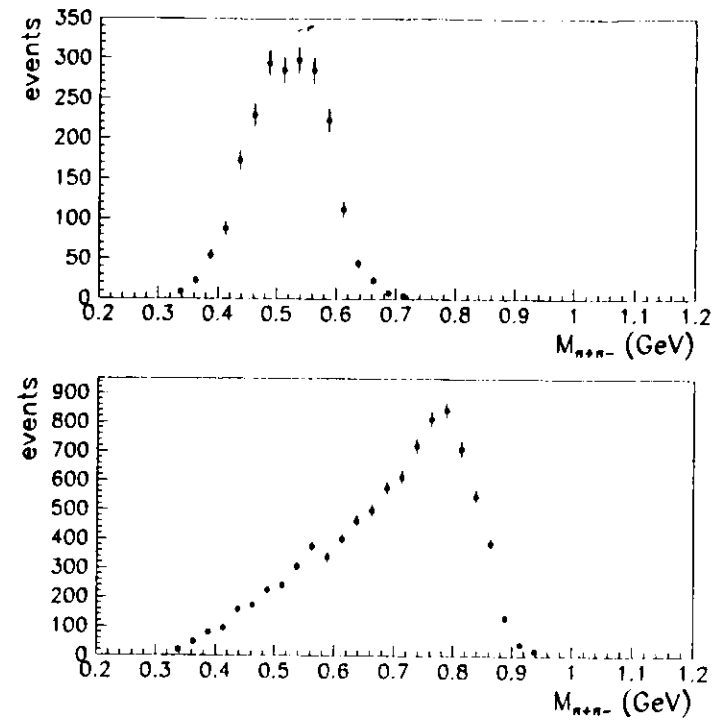

Figure 7.1: Invariant mass distribution $M_{\pi^+\pi^-}$ for ω (upper plot) and ϕ (lower plot) mesons in the three pion decay mode from a Monte Carlo simulation, after all ρ^0 selection cuts.

- background contribution from $\omega \rightarrow \pi^+\pi^-\pi^0$: 1.2±0.1%
- background contribution from $\phi \rightarrow \pi^+\pi^-\pi^0$: 0.4±0.1%

The background from elastic ϕ photoproduction is thus very small and was neglected in the further analysis. The background from elastic ω photoproduction was subtracted statistically from all distributions. Most of the results presented in chapter 9 were derived in the limited mass region of 0.55 GeV < $M_{\pi^+\pi^-}$ < 1.2 GeV. As can be seen from the upper plot of figure 7.1 the contribution from ω photoproduction in this mass region is very small (0.4±0.1%) and leads only to a small statistical subtraction.

7.3 Background from γ and Double Dissociation

Photon dissociation and double dissociation are diffractive processes of the type $\gamma p \to Xp$ and $\gamma p \to XN$, where X and N are states of mass M_X and M_N, which decay into final state hadrons (section 3.3.1). Double dissociative events contribute to the final elastic ρ^0 signal, if the mass M_N is small, so the state N escapes the detector undetected through the forward beampipe. On the other hand the decay products of the state X have to fulfill all the elastic ρ^0 selection cuts. Two Monte Carlo programs (PYTHIA and EPSOFT) were used to study the acceptance of the state X. Details on the Monte Carlo programs and on the mass distribution of X and N used in the simulation can be found in chapter 5. Monte Carlo events were generated in the $W_{\gamma p}$ range between 40 GeV and the kinematic limit. Figure 7.2 shows the generated $W_{\gamma p}$ distribution for γ dissociative events which fulfill all elastic ρ^0 selection cuts. It is seen that the background from γ dissociation is mainly caused by events from the same $W_{\gamma p}$ range as used in the analysis of elastic ρ^0 photoproduction, namely from $W_{\gamma p}$ between 50 and 100 GeV. Figure 7.3 shows the $M_{\pi^+\pi^-}$ distribution up to 1.2 GeV for events generated by the two Monte Carlo generators after applying all elastic ρ^0 selection cuts. For the events generated with PYHTIA (upper plot) an increase of the background for increasing mass is seen. In contrast, for EPSOFT (lower plot) the γ dissociative background is flat in the $M_{\pi^+\pi^-}$ region under study.

The acceptance for double dissociative events was determined using events generated with PYTHIA. The generated mass distribution for M_N starts at $M_p+2M_\pi \approx 1.2$ GeV. The shape of the reconstructed $M_{\pi^+\pi^-}$ distribution after all elastic ρ^0 selection cuts is very similar to the PYTHIA result for γ dissociation but the overall acceptance is two times smaller.

The amount of background from γ and double dissociation to the elastic ρ^0 signal depends on the acceptance for these processes and on the ratio of the cross sections of γ (or double) dissociative photoproduction to elastic ρ^0 photoproduction. Unfortunately the acceptance

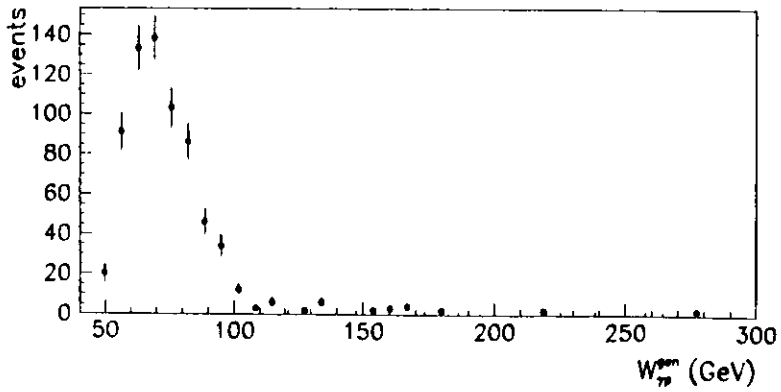

Figure 7.2: Generated center of mass energy $W_{\gamma p}$ for γ dissociative Monte Carlo events, after all ρ^0 selection cuts.

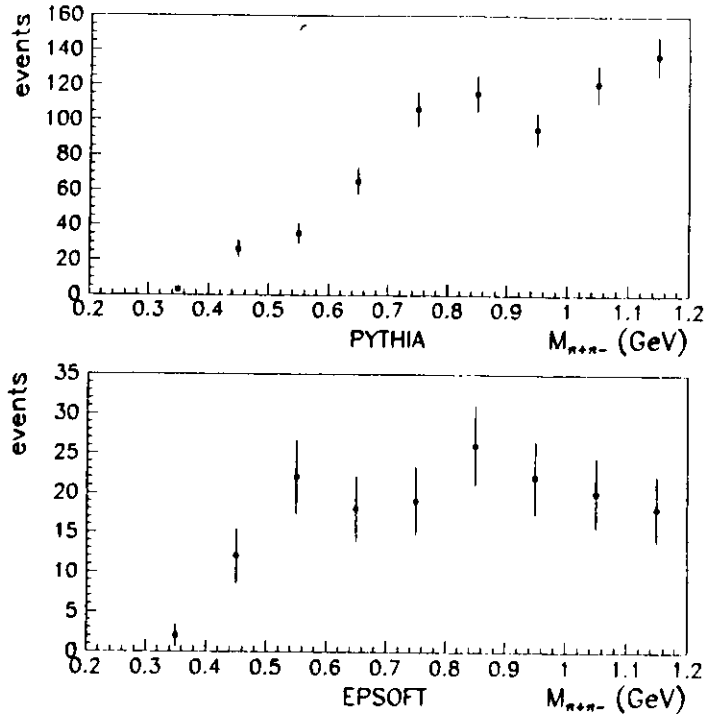

Figure 7.3: Invariant mass distribution $M_{\pi^+\pi^-}$ for γ dissociative events, after all ρ^0 selection cuts, generated by PYTHIA (upper plot) and EPSOFT (lower plot).

for γ dissociative events differed between the two Monte Carlo generators PYTHIA and EPSOFT by a factor of 1.8%/0.3% = 6. Also the ratio of the γ and double dissociative to the elastic ρ^0 photoproduction cross section is not known. Depending on the assumptions made in the analysis the values in table 7.1 were obtained at $W_{\gamma p} \approx 200$ GeV. So the background from these two processes can not be subtracted easily. Instead a background term was included in the fits to the corrected mass distributions to account for γ and double dissociation. The shape of the background was determined from the $M_{\pi^+\pi^-}$ distribution for

	assumption	$\sigma_{\gamma\ dis}/\sigma_{\rho^0}$	$\sigma_{db.\ dis}/\sigma_{\rho^0}$
H1	$0 < \sigma_{db\ dis} < 40\mu b$	1.63±0.89	1.39±1.39
ZEUS	$\sigma_{\gamma\ dis} = \sigma_{p\ dis} = 2\sigma_{db\ dis}$	0.89±0.41	0.45±0.21

Table 7.1: Measured ratios of γ and double dissociative photoproduction cross section ($\sigma_{\gamma\ dis}$, $\sigma_{db\ dis}$) to the elastic ρ^0 photoproduction cross section at $W_{\gamma p} \approx 200$ GeV [108, 50]. The errors were calculated from the individual cross section errors from the references.

the PYTHIA generator (upper plot of figure 7.3) after applying the elastic ρ^0 acceptance in $M_{\pi^+\pi^-}$ (figure 6.8):

$$f(M_{\pi^+\pi^-}) = A(1.0 + 1.5M_{\pi^+\pi^-}[\text{GeV}]). \quad (7.1)$$

In the mass fits in chapter 9 this term was added and A was a free parameter of the fits. The fitted value for A corresponds to an integrated contribution in the mass range 0.55 to 1.2 GeV typically smaller than 1% of the the total.

7.4 Proton Dissociative ρ^0 Production

The most important background to elastic ρ^0 photoproduction is proton dissociative ρ^0 photoproduction. In these events the outgoing nucleon is a state N of mass M_N which decays into final state hadrons.

The contribution of this process, $ep \to e\rho^0 N$, was determined from data and elastic ρ^0 Monte Carlo events, and not from proton dissociative Monte Carlo events. Proton dissociation was studied using subsamples of data events, which were tagged as proton dissociative by an energy deposition in the direction of the outgoing nucleon. All elastic ρ^0 selection cuts were applied, except the cut on the energy deposit in the FCAL (section 4.3.2). To have a good agreement between data and Monte Carlo for the *FCAL* BP_{FLT} trigger requirement a cut on $E_{FCAL\,BP2} < 1.2$ GeV was applied (section 4.1). This requirement limited the accepted masses M_N below ~ 10 GeV.Proton dissociative events were identified by one of the following requirement:

- a PRT tag, a signal of at least 1 MIP in each counter of one pair of counters of the PRT (section 2.2.3). The acceptance of the PRT tag in M_N increases towards very low masses and drops for $M_N \lesssim 3$ GeV. In 1994 the PRT was operating only in part of the luminosity range used in this analysis.
- a FCAL tag, an energy deposition in the two innermost rings surrounding the beampipe of $E_{FCAL\,BP2} > 0.4$ GeV. The acceptance of this tag is constant in the mass range from $\sim$3 to $\sim$10 GeV and drops to zero below 3 GeV.

Figure 7.4 shows the ratio of PRT tagged events over all events fulfilling the elastic ρ^0 selection cuts, as function of $M_{\pi^+\pi^-}$, $W_{\gamma p}$, $\cos\theta_h$ and P_T^2 in the PRT luminosity range. The ratios are flat in $M_{\pi^+\pi^-}$, $W_{\gamma p}$ and the decay angles. Under the assumption, supported by both EPSOFT and PYTHIA, that the requirement of activity in the PRT does not affect the shape of the acceptance as function of $M_{\pi^+\pi^-}$, $W_{\gamma p}$ and the decay angles, this result indicates that proton dissociative and elastic ρ^0 production have the same dependence on these variables. On the other hand the ratio increases as a function of P_T^2. Thus the t slopes of elastic and proton dissociative ρ^0 photoproduction are different. A similar behavior of the ratios as function of the kinematic variables and the decay angles is seen for the FCAL tagged events.

The P_T^2 dependence of the proton dissociative background to the elastic ρ^0 signal was determined from the ratio R_{tag} of tagged proton dissociative events (by the PRT or FCAL) over all events fulfilling the elastic ρ^0 selection cuts. Assuming an exponential shape in P_T^2 for elastic ($A_{el} e^{-b_{el} P_T^2}$) and proton dissociative ($A_{p\,dis} e^{-b_{p\,dis} P_T^2}$) ρ^0 events fulfilling the elastic ρ^0

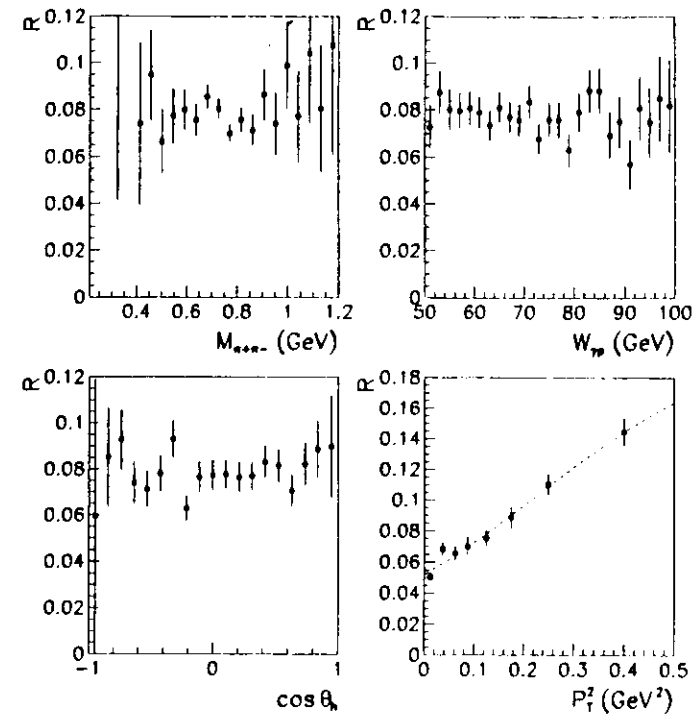

Figure 7.4: The ratio of PRT tagged events to all events fulfilling the elastic ρ^0 selection cuts as function of different kinematic variables. The ratios are flat, except for P_T^2, where the result of a fit with equation (7.2) is shown. Only statistical errors are shown.

selection cuts and the same slope in P_T^2 for proton dissociative events tagged in the PRT or FCAL (b_{tag}) and selected by the elastic ρ^0 selection cuts ($b_{p\,dis}$), the ratio R_{tag} can be written as:

$$\begin{aligned} R_{tag} &= \frac{A_{tag} e^{-b_{tag} P_T^2}}{A_{el} e^{-b_{el} P_T^2} + A_{p\,dis} e^{-b_{p\,dis} P_T^2}} = \frac{A_{tag} e^{-b_{p\,dis} P_T^2}}{A_{el} e^{-b_{el} P_T^2} + A_{p\,dis} e^{-b_{p\,dis} P_T^2}} \\ &= \frac{A_1}{A_2 e^{-(b_{el} - b_{p\,dis}) P_T^2} + 1} = \frac{A_1}{A_2 e^{-b_{diff} P_T^2} + 1}. \end{aligned} \quad (7.2)$$

The second assumption ($b_{tag} = b_{p\,dis}$) is fulfilled since tagged events cover the low M_N region, which is the main background contribution to the elastic signal as well, and the acceptance in P_T^2 has the same shape for the PRT (or FCAL) tag selection and the elastic ρ^0 selection. The slope $b_{diff} = b_{el} - b_{p\,dis}$ is the slope difference between elastic and proton dissociative ρ^0 photoproduction. This parameter is determined by fitting equation (7.2) to the measured

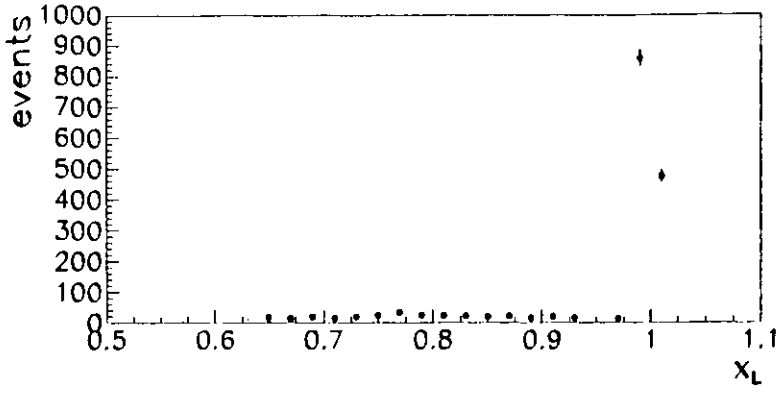

Figure 7.5: The x_L distribution as measured by the LPS in the 1994 elastic ρ^0 sample. A clear peak at $x_L \approx 1$ is seen, corresponding to quasi elastically scattered protons. Only the statistical error is shown.

ratio R_{tag} (lower right plot of figure 7.4).

$$b_{diff} = 4.79 \pm 1.47 \text{ stat.} \pm 0.52 \text{ syst. GeV}^{-2} \quad \text{PRT tag} \qquad (7.3)$$

$$b_{diff} = 4.09 \pm 1.96 \text{ stat.} \pm 3.12 \text{ syst. GeV}^{-2} \quad \text{FCAL tag} \qquad (7.4)$$

The systematic error was determined from the biggest change in b_{diff} for different fit ranges. The absolute normalization of the proton dissociative background contribution was determined by a measurement which does not depend on the simulation of proton dissociation. In 1994 the leading proton spectrometer LPS (section 2.2.3) took data for the first time. The LPS measures the scattered proton. Only for a part of the 1994 luminosity the LPS was inserted into the proton beampipe completely, so an effective (after a prescale correction with equation (4.1)) integrated luminosity with the LPS of $\mathcal{L}_{LPS} = 226 \pm 3$ nb^{-1} was available. The LPS accepts quasi elastically scattered protons with a transverse momentum squared P^2_{Tp} between $\sim$0.07 and $\sim$0.4 GeV^2. P^2_{Tp} can be used to measure the differential cross section $d\sigma/dt$ for elastic ρ^0 photoproduction [114]. In this section the LPS is used as a tagging device for elastic ρ^0 events, but the P^2_T is calculated from the ρ^0. Figure 7.5 shows the measured distribution in x_L, defined as the ratio of the measured proton momentum over the momentum of the incoming proton (820 GeV), after all elastic ρ^0 selection cuts and the following LPS selection cuts:

- one LPS track in 2 or 3 stations,
- χ^2/NDF < 6 of the LPS track fit,
- closest distance of the LPS track to a beam aperture > 0.5 mm.

On top of the LPS selection cuts, the following weight factors had to be applied.

- A factor of 1.1 to take a run dependence of the LPS pot position into account. The pot position in the Monte Carlo was set to the position in run 9720. The weight factor takes the run dependence of the LPS acceptance due to the different pot positions into account [90]. This correction is independent of P^2_{Tp}.
- A factor of 0.95 to correct for random coincidences between a LPS track from a halo proton and a ρ^0 event. This factor was determined from DIS events and the $E + P_Z$ constraint [90].

For elastic ρ^0 photoproduction x_L can be written as $x_L = 1 - (Q^2 + M^2_{\rho^0} + |t|)/W^2_{\gamma p}$, so for the sample used in this analysis the value of x_L differs from unity by at most 0.2%. In figure 7.5 a clear peak at $x_L \approx 1$ is seen which corresponds to quasi elastically scattered protons. The method to determine the normalization of proton dissociation is illustrated in figure 7.6. The P^2_T distribution as measured by the ρ^0 for all events within the LPS luminosity range is shown as a solid line. The dotted line shows the events with a proton in the LPS of $1.02 > x_L > 0.98$ and the dashed line the same events after LPS acceptance correction. The LPS acceptance was determined using the average of the Monte Carlo programs EPSOFT and DIPSI ($\epsilon_{LPS} \approx 10\%$ for $0.075 \text{ GeV}^2 < P^2_T < 0.5 \text{ GeV}^2$). For $P^2_T < 0.075$ GeV^2 the LPS acceptance decreases rapidly, so this range was not considered in the determination of the proton dissociative background contribution. The amount of proton dissociation is given by the difference between the full and the dashed line, indicated in figure 7.6 by the dark shaded area. Since the statistics of LPS tagged events in the 1994 data is limited these events were just used to determine the absolute normalization of the proton dissociative contribution

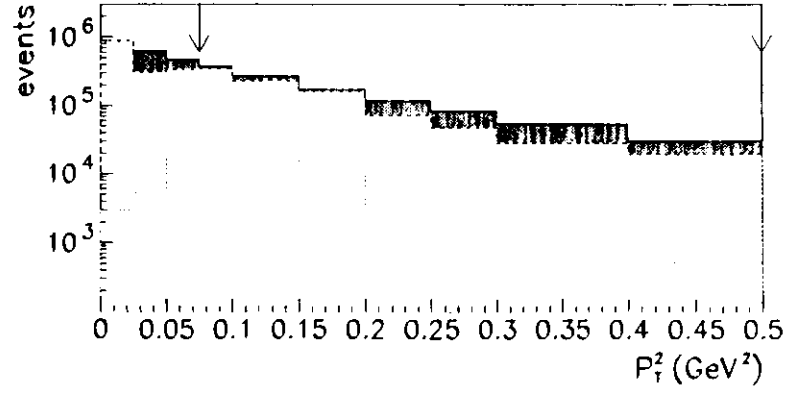

Figure 7.6: The P^2_T distribution, as measured by the ρ^0, for all events in the LPS luminosity range (full line), all events with a proton in the LPS of $1.02 > x_L > 0.98$ (dotted line) and the LPS acceptance corrected distribution (dashed line). The dark shaded area indicates the amount of proton dissociative ρ^0 events. The vertical arrows indicate the range in P^2_T used to determine the absolute normalization of proton dissociative background ($0.075 < P^2_T < 0.5$ GeV^2).

to the elastic ρ^0 signal in the P_T^2 range between 0.075 GeV^2 and 0.5 GeV^2. The PRT (or FCAL) tagged events were used to measure the P_T^2 dependence of this contribution.

Figure 7.7 shows the ratio $R_{p\,dis}$ of proton dissociative events, given by the difference between all events fulfilling the elastic ρ^0 selection cuts and the acceptance corrected events of $1.02 > x_L > 0.98$, over all events fulfilling the elastic ρ^0 selection cuts for the LPS luminosity range. Assuming again an exponential P_T^2 distribution for elastic and proton dissociative ρ^0 events the ratio $R_{p\,dis}$ is:

$$R_{p\,dis} = \frac{A_{p\,dis}\, e^{-b_{p\,dis} P_T^2}}{A_{ela}\, e^{-b_{ela} P_T^2} + A_{p\,dis}\, e^{-b_{p\,dis} P_T^2}} = \frac{1}{N e^{-b_{ela} P_T^2} + 1}. \tag{7.5}$$

A fit of equation (7.5), with a fixed slope (7.3) from PRT tagged events yields for the normalization factor N:

$$N = 7.34 \quad {}^{+1.16}_{-0.88}\ \text{stat.} \ \pm 0.74\ \text{syst. fit} \ {}^{+2.75}_{-1.64}\ \text{syst.}\ \epsilon_{LPS} \quad {}^{+1.31}_{-1.07}\ \text{syst. weight pot} \ {}^{+0.27}_{-0.26}\ \text{syst. weight halo} \tag{7.6}$$

where N is the mean value of the results derived for the two Monte Carlo generators used for the LPS acceptance correction. The listed systematic errors are the errors due to a change of the fit range, a systematic uncertainty of the LPS acceptance of ±8% (±6% uncertainty on the acceptance for a proton track in the LPS [114] and ±5% alignment uncertainty added in quadrature), an uncertainty of the pot position reweighting of ±5% and an uncertainty of halo proton reweighting of ±1%.

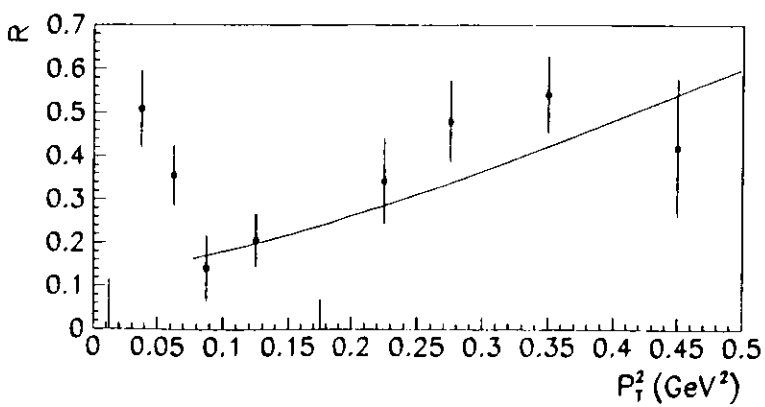

Figure 7.7: Acceptance corrected ratio of proton dissociative events over all events fulfilling the elastic ρ^0 selection cuts, determined by the LPS as a function of P_T^2. The line shows the result of a fit with equation (7.5), with a fixed slope (7.3). Only the statistical error is shown.

To correct for the proton dissociation background contribution all selected elastic ρ^0 events are weighted by:

$$R_{ela} = 1 - R_{p\,dis} \tag{7.7}$$

Reweighting the P_T^2 distribution resulted in a contribution of proton dissociation to the selected elastic sample of:

$$C_{p\,dis} = 20.3\%^{+6.3}_{-5.1}\% \quad (\text{for } P_T^2 < 0.5\ \text{GeV}^2). \tag{7.8}$$

A background contribution of 20% is consistent with a calculation of Holtmann et al.[57]. They estimate the proton dissociative background contribution to elastic ρ^0 photoproduction to be 0.20-0.22. The range corresponds to an upper limit on M_N between 5 GeV and 6 GeV. The values given in [57] had to be corrected for the P_T^2 cut taking into account the different $|t|$ slopes for elastic and proton dissociative ρ^0 production.

The measurement of the proton dissociative background did not depend on any proton dissociative Monte Carlo generator. Now the data will be compared to the two Monte Carlo programs EPSOFT and PYTHIA. For proton dissociative events the dependence on the nucleonic mass M_N, in the region above the resonances ($10\ \text{GeV}^2 < M_N^2 < 200\ \text{GeV}^2$), can be described by $d\sigma/dM_N^2 \propto 1/M_N^n$ with an effective power n. A measurement from the CDF collaboration in $pp \to pX$ at $\sqrt{s}$ =1800 GeV [19] yields $n = 2.24 \pm 0.02$ stat ± 0.02 syst.. The power n for the γp ZEUS data can be determined from the ρ^0 photoproduction events by comparing the shape of the energy distribution in FCAL between 0.8 and 2.0 GeV. A measure of the shape difference between data and Monte Carlo is given by the χ^2, calculated from the FCAL energy spectra, normalized in the region between 0.4 and 2.0 GeV:

$$\chi^2 = \sum_{bins} \frac{(n_{DATA} - n_{MC})^2}{\sigma_{DATA}^2 + \sigma_{MC}^2}. \tag{7.9}$$

In figure 7.8 χ^2 is shown versus the value of n for the generator PYTHIA. Minima in the χ^2 distribution were found for the two generators:

$$n = 2.0 \pm 0.7\ \text{stat.} \pm 0.5\ \text{syst.} \qquad \text{PYTHIA}$$
$$n = 2.4 \pm 0.4\ \text{stat.} \pm 0.1\ \text{syst.} \qquad \text{EPSOFT}$$

The statistical error is given by the change in n for a change in χ^2 by 1 unit and the systematic error is due to a change in the fit range. The minima are very broad, because the energy range which could be used is very small due to the tight *FCAL* BP_{ELT} cut. The position of the minima were independent on the t slope used in the generation of the Monte Carlo events. The measurement is consistent with the CDF measurement.

Data and a mixture of Monte Carlo events of 80% elastic and 20% proton dissociative ρ^0 events after applying all elastic ρ^0 selection cuts (including $P_T^2 < 0.5$ GeV^2) can be compared to see whether the two proton dissociative Monte Carlo generators EPSOFT and PYTHIA are able to describe the data. These two generator are frequently used in the ZEUS collaboration to determine the proton dissociative background to elastic photoproduction of vector mesons. In the simulation of proton dissociation the value of n was set to the 2.0 for PYTHIA and 2.4 for EPSOFT. Figure 7.9 shows the normalized x_L distributions as measured by the LPS for data (open dots) and the Monte Carlo mixtures (full dots). The x_L spectrum below 0.98 can be explained by proton dissociative events with a leading proton.

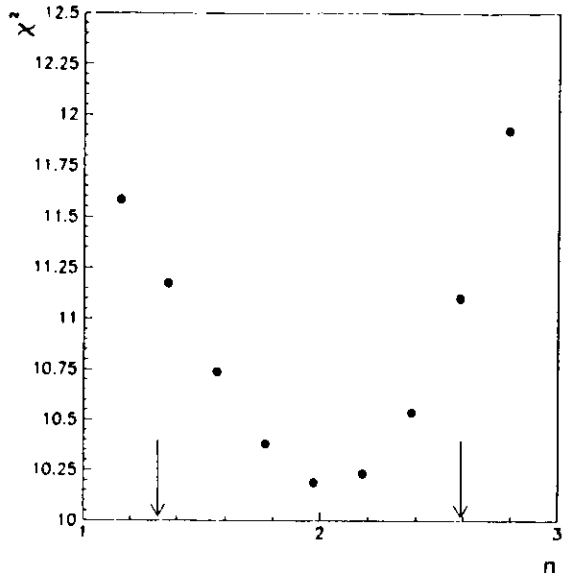

Figure 7.8: The χ^2 difference (NDF=11) between data and Monte Carlo (PYTHIA) for the FCAL energy distribution as a function of n. The arrows indicate the values for n corresponding to a change in χ^2 by 1 unit.

On the upper plot of figure 7.9 PYTHIA was used to simulate proton dissociation and on the lower plot EPSOFT. PYTHIA describes the data much better than EPSOFT. In table 7.2 the fractions of events with a leading proton in the LPS with $x_L < 0.98$ (LPS tag), a tag in the PRT (after applying all elastic ρ^0 selection cuts) and a tag in FCAL, defined above, are summarized for data and the Monte Carlo mixtures. The systematic errors on the Monte Carlo fractions were determined by changing the value of n between 2.0 and 2.8. Since the simulation of the PRT in the ZEUS detector Monte Carlo program ignored detector noise, the tagging efficiency in the Monte Carlo was too high. Therefore the PRT efficiencies in the Monte Carlo were scaled down to the efficiency measured in the 1994 data. Details on the correction procedure can be found in [11]. In table 7.2 good agreement between data

	data	PYTHIA	EPSOFT
LPS tag	$1.3 \pm 0.1\%$	$1.3 \pm 0.1 \pm 0.1\%$	$1.9 \pm 0.1 \pm 0.2\%$
PRT tag	$6.7 \pm 0.2\%$	$6.2 \pm 0.2 \pm 1.5\%$	$8.9 \pm 0.3 \pm 1.1\%$
FCAL tag	$1.2 \pm 0.1\%$	$1.7 \pm 0.1 \pm 0.6\%$	$1.0 \pm 0.1 \pm 0.4\%$

Table 7.2: Fraction of events with a leading proton in the LPS of $x_L < 0.98$ (LPS tag), a tag in the PRT (after all elastic ρ^0 selection cuts) and a tag in FCAL for data and the two Monte Carlo mixtures.

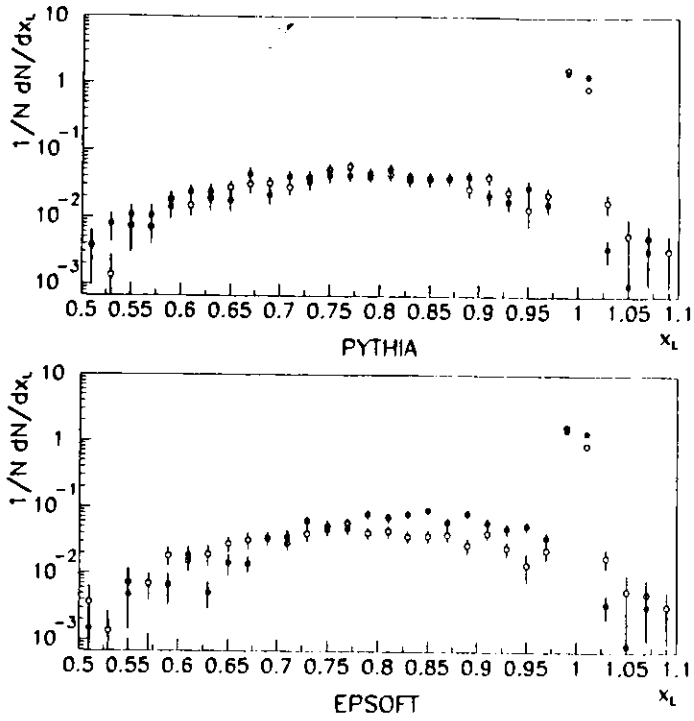

Figure 7.9: Normalized LPS x_L spectrum for data (open dots) and Monte Carlo mixtures (80% elastic, 20% proton dissociation) after all elastic ρ^0 selection cuts (including $P_T^2 < 0.5$ GeV^2). On the upper plot PYTHIA was used to describe proton dissociation and on the lower plot EPSOFT. Only the statistical errors are shown.

and PYTHIA is seen for the event fractions tagged in LPS and PRT, whereas EPSOFT does not describe the data. On the other hand EPSOFT agrees with the data in the fraction of events tagged by FCAL, whereas in PYTHIA this fraction is higher than in the data. Proton dissociative events tagged in the PRT and in FCAL leave only a small amount of energy in these detectors. Therefore a correct simulation of the forward region of the ZEUS detector, concerning for example inactive material, is very important for the efficiency of these tags. More studies are needed to determine, whether the differences between data and Monte Carlo are due to the Monte Carlo model or due to an incorrect detector simulation.

Proton dissociative Monte Carlo events can also be used to determine the acceptance correction for the measured P_T^2 distribution tagged by PRT (or FCAL). The acceptance corrected P_T^2 distribution can be corrected to $|t|$ using a correction function, calculated from the Monte Carlo samples for proton dissociation. Figure 7.10 shows the corrected $dN/d|t|$ distribution for proton dissociative events, using the PRT tag and EPSOFT for the corrections. A fit

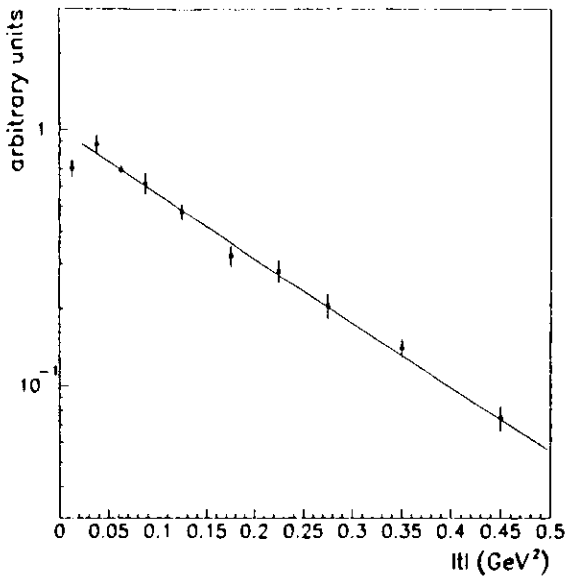

Figure 7.10: The corrected $|t|$ distribution for proton dissociative events. The PRT tag was used to identify proton dissociation and EPSOFT for the acceptance correction. A fit with an exponential yields a slope of $b = 5.8 \pm 0.6$ GeV^{-2}. Only the statistical error is shown.

with the function $dN/d|t| = A\,e^{-b|t|}$ yields:

$$b = 5.8 \pm 0.3 \text{ stat.} \pm 0.1 \text{ syst. MC} \pm 0.5 \text{ syst. tag} \pm 0.2 \text{ syst. } n \quad \text{GeV}^{-2} \tag{7.10}$$

The first systematic error gives the dependence on the Monte Carlo used for the acceptance correction, the second systematic error the dependence on the tagging method and the third systematic error the dependence on the value on n. This result is again consistent with the estimate given in [57] namely $b_{\gamma p \to \rho^0 N} \sim 0.5 b_{el}(pp)$. Measurements of $b_{el}(pp)$ at $\sqrt{s} \approx 63$ GeV yield $b_{el}(pp) \approx 13\text{GeV}^{-2}$.

The measurement of the contribution of proton dissociation to the elastic ρ^0 signal ($C_{p\,dis} = 20.3\%^{+6.3\%}_{-5.1\%}$) allowed also a determination of the ratio of the cross sections of elastic and proton dissociative ρ^0 photoproduction for $P_T^2 < 0.5$ GeV^2. This ratio is given by:

$$\frac{\sigma_{el}}{\sigma_{p\,dis}} = \frac{N_{el}/\epsilon_{el}}{N_{p\,dis}/\epsilon_{p\,dis}} = \frac{(1 - C_{p\,dis})/\epsilon_{el}}{C_{p\,dis}/\epsilon_{p\,dis}} \tag{7.11}$$

where ϵ_{el} and $\epsilon_{p\,dis}$ are the efficiencies of the elastic ρ^0 selection cuts for elastic and proton dissociative events. The efficiency $\epsilon_{p\,dis}$ is calculated with Monte Carlo generators EPSOFT and PYTHIA in which proton dissociative events have a hadronic mass M_N in the range $(M_p + 2M_\pi)^2 < M_N^2 < 0.1W_{\gamma p}^2$. While the data extends down in M_N to $M_p + M_\pi$, the lack of simulated events between $M_p + M_\pi$ and $M_p + 2M_\pi$ is not expected to have a significant effect [48]. Since $\epsilon_{p\,dis}$ depends strongly on n, the result for the cross section ratio depends on n

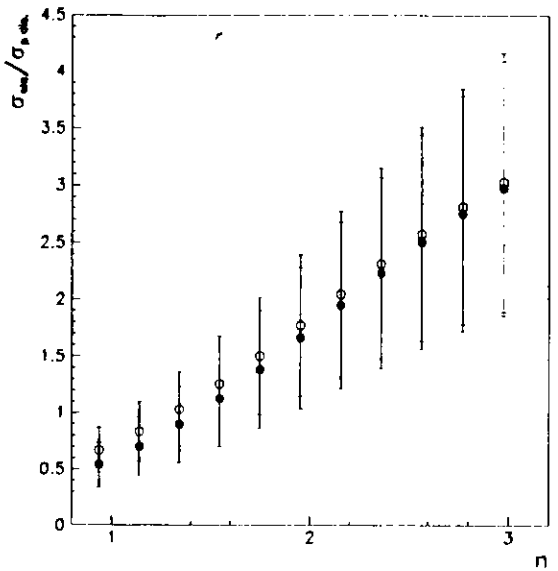

Figure 7.11: Ratio of the elastic to proton dissociative ρ^0 cross section as a function of n used in the simulation of proton dissociation by PYTHIA (full dots) or EPSOFT (open dots).

as well. In figure 7.11 $\sigma_{el}/\sigma_{p\,dis}$ is shown versus n for EPSOFT (open dots) and PYTHIA (closed dots). The error bars are given by the statistical errors of ϵ_{el}, $\epsilon_{p\,dis}$ and the error on $C_{p\,dis}$. The result is almost independent on the Monte Carlo generator and using a value of $n = 2.24$ yields:

$$\frac{\sigma_{el}}{\sigma_{p\,dis}} = 2.0 \pm 0.7 \tag{7.12}$$

Chapter 8

Low Energetic Pions in the ZEUS Calorimeter

In this chapter the energy deposition of the pions from the ρ^0 decay in the ZEUS calorimeter will be compared to test beam results. Whereas in the test beam momentum selected pions are directly sent onto the calorimeter, in the ZEUS experiment the pions, after being momentum analyzed in the CTD, have to traverse inactive material before hitting the calorimeter.

8.1 Pions from ρ^0 Decays and Test Beam Data

Selected elastic ρ^0 events in the mass range between 0.55 GeV and 1.2 GeV were used to study the energy deposition of low momentum pions in the calorimeter. Since the FLT requirement of 464 MeV in $REMC_{FLT}$ causes a bias in the energy distribution of the pions events in which the two pions hit opposite CFLT trigger regions were used in this study. After requiring that one pion triggered the event (the CFLT trigger region hit by this pion fired) the other pion is an unbiased test pion. As explained in section 4.3.2 the energy in a cone around the track impact point on the calorimeter, with a radius of 40 cm in the electromagnetic section and 55 cm in the hadronic section, was assigned to the pions. The radii were chosen to make sure that an energy deposition outside the two cones, was not caused by the pions. So all the energy deposited in the calorimeter by the pions is inside these radii. The cone size is also consistent with the fact that 95% of the energy in a hadron shower is contained in a radius of 1 λ_0 (λ_0 = 10.8 cm for the ZEUS calorimeter).

The energy inside the cone E_{CAL} was studied as a function the kinetic energy E_{kin} of the pions. The kinetic energy is given by $E_{kin} = \sqrt{p^2 + M_\pi^2} - M_\pi$, where p is the pion momentum measured by the CTD. The kinetic energy was used, since at low energies the energy response of a calorimeter for different particles is essentially a function of E_{kin} [45].

In the upper plot of figure 8.1 the ratio E_{CAL}/E_{kin} is plotted versus E_{kin} for positive and negative pions from ρ^0 decays. The ratio is obtained from the mean value of a fit with a Gaussian to the E_{CAL}/E_{kin} distribution in bins of E_{kin}. A clear difference is seen between positive (full dots) and negative (open dots) pions. The ratio increases as the energy increases up to kinetic energies of $\sim$ 500 MeV and then starts to decrease. A value of $\sim$ 0.8 is reached for E_{kin} = 1.8 GeV. E_{CAL}/E_{kin} was also determined from test beam data [45] for positive and negative pions and is shown in the lower plot of figure 8.1. For test beam data E_{CAL}/E_{kin}

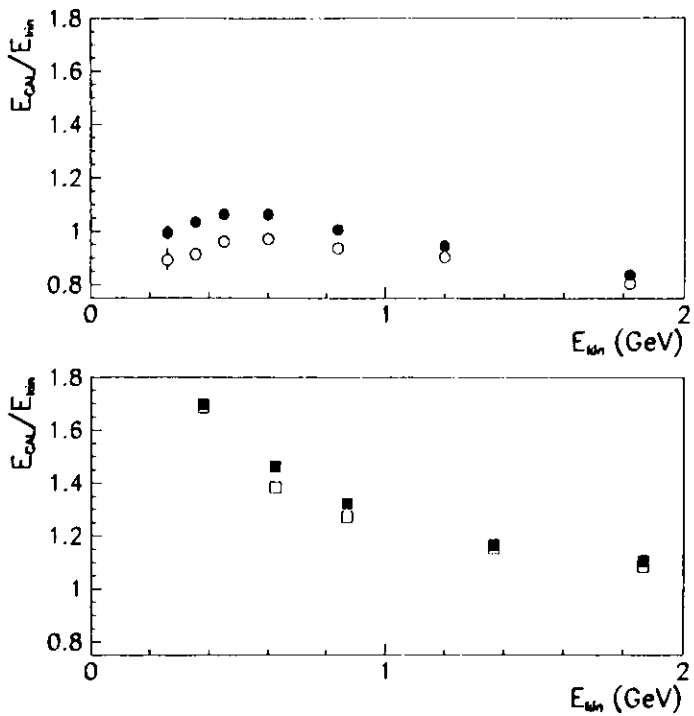

Figure 8.1: Ratio of the energy deposition in the calorimeter E_{CAL} over the kinetic energy E_{kin} as a function of E_{kin} for pions as measured in the ZEUS detector (upper plot) and test beam data (lower plot). The ratio is shown for positive (full symbols) and negative pions (open symbols) separately.

in each bin of E_{kin} was determined from the mean value of a fit with a Gaussian of the pulse height spectra, under the assumption of perfect linearity of the calorimeter with a calibration constant of $\langle Q \rangle / p = 16.24$pC/GeV. The test beam data was taken without inactive material in front of the calorimeter. Therefore the ratio E_{CAL}/E_{kin} is higher. The ratio decreases for increasing kinetic energy and reaches a value of 1 for kinetic energies above $\sim$ 2 GeV. Also in the lower plot of figures 8.1 a difference between positive (full squares) and negative (open squares) pions is seen.

The effect of the charge difference can clearly be seen in figure 8.2 and table 8.1, which show $E^{\pi^+}_{CAL}/E^{\pi^-}_{CAL}$ for pions from ρ^0 decays (full dots) and test beam data (open dots). The effect is much bigger for the pions, measured in the ZEUS experiment with inactive material in front of the calorimeter. The measured difference is up to 13% at low energy and decreases for increasing kinetic energy of the pions. For the test beam data the difference is smaller (only up to 6%) and vanishes for very small kinetic energies. For events simulating elastic

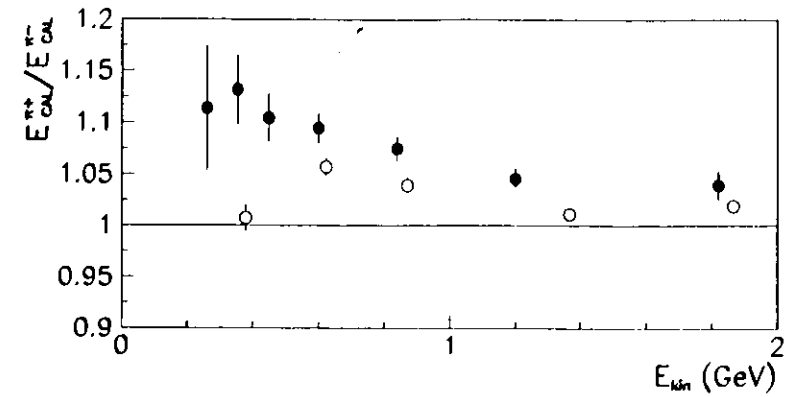

Figure 8.2: Ratio of the energy deposition of positive and negative pions in the calorimeter as a function of the kinetic energy for pions from ρ^0 decays (full dots) and test beam data (open dots).

ρ^0 photoproduction, which were passed through the ZEUS detector simulation program MOZART and selected like the data events, no difference in the energy deposition between positive and negative pions was found. So the charge difference already seen in the test beam data is not simulated in MOZART.

E_{kin} (GeV)	$E^{\pi^+}_{CAL}/E^{\pi^-}_{CAL}$ ρ^0 decays	E_{kin} (GeV)	$E^{\pi^+}_{CAL}/E^{\pi^-}_{CAL}$ test beam data
0.260	1.11±0.06		
0.355	1.13±0.03	0.380	1.01±0.01
0.450	1.10±0.02		
0.600	1.09±0.02	0.624	1.06±0.01
0.840	1.07±0.01	0.871	1.04±0.01
1.200	1.04±0.01	1.367	1.01±0.01
1.820	1.04±0.01	1.866	1.02±0.01

Table 8.1: Ratio of the energy deposition of positive and negative pions in the calorimeter for pions from ρ^0 decays (left columns) and test beam data (right columns).

Chapter 9

Results

Elastic ρ^0 photoproduction can be characterized in terms of a few variables. In this chapter those distributions used to describe ρ^0 photoproduction will be shown, namely the mass distribution, the $|t|$ distribution and the decay angular distributions. The elastic ρ^0 photoproduction cross section will be extracted from the mass distribution. In the first two sections of this chapter the correction procedure and the systematic checks are introduced. Most of the results shown is the following sections, including the systematic errors are summarized in the tables in Appendix C.

9.1 Correction Procedure

The differential cross sections, shown in the following sections, were evaluated in each bin of the variable v as

$$\frac{d\sigma}{dv} = \frac{N_v}{\epsilon \mathcal{L} \Phi \Delta B}, \tag{9.1}$$

where N_v is the number of observed events in the bin B after background subtraction (chapter 7) and correction of $REMC_{FLT}$ trigger efficiency (section 6.1.2), ϵ is the acceptance in the bin, $\mathcal{L}$ the integrated luminosity, Φ is the effective photon flux $\varphi(y, Q^2)$ (equation (3.54)) integrated over the Q^2 and $W_{\gamma p}$ range covered by the selection and ΔB is the bin-width. For the correction method (a) ϵ takes into account the geometrical acceptance and the smearing in the variable v due to the detector resolution. In an alternative approach (correction method (b)) the acceptance is given by ϵ_g, the pure geometrical acceptance, and the smearing is taken into account in the fit function applied to the corrected data (section 6.2). Correction method (b) was only applied to the invariant mass distribution for the whole sample and in $W_{\gamma p}$ bins. The statistical error of the differential cross section $d\sigma/dv$ is given by error propagation of the statistical error of N_v and the statistical error of ϵ (or ϵ_g). Differential distributions will be studied in $W_{\gamma p}$, $M_{\pi^+\pi^-}$ and $|t|$ bins. Since in the analysis presented in this thesis, the outgoing electron and proton were not measured, $|t|$ could not be determined directly. To study the $|t|$ dependence of the mass and decay angular distributions, the events were selected in P_T^2 bins and the acceptance ϵ was calculated taking into account the difference between P_T^2 and $|t|$. In this way the corrected differential distribution in a certain $|t|$ bin was determined using a correction, to account for the fact that Q^2 is non-zero, which was evaluated from the Monte Carlo simulation. In the following sections least square fits

to the the corrected differential distributions will be performed. In these fits the quantity

$$\chi^2 = \sum_{\text{bins i}} \frac{\left(\frac{\int_{\text{bin i}} f(v,\vec{a})dv}{\Delta B|_{\text{bin i}}} - \frac{d\sigma}{dv}|_{\text{bin i}} \right)^2}{\left(\delta \frac{d\sigma}{dv}|_{\text{bin i}} \right)^2} \tag{9.2}$$

was minimized. $f(v,\vec{a})$ is the functional behavior expected for $d\sigma/dv$. This function depend on the parameters $\vec{a}$. These parameters describe certain properties of elastic ρ^0 photoproduction. $\Delta B|_{\text{bin i}}$ is the bin-width of bin i, $d\sigma/dv|_{\text{bin i}}$ the differential cross section in bin i and $\delta d\sigma/dv|_{\text{bin i}}$ it's statistical error. The sum runs over all bins inside the fitrange.

9.2 Systematic Error

The systematic error due to a certain effect was determined for most contributions by changing cuts applied in the analysis or changing the reweighting factor applied to the data. The 37 systematic checks performed were grouped into 12 classes. The following list describes the 12 classes (i to xii) and the 37 systematic checks (1 to 37) considered in this analysis:

i. The tracking systematics was determined by changing the quality cuts imposed on the two tracks (section 5.3).

   1. No track quality cuts were imposed.
   2. Tighter track quality cuts were applied ($|\eta| < 1.8$ and $P_T > 200$ MeV).

ii. The systematic error due to the proton dissociative background subtraction was determined by changing the reweighting factor (equation (7.5)) applied to the data. The reweighting factor depends on two parameter, the slope b_{diff} and the absolute normalization N, which were determined independently.

   3. Decreasing the normalization N inside the error (equation (7.6)), thereby decreasing the amount of proton dissociative background.
   4. Increasing the parameter N.
   5. Increasing the slope difference b_{diff} inside the error (equation (7.3)), while keeping the absolute amount of proton dissociation background unchanged.
   6. Decreasing the slope difference b_{diff} inside the error, while keeping the absolute amount of proton dissociation background unchanged.

iii. Systematic error due to the RCAL efficiency reweighting (section 6.1.1). The RCAL trigger efficiency was determined from data by measuring the probability for a pion to trigger an event. This probability was determined from data with a certain statistical accuracy. The error of the reweighting factor is given by error propagation from the statistical error of the probability for a pion to trigger an event.

   7. Decreasing the RCAL trigger efficiency, inside the statistical error, thereby increasing the reweighting factor.

   8. Increasing the RCAL trigger efficiency, thereby decreasing the reweighting factor.

iv. Model dependence of the acceptance determination by changing the distributions in $W_{\gamma p}$, $|t|$, $M_{\pi^+\pi^-}$ and the decay angles in the Monte Carlo simulation within their uncertainty (5.2).

   9. Increasing the parameter r^{04}_{00}, $\Re r^{04}_{10}$ and r^{04}_{1-1}, describing the decay angular distribution.
   10. Decreasing the parameter r^{04}_{00}, $\Re r^{04}_{10}$ and r^{04}_{1-1}.
   11. Increasing the parameter a, used to parameterize the $W_{\gamma p}$ distribution.
   12. Decreasing the parameter a.
   13. Increasing the parameter b and c, used to parameterize the $|t|$ distribution.
   14. Decreasing the parameter b and c.
   15. Increasing the parameter n_1 and n_2, used to parameterize the shape of the invariant mass distribution $M_{\pi^+\pi^-}$.
   16. Decreasing the parameter n_1 and n_2.
   17. Reweighting the decay angular distribution according to s-channel helicity conservation, namely $\Re r^{04}_{10} = 0$ and $r^{04}_{1-1} = 0$.

v. Systematic error due to a change of the value of ξ^2, used to parameterize the ratio of the transverse to longitudinal cross section $\sigma_L/\sigma_T = \xi^2 Q^2/M^2_{\rho^0}$. The parameter ξ^2 is needed in order to reweight the Monte Carlo Q^2 distribution and in the calculation of the flux factor (equation (3.53)).

   18. Assume $\xi^2 = 0$, thus neglecting the longitudinal cross section σ_L.
   19. Assume $\xi^2 = 1$.

vi. Systematic error due to a change of the maximal Q^2 of the data Q^2_{max}. Q^2_{max} was determined from a Monte Carlo simulation to be $Q^2_{max} = 4$ GeV^2. For this systematic check the value of Q^2_{max} was changed in the Monte Carlo simulation as well as for the determination of ξ^2 (equation (5.6)) and the flux factor (equation (3.53)).

   20. Assume $Q^2_{max} = 3$ GeV^2.
   21. Assume $Q^2_{max} = 2$ GeV^2.

vii. For the mass fits in $W_{\gamma p}$ and $|t|$ bins the ρ^0 mass M_{ρ^0} and the width Γ_0 were fixed to the values as determined from fits to the whole spectrum. In bins of $W_{\gamma p}$ also the amount of skewing given by $|B/A|$ in equation (9.7) and n in equation (9.10) was fixed. For the fits to the $|t|$ distribution in $W_{\gamma p}$ and $M_{\pi^+\pi^-}$ bins the parameter c (equation (9.14)) was fixed to the value as determined from a fit the the whole $|t|$ distribution.

   22. Increasing the fixed value for M_{ρ^0} and Γ_0 inside the statistical error given by the fit to the whole distribution.
   23. Decreasing the fixed value for M_{ρ^0} and Γ_0.

24. Increasing the fixed value for $|B/A|$ and n inside the statistical error given by the fit to the whole distribution.
25. Decreasing the fixed value for $|B/A|$ and n.
26. Increasing the fixed value for c inside the statistical error given by the fit to the whole distribution.
27. Decreasing the fixed value for c.

These systematic checks have no effect for the results derived from the decay angular distributions.

viii. Systematic error due to a change of the fit procedure to the $|t|$ distribution in $M_{\pi^+\pi^-}$ and $W_{\gamma p}$ bins.

28. The parameter c was not fixed, but the absolute normalization of the $|t|$ distribution (A in equation (9.14)) was calculated as the integral over the invariant mass distribution.
29. Considering the c and A as a free parameter.

These systematic checks have no effect for the mass and the decay angular distributions.

ix. 30. Systematic change due to a decreases of the fit range. For $M_{\pi^+\pi^-}$ the range $0.6 < M_{\pi^+\pi^-} < 1.1$ GeV (nominal: $0.55 < M_{\pi^+\pi^-} < 1.2$ GeV) was used, for $\cos\theta_h$ the range $-0.84 < \cos\theta_h < 0.84$ (nominal: $-1.0 < \cos\theta_h < 1.0$) and for $\cos\theta_h$ in the two dimensional decay angular distribution the range $-13/15 < \cos\theta_h < 13/15$ (nominal: $-1.0 < \cos\theta_h < 1.0$).

x. Change in the binning of the mass distribution, the $|t|$ distribution and the decay angular distributions (nominal binning: table 4.3).

31. More bins (bin-width: 16.6 MeV in $M_{\pi^+\pi^-}$, $2/35$ in $\cos\theta_h$ and $\pi/15$ in ϕ_h).
32. Less bins (bin-width: 50 MeV in $M_{\pi^+\pi^-}$, $2/15$ in $\cos\theta_h$, $\pi/5$ in ϕ_h and ≥ 0.008 GeV^2 in $|t|$).

xi. Systematic error due to a change of the Breit-Wigner function and the momentum dependent width used in the fits to the mass distributions.

33. Breit-Wigner given by (9.3) and width given by (9.6).
34. Breit-Wigner given by (9.5) and width given by (9.4).
35. Breit-Wigner given by (9.5) and width given by (9.6).

These systematic changes have no effect for the decay angular distributions.

xii. For correction method (b) the resolution, assumed in the convolution of the resolution function and the function describing the physics, was changed.

36. Increasing the resolution as given by the parameter P_3 and P_5 in equation (4.7) by 25%.

37. Decreasing the resolution by 25%.

Further sources of the systematic error, which have an influence on the absolute normalization of the cross section only, have been taken into account in section 9.4:

- the systematic uncertainty in the luminosity measurement of 1.5% [84],
- the effect of electron initial and final state radiation and of vacuum polarization loops. The size of the correction was estimated to be smaller than 2% [66]. The effect of radiative corrections on the shape of the $M_{\pi^+\pi^-}$, $|t|$ and angular distributions are expected to be negligible. No correction was applied to the cross section, instead a 2% contribution was added to the systematic error.

For all the results quoted in the following, the systematic error was determined in the following way. For each class (i to xii) the biggest positive and negative deviation from the nominal value, due to a single check in this class, was determined. The total positive and negative systematic error was calculated as a quadratic sum of these deviations over all classes. Some classes do not affect all results, so they were not included in those results which they can not affect.

Some parameters will be determined in eight $M_{\pi^+\pi^-}$ and nine $|t|$ bins. For a few systematic checks big fluctuations from bin to bin in $M_{\pi^+\pi^-}$ and $|t|$ were observed. The reason for these fluctuations are statistical fluctuations in the data and in the Monte Carlo for these systematic checks. To overcome this problem the systematic checks were performed in only three bins in $M_{\pi^+\pi^-}$ and $|t|$, which are combinations of three (in one case two) original bins. The positive and negative systematic error for each class was determined in these three bins as before. These errors were extrapolated to the finer binning by performing a fit of a linear function in $M_{\pi^+\pi^-}$ (or $|t|$) to the errors determined in the three bins. The final positive and negative systematic error in the finer binning is again given by the quadratic sum of errors over all classes.

9.3 Study of the Invariant Mass Distribution

Figure 9.1 shows the differential cross section $d\sigma/dM_{\pi^+\pi^-}$, corrected by method (b) in the kinematic range $|t| < 0.5$ GeV^2 and $50 < W_{\gamma p} < 100$ GeV. The mass distribution is skewed compared to a Breit-Wigner distribution, namely there is an enhancement of the low mass side and a suppression of the high mass side. This skewing of the $\pi^+\pi^-$ mass shape was already observed at lower energies [10]. At low energies a distortion of the mass shape at the ω mass, due to $\rho - \omega$ interference, was observed. This effect will be discussed at end of this section.

Various prescriptions were published in the 60's and 70's to extract the "ρ^0" out of the invariant $\pi^+\pi^-$ mass spectrum. Unfortunately the resulting "ρ^0" cross section depends on the prescription used in the analysis. Therefore in this analysis different prescriptions were fitted to the mass distribution and the results were compared. Mass fits were performed to the spectrum shown in figure 9.1 as well as in $W_{\gamma p}$ and $|t|$ bins.

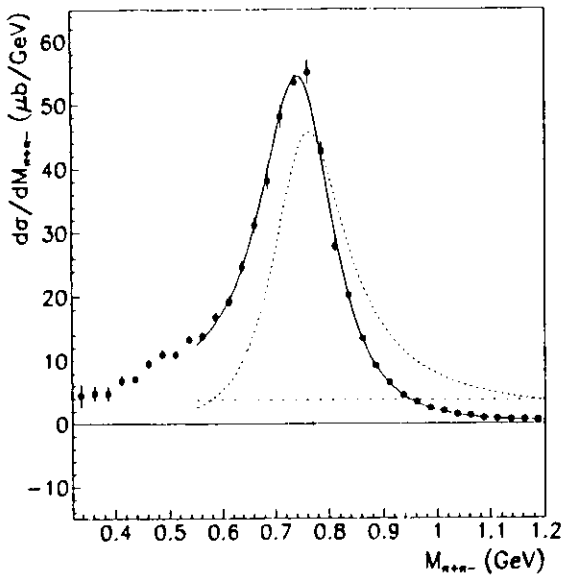

Figure 9.1: The differential cross section $d\sigma/dM_{\pi^+\pi^-}$ in the kinematic range $|t| < 0.5$ GeV^2 and $50 < W_{\gamma p} < 100$ GeV. The points represent the data and the curves indicate the result of the fit using expression (9.7) in the mass region $0.55 < M_{\pi^+\pi^-} < 1.2$ GeV. The dashed curve represents the resonant contribution, the dot-dashed curve the non-resonant contribution and the dotted curve the interference contribution. Only the statistical error is shown.

All the mass fits presented in this section were performed in the mass range $0.55 < M_{\pi^+\pi^-} < 1.2$ GeV. The resonance in the $\pi^+\pi^-$ spectrum was parameterized by a relativistic Breit-Wigner function

$$BW(M_{\pi^+\pi^-}) = \frac{M_{\pi^+\pi^-} M_{\rho^0}\Gamma_{\rho^0}}{(M^2_{\pi^+\pi^-} - M^2_{\rho^0})^2 + M^2_{\rho^0}\Gamma^2_{\rho^0}} \tag{9.3}$$

where M_{ρ^0} is the nominal ρ^0 mass and Γ_{ρ^0} the momentum dependent width [58]

$$\Gamma_{\rho^0}(M_{\pi^+\pi^-}) = \Gamma_0 \left(\frac{q^*}{q_0^*}\right)^3 \frac{M_{\rho^0}}{M_{\pi^+\pi^-}} \tag{9.4}$$

where Γ_0 is the width of the ρ^0, q^* is the π momentum in the $\pi^+\pi^-$ rest frame and q_0^* is the value of q^* at the ρ^0 nominal mass M_{ρ^0}. For the systematic error analysis (systematic checks 33-35) the following alternative expressions for the Breit-Wigner function

$$BW(M_{\pi^+\pi^-}) = \frac{1}{q^*} \frac{M_{\pi^+\pi^-} M_{\rho^0}\Gamma_{\rho^0}}{(M^2_{\pi^+\pi^-} - M^2_{\rho^0})^2 + M^2_{\rho^0}\Gamma^2_{\rho^0}} \tag{9.5}$$

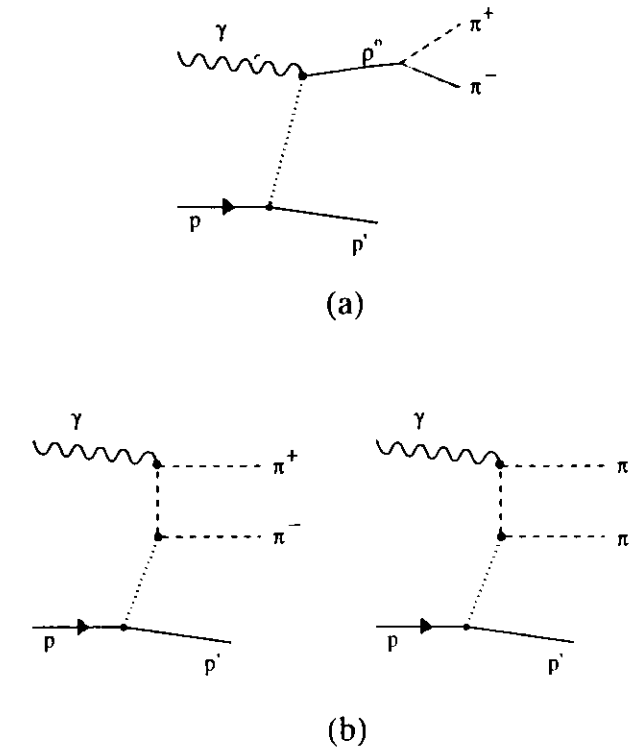

Figure 9.2: Diagrams corresponding to the three processes consider in the Söding model, namely (a) resonant ρ^0 production and (b) non-resonant $\pi^+\pi^-$ production.

and the width

$$\Gamma_{\rho^0}(M_{\pi^+\pi^-}) = \Gamma_0 \left(\frac{q^*}{q_0^*}\right)^3 \frac{2}{1 + \left(\frac{q^*}{q_0^*}\right)^2} \tag{9.6}$$

were used. The expression (9.5) was used in previous ρ^0 photoproduction experiments, e.g.[94]. The kinematic factor $1/q^*$ introduces a skewing in the Breit-Wigner function. The momentum dependent width in equation (9.4) was found in lowest order perturbation theory, whereas equation (9.6) is an empirical form of the width [58].

A model often used to describe the mass skewing was first pointed out by Söding [101]. In this model the $\pi^+\pi^-$ photoproduction amplitude is written as a sum of a directly produced Breit-Wigner shaped ρ^0 plus a non-resonant background [38]. Figure 9.2 show the diagrams considered in this approach, namely the resonant ρ^0 production (a) and the two non-resonant contributions (b). The asymmetry of the invariant mass distribution is given by the interference of these two terms. Calculations based on the Söding model were performed by Söding [101], Krass [65], Pumplin [86]. Recently Ryskin and Shabelski [88] calculated the resonant and non-resonant amplitudes in the case of ρ^0 photo- and electroproduction.

The Söding model was very successful in describing various aspects of ρ^0 photoproduction e.g.[94, 95], like the decrease of skewing for increasing $|t|$ and the dependence of the $|t|$ slope on $M_{\pi^+\pi^-}$. For the purpose of this analysis the following simplified prescription of the mass shape, according to the Söding model was used:

$$\frac{d\sigma}{dM_{\pi^+\pi^-}} = A^2 \left[\left| \frac{\sqrt{M_{\pi^+\pi^-} M_{\rho^0} \Gamma_{\rho^0}}}{M^2_{\pi^+\pi^-} - M^2_{\rho^0} + iM_{\rho^0}\Gamma_{\rho^0}} + \frac{B}{A} \right|^2 + f_{PS} \right] \tag{9.7}$$

The non-resonant amplitude is denoted by B and is assumed to be constant and real. This choice is motivated by the calculation of Ryskin and Shabelski [88], who found that the non-resonant contribution is almost flat in $M_{\pi^+\pi^-}$ for the kinematic range of the 1993 ZEUS ρ^0 photoproduction analysis. Compared to the 1993 analysis the kinematic range in this analysis was increased in $W_{\gamma p}$.

The term $f_{PS} = A_{PS}(1.0 + 1.5M_{\pi^+\pi^-})$ in equation (9.7), which is also present in all other mass parameterizations used in this analysis, accounts for residual background from γ and double dissociative photoproduction (section 7.3).

Alternatively the following parameterization, according to the Söding model, proposed by Spital and Yennie [102] was used:

$$\frac{d\sigma}{dM_{\pi^+\pi^-}} = A_0 \left\{ BW(M_{\pi^+\pi^-}) \left[1 + C_1 \left(1 - \frac{M_{\rho^0}}{M_{\pi^+\pi^-}} \right) + C_2 \left(1 - \frac{M_{\rho^0}}{M_{\pi^+\pi^-}} \right)^2 \right] + f_{PS} \right\} \tag{9.8}$$

Spital and Yennie found that correction terms $BW(M_{\pi^+\pi^-})C_i \left((M^2_{\pi^+\pi^-} - M^2_{\rho^0})/M^2_{\rho^0} \right)^i$ with $i \geq 3$ have to be added to equation (9.8), where neither the size and nor the sign of the contributions C_i can be calculated. In a mass range reasonably close to the ρ^0 mass only a finite number of terms should be important. Therefore equation (9.8) can be regarded as an approximation valid in a mass range close to the ρ^0 mass. The terms C_1 accounting for the interference and C_2 accounting for the non-resonant contribution are treated as independent parameters in equation (9.8). In fact this assumption is not correct and therefore fits according to equation (9.8) can lead to unphysical solutions, namely an interference contribution which is bigger than the sum of the resonant and non-resonant contribution at small masses. This remark is also valid for other prescriptions of the Söding model, used in fits of the invariant mass distribution, by various authors.

An alternative approach to account for the skewing of the $\pi^+\pi^-$ mass shape was proposed by Ross and Stodolsky [87]. They ignore the non-resonant background and instead introduce a mass variation in the production amplitude of the ρ^0. By relating the processes $\gamma p \to \rho^0 p$ and $\rho^0 p \to \rho^0 p$ together with a smoothness assumption they get:

$$\frac{d\sigma}{dM_{\pi^+\pi^-}} \propto BW(M_{\pi^+\pi^-}) \left(\frac{M^2_{\rho^0}}{M^2_{\pi^+\pi^-}} \right)^2 . \tag{9.9}$$

For ρ^0 electroproduction, Ross and Stodolsky predicted that the mass skewing factor $M^{-4}_{\pi^+\pi^-}$ changes to $(Q^2 + M^2_{\pi^+\pi^-})^{-2}$. Thus the mass skewing should tend to disappear at high Q^2. In the Ross Stodolsky model all $\pi^+\pi^-$ pairs are treated as coming from ρ^0 photoproduction. At lower energies it was found that the data could be described by a modification of equation (9.9). The following parameterization will be therefore used in this analysis:

$$\frac{d\sigma}{dM_{\pi^+\pi^-}} = f_{\rho^0} \left[BW(M_{\pi^+\pi^-}) \left(\frac{M_{\rho^0}}{M_{\pi^+\pi^-}} \right)^n + f_{PS} \right] . \tag{9.10}$$

where f_{ρ^0} is the absolute normalization of this prescription and n is treated as a free parameter. The parameter n in equation (9.10) can be regarded as a measure of the amount of skewing. The decrease of n with increasing $|t|$, as measured at low energies, thus means that the mass skewing decreases as the momentum transfer increases. In electroproduction experiments [27, 9, 60, 29, 18, 21, 39] it was found that n also decreases as a function of Q^2. This behavior is already expected in the Ross Stodolsky model.

In the final state interaction model the ρ^0 meson is formed by a strong final-state interaction of the p-wave $\pi^+\pi^-$ pairs produced by a process as shown in figure 9.2 (b). Kramer and Quinn [63] calculated the ρ^0 photoproduction amplitude in this model. Their result is essentially:

$$\frac{d\sigma^2}{dM_{\pi^+\pi^-}dt} \propto BW(M_{\pi^+\pi^-}) \left(\frac{M^2_{\rho^0} - t}{M^2_{\pi^+\pi^-} - t} \right)^2 \frac{d\sigma^{\pi p}}{dt} \tag{9.11}$$

where $d\sigma^{\pi p}/dt$ is the differential pion-proton cross section. For $t = 0$ the enhancement factor reduces to the Ross Stodolsky factor $(M^2_{\rho^0}/M^2_{\pi^+\pi^-})^2$. The factor $(M^2_{\rho^0} - t)^2/(M^2_{\pi^+\pi^-} - t)^2$ in equation (9.11) results in a decrease of skewing as $|t|$ increases and a change of the $|t|$ slope as a function of $M_{\pi^+\pi^-}$. The final sate interaction model was extended to ρ^0 electroproduction by the same authors [64]. For the unpolarized cross section the mass skewing factor changes to $(M^2_{\rho^0} - t + Q^2)^2/(M^2_{\pi^+\pi^-} - t + Q^2)^2$. Thus in this model the amount of skewing decreases as $|t|$ or Q^2 increases.

Recently Nieseler, Piller and Wiese [77] showed that the $M_{\pi^+\pi^-}$ distribution for elastic ρ^0 photoproduction is determined to a large extent by the two-pion contribution to the photon spectral function, as given by the pion form factor. The latter is known to high precision from $e^+e^- \to \pi^+\pi^-$ annihilation. In this process resonant and non-resonant $\pi^+\pi^-$ states are automatically accounted for. They extended their consideration to ρ^0 electroproduction at moderate Q^2. Using the vector meson dominance picture they found that the mass distribution of $\pi^+\pi^-$ pairs approaches a symmetric shape with rising Q^2. The E665 collaboration [39] found that the $M_{\pi^+\pi^-}$ distributions in the Q^2 range $0.15 < Q^2 < 20$ GeV^2 are well reproduced by this model.

The analysis of the differential cross section $d\sigma/dM_{\pi^+\pi^-}$ was performed using correction method (a) (resolution taken into account in the acceptance ϵ) and correction method (b) (resolution taken into account by a convolution of the fit function with a Gaussian). The differential cross section $d\sigma/dM_{\pi^+\pi^-}$ was fitted according to equation (9.7) (*standard Söding*), equation (9.8) (*Spital Yennie Söding*) and equation (9.10) (*Ross Stodolsky*). In figure 9.1 the result for the *standard Söding* fit is shown. Table 9.1 summarizes the results derived from all the fits to the spectrum for the two correction methods. The χ^2/NDF for all the fits is satisfactory. As can be seen from the table the value of M_{ρ^0} and Γ_0 depends on the prescription used to parameterize the mass distribution. Correction methods (a) and (b) give similar results for all the parameters, except for the width Γ_0, which is bigger for correction method (b). The values obtained for the ρ^0 mass are compatible with the PDG value ($M_{\rho^0} = 768.1 \pm 1.3$ MeV) [82], whereas the widths differ from the PDG value ($\Gamma_0 = 150.9 \pm 3.0$ MeV). The statistical errors of the parameter are similar, but tend to be bigger for correction method (b) in which bin by bin correlations are properly taken into account. The amount of background under the ρ^0 peak, as given by the parameter A_{PS}, was found to be small for all mass prescriptions. The fitted value of A_{PS} corresponds to an integrated contribution typically smaller than 1% of the total for all the mass fits performed in this analysis.

standard Söding					
M_{ρ^0} (MeV)	Γ_0 (MeV)	A^2 (μb)	B/A (GeV$^{-1/2}$)	A_{PS} (GeV^{-1})	χ^2/NDF
correction method (a)					
770 ± 2	146 ± 3	7.54 ± 0.11	-0.670 ± 0.022	0.004 ± 0.002	0.73
correction method (b)					
771 ± 2	159 ± 3	7.59 ± 0.12	-0.706 ± 0.025	0.000 ± 0.002	0.76

Spital Yennie Söding						
M_{ρ^0} (MeV)	Γ_0 (MeV)	A_0 (μb)	C_1 (GeV^{-1})	C_2 (GeV^{-1})	A_{PS} (GeV^{-1})	χ^2/NDF
correction method (a)						
771 ± 2	142 ± 3	7.85 ± 0.10	-2.58 ± 0.07	1.87 ± 0.23	0.00 ± 0.01	0.52
correction method (b)						
772 ± 2	155 ± 7	7.99 ± 0.15	-2.57 ± 0.08	1.83 ± 0.76	0.00 ± 0.04	0.77

Ross Stodolsky					
M_{ρ^0} (MeV)	Γ_0 (MeV)	f_{ρ^0} (μb)	n	A_{PS} (GeV^{-1})	χ^2/NDF
correction method (a)					
771 ± 2	138 ± 3	7.74 ± 0.11	5.13 ± 0.13	0.004 ± 0.002	0.42
correction method (b)					
772 ± 2	150 ± 3	7.87 ± 0.11	5.09 ± 0.14	0.003 ± 0.003	0.76

Table 9.1: Results of the fits for the two correction methods and the three parameterization used in this analysis (*standard Söding* equation (9.7), *Spital Yennie Söding* equation (9.8) and *Ross Stodolsky* equation (9.10)). The fits were performed in the mass region $0.55 < M_{\pi^+\pi^-} < 1.2$ GeV. The errors are the statistical errors only.

$W_{\gamma p}$ bins		
lower limit	upper limit	average
50 GeV	60 GeV	54.8 GeV
60 GeV	70 GeV	64.9 GeV
70 GeV	80 GeV	74.9 GeV
80 GeV	100 GeV	89.6 GeV

$\lvert t\rvert$ bins		
lower limit	upper limit	average
0.00 GeV^2	0.0115 GeV^2	0.006 GeV^2
0.0115 GeV^2	0.026 GeV^2	0.018 GeV^2
0.026 GeV^2	0.045 GeV^2	0.034 GeV^2
0.045 GeV^2	0.070 GeV^2	0.056 GeV^2
0.070 GeV^2	0.100 GeV^2	0.084 GeV^2
0.100 GeV^2	0.135 GeV^2	0.115 GeV^2
0.135 GeV^2	0.190 GeV^2	0.158 GeV^2
0.190 GeV^2	0.280 GeV^2	0.224 GeV^2
0.28 GeV^2	0.50 GeV^2	0.345 GeV^2

Table 9.2: $W_{\gamma p}$ and $|t|$ bins used in the study of the invariant mass distribution.

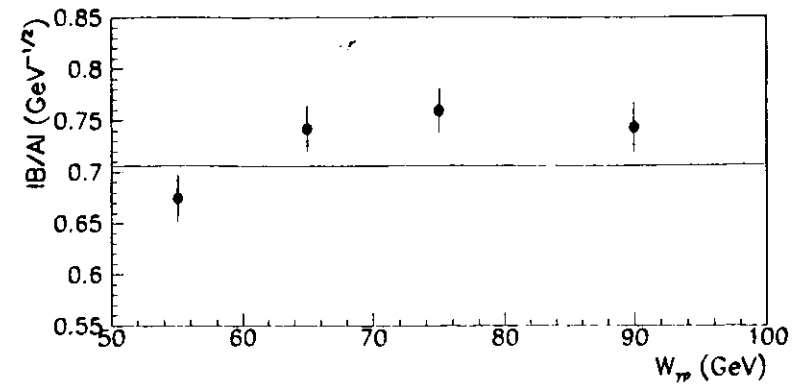

Figure 9.3: The ratio $|B/A|$ for the four W_γ intervals. Statistical errors only are shown. The line indicates the value determined from the whole sample.

The fits of the mass distribution were repeated in four $W_{\gamma p}$ and nine $|t|$ bins. The bin sizes are given in table 9.2. For these fits the ρ^0 mass and width were fixed to the values given in table 9.1. The value of $|B/A|$ (*standard Söding*), which is a measure of the amount of skewing, is shown as a function of $W_{\gamma p}$ (correction method (b)) in figure 9.3. Only statistical errors are shown. No dependence of these parameters on $W_{\gamma p}$ can be seen within this data. Therefore in the following also the amount of skewing as given by B/A in equation (9.7), C_1 and C_2 in equation (9.8) or n in equation (9.10), will be fixed, for the fits in $W_{\gamma p}$ bins. Figure 9.4 shows the differential cross section $d\sigma/dM_{\pi^+\pi^-}$ for the four $W_{\gamma p}$ bins, corrected by correction method (b), together with the result of a fit according to equation (9.7). Again the data is nicely reproduced by the parameterization. The results of the mass fits in $W_{\gamma p}$ bins will be discussed further in section 9.4.

The mass distribution (correction method (a)) in the nine $|t|$ bins is shown in figure 9.5 together with the result of fits according to equation (9.7). In these fits the mass and the width of the ρ^0 were fixed to the values given in table 9.1. The mass distributions become more symmetric as $|t|$ increases, as already observed at low energies [92, 13, 104, 94, 95, 47, 103, 4, 60, 80]. The results for $|B/A|$ and n from the mass fits are shown as a function of $|t|$ in figures 9.6 and 9.7. Statistical errors are shown by the inner error bars and the outer error bars represent the statistical and systematic errors added in quadrature. The dominant systematic error is given by the error classes i and xi, namely the tracking systematics and a change of the momentum dependent width used in the mass fits. In this study the systematic checks 34 and 35 have to be excluded from the systematic error calculation, because part of the skewing will be simply transferred to the Breit-Wigner function for these checks. Both quantities $|B/A|$ and n decrease with $|t|$, since the skewing decreases as the momentum transfer increases. In figure 9.7 the results are compared with low energy measurements [95, 47] and model predictions. The model predictions were determined as follows. Events were generated with a Monte Carlo program based on the model and were binned as a function of $|t|$. The fits performed to the $M_{\pi^+\pi^-}$ spectra from the data for different $|t|$ bins were repeated for the generated events - but with much smaller bins. The results were

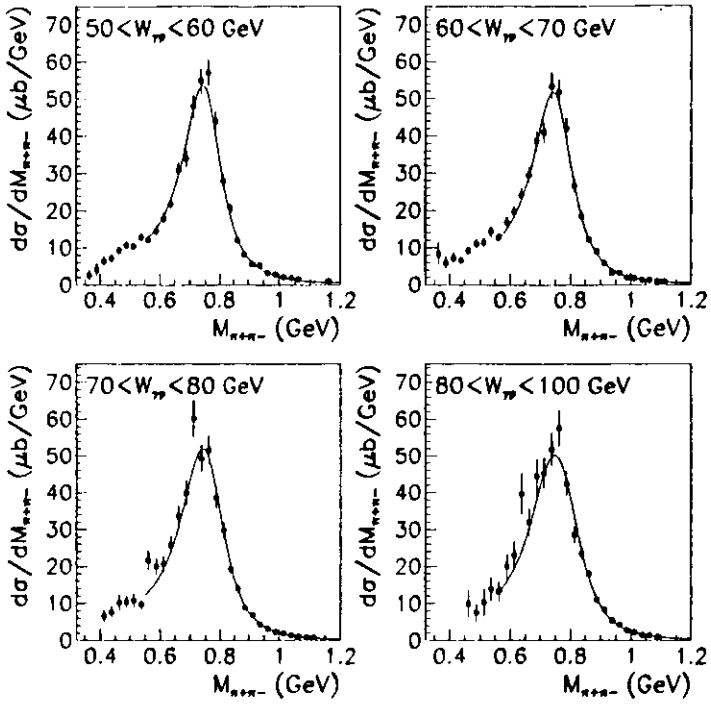

Figure 9.4: The differential cross section $d\sigma/dM_{\pi^+\pi^-}$ in different $W_{\gamma p}$ bins. The points represent the data and the curves indicate the result of the fit according to equation (9.7). The ρ^0 mass, the width and the amount of skewing as given by B/A was fixed to the values presented in table 9.1. Only the statistical errors are shown.

parameterized by functions, which are shown in figure 9.7. The Söding model prediction was determined within the framework of the calculation of Ryskin and Shabelski [85]. The only free parameter of this calculation, the pion proton cross section $\sigma^{\pi p}$, was determined from a fit of the mass distributions in figure 9.5 according to that model [116]. The prediction for the final state interaction model was obtained by reweighting a Monte Carlo sample according to equation (9.11), including the effect of non-zero Q^2 as discussed above.

The decrease of the amount of skewing with $|t|$ as measured in this analysis is in good agreement with the measurements of fixed target photoproduction experiments, indicating that the skewing of the ρ^0 mass shape does not depend on $W_{\gamma p}$. As noted above in the present analysis P_t^2 is measured, which may differ from $|t|$ when Q^2 is non-zero. The Monte Carlo simulation used to correct the data does not include the decrease of skewing as a function of Q^2, observed in previous electroproduction experiments. However for the P_t^2 bins considered the median and average Q^2 change only slightly. The median Q^2 changes from $\sim 10^{-5}$ in

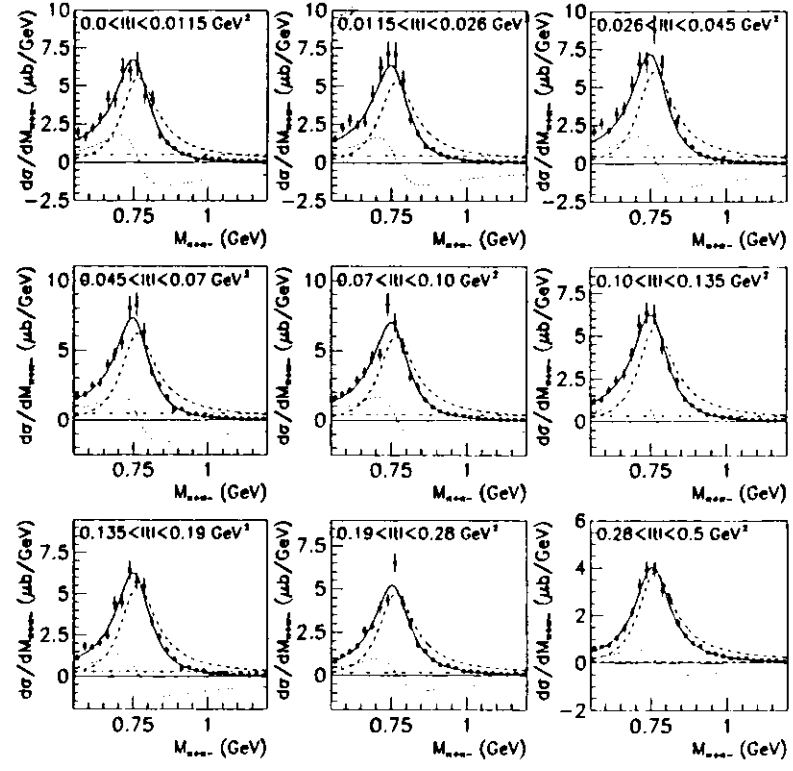

Figure 9.5: The differential cross section $d\sigma/dM_{\pi^+\pi^-}$ in different $|t|$ bins. The points represent the data and the curves indicate the result of the fit according to equation (9.7). The dashed curve represents the fitted resonant contribution, the dot-dashed curve the non-resonant contribution and the dotted curve the contribution from the interference term. The continuous curve is the sum. Only the statistical errors are shown.

the first P_t^2 bin to $\sim 10^{-6}$ in the last bin. This negligible decrease of Q^2 can not result in a considerable change of the amount of skewing. Therefore the observed decrease of skewing as a function of $|t|$ is not due to a convolution of effects due to $|t|$ and Q^2.

As is evident from figure 9.7, the Söding model calculation of Ryskin and Shabelski (full line) is able to describe the data, after evaluating the free parameter of the model ($\sigma^{\pi p}$) from the data. On the other hand figure 9.7 shows that the amount of skewing is bigger than expected in the Ross Stodolsky model (equation (9.9)), which predicts a maximum value of $n = 4$. Also the final state interaction model (dashed line), as given by equation (9.11), is

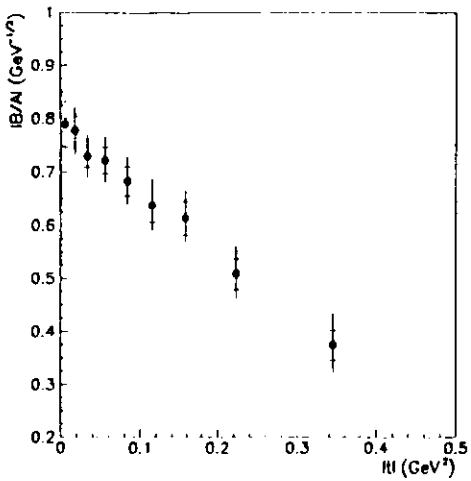

Figure 9.6: The ratio $|B/A|$ as a function of $|t|$ obtained by fitting equation (9.7) to the data. The inner error bars indicate the statistical error, the outer ones the statistical and systematic error added in quadrature.

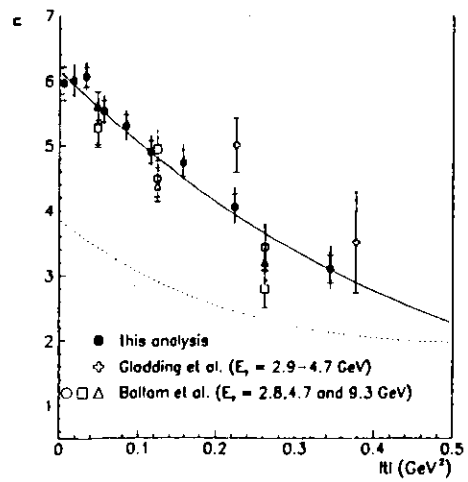

Figure 9.7: The parameter n as a function of $|t|$ (solid points). Results of fixed target experiments [95, 47] are also shown. The full line indicates the result of a Söding model calculation and the dashed line the prediction of the final state interaction model (9.11).

amount of skewing nor the $|t|$ dependence of the skewing parameter n. In this model $n = 4$ is expected for $t = 0$, whereas the data indicates a much bigger value of $n(t = 0) \approx 6$.

The values obtained for $|B/A|$ and n in bins of $|t|$ are summarized in Appendix C, together with the systematic errors from all error classes affecting the results.

At low energies it was found that the ω meson has a small amplitude to decay into $\pi^+\pi^-$. This amplitude interferes with the ρ^0 production amplitude, which leads to a distortion of the $\pi^+\pi^-$ mass spectrum at the ω mass (M_ω =781.9 MeV). To see, if this effect can change the results derived above, the following prescription including $\rho - \omega$ interference was fitted to the data:

$$\frac{d\sigma}{dM_{\pi^+\pi^-}} = A^2 \left| \sqrt{M_{\pi^+\pi^-} M_{\rho^0} \Gamma_{\rho^0}} \left(\frac{1}{M^2_{\pi^+\pi^-} - M^2_{\rho^0} + iM_{\rho^0}\Gamma_{\rho^0}} + \frac{\zeta e^{i\alpha}}{M^2_{\pi^+\pi^-} - M^2_{\omega} + iM_{\omega}\Gamma_{\omega}} \right) + \frac{B}{A} \right|^2 + f_{PS} \right] \tag{9.12}$$

This prescription is an extension of equation (9.7), in which the ρ^0 propagator is replaced by a sum of two terms. The first one describes ρ^0 production and the second one ω production in the $\pi^+\pi^-$ channel. The parameters ζ and α describe the relative magnitude and the relative phases of the ω and ρ^0 terms. M_ω and Γ_ω are the mass and the width of the ω meson. Due to the very narrow width of the ω meson (Γ_ω = 8.4 MeV) this study was performed in a very fine binning (bin width: 6.25 MeV) using correction method (b), in which the resolution was taken into account by a convolution of equation (9.12) with a Gaussian resolution function (section 6.2). To get rid of statistical fluctuations coming from the acceptance correction,

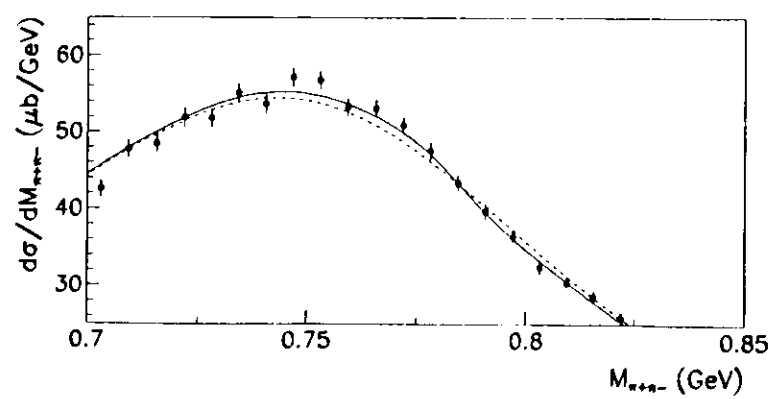

Figure 9.8: The corrected mass distribution in the mass range $700 < M_{\pi^+\pi^-} < 850$ MeV analyzed using correction method (b). The dashed line shows the result of the fit according to equation (9.12) with ζ set to zero (no $\rho - \omega$ interference). The full line shows the result, if ζ is treated as a free parameter in the fit thus allowing for $\rho - \omega$ interference. The errors are the statistical errors only.

parameter	no $\rho-\omega$ interference	with $\rho-\omega$ interference
M_{ρ^0} (MeV)	773 ± 1	773 (fixed)
Γ_0 (MeV)	158 ± 1	158 (fixed)
A^2 (μb)	7.43 ± 0.06	7.51 ± 0.05
B/A (GeV$^{-1/2}$)	-0.758 ± 0.015	-0.742 ± 0.008
M_ω (MeV)		788 ± 2
ζ	0.0 (fixed)	0.005 ± 0.001
α (deg)		99 ± 12
χ^2/NDF	83.8/76	71.9/75

Table 9.3: Results for the fits according to equation (9.12). The errors are the statistical errors only.

the acceptance ϵ_g was fitted by a second order polynomial and the acceptance correction in each $M_{\pi^+\pi^-}$ bin was calculated by this function. The study was restricted to the mass range the 500 < $M_{\pi^+\pi^-}$ < 1000 MeV. In figure 9.8 the corrected mass distribution in the limited mass range 700 < $M_{\pi^+\pi^-}$ < 850 MeV is shown, in which $\rho-\omega$ interference should show up. The value of A_{PS} in all the fits according to equation (9.12) was fixed to the value given in table 9.1. The fit was performed in two steps. First a fit was made in which ζ was set to zero (no $\rho-\omega$ interference). The result of this fit is shown as the dashed line in figure 9.8. Afterwards a second fit according to equation (9.12) was performed, fixing the mass and the width of the ρ^0 to the values obtained in the first fit. Since the mass resolution in this study ($\approx$ 7 MeV) is of the order of the width of the ω meson, it would be difficult to determine Γ_ω from the fit of equation (9.12). Therefore Γ_ω was fixed to the PDG value (Γ_ω = 8.4 MeV). The result of the second fit is shown as the full line in figure 9.8. This fit is able to describe the data in the region of the ω mass. Outside the ω resonance region the two curves coincide. The parameters derived from the two fits are summarized in table 9.3. The χ^2/NDF improves from 83.8/76 to 71.9/75, if $\rho-\omega$ interference is included in the fit. The result of the fit for the ω mass is higher than the PDG value of M_ω = 781.9 ± 0.1 MeV and the relative magnitude and phase were found to be ζ = 0.005 ± 0.001 and α = 99° ± 12°. Changing the mass resolution in the fits by ± 25% changes the fitresults for ζ by ± 0.002 and for α by ± 3°. The magnitude is smaller than that measured at lower energies ($\zeta \approx 0.01$ for $W_{\gamma p} \lesssim 4.5$ GeV), whereas the phase is in agreement with previous measurements ($\alpha \approx 100°$) [10].

The values of A^2 and B/A do not change significantly when $\rho-\omega$ interference was included in the fit. Thus the effect of this interference phenomena on the results derived above is negligible.

9.4 The Elastic ρ^0 Photoproduction Cross Section

In the previous section different mass prescriptions were fitted to the differential cross section $d\sigma/dM_{\pi^+\pi^-}$. In this section the elastic ρ^0 photoproduction cross section will be extracted from these fits. Since the cross section depends on the procedure used to extract the resonant part from the mass distribution, in this analysis the following techniques of determining the

ρ^0 cross section were used and compared:

- The *Söding model cross section*. In the Söding model the resonant ρ^0 cross section is proportional to the area of the Breit-Wigner curve, that is the area under the dashed curve in figure 9.1. The area was obtained by integrating the Breit-Wigner function multiplied by the normalization parameter as determined by the fit (A^2 in equation (9.7), A_0 in equation (9.8)). In this analysis two different parameterizations according to the Söding model were considered (*standard Söding* equation (9.7) and *Spital Yennie Söding* equation (9.8)). The values of M_{ρ^0} and Γ_0 used in the integration of the Breit-Wigner function are those given in table 9.1. The Söding model cross section given in the following was determined using the fitresults of the *standard Söding* fit. The difference in the cross section, obtained using the fitresults of the *standard Söding* and the *Spital Yennie Söding* fit, was included in the systematic error. This systematic error can be regarded as an estimate of the error due to uncertainties in the Söding model. The integration limits used for the integration will be discussed below.

- The *parameterization cross section*. In this procedure the cross section is given by the integral over the resonant part of the *Ross Stodolsky* prescription, namely the integral over $f_{\rho^0}BW(M_{\pi^+\pi^-})(M_{\rho^0}/M_{\pi^+\pi^-})^n$. The parameters M_{ρ^0} and Γ_0 were those as determined from the fits according to equation (9.10) (table 9.1). In this approach all $\pi^+\pi^-$ pairs, other than the ones originating from the background given by f_{PS}, are considered as coming from elastic ρ^0 photoproduction. The same integration limit as for the *Söding model cross section* were used.

- The *phenomenological Söding model cross section*. This cross section was extracted from the invariant mass distributions by a procedure suggested by Spital and Yennie [102]. Spital and Yennie argued that in the Söding model, the non-resonant background has the property of going to zero at the ρ^0 mass. Thus they have suggested that the ρ^0 cross section be defined as:

$$\sigma^{\gamma p\to\rho^0 p} = \frac{\pi\Gamma_0}{2}\left.\frac{d\sigma}{dM_{\pi^+\pi^-}}\right|_{M_{\pi^+\pi^-}=M_{\rho^0}} \tag{9.13}$$

  where the ρ^0 mass M_{ρ^0} and width Γ_0 are taken from external sources, such as colliding beam measurements. The recommended procedure is to measure the whole spectrum, fit it appropriately, and use the fit to determine the cross section at the ρ^0 mass. In the present analysis, the *phenomenological Söding model cross section* was determined with M_{ρ^0} = 770 MeV and Γ_0 = 155 MeV and using the result of the fit according to equation (9.10). The values for M_{ρ^0} and Γ_0 are those, chosen by Bauer et al. [10]. Using the same values for M_{ρ^0} and Γ_0 is essential in order to compare the results from different experiments.

The integrals in the determination of the *Söding model cross section* and the *parameterization cross section* were carried out in the range $2M_\pi < M_{\pi^+\pi^-} < M_{\rho^0} + 5\Gamma_0$, where the ρ^0 mass and width were taken from the different fits respectively (table 9.1) and M_π is the pion mass. The integration requires an extrapolation beyond the measured range. The upper limit of the integration range approximately corresponds to the mass of the nearest resonance, the $\rho'(1450)$, with the same quantum numbers and quark content as the ρ^0. Changing the upper

Söding model cross section (9.7)		
$\langle W_{\gamma p} \rangle$ (GeV)	$\sigma^{\gamma p \to \rho^0 p}$ (μb) for correction method (a)	$\sigma^{\gamma p \to \rho^0 p}$ (μb) for correction method (b)
71.7	$11.27 \pm 0.16^{+1.22}_{-1.21}$	$11.37 \pm 0.17^{+1.30}_{-1.22}$
54.8	$10.90 \pm 0.21^{+1.45}_{-1.29}$	$10.88 \pm 0.21^{+1.56}_{-1.29}$
64.9	$10.76 \pm 0.21^{+1.26}_{-1.14}$	$10.67 \pm 0.19^{+1.20}_{-1.14}$
74.9	$11.39 \pm 0.26^{+1.04}_{-1.17}$	$11.15 \pm 0.22^{+1.19}_{-1.13}$
89.6	$11.67 \pm 0.26^{+1.08}_{-1.33}$	$11.46 \pm 0.22^{+1.21}_{-1.30}$
a	$0.157 \pm 0.059^{+0.111}_{-0.148}$	$0.126 \pm 0.054^{+0.114}_{-0.131}$

parameterization cross section (9.10)		
$\langle W_{\gamma p} \rangle$ (GeV)	$\sigma^{\gamma p \to \rho^0 p}$ (μb) for correction method (a)	$\sigma^{\gamma p \to \rho^0 p}$ (μb) for correction method (b)
71.7	$12.63 \pm 0.18^{+1.29}_{-1.32}$	$12.85 \pm 0.19^{+1.31}_{-1.34}$
54.8	$12.20 \pm 0.24^{+1.56}_{-1.41}$	$12.29 \pm 0.24^{+1.63}_{-1.43}$
64.9	$12.06 \pm 0.24^{+1.18}_{-1.24}$	$12.11 \pm 0.24^{+1.20}_{-1.26}$
74.9	$12.77 \pm 0.29^{+1.14}_{-1.29}$	$12.78 \pm 0.25^{+1.18}_{-1.32}$
89.6	$13.11 \pm 0.32^{+1.18}_{-1.49}$	$13.06 \pm 0.31^{+1.20}_{-1.57}$
a	$0.162 \pm 0.061^{+0.105}_{-0.146}$	$0.142 \pm 0.059^{+0.118}_{-0.140}$

phenomenological Söding model cross section (9.13)		
$\langle W_{\gamma p} \rangle$ (GeV)	$\sigma^{\gamma p \to \rho^0 p}$ (μb) for correction method (a)	$\sigma^{\gamma p \to \rho^0 p}$ (μb) for correction method (b)
71.7	$13.72 \pm 0.19^{+1.39}_{-1.43}$	$12.91 \pm 0.19^{+1.47}_{-1.44}$
54.8	$13.25 \pm 0.26^{+1.69}_{-1.53}$	$12.35 \pm 0.24^{+1.89}_{-1.50}$
64.9	$13.10 \pm 0.26^{+1.27}_{-1.36}$	$12.17 \pm 0.24^{+1.37}_{-1.39}$
74.9	$13.87 \pm 0.31^{+1.22}_{-1.40}$	$12.85 \pm 0.25^{+1.25}_{-1.43}$
89.6	$14.24 \pm 0.35^{+1.28}_{-1.58}$	$13.12 \pm 0.31^{+1.14}_{-1.42}$
a	$0.162 \pm 0.061^{+0.105}_{-0.146}$	$0.142 \pm 0.059^{+0.118}_{-0.140}$

Table 9.4: The integrated cross section $\sigma^{\gamma p \to \rho^0 p}$ for two correction methods and the different extraction procedures. The values for the *Söding model cross section* and the *parameterization cross section* are given for the range $2M_\pi < M_{\pi^+\pi^-} < M_{\rho^0} + 5\Gamma_0$. All cross sections are obtained for $|t| < 0.5$ GeV^2. The bottom line of each table shows the results of fits to the data with a function of the type $W^a_{\gamma p}$.

integration limit has a negligible effect on the *parameterization cross section*, whereas the *Söding model cross section* changes considerably. For example, if the integral is computed up to $M_{\rho^0} + 4\Gamma_0$, the *Söding model cross section* decreases by 3%. If instead the upper limit is extended to $M_{\rho^0} + 6\Gamma_0$ it increases by 2%. On the other hand the *parameterization cross section* changes by less than 1‰ for the same change of the upper integration limit. The reason of this dependence of the *Söding model cross section* on the integration limit is obvious from figure 9.1. For masses above the ρ^0 mass the Breit-Wigner curve (dashed curve), representing the resonant production, is above the data and compensated by a negative interference contribution (dotted curve). The resonant contribution is thus still sizeable even for masses above 1.2 GeV, where the measured cross section is quite small. For the *parameterization cross section* all pion pairs in a given mass region are considered as ρ^0 production. Due to the skewing effect the differential cross section $d\sigma/dM_{\pi^+\pi^-}$ decreases very quickly for increasing mass and therefore the *parameterization cross section* is insensitive to the upper integration limit.

In low energy photoproduction experiments the *Söding model cross section* was determined by an integration of the Breit-Wigner curve over the available phase space. At HERA energies this would result in a very big upper integration limit and due to the Söding effect (positive Breit-Wigner is compensated by a negative interference contribution at high masses) this would lead to a big contribution to the cross section from the mass region above the measurement. It seems questionable to apply the Söding model for masses much bigger than the ρ^0 mass. Therefore an upper integration limit of $M_{\rho^0} + 5\Gamma_0$ is a reasonable choice for the upper integration limit.

In section 9.3 the invariant mass distribution was studied in four $W_{\gamma p}$ bins. Two different correction methods were used in the analysis. The integrated $\gamma p \to \rho^0 p$ cross section for $|t| < 0.5$ GeV^2 is shown in table 9.4 for the two correction methods and the three different procedures of the cross section extraction. The cross section is given for the whole sample and the four $W_{\gamma p}$ bins. The results obtained for the two correction methods are in good agreement for the *Söding model cross section* and the *parameterization cross section*, whereas the *phenomenological Söding model cross section* shows differences of 8% in all $W_{\gamma p}$. This difference is due to the different way the mass resolution is treated in the two correction methods. Treating the resolution in the fit function, results in a lower value of $d\sigma/dM_{\pi^+\pi^-}$ at $M_{\pi^+\pi^-} = M_{\rho^0}$ and thus in a lower *phenomenological Söding model cross section*. The cross section depends strongly on the extraction procedure. The *Söding model cross section* is the smallest, followed by *parameterization cross section* and the *phenomenological Söding model cross section*. The systematic uncertainty is dominated by the uncertainty on the RCAL trigger correction (systematic checks 7 and 8) and the proton dissociative background subtraction (systematic checks 3 and 4). In table 9.5 the typical systematic uncertainties, due to the different error classes, are summarized. Two of the error classes show a dependence on $W_{\gamma p}$, namely the RCAL trigger correction and the tracking systematic. The total systematic error is on the order of 10-15%.

The cross section measured in the four $W_{\gamma p}$ bins was fitted with a function of the type $W^a_{\gamma p}$. The value of a obtained for the different correction methods and extraction procedures is also given in table 9.4. The systematic uncertainty of a was determined by repeating the fit to the cross section values shifted by a systematic check. The systematic error classes i to xii were considered and the total systematic error was calculated as the quadratic sum, over all error classes, of the biggest positive and negative differences from the nominal result in each class.

contribution from	typical uncertainty
error class i	2-4%
error class ii	8.5%
error class iii	4-10%
error class iv	1%
error class v	1.5%
error class vi	< 1%
error class vii	1.5%
error class ix	1%
error class x	0.5%
error class xi	1.5%
error class xii (method (b) only)	0.5%
model uncertainty (Söding model only)	4%
luminosity	1.5%
radiative correction	2%

Table 9.5: Typical individual contributions to the systematic uncertainty on the integrated cross section.

The error class i (tracking systematic) was not considered in the total systematic error of a, since the tighter tracking cuts (systematic check 2) result in cross section values compatible with the nominal ones, but with statistical errors in the highest $W_{\gamma p}$ bins increased by up to a factor of two. This increase is due to the fact that most of the tracks for high $W_{\gamma p}$ have very small η. The bigger statistical error on the cross section for systematic check 2 thus reflects the effect that many events are rejected by the tighter $|\eta|$ cut. The bigger statistical error at high $W_{\gamma p}$ makes it impossible to fit the $W_{\gamma p}$ dependence of the cross section, since the two low $W_{\gamma p}$ bins dominate the determination of a completely and these two bins alone have a too small lever arm in $W_{\gamma p}$. It should be noted that systematic check 1 (no tracking cuts) results in values of a compatible with the nominal ones. The uncertainty on the RCAL trigger efficiency (error class iii) yields the biggest contribution to the systematic error of a. The remaining contributions to the systematic error of a are given by the error class vii (changing the fixed values in the mass fits inside their errors), the error class ix (decreasing the fit range), the error class xii (changing the resolution assumed in correction method (b)) and the Söding model uncertainty. All the other error classes considered in the determination of the cross section in $W_{\gamma p}$ bins are correlated and thus they do not contribute to the systematic error of a.

The cross sections in the four $W_{\gamma p}$ bins and the slopes a for all systematic checks, affecting the results, are given in Appendix C.

The value of a obtained for the different procedures of extracting the cross section and the two correction methods are all consistent with the value expected for a soft Pomeron, where $a \approx 0.22$ e.g.[37].

In figure 9.9 and 9.10 the cross sections as determined by correction method (b) for the different extraction procedures are compared to a partial compilation of low energy measurements and recent ZEUS [110] and H1 [51] results. The inner error bars in figure 9.9 represent the quadratic sum of the statistical and the uncorrelated systematic errors (tracking systematics and RCAL trigger efficiency) and the outer error bars are the quadratic sum of statistical

and systematic errors. In all the plots those measurements were included, which use the same extraction procedure. In figure 9.9 the *Söding model cross section* is also compared to a parameterization based on Regge theory which assumes the value of the Pomeron intercept $\alpha_{I\!P}(0)$ found by Donnachie and Landshoff and by Cudell et al., as introduced in section 3.3.3 (see figure 3.4) respectively. The parameterizations were normalized to the cross section measured in [42, 80], which were extracted with the Söding procedure and therefore the curves are just included in figure 9.9. Actually the author of [42] claimed to have used the

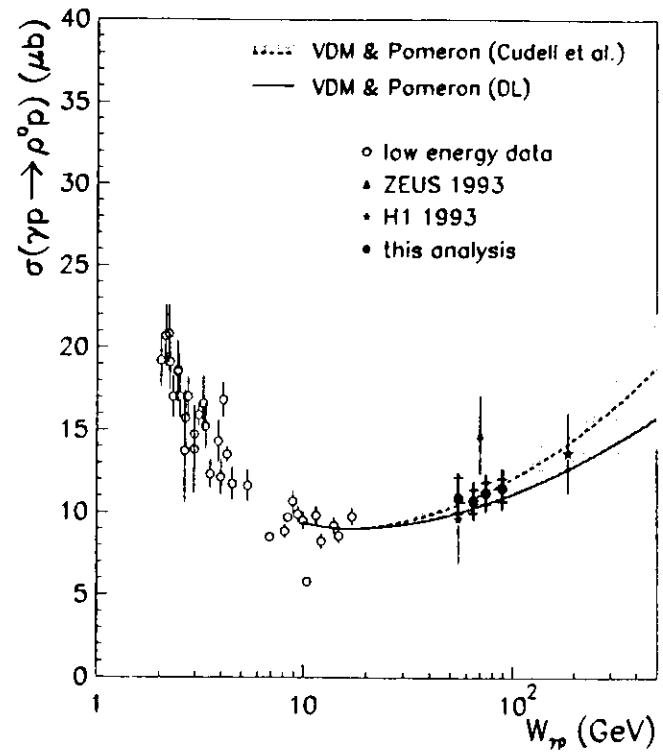

Figure 9.9: The integrated *Söding model cross section* $\sigma^{\gamma p \to \rho^0 p}$ as a function of the center of mass energy $W_{\gamma p}$. The results of this analysis were determined with correction method (b) and are given for the range $2M_\pi < M_{\pi^+\pi^-} < M_{\rho^0} + 5\Gamma_0$ and $|t| < 0.5$ GeV^2. The inner error bars on the points of this analysis represent the quadratic sum of the statistical and the uncorrelated systematic errors and the outer error bars are the quadratic sum of statistical and systematic errors. Other HERA results and a compilation of low energy data [13, 104, 81, 95, 47, 103, 42, 80, 110, 51] are also shown. The continuous and dashed line are parameterizations based on Regge theory which assume the value of the Pomeron intercept found by Donnachie and Landshoff and by Cudell et al. respectively.

Spital and Yennie procedure (equation (9.13)), but they used their measured values for the ρ^0 mass and width in equation (9.13) and thus the result is equivalent to an integration of the Breit-Wigner curve. It can be seen in figure 9.9 that a Pomeron intercept of $\alpha_{I\!P}(0) = 1.096$ (dashed curve in figure 9.9) nicely describes the data above 9 GeV in $W_{\gamma p}$. The systematic error of the data presented in this analysis is on the other hand still too big to allow a discrimination between different $\alpha_{I\!P}(0)$ values. It should be also kept in mind that the absolute normalization of the cross section depends on the details of the procedure used to extract the cross section from the mass distribution. Therefore it seems to be reasonable to determine $\alpha_{I\!P}(0)$ from elastic ρ^0 production in one experiment instead of comparing different measurements. The measurement presented in this thesis does not allow to determine $\alpha_{I\!P}(0)$

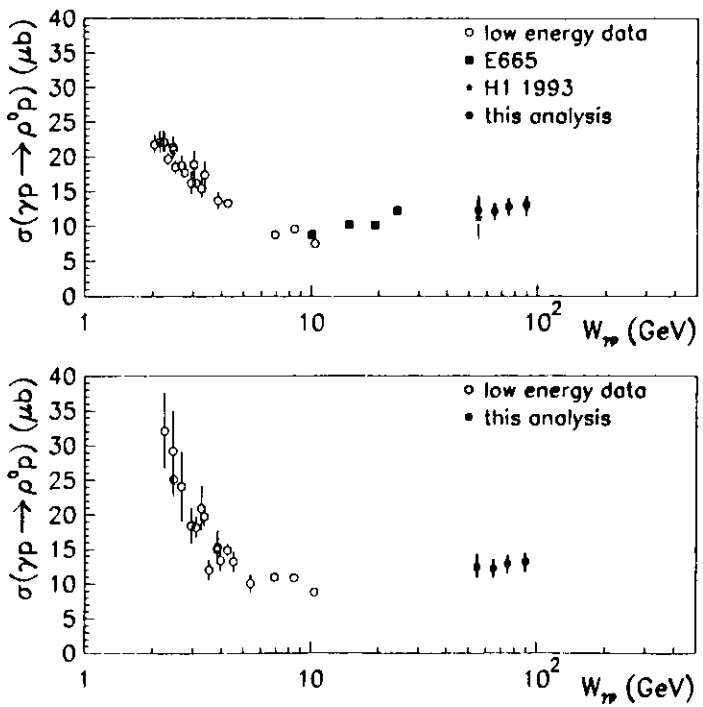

Figure 9.10: The integrated *parameterization cross section* (upper plot) and the *phenomenological Söding model cross section* (lower plot) $\sigma^{\gamma p \to \rho^0 p}$ as a function of the center of mass energy $W_{\gamma p}$. The results of this analysis were determined with correction method (b) and are given for the range $|t| < 0.5$ GeV^2 and $2M_\pi < M_{\pi^+\pi^-} < M_{\rho^0} + 5\Gamma_0$ for the *parameterization cross section*. Low energy data obtained with the same extraction procedure are also shown. In the upper plot measurements by [104, 95, 103, 80, 51, 39] were included in the plot and in the lower plot measurements by [75, 104, 81, 95, 80].

precisely, since the lever arm in $W_{\gamma p}$ is small.

As can be seen from equation (9.13) the *phenomenological Söding model cross section* depends linearly on the value of Γ_0 used. A value of $\Gamma_0 = 155$ MeV was suggested by Bauer et al. [10]. However the latest value of Γ_0 from various reactions except photoproduction, given in the PDG, is $\Gamma_0 = 151.9$ MeV [82]. Using this smaller value for Γ_0 shifts all points in the lower plot of figure 9.10 downwards by 2%.

The results presented are compatible with, but systematically lower than those presented in [110]. The reason is twofold. The proton dissociative background determined in this analysis with the use of the LPS (section 7.4) is larger than the 1993 estimate. The RCAL trigger efficiency has been determined from data in this analysis (section 6.1.1) and is approximately 10-20% higher than that estimated in [110].

9.5 The $|t|$ Distribution

The differential cross section $d\sigma/d|t|$ was obtained by first calculating the differential cross section $d\sigma/dP_T^2$ and afterwards applying the correction function F (equation (4.8)). As explained in section 4.2 the function F accounts for the difference between P_T^2 and $|t|$ due to the non-zero Q^2. The differential cross section $d\sigma/d|t|$ was determined for all events in the mass region $0.55 < M_{\pi^+\pi^-} < 1.2$ GeV and in eight bins of $M_{\pi^+\pi^-}$. The bins are given in table 9.6. The function F was calculated for the whole mass range and in the eight mass bins separately. The corrected differential cross section obtained in this way is shown in figure 9.11 by the full dots. The open dots in figure 9.11 show the differential cross section $d\sigma/d|t|$ measured with the LPS. For this measurement elastic events were selected using the LPS ($0.98 \leq x_L \leq 1.02$). The variable $|t|$ was measured directly by the transverse momentum of the outgoing proton, measured in the LPS. The bigger statistical error bars reflect the smaller statistics available for this measurement. The LPS acceptance is almost zero below $|t|$ of 0.08 GeV^2. Therefore the LPS points are only shown for $0.08 < |t| < 0.5$ GeV^2. The results obtained for the untagged sample (full dots) and the LPS sample (open dots) are in good agreement. The agreement in the absolute normalization however is trivial in this analysis, since the LPS tagged events were used to determine the amount of proton dissociative background in the untagged sample (section 7.4). The agreement on the slope in $|t|$ on the other hand shows that the procedure used to correct the measured P_T^2 to $|t|$, by the correction function F, gives the correct value of $|t|$. A measurement of the $|t|$ slope

$M_{\pi^+\pi^-}$ bins		
lower limit	upper limit	average
0.550 GeV	0.667 GeV	0.617 GeV
0.667 GeV	0.707 GeV	0.688 GeV
0.707 GeV	0.735 GeV	0.721 GeV
0.735 GeV	0.757 GeV	0.746 GeV
0.757 GeV	0.782 GeV	0.769 GeV
0.782 GeV	0.815 GeV	0.797 GeV
0.815 GeV	0.870 GeV	0.838 GeV
0.87 GeV	1.20 GeV	0.951 GeV

Table 9.6: $M_{\pi^+\pi^-}$ bins used in the study of the $|t|$ distribution.

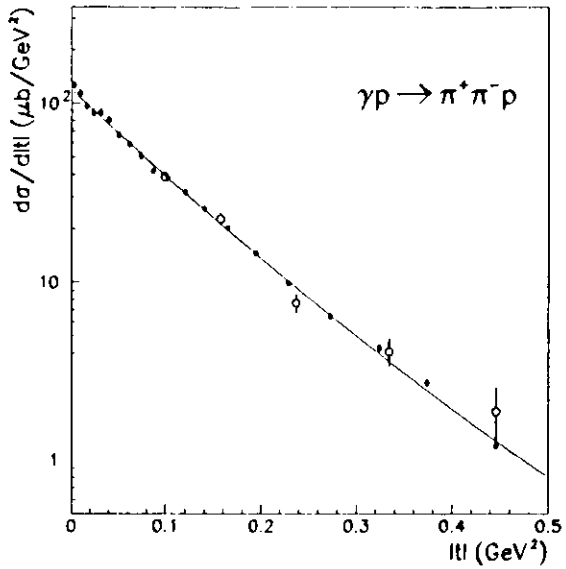

Figure 9.11: The differential cross section $d\sigma/d|t|$ for the process $\gamma p \rightarrow \pi^+\pi^- p$ in the kinematic range $0.55 < M_{\pi^+\pi^-} < 1.2$ GeV and $50 < W_{\gamma p} < 100$ GeV. The full dots show the results obtained for the whole sample and the open dots the result for a subsample of the events in which the outgoing proton was measured in the LPS. For the open dots $|t|$ was measured using the transverse momentum of the outgoing proton as measured by the LPS. The continuous line represents the result of the fit with the functional form (9.14) to the full dots. Only statistical errors are shown.

using the LPS tagged events is shown in [114].

The cross section $d\sigma/d|t|$ exhibits an exponential fall characteristic of diffractive processes (section 3.3.2). As already found in hadronic interactions the $|t|$ distribution can be fitted:

$$\frac{d\sigma}{d|t|} = A_{\pi\pi} e^{-b_{\pi\pi}|t| + c_{\pi\pi}t^2}. \qquad (9.14)$$

The fitted values are $b_{\pi\pi} = 11.4 \pm 0.3$ stat. $^{+0.3}_{-0.5}$ syst. GeV^{-2} and $c_{\pi\pi} = 2.8 \pm 0.7$ stat. $^{+1.2}_{-1.8}$ syst. GeV^{-4}.

Fits according to equation (9.14) were repeated in the $M_{\pi^+\pi^-}$ bins. In figure 9.12 the parameter $c_{\pi\pi}$ is shown as a function of $M_{\pi^+\pi^-}$. No dependence can be seen in the data. Therefore in the following the value of $c_{\pi\pi}$ in the fits according to equation (9.14) was fixed to $c_{\pi\pi} = 2.8$ GeV^{-4}. Fits according to equation (9.14) were repeated in $M_{\pi^+\pi^-}$ bins and the slope parameter $b_{\pi\pi}$ is shown in figure 9.13 as a function of $M_{\pi^+\pi^-}$. The statistical errors are

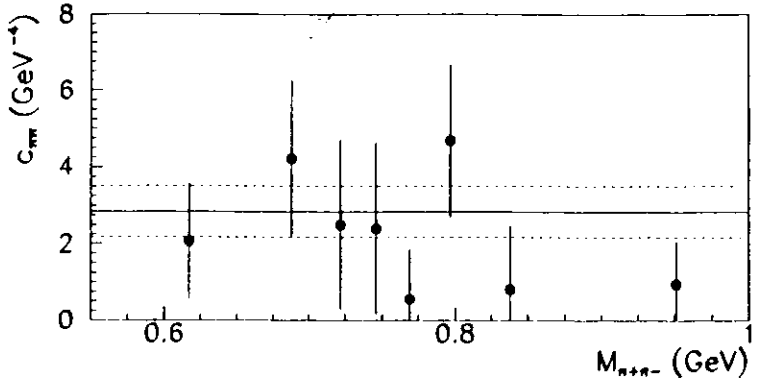

Figure 9.12: The curvature parameter $c_{\pi\pi}$ resulting from a fit of equation (9.14) in different mass bins for the reaction $\gamma p \rightarrow \pi^+\pi^- p$. The kinematic range is $50 < W_{\gamma p} < 100$ GeV and $|t| < 0.5$ GeV^2. The error are statistical errors only. The full line represents the result of the fit for the whole sample and the dashed lines it's statistical error.

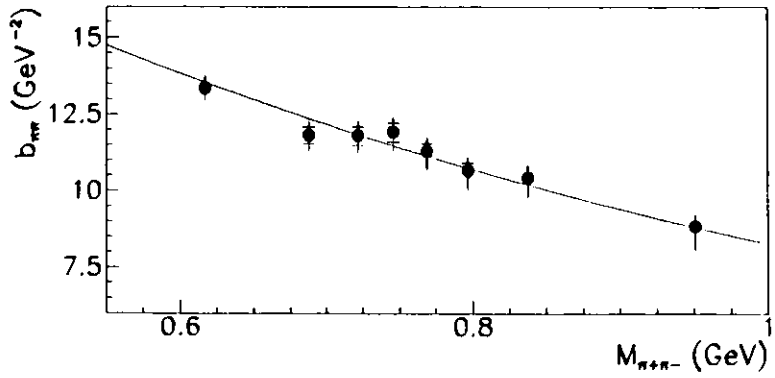

Figure 9.13: The slope parameter $b_{\pi\pi}$ resulting from a fit of equation (9.14) in different mass bins for the reaction $\gamma p \rightarrow \pi^+\pi^- p$. The kinematic range is $50 < W_{\gamma p} < 100$ GeV and $|t| < 0.5$ GeV^2. The full line represents the result of a calculation by Ryskin and Shabelski (see text). The inner error bars indicate the statistical uncertainty and the outer ones the statistical and systematic uncertainties summed in quadrature.

shown as the inner error bars and the outer error bars represent the statistical and systematic errors added in quadrature. The rapid decrease of $b_{\pi\pi}$ with increasing mass is consistent with the observation that the amount of skewing decreases as a function of $|t|$ (figures 9.6 and 9.7). In the framework of geometric diffractive models the decrease of the slope, indicates that the radius of the $\rho^0 p$ interaction decreases as the mass of the ρ^0 increases. The decrease of $b_{\pi\pi}$ as a function of mass was already observed in earlier measurements [1, 92, 28, 13, 104, 94, 95, 80, 2] and is expected in the Söding model and in the final state interaction model. In figure 9.13 the prediction of the Söding model calculation of Ryskin and Shabelski [88] is shown as a full line. This curve was obtained as discussed in more detail in section 9.3. The curve nicely reproduces the data.

The values obtained for $b_{\pi\pi}$ in bins of $M_{\pi^+\pi^-}$ are summarized in Appendix C, together with the systematic errors from all error classes affecting the result.

Since the amount of skewing decreases as a function of $|t|$, the differential cross section $d\sigma/d|t|$ for the resonant process $\gamma p \to \rho^0 p$ was determined as follows. Mass fits were carried out in bins of P_T^2 using correction method (a). The ρ^0 mass and width were fixed to the values given in table 9.1. The resonant part of the cross section was extracted as a function of P_T^2 as explained in the previous section. All three extraction procedures were considered. Again the *Söding model cross section* was obtained from the fits of equation (9.7) and the results obtained from the fits according to equation (9.8) is considered as an estimate of the systematic uncertainty of the Söding model. The differential cross section $d\sigma/dP_T^2$ was corrected to $d\sigma/d|t|$ again by applying a correction function F.

The cross section $d\sigma/d|t|$ obtained from the mass fits according to equation (9.7) is plotted in figure 9.14 and the result of the fit with the function

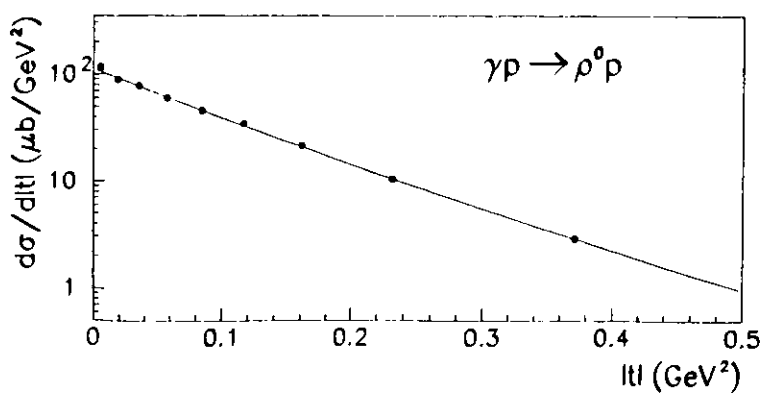

Figure 9.14: The differential cross section $d\sigma/d|t|$ for the process $\gamma p \to \rho^0 p$ determined from the *Söding model cross section* in the kinematic range $2M_\pi < M_{\pi^+\pi^-} < M_{\rho^0} + 5\Gamma_0$ 50 $< W_{\gamma p} <$ 100 GeV. The continuous line represents the result of the fit with the functional form (9.15) to the full dots. The statistical errors are smaller than the size of the symbols.

Söding model		
A_{ρ^0} (μb/GeV)	b_{ρ^0} (GeV^{-2})	c_{ρ^0} (GeV^{-4})
$112.4 \pm 2.5\ ^{+16.5}_{-9.6}$	$10.88 \pm 0.34\ ^{+0.97}_{-0.45}$	$2.70 \pm 0.91\ ^{+1.91}_{-1.73}$

parameterization		
A_{ρ^0} (μb/GeV)	b_{ρ^0} (GeV^{-2})	c_{ρ^0} (GeV^{-4})
$148.8 \pm 3.4\ ^{+13.1}_{-12.4}$	$12.61 \pm 0.34\ ^{+0.30}_{-0.34}$	$4.97 \pm 0.89\ ^{+1.27}_{-1.66}$

phenomenological Söding model		
A_{ρ^0} (μb/GeV)	b_{ρ^0} (GeV^{-2})	c_{ρ^0} (GeV^{-4})
$140.9 \pm 3.2\ ^{+11.9}_{-11.8}$	$11.12 \pm 0.34\ ^{+0.31}_{-0.32}$	$2.99 \pm 0.89\ ^{+1.27}_{-1.65}$

Table 9.7: Results of the fits according to equation (9.15), to the differential cross section $d\sigma/d|t|$ for the process $\gamma p \to \rho^0 p$. The results are given for all three extraction procedures used in this analysis.

$$\frac{d\sigma}{d|t|} = A_{\rho^0} e^{-b_{\rho^0}|t| + c_{\rho^0} t^2} \tag{9.15}$$

is superimposed. The parameters obtained for the different procedures of cross section extraction are summarized in table 9.7. The systematic errors were obtained by repeating the whole procedure, while including a systematic check. For the Söding model the positive systematic error is bigger than for the other two procedures, since the difference between the results obtained from the mass fits according to equation (9.7) and (9.8) was considered as an extra contribution to the systematics. For b_{ρ^0} the model dependence of the Söding model is $\delta b_{\rho^0} = 0.65$ GeV^{-2}. The values for the slopes b_{ρ^0} and c_{ρ^0} are very similar for the Söding model procedure and the Spital and Yennie method, whereas the parameterization cross section gives systematically higher values. This difference is expected, since for the *Söding model cross section* and the *parameterization cross section* skewing is treated differently. The slope parameter b_{ρ^0} determined from the *parameterization cross section* is bigger than $b_{\pi\pi}$ since the latter was determined in the limited mass range $0.55 < M_{\pi^+\pi^-} < 1.2$ GeV.

Finally the $|t|$ distribution was studied in different $W_{\gamma p}$ bins. The bin sizes are given in table 9.2, where the last two bins are merged to one (70-100 GeV). Again mass fits were performed in P_T^2 bins. Afterwards a correction function F was applied to determine $d\sigma/d|t|$. The function F was determined for each $W_{\gamma p}$ bin separately. Figure 9.15 shows the differential cross section in the three $W_{\gamma p}$ bins, obtained according to the Söding model procedure, together with the result of a fit according to equation (9.15). For these fits the value of c_{ρ^0} was fixed to the value given in table 9.7.

In table 9.8 the values of b_{ρ^0} obtained for the different cross section definitions are given for the three $W_{\gamma p}$ bins. Again the bigger positive systematic error for the Söding model is due to the model uncertainty, as estimated by the difference between the results obtained using equation (9.7) and (9.8) ($\delta b_{\rho^0} \approx 0.6$ GeV^{-2}). In figure 9.16 the Söding model result is compared to an other recent result from HERA [110] and a compilation of low energy

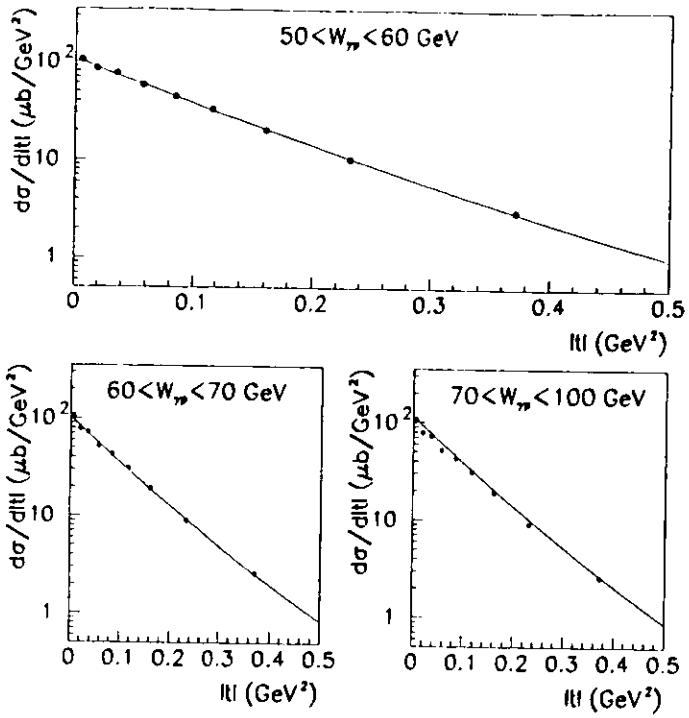

Figure 9.15: The differential cross section $d\sigma/d|t|$, like in figure 9.14, for the three $W_{\gamma p}$ bins considered.

data [59, 13, 94, 47, 80]. Measurements of the slope b by H1 [51] and by ZEUS using the LPS [114] are not included in the figure, since in those measurements the t distribution was parameterized by a single exponential ($d/sigma/d|t| \propto exp(-b|t|)$) and the t distribution was not corrected for the Söding effect. A fit of the form (equation (3.46))

$$b_{\rho^0}(W_{\gamma p}) = b_0 + 2\alpha'_{\mathbb{P}} \ln W^2_{\gamma p} \qquad (9.16)$$

to the present data was performed. The resulting values for $\alpha'_{\mathbb{P}}$ are summarized at the bottom of table 9.8. The systematic uncertainty was determined by repeating the fit to the b_{ρ^0} values as modified by the effect of each systematic check. The systematic error classes i and viii were not included in the total systematic error of $\alpha'_{\mathbb{P}}$. For error class i the reason is again a lack of statistics at high $W_{\gamma p}$ for the tighter tracking cuts (check 2), which make the determination of $\alpha'_{\mathbb{P}}$ unreasonable, whereas the error class viii was not considered, because for the checks 28 and 29 the parameter c_{ρ^0} was treated as a free parameter. Due to strong correlations between b and c, small changes of c can result in sizeable changes for b. It is thus impossible to see the energy dependence of b, if the curvature parameter c is also treated

$\langle W_{\gamma p} \rangle$ (GeV)	$b_{\rho^0 1}$ (GeV^{-2})	$b_{\rho^0 2}$ (GeV^{-2})	$b_{\rho^0 3}$ (GeV^{-2})
54.8	$10.64 \pm 0.23^{+0.93}_{-0.43}$	$12.31 \pm 0.21^{+0.48}_{-0.45}$	$10.90 \pm 0.21^{+0.48}_{-0.39}$
64.8	$10.98 \pm 0.21^{+0.94}_{-0.49}$	$12.66 \pm 0.20^{+0.50}_{-0.51}$	$11.14 \pm 0.20^{+0.47}_{-0.44}$
83.9	$11.10 \pm 0.14^{+0.97}_{-0.64}$	$12.84 \pm 0.15^{+0.46}_{-0.65}$	$11.34 \pm 0.15^{+0.44}_{-0.58}$
$\alpha'_{\mathbb{P}}$ (GeV^{-2})	$0.23 \pm 0.15^{+0.10}_{-0.07}$	$0.28 \pm 0.14^{+0.11}_{-0.08}$	$0.24 \pm 0.14^{+0.09}_{-0.12}$

Table 9.8: Results for the slope parameter b_{ρ^0} for fits according to equation (9.15), to the differential cross section $d\sigma/d|t|$ for the process $\gamma p \to \rho^0 p$ in the three $W_{\gamma p}$ bins considered. The results are given for all three extraction procedures used in this analysis. The bottom line of each table shows results for $\alpha'_{\mathbb{P}}$ of fits to the present data with a function (9.16).

as a free parameter, due to statistical fluctuation of c from bin to bin in $W_{\gamma p}$. The main contributions to the systematic error of $\alpha'_{\mathbb{P}}$ are given by error class x (changing the binning of the mass distributions) and error class xi (changing the Breit-Wigner function and the momentum dependent width in the mass fits). All the remaining error classes considered in the determination of b_{ρ^0} in $W_{\gamma p}$ bins are to a big extent correlated in $W_{\gamma p}$ and thus they do not contribute to the systematic error of $\alpha'_{\mathbb{P}}$. The total systematic error of $\alpha'_{\mathbb{P}}$ is smaller than the statistical error.

The results obtained for $\alpha'_{\mathbb{P}}$ are consistent with $\alpha'_{\mathbb{P}} = 0.25$ GeV^{-2} obtained from fits to pp and $p\bar{p}$ data [33, 34].

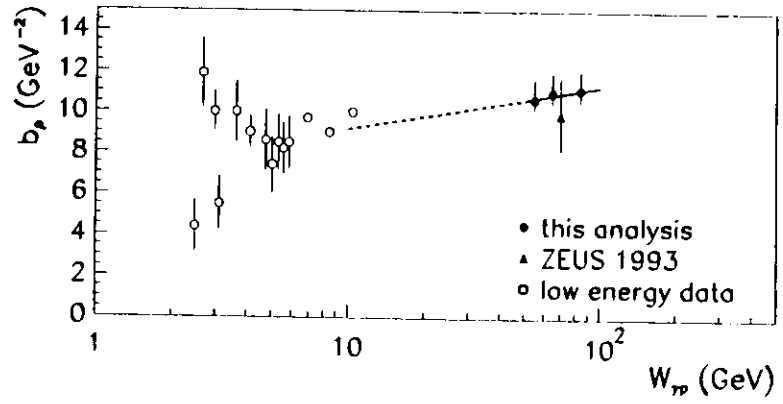

Figure 9.16: The slope parameter b_{ρ^0} for the elastic reaction $\gamma p \to \rho^0 p$, obtained from the *Söding model cross section*, in the kinematic region $|t| < 0.5$ GeV^2 as a function of $W_{\gamma p}$ together a compilation of low energy data [59, 13, 94, 47, 80]. The line indicates the result of the fit discussed in the text. The error bars on the ZEUS data indicate the statistical and systematic error summed in quadrature.

It can be seen in figure 9.16 that the measured value for the slope of the Pomeron trajectory of $\alpha'_{I\!P} = 0.23$ describes also part of the low energy data (dashed line in figure 9.16). But it should be kept in mind that the value obtained for b_{ρ^0} depends on the details of the procedure used to extract the cross section from the mass distribution. Therefore it seems to be reasonable to determine $\alpha'_{I\!P}$ in one experiment instead of comparing different measurements.
The slope b_{ρ^0} in the three $W_{\gamma p}$ bins and the values of $\alpha'_{I\!P}$ for all systematic checks, affecting the results, are given in Appendix C.

9.6 Decay Angular Distribution

In the analysis of untagged ρ^0 photoproduction the two angles θ_h and ϕ_h in the s-channel helicity frame can be measured. Before the angular distributions were studied, mass fits according to equation (9.7) were performed in $\cos\theta_h$ and ϕ_h bins. Correction method (a)

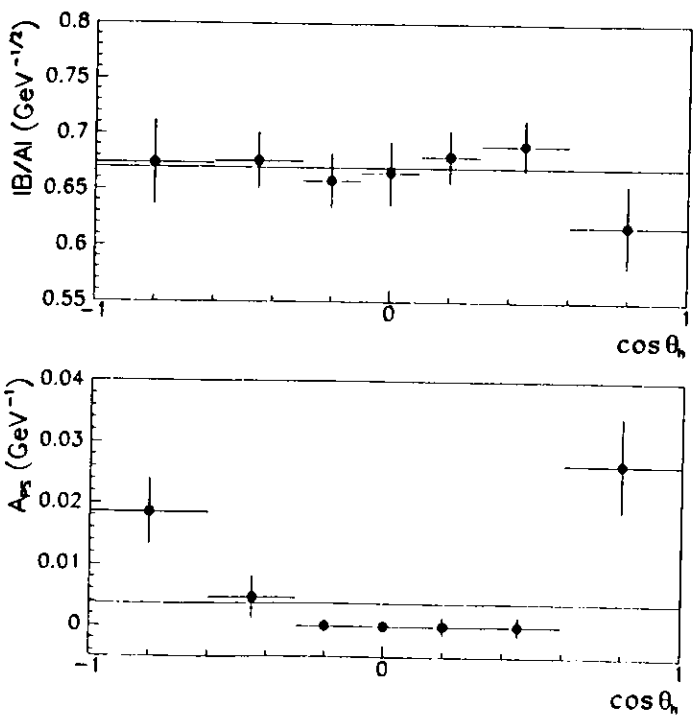

Figure 9.17: Amount of skewing as measured by $|B/A|$ and the background contribution A_{PS} as a function of the decay angle $\cos\theta_h$. Only statistical errors are shown. The horizontal error bars indicate the size of the bins.

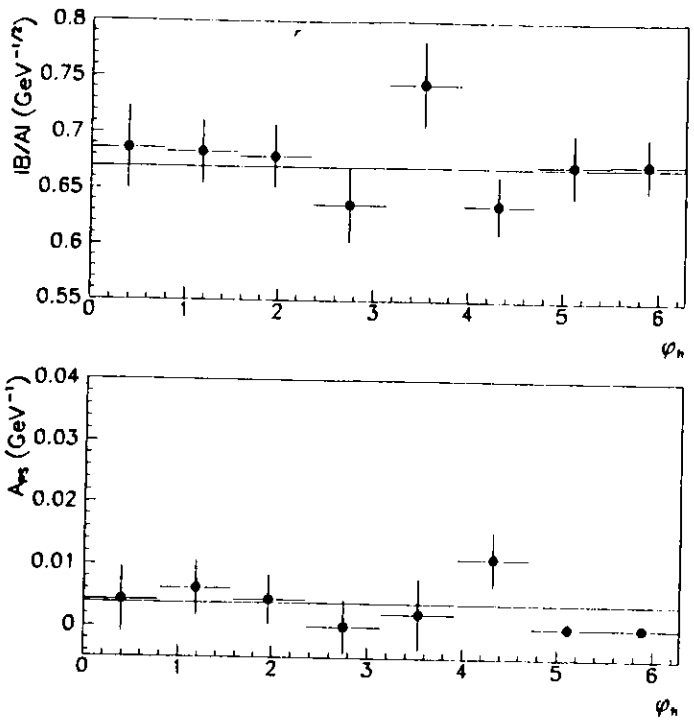

Figure 9.18: The amount of skewing as measured by $|B/A|$ and the background contribution A_{PS} as a function of the decay angle ϕ_h. Only statistical errors are shown. The horizontal error bars indicate the size of the bins.

was used and the ρ^0 mass and width were fixed to the values given in table 9.1. Figures 9.17 and 9.18 show the amount of skewing, as measured by $|B/A|$, and the amount of background under the the ρ^0 peak as given by A_{PS} as function of $\cos\theta_h$ and ϕ_h. The amount of skewing does not show any dependence on the decay angles. On the other hand the background contribution increases as $|\cos\theta_h|$ increases, but A_{PS} is below 0.03 in the whole $\cos\theta_h$ range. No dependence of A_{PS} on ϕ_h can be seen in the data. In summary the mass shape does not change significantly, as function of the decay angles. Therefore in the following, the decay angular distributions contain all events in the mass range $0.55 < M_{\pi^+\pi^-} < 1.2$ GeV. No correction for the background was applied.
The decay angular distributions of the decay pions allow to determine the ρ^0 spin density matrix elements. As introduced in section 3.3.4 the dependence on $\cos\theta_h$ and ϕ_h can be written as (equation (3.72)):

$$W(\cos\theta_h, \phi_h) = \frac{3}{4\pi}\left[\frac{1}{2}(1 - r^{04}_{00}) + \frac{1}{2}(3r^{04}_{00} - 1)\cos^2\theta_h - \sqrt{2}\Re r^{04}_{10}\sin 2\theta_h \cos\phi_h -\right.$$

$$r^{04}_{1-1}\sin^2\theta_h\cos 2\phi_h\Big].$$

After integrating over $\cos\theta_h$ or ϕ_h the following one dimensional distributions are obtained:

$$W(\cos\theta_h) = \frac{3}{4}\left[1 - r^{04}_{00} + (3r^{04}_{00} - 1)\cos^2\theta_h\right] \quad (9.17)$$

$$W(\phi_h) = \frac{1}{2\pi}(1 - r^{04}_{1-1}\cos 2\phi_h). \quad (9.18)$$

Thus the spin density matrix elements r^{04}_{00} and r^{04}_{1-1} can be measured by fitting the two dimensional distribution (equation (3.72)) or the one dimensional distributions (equation (9.17) or (9.18)). The spin density matrix element r^{04}_{00} represents the probability that the produced ρ^0 meson has helicity 0. The element r^{04}_{1-1} measures the interference of helicity non-flip and double flip amplitudes, while $\Re r^{04}_{10}$ is related to the interference between non-flip and helicity single flip amplitudes. As already mentioned in section 3.3.4, if s-channel

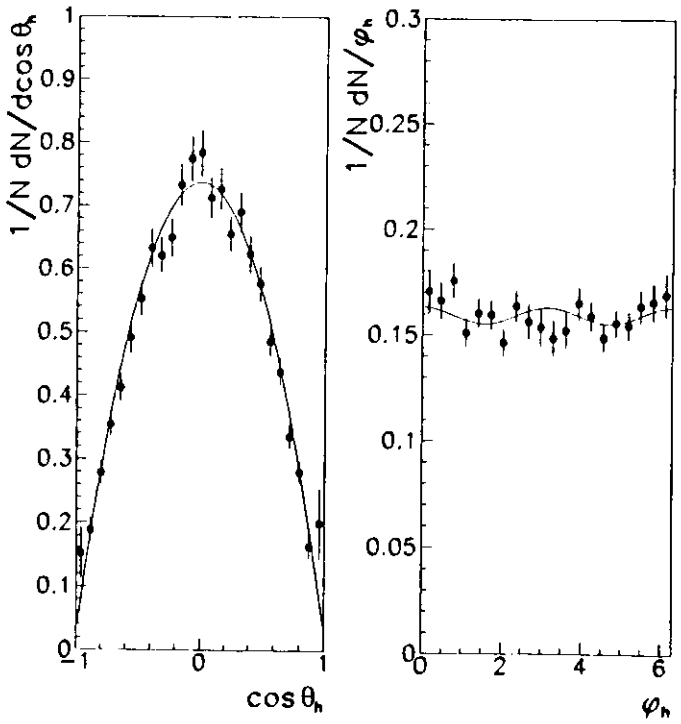

Figure 9.19: Differential distributions $1/NdN/d\cos\theta_h$ and $1/NdN/d\phi_h$ for the reaction $\gamma p \to \pi^+\pi^- p$ in the kinematic range $50 < W_{\gamma p} < 100$ GeV and $|t| < 0.5$ GeV^2. The continuous lines represent the results of the fit discussed in the text. Only statistical errors are shown.

helicity conservation (SCHC) holds, r^{04}_{1-1} and $\Re r^{04}_{10}$ should be zero. In case of SCHC r^{04}_{00} is related to R, the ratio of the longitudinal to transverse cross section (equation (3.71)). Since in the kinematic range of the present data the cross section for longitudinally polarized photons is very small, r^{04}_{00} should be small.

In figure 9.19 the one dimensional distributions are shown together with the fits according to equation (9.17) and (9.18). The values obtained for the spin density matrix elements from the fits of the one and two dimensional distributions are summarized in table 9.9. The results obtained from the two different fits are in agreement. For the spin density matrix element $\Re r^{04}_{10}$ a positive value was found, whereas r^{04}_{1-1} tends to be negative. Both elements are very small and consistent with zero inside the systematic error. Thus the data is consistent with s-channel helicity conservation. Assuming s-channel helicity conservation the measured value of r^{04}_{00} can be used to extract the parameter ξ^2 in the vector meson dominance model relation:

$$R = \frac{\sigma_L}{\sigma_T} = \xi^2\frac{Q^2}{M^2_{\rho^0}}. \quad (9.19)$$

The fitted value of $r^{04}_{00} = 0.014 \pm 0.007\ \text{stat.}^{+0.009}_{-0.017}\ \text{syst.}$ inserted in equation (5.6) yields $\xi^2 = 0.22^{+0.14}_{-0.22}$. The average Q^2 of the data is $\langle Q^2\rangle \approx 0.04$ GeV^2. A value of $\xi^2 < 1.0$ is consistent with low energy electroproduction measurements [41, 27, 9, 60, 29, 18, 21, 43, 39].

The spin density matrix elements r^{04}_{00}, $\Re r^{04}_{10}$ and r^{04}_{1-1} are also studied as function of $|t|$ and $M_{\pi^+\pi^-}$. In the present analysis $|t|$ was not measured directly. Thus the spin density matrix elements were measured in P_T^2 bins and corrected to $|t|$ by means of a Monte Carlo simulation. Using Monte Carlo events it was found, that the distribution of the angle Φ, which can not be measured in this analysis as well, is correlated with P_T^2. Therefore the correction for the $\cos\theta_h$-ϕ_h distribution in $|t|$ bins depends on the Φ distribution assumed in the Monte Carlo. In this analysis the Φ distribution was generated according to s-channel helicity conservation (section 5.3).

The size of the bins in $|t|$ and $M_{\pi^+\pi^-}$ are given in tables 9.2 and 9.6. In figure 9.20 the spin density matrix elements are shown as a function of $|t|$. Open dots show the results of the fit to the two dimensional distribution and full dots the results obtained from the one dimensional distributions. Statistical errors are indicated by the inner error bars and the outer error bars

Results of the fits according to (9.17) and (9.18)	
r^{04}_{00}	r^{04}_{1-1}
$0.017 \pm 0.008^{+0.007}_{-0.015}$	$-0.012 \pm 0.008^{+0.009}_{-0.007}$

Results of the fit according to (3.72)		
r^{04}_{00}	$\Re r^{04}_{10}$	r^{04}_{1-1}
$0.014 \pm 0.007^{+0.009}_{-0.017}$	$0.012 \pm 0.005^{+0.005}_{-0.007}$	$-0.010 \pm 0.008^{+0.007}_{-0.007}$

Table 9.9: The values for the spin density matrix elements obtained from fits to the decay angular distributions.

represent the statistical and systematic error added in quadrature. The biggest contributions to the systematic error are given by error classes i and x. The big positive systematic error on r^{04}_{1-1} for the two dimensional fit is given by the tracking systematics. Fits to the two and one dimensional distributions give consistent results. No dependence of the spin density matrix elements on $|t|$ can be seen in the present data. The data is consistent with s-channel helicity conservation inside the systematic error for the whole $|t|$ considered in this analysis.

In figure 9.21 the spin density matrix elements are plotted as a function of $M_{\pi^+\pi^-}$. Again open dots represent the results of the analysis of the two dimensional distributions and full dots the results for the one dimensional case. The big positive systematic error on r^{04}_{1-1} for the two dimensional fit is given by the tracking systematics. The data do not indicate a strong dependence on $M_{\pi^+\pi^-}$.

All spin density matrix elements measured in this analysis in bins of $|t|$ and $M_{\pi^+\pi^-}$ are

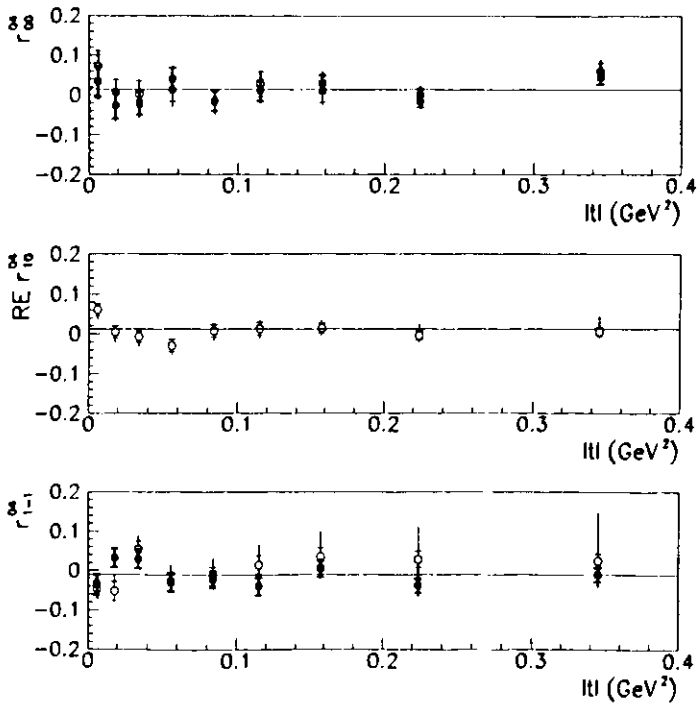

Figure 9.20: The results for the spin density matrix elements as a function of $|t|$. The full dots represent the results of the fits according to equations (9.17) and (9.18) and the open dots the results of the fits according to equation (3.72). The inner error bars indicate the statistical uncertainty and the outer the statistical and systematic uncertainties summed in quadrature.

summarized in Appendix C together with the systematic error from all error classes affecting the results.

In low energy photoproduction data is was found that at small momentum transfer s-channel helicity is conserved at the γp vertex and that ρ^0-production is dominated by natural parity exchange for all t e.g.[10, 93, 95, 80]. Violation of s-channel helicity conservation was observed for $|t| \gtrsim 0.4$ GeV^2. It was found that the single spin flip amplitude has the same sign as the non-flip amplitude, whereas the double spin flip amplitude has opposite in sign. In ρ^0 electroproduction e.g.[10, 9, 60, 29, 21] it was observed that ρ^0 production is dominated by SCHC amplitudes and that the helicity flip amplitude is of the order of 15-20% of the non-flip amplitude for $|t| \lesssim 0.5$ GeV^2. $\Re r^{04}_{10}$ and r^{04}_{1-1} are measured to have opposite sign and $\Re r^{04}_{10}$ was found to be bigger than r^{04}_{1-1}. In low energy photoproduction [95] changes of the spin density matrix elements as a function of $M_{\pi^+\pi^-}$ were observed. For $\Re\rho^0_{10}$ and ρ^0_{1-1} a variation

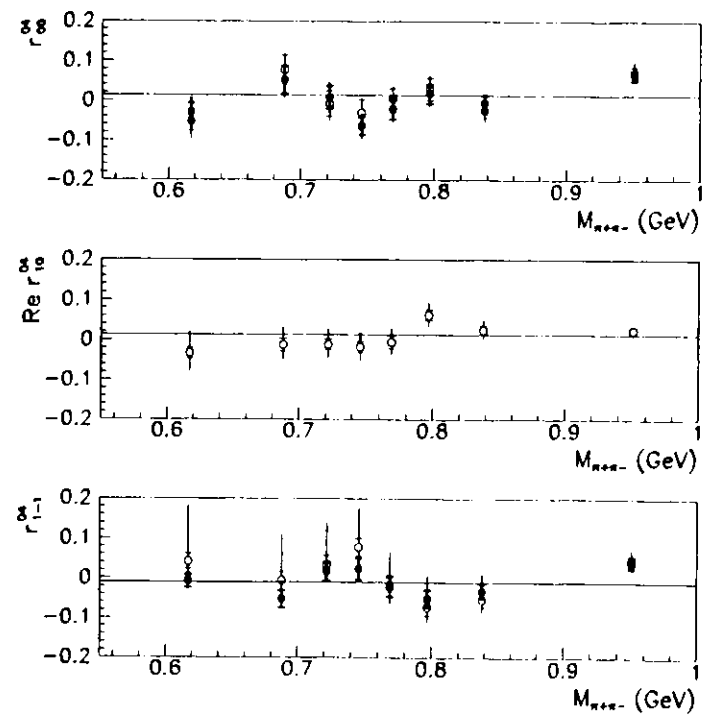

Figure 9.21: The results for the spin density matrix elements as a function of $M_{\pi^+\pi^-}$. The full dots represent the results of the fits according to equations (9.17) and (9.18) and the open dots the results of the fits according to equation (3.72). The inner error bars indicate the statistical uncertainty and the outer the statistical and systematic uncertainties summed in quadrature.

through the ρ^0 region and a change in sign around the ρ^0 mass were observed. The variation was ascribed to coherent background. The Söding model reproduced the main features of the spin density matrix elements as a function of $M_{\pi^+\pi^-}$, but the model did not gave a quantitative description of the helicity flip amplitudes in the ρ^0 region. The present accuracy and relatively big binning in $M_{\pi^+\pi^-}$ does not allow strong conclusions about variations of the spin density matrix elements as a function of $M_{\pi^+\pi^-}$. In the Söding model as calculated by Ryskin and Shabelski [89], r^{04}_{00} is expected to vary with $M_{\pi^+\pi^-}$ for finite Q^2.

The results obtained on the spin density matrix elements r^{04}_{00}, $\Re r^{04}_{10}$ and r^{04}_{1-1} in this analysis are consistent with the results obtained in low energy photo- and electroproduction experiments and with the results obtained in previous measurements of ρ^0 electroproduction at HERA by H1 [51] and ZEUS [110].

Chapter 10

Conclusions

The properties of elastic ρ^0 photoproduction $\gamma p \to \rho^0 p$ for $50 < W_{\gamma p} < 100$ GeV and $|t| < 0.5$ GeV^2 were studied using the ZEUS detector at the HERA collider.

The $\pi^+\pi^-$ invariant mass spectrum is skewed and the amount of skewing decreases with increasing $|t|$ in agreement with the Söding model prediction. The mass skewing appears to be independent of $W_{\gamma p}$, if the present data is compared to low energy fixed target measurements. The cross section for resonant ρ^0 production, $\gamma p \to \rho^0 p$ depends on the procedure used to extract the cross section from the mass distribution. For an extraction procedure according to the Söding model the cross section is $\sigma^{\gamma p \to \rho^0 p} = 11.37 \pm 0.17$ stat. $^{+1.30}_{-1.22}$ syst. μb for $W_{\gamma p} = 72$ GeV. Independent of the extraction procedure the cross section varies slowly with $W_{\gamma p}$, exhibiting a power like behavior $W^a_{\gamma p}$ with a value for $a = 0.13 \pm 0.05$ stat. $^{+0.11}_{-0.13}$ syst. consistent with the soft Pomeron approach.

The $|t|$ distribution is well described by an exponential of the form $e^{-b|t|+ct^2}$. The slope b decreases as the invariant mass $M_{\pi^+\pi^-}$ increases. This decrease is equivalent to the decrease of skewing as a function of $|t|$. The value of the slope for the resonant production again depends on the extraction procedure used in the analysis. For an extraction procedure according to the Söding model the slope was found to be $b_{\rho^0} = 10.88 \pm 0.34$ stat. $^{+0.97}_{-0.45}$ syst. GeV^{-2} and $c_{\rho^0} = 2.70 \pm 0.91$ stat. $^{+1.91}_{-1.73}$ syst. GeV^{-4}. A fit to the obtained b_{ρ^0} values for different $W_{\gamma p}$ with the function $b_{\rho^0}(W_{\gamma p}) = b_0 + 2\alpha'_{\mathbb{P}} \ln W^2_{\gamma p}$ yields $\alpha'_{\mathbb{P}} = 0.23 \pm 0.15$ stat. $^{+0.10}_{-0.07}$ syst. GeV^{-2} consistent with results obtained from fits to pp and $\bar{p}p$ data.

The ρ^0 spin density matrix elements r^{04}_{00}, $\Re r^{04}_{10}$ and r^{04}_{1-1} were obtained from the angular distributions of the decay pions in the s-channel helicity frame. The measured values for the matrix elements are $r^{04}_{00} = 0.014 \pm 0.017$ stat. $^{+0.009}_{-0.007}$ syst., $\Re r^{04}_{10} = 0.012 \pm 0.005$ stat. $^{+0.005}_{-0.007}$ syst. and $r^{04}_{1-1} = -0.010 \pm 0.008$ stat. $^{+0.007}_{-0.007}$ syst., consistent with the expectation from s-channel helicity conservation where $\Re r^{04}_{10}$ and r^{04}_{1-1} are expected to be zero and r^{04}_{00} is expected to be small. This result also holds as a function of $|t|$ and $M_{\pi^+\pi^-}$ in the range of this analysis ($|t| < 0.5$ GeV^2, $0.55 < M_{\pi^+\pi^-} < 1.2$ GeV). The results indicate that the ρ^0 not only carries the quantum numbers of the photon, but also its helicity is equal to that of the photon.

Measurements of elastic ω and ϕ photoproduction at HERA [111, 112] together with the present analysis show that photoproduction of light vector mesons (ρ^0, ω, ϕ) exhibits all features of a soft diffractive process, namely a weak energy dependence of the cross section and a dependence on t which is approximately exponential. On the other hand elastic J/ψ photoproduction exhibits a strong $W_{\gamma p}$ dependence of the cross section ($\sigma \propto W^a_{\gamma p}$ with $a \sim 1$). Figure 10.1 shows the cross sections for elastic ρ^0, ω, ϕ and J/ψ photoproduction measured

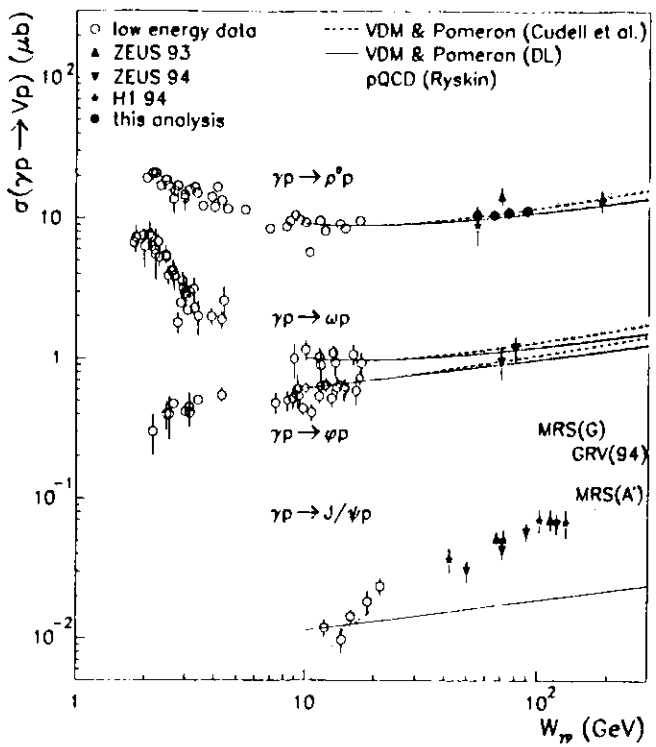

Figure 10.1: Cross section for vector meson production in photoproduction measured by fixed target experiments and the HERA experiments ZEUS and H1 [19].

in the two HERA experiments and compares them to measurements at lower energies. The differences between the ω and ϕ production observed at low energies are attributed to the fact that only Pomeron exchange contributes to ϕ production. These differences are absent in the HERA energy region. The light vector mesons show a weak energy dependence, expected in models based on VDM and Regge theory (soft Pomeron). The strong increase of the J/ψ photoproduction cross section is inconsistent with the soft Pomeron model, but models in the framework of perturbative QCD have been able to successfully describe the photoproduction of J/ψ mesons. Perturbative calculations are applicable in the case of J/ψ photoproduction since the mass of the J/ψ meson provides the necessary large scale. In QCD inspired models the interaction between the proton and the $c\bar{c}$ pair in the photon is mediated by a gluon ladder. The strong increase of the J/ψ cross section as a function of $W_{\gamma p}$ is thus related to the rise of the gluon distribution in the proton at small x. In figure 10.1 the J/ψ measurements at HERA [53, 115] are compared with the results of perturbative QCD

calculations for three different gluon density parameterizations, which exhibit significantly different slopes in the HERA energy region.

Recently elastic production of ρ^0 mesons was also studied for intermediate Q^2 and for 5 GeV$^2 \lesssim Q^2 \lesssim 30$ GeV^2. In the intermediate Q^2 region [113, 39] the growth of the cross section with increasing $W_{\gamma p}$ is weak, consistent with that observed in photoproduction. By contrast, the cross section for elastic ρ^0 production in deep inelastic scattering ($Q^2 \gtrsim 5$ GeV^2) exhibits a stronger $W_{\gamma p}$ dependence. The determination of the $W_{\gamma p}$ dependence of the cross section from a fit to the low energy fixed target measurements [78, 39] and the recent HERA measurements [109, 52] is however difficult, since the two low energy experiments exhibit a significant disagreement. Therefore the rise of the elastic ρ^0 as a function of $W_{\gamma p}$ in deep inelastic scattering was determined from the ZEUS data alone [11]. At large Q^2 ($Q^2 > 15$ GeV^2) the $W_{\gamma p}$ dependence of the cross section exhibits a rise which is faster than the one predicted by the soft Pomeron model. Again the strong rise of the cross section is consistent with predictions by models based on perturbative QCD, in which the rise is explained by the increase of the gluon density in the proton at small x.

In conclusion the cross section for elastic vector meson production has a weak dependence on $W_{\gamma p}$, if there is no hard scale in the process. Such a behavior is seen in elastic ρ^0, ω and ϕ photoproduction. By contrast, if a hard scale is provided, the cross section for elastic vector meson production exhibits a strong $W_{\gamma p}$ dependence. In photoproduction of J/ψ mesons the mass of the J/ψ meson provides the hard scale and for vector meson production in deep inelastic scattering the scale is set by Q^2.

Appendix A

List of *Hot* Calorimeter Cells

In the 1994 data taking period some calorimeter channels showed additional noise, visible as tails in the noise spectra. For the study of elastic ρ^0 photoproduction it is essential to identify and remove these cells from the analysis, before applying the cut on the most energetic cell apart from the tracks (section 4.3.2). The energy for these *hot* cells in the affected run range is set to zero, if it is below a certain threshold. This threshold minimizes the loss of physics and is given by the highest energy deposit in randomly triggered events for each *hot* cell. The list of all *hot* cells with the corresponding energy threshold and the affected run range is given in table A.1 for the different calorimeter sections separately. In some cases the cell was excluded from the analysis even, if the cell was not isolated, since some noisy channels are grouped.

calorimeter cell ID	run range affected	energy threshold (GeV)	excluded only if the cell is isolated
FHAC			
8284	9509-9602	0.4	yes
6924	9890-9962	0.5	yes
FEMC			
7746	9284-9539	0.4	yes
6742	9284-10015	0.5	no
6744	9284-9715	0.5	no
2194	9284-10149	0.5	no
6200	9509-10149	0.5	no
9858	9575-9909	0.4	yes
BHAC			
29404	9509-9921	0.5	no
29390	9509-9997	0.5	no
29388	9509-9927	0.5	no
29406	9509-9927	0.5	no
20604	9600-9927	0.4	yes
26846	9644-9858	0.5	yes
BEMC			
29384	9509-9927	0.5	no
28196	9509-10020	0.6	no
29378	9509-9927	0.5	no
29394	9509-9920	0.5	no
29380	9509-9927	0.5	no
29396	9509-9927	0.5	no
23656	9509-10015	0.6	yes
21542	9509-10060	0.8	yes
23252	9693-10050	0.6	yes
26308	9251-9593	0.4	yes
27348	9310-10038	0.4	yes
21158	9310-10082	0.4	yes
20674	9509-9611	0.4	yes
	9968-10149	0.4	yes
21574	9509-10060	0.4	yes
27234	9509-9776	0.4	yes
	9915-10149	0.4	yes
22552	9633-9654	0.5	yes
	10007-10149	0.5	yes
29266	9644-10060	0.4	yes
16500	9665-9920	0.4	yes
28310	9665-9997	0.6	yes
31286	9693-10149	0.4	yes
30776	9843-9927	0.4	yes
28770	9960-10029	0.4	yes
16584	9843-9874	0.4	yes
RHAC			
37210	9622-9761	1.2	yes

Table A.1: The list of noisy calorimeter cells in 1994.

Appendix B

List of Excluded Runs

For the analysis presented in this thesis only those runs, from the 1994 data taking period, with nominal vertex and positron beam were used. Runs from the electron running period in 1994 were not used since the CFLT was not calibrated for these runs, which results in a lower efficiency of the $REMC_{FLT}$ cut. Runs taken after the shifted vertex runs are also rejected, because in these runs extra noise in the forward calorimeter showed up (section 4.4). Two selection criteria were imposed on the remaining runs. A run summary must have been created and the luminosity of the run has to be bigger than 500 μb^{-1}. To select those runs for which the ZEUS detector was running stably the mean and RMS values for each run for the following distributions are determined: energies in REMC, RHAC, BCAL and FCAL and number of hits in the CTD for each track in the axial layers, stereo layers and z by timing layers. A run was rejected, if the distribution in one of these variables differs in its mean value by more than three times the RMS/$\sqrt{N}$ from the mean over all runs (section 4.4). Two independent TLT trigger streams were used in this analysis, so two lists of *bad* runs were created. All runs in a single HERA electron fill were excluded from the analysis, if one of the runs in the fill is identified as a *bad* run for one of the trigger streams. All suspicious fills given below were however found for both trigger streams. A list of all runs excluded from the analysis, after the standard ZEUS run selection, is given in table B.1.

	run number
no run summary:	9271,9272,9299,9607,9637,9990
low luminosity ($< 500\ \mu b^{-1}$):	9252,9257,9270,9302,9305,9365,
	9388,9389,9390,9410,9411,9463,
	9464,9509,9513,9544,9560,9565,
	9566,9575,9602,9633,9650,9665,
	9700,9710,9794,9812,9872,9892,
	9909,9977,10028,10047,10074,10085,
	10091,10114,10118,10135
suspicious fills:	9256,
	9301,9304,9306,
	9310,9311,9312,
	9350,9351,9352,
	9362,
	9380,9381,9382,
	9385,9386,9387,
	9393,9394,
	9406,9407,9408,
	9412,9413,
	9534,9536,9536,9537,
	9543,
	9561,9567,
	9570,9571,
	9576,9577,9579,9581,9582,9684,
	9586,9587,
	9589,9590,9591,9592,9593,
	9622,9623,
	9624,9625,9626,9627,9628,
	9719,9720,9721,9722,
	9773,
	9804,9805,9806,
	9823

Table B.1: List of runs excluded from the analysis after applying the standard ZEUS run selection.

Appendix C

Tables of Data

$\langle W_{\gamma p} \rangle$ (GeV)	σ (μb)	σ_1 (μb)	σ_2 (μb)	σ_3 (μb)	σ_4 (μb)	σ_5 (μb)	σ_6 (μb)	σ_7 (μb)	σ_8 (μb)
54.8	10.90 ± 0.21	10.93 ± 0.21	11.23 ± 0.24	10.07 ± 0.20	11.57 ± 0.23	11.18 ± 0.22	10.59 ± 0.21	12.03 ± 0.24	10.01 ± 0.20
64.9	10.76 ± 0.21	10.59 ± 0.20	10.75 ± 0.24	9.92 ± 0.20	11.44 ± 0.23	11.02 ± 0.22	10.47 ± 0.21	11.48 ± 0.23	10.13 ± 0.20
74.9	11.39 ± 0.26	11.17 ± 0.21	11.20 ± 0.32	10.49 ± 0.24	12.13 ± 0.28	11.65 ± 0.26	11.10 ± 0.25	11.98 ± 0.27	10.87 ± 0.25
89.6	11.67 ± 0.26	11.34 ± 0.22	11.17 ± 0.43	10.66 ± 0.24	12.52 ± 0.28	11.85 ± 0.26	11.48 ± 0.26	12.15 ± 0.27	11.24 ± 0.25
a	0.16 ± 0.06	0.10 ± 0.05	-0.01 ± 0.08	0.14 ± 0.06	0.18 ± 0.06	0.14 ± 0.06	0.18 ± 0.06	0.04 ± 0.06	0.25 ± 0.06

$\langle W_{\gamma p} \rangle$ (GeV)	σ_9 (μb)	σ_{10} (μb)	σ_{11} (μb)	σ_{12} (μb)	σ_{13} (μb)	σ_{14} (μb)	σ_{15} (μb)	σ_{16} (μb)	σ_{17} (μb)
54.8	10.93 ± 0.21	10.87 ± 0.21	10.91 ± 0.21	10.89 ± 0.21	10.90 ± 0.21	10.90 ± 0.21	10.90 ± 0.21	10.90 ± 0.21	10.88 ± 0.22
64.9	10.81 ± 0.21	10.71 ± 0.21	10.76 ± 0.21	10.75 ± 0.21	10.76 ± 0.21	10.76 ± 0.21	10.76 ± 0.21	10.75 ± 0.21	10.70 ± 0.22
74.9	11.47 ± 0.26	11.32 ± 0.26	11.39 ± 0.26	11.39 ± 0.26	11.39 ± 0.26	11.39 ± 0.26	11.40 ± 0.26	11.38 ± 0.26	11.28 ± 0.26
89.6	11.76 ± 0.26	11.59 ± 0.26	11.63 ± 0.26	11.71 ± 0.26	11.67 ± 0.26	11.67 ± 0.26	11.64 ± 0.26	11.70 ± 0.26	11.55 ± 0.26
a	0.17 ± 0.06	0.15 ± 0.06	0.15 ± 0.06	0.17 ± 0.06	0.16 ± 0.06	0.16 ± 0.06	0.15 ± 0.06	0.16 ± 0.06	0.14 ± 0.06

$\langle W_{\gamma p} \rangle$ (GeV)	σ_{18} (μb)	σ_{19} (μb)	σ_{20} (μb)	σ_{21} (μb)	σ_{22} (μb)	σ_{23} (μb)	σ_{24} (μb)	σ_{25} (μb)	σ_{30} (μb)
54.8	10.94 ± 0.21	10.78 ± 0.21	10.90 ± 0.21	10.89 ± 0.21	10.88 ± 0.21	10.90 ± 0.21	10.99 ± 0.21	10.80 ± 0.21	10.97 ± 0.23
64.9	10.80 ± 0.21	10.64 ± 0.21	10.75 ± 0.21	10.75 ± 0.21	10.70 ± 0.21	10.81 ± 0.21	10.80 ± 0.21	10.71 ± 0.21	10.74 ± 0.23
74.9	11.43 ± 0.26	11.26 ± 0.26	11.38 ± 0.26	11.38 ± 0.26	11.23 ± 0.23	11.49 ± 0.26	11.38 ± 0.25	11.39 ± 0.26	11.33 ± 0.28
89.6	11.74 ± 0.26	11.46 ± 0.26	11.66 ± 0.26	11.63 ± 0.26	11.33 ± 0.25	11.99 ± 0.32	11.51 ± 0.26	11.80 ± 0.26	11.75 ± 0.28
a	0.16 ± 0.06	0.14 ± 0.06	0.16 ± 0.06	0.16 ± 0.06	0.10 ± 0.06	0.20 ± 0.06	0.11 ± 0.06	0.20 ± 0.06	0.16 ± 0.06

$\langle W_{\gamma p} \rangle$ (GeV)	σ_{31} (μb)	σ_{32} (μb)	σ_{33} (μb)	σ_{34} (μb)	σ_{35} (μb)	σ_{SY} (μb)
54.8	10.86 ± 0.21	10.91 ± 0.22	10.80 ± 0.21	10.66 ± 0.21	10.61 ± 0.21	11.33 ± 0.22
64.9	10.73 ± 0.21	10.77 ± 0.22	10.65 ± 0.21	10.52 ± 0.21	10.46 ± 0.21	11.19 ± 0.22
74.9	11.26 ± 0.26	11.42 ± 0.26	11.28 ± 0.26	11.13 ± 0.25	11.07 ± 0.25	11.69 ± 0.23
89.6	11.58 ± 0.26	11.71 ± 0.27	11.67 ± 0.31	11.52 ± 0.30	11.46 ± 0.30	11.76 ± 0.26
a	0.14 ± 0.06	0.16 ± 0.06	0.17 ± 0.06	0.17 ± 0.06	0.17 ± 0.06	0.09 ± 0.06

Table C.1: The *Söding model cross section* in $W_{\gamma p}$ bins obtained using correction method (a). The cross section for all systematic checks affecting the cross section is given. The result of fit with a function of the type $W_{\gamma p}^a$ is given for each check in the bottom line of the table.

$\langle W_{\gamma p} \rangle$ (GeV)	σ (μb)	σ_1 (μb)	σ_2 (μb)	σ_3 (μb)	σ_4 (μb)	σ_5 (μb)	σ_6 (μb)	σ_7 (μb)	σ_8 (μb)
54.8	10.88 ± 0.21	10.90 ± 0.21	11.38 ± 0.24	10.07 ± 0.20	11.55 ± 0.22	11.17 ± 0.22	10.57 ± 0.21	12.02 ± 0.23	9.99 ± 0.19
64.9	10.67 ± 0.19	10.47 ± 0.18	10.86 ± 0.24	9.84 ± 0.17	11.35 ± 0.20	10.93 ± 0.19	10.39 ± 0.18	11.40 ± 0.20	10.04 ± 0.17
74.9	11.15 ± 0.22	10.88 ± 0.20	11.25 ± 0.29	10.28 ± 0.20	11.87 ± 0.23	11.41 ± 0.22	10.86 ± 0.21	11.75 ± 0.23	10.62 ± 0.21
89.6	11.46 ± 0.22	11.30 ± 0.19	10.91 ± 0.44	10.50 ± 0.21	12.27 ± 0.24	11.67 ± 0.23	11.24 ± 0.22	11.94 ± 0.23	11.03 ± 0.22
a	0.13 ± 0.05	0.10 ± 0.05	-0.06 ± 0.08	0.11 ± 0.05	0.14 ± 0.05	0.11 ± 0.05	0.13 ± 0.05	0.01 ± 0.05	0.22 ± 0.05

$\langle W_{\gamma p} \rangle$ (GeV)	σ_9 (μb)	σ_{10} (μb)	σ_{11} (μb)	σ_{12} (μb)	σ_{13} (μb)	σ_{14} (μb)	σ_{15} (μb)	σ_{16} (μb)	σ_{17} (μb)
54.8	10.92 ± 0.21	10.85 ± 0.21	10.90 ± 0.21	10.87 ± 0.21	10.88 ± 0.21	10.89 ± 0.21	10.89 ± 0.21	10.88 ± 0.21	10.86 ± 0.22
64.9	10.72 ± 0.19	10.62 ± 0.19	10.67 ± 0.19	10.68 ± 0.19	10.67 ± 0.19	10.67 ± 0.19	10.67 ± 0.19	10.67 ± 0.19	10.61 ± 0.19
74.9	11.23 ± 0.22	11.08 ± 0.22	11.14 ± 0.22	11.16 ± 0.22	11.15 ± 0.22	11.15 ± 0.22	11.15 ± 0.22	11.15 ± 0.22	11.04 ± 0.22
89.6	11.55 ± 0.23	11.38 ± 0.22	11.43 ± 0.22	11.50 ± 0.23	11.46 ± 0.22	11.46 ± 0.22	11.46 ± 0.22	11.46 ± 0.22	11.33 ± 0.23
a	0.14 ± 0.05	0.12 ± 0.05	0.12 ± 0.05	0.13 ± 0.05	0.13 ± 0.05	0.13 ± 0.05	0.13 ± 0.05	0.13 ± 0.05	0.11 ± 0.06

$\langle W_{\gamma p} \rangle$ (GeV)	σ_{18} (μb)	σ_{19} (μb)	σ_{20} (μb)	σ_{21} (μb)	σ_{22} (μb)	σ_{23} (μb)	σ_{24} (μb)	σ_{25} (μb)	σ_{30} (μb)
54.8	10.93 ± 0.21	10.73 ± 0.21	10.89 ± 0.21	10.88 ± 0.21	10.86 ± 0.21	10.90 ± 0.21	10.98 ± 0.21	10.78 ± 0.21	11.10 ± 0.23
64.9	10.72 ± 0.19	10.50 ± 0.18	10.67 ± 0.19	10.66 ± 0.19	10.52 ± 0.18	10.79 ± 0.21	10.66 ± 0.19	10.65 ± 0.19	10.70 ± 0.20
74.9	11.20 ± 0.22	10.98 ± 0.21	11.15 ± 0.22	11.14 ± 0.22	10.92 ± 0.21	11.37 ± 0.22	11.08 ± 0.22	11.19 ± 0.22	11.17 ± 0.23
89.6	11.53 ± 0.23	11.21 ± 0.22	11.46 ± 0.22	11.45 ± 0.22	11.17 ± 0.22	11.75 ± 0.24	11.35 ± 0.22	11.54 ± 0.23	11.56 ± 0.24
a	0.13 ± 0.05	0.11 ± 0.05	0.12 ± 0.05	0.12 ± 0.05	0.08 ± 0.05	0.17 ± 0.06	0.09 ± 0.05	0.16 ± 0.05	0.11 ± 0.06

$\langle W_{\gamma p} \rangle$ (GeV)	σ_{31} (μb)	σ_{32} (μb)	σ_{33} (μb)	σ_{34} (μb)	σ_{35} (μb)	σ_{36} (μb)	σ_{37} (μb)	σ_{SY} (μb)
54.8	10.83 ± 0.21	10.84 ± 0.21	10.76 ± 0.21	10.61 ± 0.21	10.86 ± 0.21	10.92 ± 0.21	10.87 ± 0.21	11.44 ± 0.22
64.9	10.63 ± 0.19	10.64 ± 0.19	10.60 ± 0.21	10.46 ± 0.20	10.70 ± 0.21	10.74 ± 0.21	10.65 ± 0.19	11.23 ± 0.20
74.9	11.12 ± 0.22	11.17 ± 0.22	11.26 ± 0.25	11.11 ± 0.24	11.36 ± 0.25	11.17 ± 0.22	11.17 ± 0.22	11.74 ± 0.23
89.6	11.39 ± 0.22	11.48 ± 0.23	11.48 ± 0.27	11.32 ± 0.27	11.59 ± 0.27	11.32 ± 0.23	11.61 ± 0.23	12.06 ± 0.24
a	0.12 ± 0.05	0.14 ± 0.05	0.15 ± 0.06	0.15 ± 0.06	0.15 ± 0.06	0.09 ± 0.05	0.16 ± 0.05	0.13 ± 0.05

Table C.2: Like table C.1 but the *Söding model cross section* in $W_{\gamma p}$ bins obtained using correction method (b).

$\langle W_{\gamma p} \rangle$ (GeV)	σ (μb)	σ_1 (μb)	σ_2 (μb)	σ_3 (μb)	σ_4 (μb)	σ_5 (μb)	σ_6 (μb)	σ_7 (μb)	σ_8 (μb)
54.8	12.20 ± 0.24	12.50 ± 0.24	12.63 ± 0.27	11.30 ± 0.22	12.93 ± 0.25	12.53 ± 0.25	11.83 ± 0.23	13.46 ± 0.26	11.20 ± 0.22
64.9	12.06 ± 0.24	12.12 ± 0.23	12.12 ± 0.27	11.14 ± 0.22	12.80 ± 0.25	12.37 ± 0.24	11.71 ± 0.23	12.88 ± 0.25	11.34 ± 0.22
74.9	12.77 ± 0.29	12.83 ± 0.27	12.61 ± 0.36	11.79 ± 0.27	13.57 ± 0.31	13.08 ± 0.30	12.42 ± 0.28	13.44 ± 0.30	12.17 ± 0.28
89.6	13.11 ± 0.32	13.09 ± 0.29	12.62 ± 0.59	12.02 ± 0.29	14.01 ± 0.35	13.34 ± 0.31	12.84 ± 0.32	13.66 ± 0.34	12.60 ± 0.30
a	0.16 ± 0.06	0.12 ± 0.06	-0.01 ± 0.09	0.14 ± 0.06	0.18 ± 0.06	0.15 ± 0.06	0.18 ± 0.06	0.04 ± 0.06	0.26 ± 0.06

$\langle W_{\gamma p} \rangle$ (GeV)	σ_9 (μb)	σ_{10} (μb)	σ_{11} (μb)	σ_{12} (μb)	σ_{13} (μb)	σ_{14} (μb)	σ_{15} (μb)	σ_{16} (μb)	σ_{17} (μb)
54.8	12.24 ± 0.24	12.16 ± 0.24	12.20 ± 0.24	12.20 ± 0.24	12.20 ± 0.24	12.20 ± 0.24	12.22 ± 0.24	12.18 ± 0.24	12.17 ± 0.24
64.9	12.13 ± 0.24	11.99 ± 0.24	12.05 ± 0.24	12.07 ± 0.24	12.06 ± 0.24	12.06 ± 0.24	12.08 ± 0.24	12.03 ± 0.24	11.98 ± 0.24
74.9	12.87 ± 0.29	12.67 ± 0.29	12.75 ± 0.29	12.79 ± 0.29	12.77 ± 0.29	12.77 ± 0.29	12.79 ± 0.29	12.74 ± 0.29	12.64 ± 0.29
89.6	13.22 ± 0.32	13.00 ± 0.31	13.04 ± 0.31	13.18 ± 0.33	13.11 ± 0.32	13.11 ± 0.32	13.11 ± 0.32	13.10 ± 0.31	12.96 ± 0.33
a	0.17 ± 0.06	0.15 ± 0.06	0.15 ± 0.06	0.17 ± 0.06	0.16 ± 0.06	0.16 ± 0.06	0.16 ± 0.06	0.17 ± 0.06	0.14 ± 0.06

$\langle W_{\gamma p} \rangle$ (GeV)	σ_{18} (μb)	σ_{19} (μb)	σ_{20} (μb)	σ_{21} (μb)	σ_{22} (μb)	σ_{23} (μb)	σ_{24} (μb)	σ_{25} (μb)	σ_{30} (μb)
54.8	12.25 ± 0.24	12.02 ± 0.24	12.20 ± 0.24	12.19 ± 0.24	12.18 ± 0.24	12.21 ± 0.24	12.26 ± 0.24	12.13 ± 0.24	12.20 ± 0.26
64.9	12.10 ± 0.24	11.88 ± 0.23	12.05 ± 0.24	12.05 ± 0.24	12.01 ± 0.24	12.10 ± 0.24	12.17 ± 0.24	11.94 ± 0.24	11.95 ± 0.26
74.9	12.82 ± 0.29	12.58 ± 0.28	12.76 ± 0.29	12.75 ± 0.29	12.69 ± 0.29	12.84 ± 0.29	12.94 ± 0.29	12.58 ± 0.27	12.50 ± 0.26
89.6	13.19 ± 0.32	12.81 ± 0.32	13.10 ± 0.32	13.08 ± 0.32	12.89 ± 0.29	13.30 ± 0.35	13.42 ± 0.35	12.69 ± 0.28	12.74 ± 0.30
a	0.17 ± 0.06	0.15 ± 0.06	0.16 ± 0.06	0.16 ± 0.06	0.13 ± 0.06	0.19 ± 0.06	0.20 ± 0.06	0.11 ± 0.06	0.10 ± 0.06

$\langle W_{\gamma p} \rangle$ (GeV)	σ_{31} (μb)	σ_{32} (μb)	σ_{33} (μb)	σ_{34} (μb)	σ_{35} (μb)
54.8	12.17 ± 0.24	12.25 ± 0.24	12.01 ± 0.24	12.42 ± 0.24	12.19 ± 0.24
64.9	12.05 ± 0.24	12.12 ± 0.24	11.87 ± 0.23	12.27 ± 0.24	12.04 ± 0.24
74.9	12.63 ± 0.29	12.85 ± 0.29	12.57 ± 0.28	12.99 ± 0.29	12.75 ± 0.29
89.6	13.03 ± 0.32	13.21 ± 0.35	12.95 ± 0.34	13.27 ± 0.30	13.14 ± 0.35
a	0.15 ± 0.06	0.17 ± 0.06	0.17 ± 0.06	0.15 ± 0.06	0.17 ± 0.06

Table C.3: Like table C.1 but the *parameterization cross section* in $W_{\gamma p}$ bins obtained using correction method (a).

$\langle W_{\gamma p} \rangle$ (GeV)	σ (μb)	σ_1 (μb)	σ_2 (μb)	σ_3 (μb)	σ_4 (μb)	σ_5 (μb)	σ_6 (μb)	σ_7 (μb)	σ_8 (μb)
54.8	12.29 ± 0.24	12.55 ± 0.24	12.82 ± 0.27	11.38 ± 0.22	13.02 ± 0.25	12.62 ± 0.25	11.91 ± 0.23	13.56 ± 0.26	11.28 ± 0.22
64.9	12.11 ± 0.24	12.13 ± 0.23	12.28 ± 0.27	11.19 ± 0.22	12.86 ± 0.25	12.42 ± 0.24	11.76 ± 0.23	12.93 ± 0.25	11.39 ± 0.22
74.9	12.78 ± 0.25	12.83 ± 0.25	12.67 ± 0.33	11.79 ± 0.23	13.59 ± 0.27	13.08 ± 0.25	12.44 ± 0.25	13.46 ± 0.26	12.16 ± 0.24
89.6	13.06 ± 0.31	13.19 ± 0.26	12.27 ± 0.50	11.98 ± 0.28	13.95 ± 0.33	13.31 ± 0.31	12.78 ± 0.30	13.59 ± 0.32	12.57 ± 0.30
a	0.14 ± 0.06	0.13 ± 0.05	-0.07 ± 0.08	0.12 ± 0.06	0.16 ± 0.06	0.13 ± 0.06	0.16 ± 0.06	0.02 ± 0.06	0.24 ± 0.06

$\langle W_{\gamma p} \rangle$ (GeV)	σ_9 (μb)	σ_{10} (μb)	σ_{11} (μb)	σ_{12} (μb)	σ_{13} (μb)	σ_{14} (μb)	σ_{15} (μb)	σ_{16} (μb)	σ_{17} (μb)
54.8	12.33 ± 0.24	12.24 ± 0.24	12.29 ± 0.24	12.29 ± 0.24	12.28 ± 0.24	12.29 ± 0.24	12.29 ± 0.24	12.28 ± 0.24	12.25 ± 0.24
64.9	12.18 ± 0.24	12.04 ± 0.23	12.10 ± 0.24	12.12 ± 0.24	12.11 ± 0.24	12.11 ± 0.24	12.12 ± 0.24	12.10 ± 0.24	12.03 ± 0.24
74.9	12.88 ± 0.25	12.69 ± 0.25	12.75 ± 0.25	12.81 ± 0.25	12.78 ± 0.25	12.78 ± 0.25	12.79 ± 0.25	12.77 ± 0.25	12.65 ± 0.25
89.6	13.17 ± 0.31	12.95 ± 0.30	13.00 ± 0.31	13.11 ± 0.31	13.06 ± 0.31	13.06 ± 0.31	13.06 ± 0.31	13.05 ± 0.31	12.90 ± 0.31
a	0.15 ± 0.06	0.13 ± 0.06	0.13 ± 0.06	0.15 ± 0.06	0.14 ± 0.06	0.14 ± 0.06	0.14 ± 0.06	0.14 ± 0.06	0.12 ± 0.06

$\langle W_{\gamma p} \rangle$ (GeV)	σ_{18} (μb)	σ_{19} (μb)	σ_{20} (μb)	σ_{21} (μb)	σ_{22} (μb)	σ_{23} (μb)	σ_{24} (μb)	σ_{25} (μb)	σ_{30} (μb)
54.8	12.33 ± 0.24	12.11 ± 0.24	12.29 ± 0.24	12.28 ± 0.24	12.26 ± 0.24	12.30 ± 0.24	12.37 ± 0.24	12.20 ± 0.24	12.46 ± 0.26
64.9	12.16 ± 0.24	11.92 ± 0.23	12.10 ± 0.24	12.09 ± 0.24	12.05 ± 0.23	12.16 ± 0.24	12.26 ± 0.24	11.92 ± 0.21	12.00 ± 0.22
74.9	12.83 ± 0.25	12.58 ± 0.25	12.77 ± 0.25	12.76 ± 0.25	12.62 ± 0.25	12.93 ± 0.28	13.08 ± 0.29	12.43 ± 0.24	12.52 ± 0.26
89.6	13.14 ± 0.31	12.76 ± 0.30	13.05 ± 0.31	13.03 ± 0.31	12.92 ± 0.30	13.19 ± 0.31	13.35 ± 0.31	12.74 ± 0.27	12.96 ± 0.27
a	0.13 ± 0.06	0.13 ± 0.06	0.14 ± 0.06	0.14 ± 0.06	0.12 ± 0.06	0.16 ± 0.06	0.18 ± 0.06	0.11 ± 0.06	0.11 ± 0.06

$\langle W_{\gamma p} \rangle$ (GeV)	σ_{31} (μb)	σ_{32} (μb)	σ_{33} (μb)	σ_{34} (μb)	σ_{35} (μb)	σ_{36} (μb)	σ_{37} (μb)
54.8	12.23 ± 0.24	12.34 ± 0.24	12.08 ± 0.23	12.52 ± 0.24	12.27 ± 0.24	12.27 ± 0.24	12.19 ± 0.24
64.9	12.04 ± 0.23	12.20 ± 0.24	11.91 ± 0.23	12.34 ± 0.24	12.10 ± 0.24	12.08 ± 0.24	12.13 ± 0.24
74.9	12.75 ± 0.25	12.98 ± 0.26	12.63 ± 0.28	12.97 ± 0.25	12.83 ± 0.28	12.71 ± 0.27	12.83 ± 0.25
89.6	13.01 ± 0.30	13.23 ± 0.31	12.85 ± 0.30	13.30 ± 0.31	13.05 ± 0.31	12.76 ± 0.30	13.28 ± 0.31
a	0.15 ± 0.06	0.17 ± 0.06	0.15 ± 0.06	0.14 ± 0.06	0.14 ± 0.06	0.10 ± 0.06	0.19 ± 0.06

Table C.4: Like table C.1 but the *parameterization cross section* in $W_{\gamma p}$ bins obtained using correction method (b).

$\langle W_{\gamma p} \rangle$ (GeV)	σ (μb)	σ_1 (μb)	σ_2 (μb)	σ_3 (μb)	σ_4 (μb)	σ_5 (μb)	σ_6 (μb)	σ_7 (μb)	σ_8 (μb)
54.8	13.25 ± 0.26	13.22 ± 0.26	13.71 ± 0.29	12.25 ± 0.24	14.06 ± 0.28	13.60 ± 0.27	12.86 ± 0.25	14.62 ± 0.29	12.17 ± 0.24
64.9	13.10 ± 0.26	12.82 ± 0.24	13.16 ± 0.29	12.09 ± 0.24	13.92 ± 0.27	13.42 ± 0.26	12.74 ± 0.25	13.98 ± 0.28	12.33 ± 0.24
74.9	13.87 ± 0.31	13.59 ± 0.29	13.68 ± 0.39	12.78 ± 0.29	14.76 ± 0.33	14.20 ± 0.32	13.50 ± 0.31	14.59 ± 0.33	13.23 ± 0.30
89.6	14.24 ± 0.35	13.84 ± 0.31	13.70 ± 0.64	13.03 ± 0.31	15.24 ± 0.38	14.48 ± 0.34	13.97 ± 0.35	14.83 ± 0.37	13.69 ± 0.32
a	0.16 ± 0.06	0.12 ± 0.06	-0.01 ± 0.09	0.14 ± 0.06	0.18 ± 0.06	0.13 ± 0.06	0.18 ± 0.06	0.04 ± 0.06	0.26 ± 0.06

$\langle W_{\gamma p} \rangle$ (GeV)	σ_9 (μb)	σ_{10} (μb)	σ_{11} (μb)	σ_{12} (μb)	σ_{13} (μb)	σ_{14} (μb)	σ_{15} (μb)	σ_{16} (μb)	σ_{17} (μb)
54.8	13.30 ± 0.26	13.21 ± 0.26	13.26 ± 0.26	13.24 ± 0.26	13.25 ± 0.26	13.25 ± 0.26	13.26 ± 0.26	13.25 ± 0.26	13.22 ± 0.26
64.9	13.17 ± 0.26	13.03 ± 0.26	13.09 ± 0.26	13.10 ± 0.26	13.10 ± 0.26	13.10 ± 0.26	13.11 ± 0.26	13.09 ± 0.26	13.02 ± 0.26
74.9	13.97 ± 0.32	13.77 ± 0.31	13.86 ± 0.31	13.88 ± 0.31	13.87 ± 0.31	13.87 ± 0.31	13.88 ± 0.31	13.86 ± 0.31	13.74 ± 0.32
89.6	14.36 ± 0.35	14.12 ± 0.34	14.17 ± 0.34	14.31 ± 0.36	14.24 ± 0.35	14.24 ± 0.35	14.22 ± 0.35	14.25 ± 0.34	14.08 ± 0.36
a	0.17 ± 0.06	0.15 ± 0.06	0.15 ± 0.06	0.17 ± 0.06	0.16 ± 0.06	0.16 ± 0.06	0.16 ± 0.06	0.17 ± 0.06	0.14 ± 0.06

$\langle W_{\gamma p} \rangle$ (GeV)	σ_{18} (μb)	σ_{19} (μb)	σ_{20} (μb)	σ_{21} (μb)	σ_{22} (μb)	σ_{23} (μb)	σ_{24} (μb)	σ_{25} (μb)	σ_{30} (μb)
54.8	13.29 ± 0.26	13.10 ± 0.26	13.25 ± 0.26	13.24 ± 0.26	13.12 ± 0.26	13.37 ± 0.26	13.13 ± 0.26	13.36 ± 0.26	13.32 ± 0.28
64.9	13.14 ± 0.26	12.94 ± 0.26	13.09 ± 0.26	13.08 ± 0.26	12.94 ± 0.26	13.25 ± 0.26	13.03 ± 0.26	13.15 ± 0.26	13.04 ± 0.28
74.9	13.91 ± 0.32	13.70 ± 0.31	13.86 ± 0.31	13.85 ± 0.31	13.66 ± 0.31	14.06 ± 0.32	13.86 ± 0.31	13.85 ± 0.30	13.64 ± 0.29
89.6	14.31 ± 0.35	13.95 ± 0.35	14.23 ± 0.34	14.20 ± 0.35	13.88 ± 0.31	14.36 ± 0.38	14.37 ± 0.38	13.98 ± 0.31	13.91 ± 0.33
a	0.17 ± 0.06	0.15 ± 0.06	0.16 ± 0.06	0.16 ± 0.06	0.13 ± 0.06	0.19 ± 0.06	0.20 ± 0.06	0.11 ± 0.06	0.10 ± 0.06

$\langle W_{\gamma p} \rangle$ (GeV)	σ_{31} (μb)	σ_{32} (μb)	σ_{33} (μb)	σ_{34} (μb)	σ_{35} (μb)
54.8	13.22 ± 0.26	13.32 ± 0.26	13.19 ± 0.26	13.28 ± 0.26	13.21 ± 0.26
64.9	13.10 ± 0.26	13.17 ± 0.26	13.03 ± 0.26	13.12 ± 0.26	13.06 ± 0.26
74.9	13.73 ± 0.31	13.98 ± 0.32	13.80 ± 0.31	13.90 ± 0.31	13.83 ± 0.31
89.6	14.16 ± 0.35	14.37 ± 0.38	14.22 ± 0.38	14.19 ± 0.32	14.24 ± 0.38
a	0.15 ± 0.06	0.17 ± 0.06	0.17 ± 0.06	0.15 ± 0.06	0.17 ± 0.06

Table C.5: Like table C.1 but the *phenomenological Söding model cross section* in $W_{\gamma p}$ bins obtained using correction method (a).

$\langle W_{\gamma p} \rangle$ (GeV)	σ (μb)	σ_1 (μb)	σ_2 (μb)	σ_3 (μb)	σ_4 (μb)	σ_5 (μb)	σ_6 (μb)	σ_7 (μb)	σ_8 (μb)
54.8	12.35 ± 0.24	11.98 ± 0.23	13.45 ± 0.29	11.42 ± 0.22	13.11 ± 0.25	12.68 ± 0.25	11.99 ± 0.23	13.62 ± 0.27	11.34 ± 0.22
64.9	12.17 ± 0.24	11.58 ± 0.22	12.86 ± 0.29	11.23 ± 0.22	12.94 ± 0.25	12.47 ± 0.24	11.84 ± 0.23	12.99 ± 0.25	11.46 ± 0.22
74.9	12.85 ± 0.25	12.27 ± 0.24	13.29 ± 0.37	11.83 ± 0.23	13.68 ± 0.27	13.14 ± 0.26	12.52 ± 0.25	13.52 ± 0.27	12.23 ± 0.24
89.6	13.12 ± 0.31	12.59 ± 0.25	12.84 ± 0.52	12.02 ± 0.28	14.04 ± 0.33	13.37 ± 0.31	12.86 ± 0.30	13.65 ± 0.32	12.65 ± 0.30
a	0.14 ± 0.06	0.13 ± 0.05	-0.07 ± 0.08	0.12 ± 0.06	0.16 ± 0.06	0.13 ± 0.06	0.16 ± 0.06	0.02 ± 0.06	0.24 ± 0.06

$\langle W_{\gamma p} \rangle$ (GeV)	σ_9 (μb)	σ_{10} (μb)	σ_{11} (μb)	σ_{12} (μb)	σ_{13} (μb)	σ_{14} (μb)	σ_{15} (μb)	σ_{16} (μb)	σ_{17} (μb)
54.8	12.39 ± 0.24	12.31 ± 0.24	12.37 ± 0.24	12.33 ± 0.24	12.35 ± 0.24	12.35 ± 0.24	12.35 ± 0.24	12.35 ± 0.24	12.32 ± 0.25
64.9	12.24 ± 0.24	12.11 ± 0.24	12.18 ± 0.24	12.16 ± 0.24	12.17 ± 0.24	12.17 ± 0.24	12.17 ± 0.24	12.17 ± 0.24	12.10 ± 0.24
74.9	12.94 ± 0.25	12.76 ± 0.25	12.83 ± 0.25	12.86 ± 0.25	12.85 ± 0.25	12.85 ± 0.25	12.85 ± 0.25	12.84 ± 0.25	12.72 ± 0.25
89.6	13.23 ± 0.31	13.02 ± 0.31	13.09 ± 0.31	13.16 ± 0.31	13.12 ± 0.31	13.12 ± 0.31	13.12 ± 0.31	13.12 ± 0.31	12.97 ± 0.31
a	0.15 ± 0.06	0.13 ± 0.06	0.13 ± 0.06	0.15 ± 0.06	0.14 ± 0.06	0.14 ± 0.06	0.14 ± 0.06	0.14 ± 0.06	0.12 ± 0.06

$\langle W_{\gamma p} \rangle$ (GeV)	σ_{18} (μb)	σ_{19} (μb)	σ_{20} (μb)	σ_{21} (μb)	σ_{22} (μb)	σ_{23} (μb)	σ_{24} (μb)	σ_{25} (μb)	σ_{30} (μb)
54.8	12.39 ± 0.24	12.20 ± 0.24	12.35 ± 0.24	12.34 ± 0.24	12.23 ± 0.24	12.46 ± 0.24	12.23 ± 0.24	12.45 ± 0.24	12.30 ± 0.26
64.9	12.22 ± 0.24	12.00 ± 0.23	12.17 ± 0.24	12.15 ± 0.24	12.02 ± 0.23	12.31 ± 0.24	12.12 ± 0.24	12.17 ± 0.24	12.04 ± 0.22
74.9	12.89 ± 0.25	12.68 ± 0.25	12.84 ± 0.25	12.82 ± 0.25	12.58 ± 0.25	13.10 ± 0.29	12.93 ± 0.28	12.69 ± 0.25	12.56 ± 0.26
89.6	13.20 ± 0.31	12.85 ± 0.30	13.12 ± 0.31	13.10 ± 0.31	12.88 ± 0.30	13.36 ± 0.31	13.20 ± 0.31	13.01 ± 0.28	13.00 ± 0.27
a	0.15 ± 0.06	0.13 ± 0.06	0.14 ± 0.06	0.14 ± 0.06	0.12 ± 0.06	0.16 ± 0.06	0.18 ± 0.06	0.11 ± 0.06	0.11 ± 0.06

$\langle W_{\gamma p} \rangle$ (GeV)	σ_{31} (μb)	σ_{32} (μb)	σ_{33} (μb)	σ_{34} (μb)	σ_{35} (μb)	σ_{36} (μb)	σ_{37} (μb)
54.8	12.35 ± 0.24	12.28 ± 0.24	12.28 ± 0.24	12.38 ± 0.24	12.31 ± 0.24	12.55 ± 0.24	12.09 ± 0.24
64.9	12.17 ± 0.24	12.15 ± 0.24	12.10 ± 0.24	12.20 ± 0.24	12.13 ± 0.24	12.35 ± 0.24	12.03 ± 0.23
74.9	12.88 ± 0.25	12.92 ± 0.26	12.84 ± 0.28	12.83 ± 0.25	12.87 ± 0.28	13.00 ± 0.27	12.72 ± 0.25
89.6	13.14 ± 0.31	13.18 ± 0.31	13.06 ± 0.31	13.15 ± 0.31	13.09 ± 0.31	13.05 ± 0.31	13.16 ± 0.31
a	0.15 ± 0.06	0.17 ± 0.06	0.15 ± 0.06	0.14 ± 0.06	0.14 ± 0.06	0.10 ± 0.06	0.19 ± 0.06

Table C.6: Like table C.1 but the *phenomenological Söding model cross section* in $W_{\gamma p}$ bins obtained using correction method (b).

$\langle\|t\|\rangle$ (GeV^2)	$\|B/A\|$ (GeV$^{-1/2}$)	$\delta\|B/A\|_{\mathrm{fi}}$ (GeV$^{-1/2}$)	$\delta\|B/A\|_{\mathrm{ns}}$ (GeV$^{-1/2}$)	$\delta\|B/A\|_{\mathrm{iii}}$ (GeV$^{-1/2}$)	$\delta\|B/A\|_{\mathrm{iv}}$ (GeV$^{-1/2}$)	$\delta\|B/A\|_{\mathrm{v}}$ (GeV$^{-1/2}$)	$\delta\|B/A\|_{\mathrm{vi}}$ (GeV$^{-1/2}$)	$\delta\|B/A\|_{\mathrm{vii}}$ (GeV$^{-1/2}$)	$\delta\|B/A\|_{\mathrm{ix}}$ (GeV$^{-1/2}$)	$\delta\|B/A\|_{\mathrm{x}}$ (GeV$^{-1/2}$)
0.006	0.789	+0.025	+0.000	+0.001	+0.001	+0.000	+0.000	+0.017	+0.004	+0.018
	±0.042	-0.004	-0.000	-0.002	-0.002	-0.000	-0.000	-0.018	-0.001	-0.000
0.018	0.777	+0.026	+0.000	+0.001	+0.001	+0.000	+0.000	+0.017	+0.004	+0.018
	±0.027	-0.004	-0.000	-0.002	-0.002	-0.000	-0.000	-0.018	-0.002	-0.000
0.034	0.729	+0.027	+0.000	+0.001	+0.001	+0.000	+0.000	+0.018	+0.004	+0.017
	±0.019	-0.004	-0.000	-0.002	-0.002	-0.001	-0.000	-0.018	-0.004	-0.000
0.056	0.722	+0.028	+0.000	+0.001	+0.001	+0.000	+0.000	+0.018	+0.003	+0.016
	±0.025	-0.004	-0.000	-0.001	-0.002	-0.001	-0.000	-0.018	-0.006	-0.000
0.084	0.683	+0.030	+0.000	+0.001	+0.001	+0.000	+0.000	+0.018	+0.003	+0.015
	±0.028	-0.004	-0.000	-0.001	-0.002	-0.001	-0.000	-0.018	-0.008	-0.000
0.115	0.638	+0.033	+0.000	+0.001	+0.002	+0.000	+0.000	+0.018	+0.003	+0.013
	±0.032	-0.004	-0.000	-0.001	-0.002	-0.002	-0.000	-0.018	-0.011	-0.000
0.158	0.614	+0.036	+0.000	+0.001	+0.002	+0.000	+0.000	+0.018	+0.003	+0.012
	±0.031	-0.003	-0.000	-0.001	-0.002	-0.002	-0.000	-0.018	-0.015	-0.000
0.224	0.509	+0.040	+0.000	+0.001	+0.003	+0.001	+0.000	+0.018	+0.003	+0.009
	±0.029	-0.003	-0.000	-0.001	-0.003	-0.003	-0.000	-0.018	-0.021	-0.000
0.345	0.375	+0.049	+0.001	+0.001	+0.004	+0.001	+0.000	+0.019	+0.002	+0.004
	±0.028	-0.002	-0.001	-0.001	-0.004	-0.004	-0.000	-0.018	-0.032	-0.000

$\langle\|t\|\rangle$ (GeV^2)	n	δn_{i}	δn_{ii}	δn_{iii}	δn_{iv}	δn_{v}	δn_{vi}	δn_{vii}	δn_{ix}	δn_{x}
0.006	3.96	+0.15	+0.00	+0.02	+0.01	+0.00	+0.00	+0.08	+0.00	+0.02
	± 0.26	-0.00	-0.00	-0.02	-0.01	-0.00	-0.00	-0.06	-0.01	-0.00
0.018	6.00	+0.16	+0.00	+0.02	+0.01	+0.00	+0.00	+0.06	+0.00	+0.03
	± 0.22	-0.00	-0.00	-0.02	-0.01	-0.00	-0.00	-0.06	-0.02	-0.00
0.034	6.06	+0.16	+0.00	+0.02	+0.01	+0.00	+0.00	+0.06	+0.00	+0.03
	± 0.15	-0.00	-0.00	-0.01	-0.01	-0.01	-0.00	-0.06	-0.03	-0.00
0.056	5.54	+0.17	+0.00	+0.02	+0.01	+0.00	+0.00	+0.06	+0.00	+0.03
	± 0.16	-0.00	-0.00	-0.01	-0.01	-0.01	-0.00	-0.07	-0.04	-0.00
0.084	5.30	+0.18	+0.00	+0.01	+0.01	+0.00	+0.00	+0.07	+0.00	+0.04
	± 0.18	-0.00	-0.00	-0.01	-0.01	-0.01	-0.00	-0.07	-0.05	-0.00
0.115	4.91	+0.19	+0.00	+0.01	+0.01	+0.00	+0.00	+0.07	+0.00	+0.04
	± 0.17	-0.00	-0.00	-0.01	-0.01	-0.01	-0.00	-0.07	-0.07	-0.00
0.158	4.73	+0.20	+0.00	+0.01	+0.02	+0.00	+0.00	+0.07	+0.00	+0.05
	± 0.20	-0.00	-0.00	-0.01	-0.02	-0.02	-0.00	-0.07	-0.09	-0.00
0.224	4.05	+0.22	+0.00	+0.01	+0.02	+0.00	+0.00	+0.07	+0.00	+0.06
	± 0.20	-0.00	-0.00	-0.01	-0.02	-0.02	-0.00	-0.08	-0.13	-0.00
0.345	3.11	+0.26	+0.00	+0.01	+0.02	+0.01	+0.00	+0.08	+0.00	+0.08
	± 0.21	-0.00	-0.00	-0.01	-0.02	-0.03	-0.00	-0.08	-0.20	-0.00

Table C.7: The ratio $|B/A|$ and the parameter n, measuring the amount of skewing, from fits to the invariant mass distribution according to equations (9.7) and (9.10) in $|t|$ bins. The systematic errors obtained for the error classes affecting the result are also given.

$\langle W_{\gamma p}\rangle$ (GeV)	b (GeV^{-2})	b_{i} (GeV^{-2})	b_{ii} (GeV^{-2})	b_3 (GeV^{-2})	b_4 (GeV^{-2})	b_5 (GeV^{-2})	b_6 (GeV^{-2})
54.8	10.64 ± 0.23	10.50 ± 0.20	10.44 ± 0.26	10.95 ± 0.24	10.45 ± 0.21	10.52 ± 0.24	10.68 ± 0.21
64.9	10.98 ± 0.21	10.77 ± 0.19	10.68 ± 0.23	11.21 ± 0.21	10.78 ± 0.20	10.79 ± 0.21	10.98 ± 0.20
84.0	11.10 ± 0.14	10.85 ± 0.13	10.63 ± 0.20	11.34 ± 0.14	10.90 ± 0.14	10.91 ± 0.14	11.10 ± 0.14
$\alpha'_{\mathbb{P}}$ (GeV^{-2})	0.23 ± 0.14	0.17 ± 0.13	0.08 ± 0.19	0.20 ± 0.15	0.23 ± 0.14	0.20 ± 0.15	0.22 ± 0.14

$\langle W_{\gamma p}\rangle$ (GeV)	b_7 (GeV^{-2})	b_8 (GeV^{-2})	b_9 (GeV^{-2})	b_{10} (GeV^{-2})	b_{11} (GeV^{-2})	b_{12} (GeV^{-2})	b_{13} (GeV^{-2})
54.8	10.68 ± 0.20	10.61 ± 0.23	10.62 ± 0.23	10.66 ± 0.23	10.63 ± 0.23	10.64 ± 0.23	10.66 ± 0.23
64.9	10.98 ± 0.20	10.95 ± 0.21	10.95 ± 0.21	11.01 ± 0.21	10.98 ± 0.21	10.98 ± 0.21	11.00 ± 0.21
84.0	11.12 ± 0.14	11.07 ± 0.14	11.06 ± 0.14	11.13 ± 0.14	11.09 ± 0.14	11.10 ± 0.14	11.11 ± 0.14
$\alpha'_{\mathbb{P}}$ (GeV^{-2})	0.23 ± 0.14	0.23 ± 0.15	0.22 ± 0.14	0.24 ± 0.14	0.23 ± 0.14	0.23 ± 0.14	0.23 ± 0.14

$\langle W_{\gamma p}\rangle$ (GeV)	b_{14} (GeV^{-2})	b_{15} (GeV^{-2})	b_{16} (GeV^{-2})	b_{17} (GeV^{-2})	b_{18} (GeV^{-2})	b_{19} (GeV^{-2})	b_{20} (GeV^{-2})
54.8	10.62 ± 0.23	10.63 ± 0.23	10.65 ± 0.23	10.69 ± 0.23	10.63 ± 0.23	10.68 ± 0.24	10.64 ± 0.23
64.9	10.96 ± 0.21	10.98 ± 0.21	10.99 ± 0.21	11.05 ± 0.21	10.97 ± 0.20	11.03 ± 0.21	10.98 ± 0.21
84.0	11.08 ± 0.14	11.10 ± 0.14	11.10 ± 0.14	11.18 ± 0.14	11.09 ± 0.14	11.14 ± 0.14	11.10 ± 0.14
$\alpha'_{\mathbb{P}}$ (GeV^{-2})	0.23 ± 0.14	0.23 ± 0.14	0.22 ± 0.14	0.25 ± 0.15	0.23 ± 0.14	0.23 ± 0.15	0.23 ± 0.14

$\langle W_{\gamma p}\rangle$ (GeV)	b_{21} (GeV^{-2})	b_{22} (GeV^{-2})	b_{23} (GeV^{-2})	b_{24} (GeV^{-2})	b_{25} (GeV^{-2})	b_{26} (GeV^{-2})	b_{27} (GeV^{-2})
54.8	10.63 ± 0.23	10.52 ± 0.23	10.76 ± 0.23	10.97 ± 0.22	10.32 ± 0.23	11.03 ± 0.74	11.00 ± 0.75
64.9	10.97 ± 0.21	10.86 ± 0.21	11.09 ± 0.21	11.30 ± 0.20	10.66 ± 0.21	11.29 ± 0.66	11.14 ± 0.69
84.0	11.09 ± 0.14	10.95 ± 0.14	11.22 ± 0.14	11.43 ± 0.14	10.77 ± 0.14	11.12 ± 0.48	10.89 ± 0.51
$\alpha'_{\mathbb{P}}$ (GeV^{-2})	0.23 ± 0.14	0.22 ± 0.14	0.23 ± 0.15	0.24 ± 0.14	0.22 ± 0.15	0.01 ± 0.48	-0.10 ± 0.50

$\langle W_{\gamma p}\rangle$ (GeV)	b_{30} (GeV^{-2})	b_{31} (GeV^{-2})	b_{32} (GeV^{-2})	b_{33} (GeV^{-2})	b_{34} (GeV^{-2})	b_{35} (GeV^{-2})	b_{SY} (GeV^{-2})
54.8	10.69 ± 0.23	10.79 ± 0.25	10.62 ± 0.20	10.93 ± 0.23	11.02 ± 0.22	11.11 ± 0.22	11.21 ± 0.21
64.9	10.96 ± 0.20	11.19 ± 0.22	10.90 ± 0.18	11.30 ± 0.20	11.40 ± 0.20	11.49 ± 0.20	11.55 ± 0.19
84.0	11.09 ± 0.15	11.19 ± 0.14	11.03 ± 0.14	11.49 ± 0.15	11.60 ± 0.15	11.70 ± 0.15	11.74 ± 0.15
$\alpha'_{\mathbb{P}}$ (GeV^{-2})	0.20 ± 0.16	0.17 ± 0.15	0.22 ± 0.16	0.30 ± 0.15	0.30 ± 0.15	0.31 ± 0.15	0.28 ± 0.14

Table C.8: The slope parameter b_{p^0} in $W_{\gamma p}$ bins from fits according to equation (9.15) as obtained from the *Söding model cross section*. The slope parameter for all systematic checks affecting the result is given. The result for $\alpha'_{\mathbb{P}}$, of a fit according to equation (9.16) for each check is given in the bottom line of the table.

$\langle W_{\gamma p} \rangle$ (GeV)	b (GeV^{-2})	b_1 (GeV^{-2})	b_2 (GeV^{-2})	b_3 (GeV^{-2})	b_4 (GeV^{-2})	b_5 (GeV^{-2})	b_6 (GeV^{-2})
54.8	12.31 ± 0.21	12.09 ± 0.22	12.33 ± 0.24	12.62 ± 0.23	12.11 ± 0.21	12.20 ± 0.23	12.34 ± 0.21
64.9	12.66 ± 0.20	12.32 ± 0.18	12.57 ± 0.22	12.89 ± 0.20	12.47 ± 0.19	12.47 ± 0.20	12.67 ± 0.19
84.0	12.84 ± 0.14	12.54 ± 0.13	12.41 ± 0.21	13.07 ± 0.15	12.65 ± 0.14	12.65 ± 0.14	12.85 ± 0.14
$\alpha'_{\mathbb{P}}$ (GeV^{-2})	0.28 ± 0.14	0.25 ± 0.14	0.02 ± 0.18	0.24 ± 0.15	0.28 ± 0.14	0.24 ± 0.13	0.27 ± 0.14

$\langle W_{\gamma p} \rangle$ (GeV)	b_7 (GeV^{-2})	b_8 (GeV^{-2})	b_9 (GeV^{-2})	b_{10} (GeV^{-2})	b_{11} (GeV^{-2})	b_{12} (GeV^{-2})	b_{13} (GeV^{-2})
54.8	12.29 ± 0.21	12.30 ± 0.22	12.30 ± 0.21	12.32 ± 0.21	12.30 ± 0.21	12.32 ± 0.21	12.33 ± 0.21
64.9	12.68 ± 0.19	12.64 ± 0.20	12.64 ± 0.20	12.69 ± 0.20	12.66 ± 0.20	12.67 ± 0.20	12.68 ± 0.20
84.0	12.85 ± 0.14	12.81 ± 0.14	12.81 ± 0.14	12.86 ± 0.14	12.82 ± 0.14	12.85 ± 0.14	12.85 ± 0.14
$\alpha'_{\mathbb{P}}$ (GeV^{-2})	0.29 ± 0.14	0.27 ± 0.14	0.27 ± 0.14	0.28 ± 0.14	0.27 ± 0.14	0.28 ± 0.14	0.28 ± 0.14

$\langle W_{\gamma p} \rangle$ (GeV)	b_{14} (GeV^{-2})	b_{15} (GeV^{-2})	b_{16} (GeV^{-2})	b_{17} (GeV^{-2})	b_{18} (GeV^{-2})	b_{19} (GeV^{-2})	b_{20} (GeV^{-2})
54.8	12.29 ± 0.21	12.30 ± 0.21	12.32 ± 0.21	12.36 ± 0.22	12.31 ± 0.21	12.31 ± 0.22	12.31 ± 0.21
64.9	12.64 ± 0.20	12.66 ± 0.20	12.66 ± 0.20	12.72 ± 0.20	12.67 ± 0.20	12.66 ± 0.21	12.66 ± 0.20
84.0	12.82 ± 0.14	12.83 ± 0.14	12.83 ± 0.14	12.90 ± 0.15	12.83 ± 0.14	12.85 ± 0.15	12.83 ± 0.14
$\alpha'_{\mathbb{P}}$ (GeV^{-2})	0.28 ± 0.14	0.28 ± 0.14	0.27 ± 0.14	0.28 ± 0.13	0.27 ± 0.14	0.28 ± 0.15	0.27 ± 0.14

$\langle W_{\gamma p} \rangle$ (GeV)	b_{21} (GeV^{-2})	b_{22} (GeV^{-2})	b_{23} (GeV^{-2})	b_{26} (GeV^{-2})	b_{27} (GeV^{-2})	b_{28} (GeV^{-2})	b_{29} (GeV^{-2})
54.8	12.30 ± 0.21	12.33 ± 0.21	12.31 ± 0.21	12.63 ± 0.21	12.00 ± 0.22	12.39 ± 0.70	12.39 ± 0.71
64.9	12.65 ± 0.20	12.69 ± 0.20	12.65 ± 0.20	12.98 ± 0.20	12.35 ± 0.20	12.91 ± 0.66	12.90 ± 0.67
84.0	12.82 ± 0.14	12.88 ± 0.14	12.81 ± 0.14	13.17 ± 0.14	12.51 ± 0.13	12.54 ± 0.53	12.54 ± 0.54
$\alpha'_{\mathbb{P}}$ (GeV^{-2})	0.28 ± 0.14	0.29 ± 0.14	0.26 ± 0.14	0.29 ± 0.14	0.26 ± 0.14	0.01 ± 0.49	0.01 ± 0.50

$\langle W_{\gamma p} \rangle$ (GeV)	b_{30} (GeV^{-2})	b_{31} (GeV^{-2})	b_{32} (GeV^{-2})	b_{33} (GeV^{-2})	b_{34} (GeV^{-2})	b_{35} (GeV^{-2})
54.8	12.34 ± 0.24	12.41 ± 0.24	12.26 ± 0.20	12.23 ± 0.22	12.45 ± 0.21	12.34 ± 0.21
64.9	12.66 ± 0.20	12.76 ± 0.21	12.65 ± 0.19	12.57 ± 0.20	12.81 ± 0.20	12.69 ± 0.20
84.0	12.82 ± 0.16	12.84 ± 0.14	12.97 ± 0.14	12.73 ± 0.14	12.99 ± 0.14	12.85 ± 0.14
$\alpha'_{\mathbb{P}}$ (GeV^{-2})	0.25 ± 0.16	0.21 ± 0.15	0.39 ± 0.16	0.26 ± 0.14	0.28 ± 0.14	0.27 ± 0.14

Table C.9: Like table C.8 but for the *parameterization cross section*.

$\langle W_{\gamma p} \rangle$ (GeV)	b (GeV^{-2})	b_1 (GeV^{-2})	b_2 (GeV^{-2})	b_3 (GeV^{-2})	b_4 (GeV^{-2})	b_5 (GeV^{-2})	b_6 (GeV^{-2})
54.8	10.90 ± 0.21	10.80 ± 0.22	10.82 ± 0.24	11.21 ± 0.23	10.69 ± 0.21	10.79 ± 0.23	10.93 ± 0.21
64.9	11.14 ± 0.20	11.04 ± 0.18	10.91 ± 0.22	11.36 ± 0.20	10.94 ± 0.19	10.95 ± 0.20	11.14 ± 0.19
84.0	11.34 ± 0.15	11.23 ± 0.13	10.92 ± 0.21	11.56 ± 0.15	11.14 ± 0.14	11.15 ± 0.15	11.33 ± 0.14
$\alpha'_{\mathbb{P}}$ (GeV^{-2})	0.24 ± 0.14	0.23 ± 0.14	0.05 ± 0.18	0.20 ± 0.15	0.25 ± 0.14	0.21 ± 0.15	0.23 ± 0.14

$\langle W_{\gamma p} \rangle$ (GeV)	b_7 (GeV^{-2})	b_8 (GeV^{-2})	b_9 (GeV^{-2})	b_{10} (GeV^{-2})	b_{11} (GeV^{-2})	b_{12} (GeV^{-2})	b_{13} (GeV^{-2})
54.8	10.91 ± 0.21	10.88 ± 0.22	10.88 ± 0.21	10.91 ± 0.21	10.89 ± 0.21	10.90 ± 0.21	10.91 ± 0.21
64.9	11.16 ± 0.19	11.11 ± 0.20	11.11 ± 0.20	11.16 ± 0.20	11.13 ± 0.20	11.14 ± 0.20	11.15 ± 0.20
84.0	11.35 ± 0.14	11.30 ± 0.15	11.31 ± 0.15	11.36 ± 0.14	11.33 ± 0.15	11.35 ± 0.15	11.35 ± 0.15
$\alpha'_{\mathbb{P}}$ (GeV^{-2})	0.24 ± 0.14	0.23 ± 0.14	0.23 ± 0.14	0.25 ± 0.14	0.24 ± 0.14	0.25 ± 0.14	0.24 ± 0.14

$\langle W_{\gamma p} \rangle$ (GeV)	b_{14} (GeV^{-2})	b_{15} (GeV^{-2})	b_{16} (GeV^{-2})	b_{17} (GeV^{-2})	b_{18} (GeV^{-2})	b_{19} (GeV^{-2})	b_{20} (GeV^{-2})
54.8	10.88 ± 0.21	10.89 ± 0.21	10.90 ± 0.21	10.94 ± 0.22	10.89 ± 0.21	10.92 ± 0.22	10.90 ± 0.21
64.9	11.12 ± 0.20	11.13 ± 0.20	11.14 ± 0.20	11.20 ± 0.20	11.13 ± 0.20	11.18 ± 0.20	11.14 ± 0.20
84.0	11.32 ± 0.15	11.34 ± 0.15	11.33 ± 0.14	11.42 ± 0.15	11.33 ± 0.14	11.37 ± 0.15	11.33 ± 0.15
$\alpha'_{\mathbb{P}}$ (GeV^{-2})	0.24 ± 0.14	0.25 ± 0.14	0.24 ± 0.14	0.26 ± 0.15	0.24 ± 0.14	0.25 ± 0.15	0.24 ± 0.14

$\langle W_{\gamma p} \rangle$ (GeV)	b_{21} (GeV^{-2})	b_{22} (GeV^{-2})	b_{23} (GeV^{-2})	b_{26} (GeV^{-2})	b_{27} (GeV^{-2})	b_{28} (GeV^{-2})	b_{29} (GeV^{-2})
54.8	10.89 ± 0.21	10.87 ± 0.21	10.92 ± 0.21	11.21 ± 0.21	10.59 ± 0.22	11.02 ± 0.69	11.01 ± 0.70
64.9	11.13 ± 0.20	11.11 ± 0.20	11.16 ± 0.20	11.46 ± 0.19	10.82 ± 0.20	11.36 ± 0.64	11.17 ± 0.68
84.0	11.33 ± 0.15	11.32 ± 0.14	11.35 ± 0.15	11.67 ± 0.14	11.01 ± 0.15	11.41 ± 0.50	11.24 ± 0.53
$\alpha'_{\mathbb{P}}$ (GeV^{-2})	0.24 ± 0.14	0.25 ± 0.14	0.23 ± 0.14	0.25 ± 0.14	0.23 ± 0.15	0.19 ± 0.47	0.12 ± 0.49

$\langle W_{\gamma p} \rangle$ (GeV)	b_{30} (GeV^{-2})	b_{31} (GeV^{-2})	b_{32} (GeV^{-2})	b_{33} (GeV^{-2})	b_{34} (GeV^{-2})	b_{35} (GeV^{-2})
54.8	10.92 ± 0.24	11.03 ± 0.24	10.90 ± 0.20	10.92 ± 0.22	10.90 ± 0.21	10.90 ± 0.21
64.9	11.10 ± 0.20	11.27 ± 0.21	11.17 ± 0.19	11.17 ± 0.20	11.14 ± 0.20	11.15 ± 0.20
84.0	11.27 ± 0.16	11.33 ± 0.15	11.49 ± 0.14	11.36 ± 0.15	11.34 ± 0.14	11.35 ± 0.15
$\alpha'_{\mathbb{P}}$ (GeV^{-2})	0.19 ± 0.15	0.14 ± 0.14	0.33 ± 0.14	0.24 ± 0.14	0.24 ± 0.15	0.24 ± 0.15

Table C.10: Like table C.8 but for the *phenomenological Söding model cross section*.

$\langle M_{\pi^+\pi^-}\rangle$ (GeV^2)	b (GeV^{-2})	$\delta b_{\rm i}$ (GeV^{-2})	$\delta b_{\rm ii}$ (GeV^{-2})	$\delta b_{\rm iii}$ (GeV^{-2})	$\delta b_{\rm iv}$ (GeV^{-2})	$\delta b_{\rm v}$ (GeV^{-2})	$\delta b_{\rm vi}$ (GeV^{-2})	$\delta b_{\rm vii}$ (GeV^{-2})	$\delta b_{\rm viii}$ (GeV^{-2})	$\delta b_{\rm ix}$ (GeV^{-2})	$\delta b_{\rm x}$ (GeV^{-2})
0.617	13.34	+0.00	+0.25	+0.04	+0.05	+0.11	+0.00	+0.26	+0.07	+0.00	+0.02
	± 0.19	-0.16	-0.22	-0.03	-0.06	-0.02	-0.00	-0.26	-0.12	-0.06	-0.00
0.688	11.80	+0.00	+0.25	+0.04	+0.06	+0.09	+0.00	+0.27	+0.06	+0.00	+0.03
	± 0.28	-0.24	-0.22	-0.03	-0.05	-0.02	-0.00	-0.26	-0.19	-0.06	-0.00
0.721	11.78	+0.00	+0.25	+0.04	+0.06	+0.08	+0.00	+0.27	+0.05	+0.00	+0.03
	± 0.30	-0.28	-0.22	-0.03	-0.04	-0.02	-0.00	-0.27	-0.22	-0.06	-0.00
0.746	11.90	+0.00	+0.25	+0.04	+0.06	+0.08	+0.00	+0.27	+0.05	+0.00	+0.03
	± 0.31	-0.31	-0.22	-0.03	-0.04	-0.02	-0.00	-0.27	-0.24	-0.06	-0.00
0.769	11.27	+0.00	+0.25	+0.04	+0.06	+0.07	+0.00	+0.27	+0.05	+0.00	+0.03
	± 0.26	-0.33	-0.22	-0.03	-0.04	-0.02	-0.00	-0.27	-0.26	-0.06	-0.00
0.797	10.64	+0.00	+0.25	+0.04	+0.06	+0.06	+0.00	+0.28	+0.04	+0.00	+0.04
	± 0.27	-0.37	-0.22	-0.03	-0.03	-0.01	-0.00	-0.27	-0.29	-0.07	-0.00
0.838	10.41	+0.00	+0.25	+0.04	+0.06	+0.05	+0.00	+0.28	+0.03	+0.00	+0.04
	± 0.21	-0.41	-0.22	-0.03	-0.03	-0.01	-0.00	-0.28	-0.33	-0.07	-0.00
0.951	8.83	+0.00	+0.24	+0.04	+0.07	+0.02	+0.00	+0.29	+0.01	+0.00	+0.05
	± 0.14	-0.54	-0.23	-0.03	-0.01	-0.01	-0.00	-0.29	-0.43	-0.07	-0.00

Table C.11: The slope parameter $b_{\pi\pi}$ obtained from fits according to equation (9.14) in $M_{\pi^+\pi^-}$ bins. The systematic errors obtained for the error classes affecting the result are also given.

$\langle\lvert t\rvert\rangle$ (GeV^2)	r_{00}^{04}	$\delta r_{\rm i}$	$\delta r_{\rm ii}$	$\delta r_{\rm iii}$	$\delta r_{\rm iv}$	$\delta r_{\rm v}$	$\delta r_{\rm vi}$	$\delta r_{\rm ix}$	$\delta r_{\rm x}$
0.006	0.033	+0.001	+0.000	+0.003	+0.003	+0.000	+0.000	+0.003	+0.007
	±0.038	-0.021	-0.000	-0.005	-0.005	-0.000	-0.000	-0.009	-0.005
0.018	-0.027	+0.003	+0.000	+0.003	+0.003	+0.000	+0.000	+0.003	+0.006
	±0.033	-0.020	-0.000	-0.004	-0.005	-0.000	-0.000	-0.009	-0.004
0.034	-0.021	+0.004	+0.000	+0.003	+0.003	+0.001	+0.000	+0.004	+0.006
	±0.030	-0.020	-0.001	-0.004	-0.004	-0.000	-0.000	-0.008	-0.004
0.056	0.040	+0.007	+0.000	+0.003	+0.003	+0.001	+0.000	+0.004	+0.006
	±0.028	-0.019	-0.001	-0.004	-0.004	-0.000	-0.000	-0.008	-0.004
0.084	-0.016	+0.010	+0.000	+0.003	+0.003	+0.001	+0.000	+0.005	+0.005
	±0.025	-0.018	-0.001	-0.004	-0.004	-0.000	-0.000	-0.007	-0.004
0.115	0.011	+0.013	+0.000	+0.003	+0.003	+0.001	+0.000	+0.006	+0.005
	±0.026	-0.016	-0.001	-0.004	-0.004	-0.000	-0.000	-0.007	-0.003
0.158	0.029	+0.018	+0.001	+0.002	+0.002	+0.001	+0.000	+0.008	+0.004
	±0.021	-0.015	-0.001	-0.004	-0.003	-0.000	-0.000	-0.006	-0.003
0.224	-0.016	+0.025	+0.001	+0.002	+0.002	+0.001	+0.000	+0.010	+0.003
	±0.015	-0.012	-0.001	-0.003	-0.003	-0.000	-0.000	-0.005	-0.002
0.345	0.045	+0.039	+0.001	+0.002	+0.001	+0.002	+0.000	+0.014	+0.001
	±0.017	-0.007	-0.002	-0.002	-0.001	-0.000	-0.000	-0.002	-0.001

$\langle\lvert t\rvert\rangle$ (GeV^2)	r_{00}^{04}	$\delta r_{\rm i}$	$\delta r_{\rm ii}$	$\delta r_{\rm iii}$	$\delta r_{\rm iv}$	$\delta r_{\rm v}$	$\delta r_{\rm vi}$	$\delta r_{\rm ix}$	$\delta r_{\rm x}$
0.006	0.072	+0.000	+0.000	+0.003	+0.002	+0.002	+0.000	+0.001	+0.009
	±0.038	-0.023	-0.000	-0.005	-0.004	-0.001	-0.000	-0.006	-0.030
0.018	0.006	+0.000	+0.000	+0.003	+0.002	+0.002	+0.000	+0.001	+0.010
	±0.033	-0.022	-0.000	-0.005	-0.003	-0.001	-0.000	-0.006	-0.029
0.034	0.002	+0.000	+0.000	+0.003	+0.002	+0.002	+0.000	+0.001	+0.010
	±0.034	-0.021	-0.000	-0.004	-0.003	-0.001	-0.000	-0.006	-0.028
0.056	0.012	+0.000	+0.000	+0.003	+0.002	+0.002	+0.000	+0.002	+0.011
	±0.028	-0.020	-0.000	-0.004	-0.003	-0.001	-0.000	-0.006	-0.026
0.084	-0.016	+0.000	+0.000	+0.003	+0.002	+0.002	+0.000	+0.002	+0.012
	±0.025	-0.019	-0.000	-0.004	-0.003	-0.001	-0.000	-0.005	-0.024
0.115	0.027	+0.000	+0.000	+0.002	+0.002	+0.002	+0.000	+0.002	+0.013
	±0.032	-0.017	-0.000	-0.004	-0.003	-0.001	-0.000	-0.005	-0.022
0.158	0.010	+0.000	+0.000	+0.002	+0.002	+0.002	+0.000	+0.003	+0.015
	±0.028	-0.014	-0.000	-0.003	-0.002	-0.001	-0.000	-0.005	-0.019
0.224	0.000	+0.000	+0.000	+0.002	+0.001	+0.002	+0.000	+0.004	+0.017
	±0.017	-0.011	-0.000	-0.003	-0.002	-0.001	-0.000	-0.004	-0.014
0.345	0.060	+0.000	+0.000	+0.001	+0.001	+0.002	+0.000	+0.006	+0.021
	±0.021	-0.004	-0.000	-0.002	-0.001	-0.001	-0.000	-0.002	-0.005

Table C.12: The spin density matrix element r_{00}^{04} as obtained from fits according to equation (3.72) (upper table) and equation (9.17) (lower table) in $|t|$ bins. The systematic errors obtained for the error classes affecting the result are also given.

$\langle\|t\|\rangle$ (GeV^2)	$\Re r_{10}^{04}$	δr_i	δr_{ii}	δr_{iii}	δr_{iv}	δr_v	δr_{vi}	δr_{ix}	δr_x
0.006	0.060	+0.004	+0.000	+0.001	+0.001	+0.001	+0.000	+0.000	+0.001
	±0.015	-0.018	-0.000	-0.001	-0.001	-0.002	-0.000	-0.002	-0.018
0.018	0.004	+0.004	+0.000	+0.001	+0.001	+0.001	+0.000	+0.001	+0.002
	±0.015	-0.018	-0.000	-0.001	-0.001	-0.002	-0.000	-0.002	-0.017
0.034	-0.007	+0.004	+0.001	+0.001	+0.001	+0.001	+0.000	+0.001	+0.004
	±0.014	-0.018	-0.000	-0.001	-0.001	-0.002	-0.000	-0.001	-0.016
0.056	-0.029	+0.004	+0.001	+0.001	+0.001	+0.001	+0.000	+0.001	+0.006
	±0.016	-0.017	-0.000	-0.001	-0.001	-0.001	-0.000	-0.001	-0.015
0.084	0.001	+0.003	+0.001	+0.001	+0.001	+0.001	+0.000	+0.002	+0.010
	±0.016	-0.017	-0.000	-0.001	-0.002	-0.001	-0.000	-0.001	-0.014
0.115	0.013	+0.003	+0.001	+0.001	+0.001	+0.001	+0.000	+0.002	+0.013
	±0.016	-0.017	-0.000	-0.001	-0.002	-0.001	-0.000	-0.001	-0.013
0.158	0.014	+0.003	+0.002	+0.001	+0.002	+0.001	+0.000	+0.003	+0.018
	±0.013	-0.016	-0.000	-0.001	-0.002	-0.001	-0.000	-0.001	-0.011
0.224	0.000	+0.002	+0.002	+0.001	+0.002	+0.001	+0.000	+0.004	+0.025
	±0.012	-0.015	-0.000	-0.001	-0.002	-0.001	-0.000	-0.001	-0.008
0.345	0.006	+0.001	+0.003	+0.001	+0.002	+0.001	+0.000	+0.007	+0.038
	±0.011	-0.014	-0.000	-0.001	-0.002	-0.001	-0.000	-0.001	-0.003

Table C.13: The spin density matrix element $\Re r_{10}^{04}$ as obtained from fits according to equation (3.72) in $|t|$ bins. The systematic errors obtained for the error classes affecting the result are also given.

$\langle\|t\|\rangle$ (GeV^2)	r_{1-1}^{04}	δr_i	δr_{ii}	δr_{iii}	δr_{iv}	δr_v	δr_{vi}	δr_{ix}	δr_x
0.006	-0.036	+0.000	+0.000	+0.001	+0.004	+0.001	+0.000	+0.001	+0.000
	±0.026	-0.005	-0.000	-0.001	-0.002	-0.000	-0.000	-0.000	-0.003
0.018	0.032	+0.000	+0.000	+0.001	+0.004	+0.001	+0.000	+0.001	+0.001
	±0.024	-0.006	-0.000	-0.001	-0.002	-0.000	-0.000	-0.001	-0.003
0.034	0.029	+0.000	+0.000	+0.001	+0.005	+0.001	+0.000	+0.001	+0.002
	±0.023	-0.007	-0.000	-0.001	-0.002	-0.000	-0.000	-0.001	-0.003
0.056	-0.030	+0.000	+0.000	+0.001	+0.005	+0.002	+0.000	+0.001	+0.002
	±0.022	-0.009	-0.000	-0.001	-0.002	-0.000	-0.000	-0.001	-0.003
0.084	-0.022	+0.000	+0.000	+0.002	+0.006	+0.002	+0.000	+0.001	+0.004
	±0.021	-0.010	-0.000	-0.001	-0.002	-0.001	-0.000	-0.002	-0.003
0.115	-0.039	+0.000	+0.000	+0.002	+0.006	+0.002	+0.000	+0.001	+0.005
	±0.022	-0.012	-0.000	-0.001	-0.002	-0.001	-0.000	-0.002	-0.002
0.158	0.005	+0.000	+0.000	+0.002	+0.007	+0.003	+0.000	+0.001	+0.007
	±0.021	-0.015	-0.000	-0.001	-0.003	-0.001	-0.000	-0.003	-0.002
0.224	-0.038	+0.000	+0.000	+0.002	+0.008	+0.004	+0.000	+0.001	+0.009
	±0.018	-0.019	-0.000	-0.001	-0.003	-0.001	-0.000	-0.004	-0.002
0.345	-0.011	+0.000	+0.000	+0.003	+0.010	+0.006	+0.000	+0.000	+0.014
	±0.018	-0.027	-0.000	-0.002	-0.004	-0.002	-0.000	-0.007	-0.001

$\langle\|t\|\rangle$ (GeV^2)	r_{1-1}^{04}	δr_i	δr_{ii}	δr_{iii}	δr_{iv}	δr_v	δr_{vi}	δr_{ix}	δr_x
0.006	-0.047	+0.003	+0.000	+0.000	+0.001	+0.003	+0.000	+0.000	+0.032
	±0.022	-0.009	-0.000	-0.000	-0.001	-0.001	-0.001	-0.006	-0.010
0.018	-0.052	+0.007	+0.000	+0.000	+0.001	+0.004	+0.000	+0.000	+0.031
	±0.024	-0.010	-0.000	-0.000	-0.001	-0.001	-0.001	-0.006	-0.011
0.034	0.054	+0.012	+0.000	+0.000	+0.001	+0.004	+0.000	+0.000	+0.029
	±0.021	-0.011	-0.001	-0.000	-0.001	-0.001	-0.001	-0.006	-0.012
0.056	-0.026	+0.020	+0.000	+0.000	+0.002	+0.004	+0.000	+0.000	+0.028
	±0.023	-0.013	-0.001	-0.000	-0.001	-0.001	-0.001	-0.007	-0.015
0.084	-0.014	+0.030	+0.000	+0.001	+0.002	+0.005	+0.000	+0.000	+0.025
	±0.023	-0.016	-0.001	-0.000	-0.001	-0.001	-0.001	-0.008	-0.017
0.115	0.015	+0.041	+0.000	+0.001	+0.003	+0.005	+0.000	+0.000	+0.023
	±0.024	-0.019	-0.001	-0.000	-0.001	-0.001	-0.001	-0.008	-0.021
0.158	0.036	+0.056	+0.000	+0.001	+0.004	+0.006	+0.000	+0.000	+0.020
	±0.022	-0.024	-0.001	-0.001	-0.001	-0.001	-0.001	-0.010	-0.025
0.224	0.029	+0.079	+0.000	+0.001	+0.005	+0.007	+0.000	+0.000	+0.014
	±0.021	-0.030	-0.002	-0.001	-0.001	-0.002	-0.001	-0.011	-0.031
0.345	0.025	+0.122	+0.000	+0.001	+0.008	+0.009	+0.000	+0.000	+0.005
	±0.019	-0.042	-0.002	-0.001	-0.002	-0.002	-0.001	-0.014	-0.044

Table C.14: The spin density matrix element r_{1-1}^{04} as obtained from fits according to equation (3.72) (upper table) and equation (9.17) (lower table) in $|t|$ bins. The systematic errors obtained for the error classes affecting the result are also given.

$\langle M_{\pi^+\pi^-} \rangle$ (GeV)	r_{00}^{04}	δr_i	δr_{ii}	δr_{iii}	δr_{iv}	δr_v	δr_{vi}	δr_{ix}	δr_x
0.617	0.030	+0.026	+0.009	+0.003	+0.002	+0.001	+0.000	+0.003	+0.005
	±0.023	-0.015	-0.008	-0.005	-0.001	-0.005	-0.000	-0.003	-0.031
0.688	0.052	+0.021	+0.008	+0.003	+0.002	+0.001	+0.000	+0.003	+0.005
	±0.035	-0.012	-0.007	-0.004	-0.002	-0.004	-0.000	-0.002	-0.025
0.721	0.008	+0.019	+0.007	+0.003	+0.002	+0.001	+0.000	+0.003	+0.005
	±0.029	-0.011	-0.007	-0.004	-0.002	-0.003	-0.000	-0.002	-0.022
0.746	-0.064	+0.018	+0.007	+0.002	+0.002	+0.001	+0.000	+0.003	+0.004
	±0.022	-0.010	-0.007	-0.004	-0.002	-0.003	-0.000	-0.002	-0.020
0.769	-0.022	+0.016	+0.007	+0.002	+0.002	+0.001	+0.000	+0.003	+0.004
	±0.026	-0.009	-0.007	-0.004	-0.002	-0.003	-0.000	-0.002	-0.019
0.797	0.016	+0.014	+0.006	+0.002	+0.002	+0.001	+0.000	+0.003	+0.004
	±0.024	-0.008	-0.007	-0.003	-0.003	-0.003	-0.000	-0.002	-0.016
0.838	-0.006	+0.011	+0.006	+0.002	+0.002	+0.001	+0.000	+0.003	+0.004
	±0.019	-0.006	-0.006	-0.003	-0.003	-0.002	-0.000	-0.001	-0.013
0.951	0.062	+0.004	+0.004	+0.001	+0.002	+0.001	+0.000	+0.004	+0.003
	±0.013	-0.002	-0.005	-0.002	-0.004	-0.001	-0.000	-0.001	-0.004

$\langle M_{\pi^+\pi^-} \rangle$ (GeV)	r_{00}^{04}	δr_i	δr_{ii}	δr_{iii}	δr_{iv}	δr_v	δr_{vi}	δr_{ix}	δr_x
0.617	0.053	+0.006	+0.009	+0.007	+0.001	+0.000	+0.000	+0.001	+0.006
	±0.023	-0.017	-0.009	-0.007	-0.006	-0.008	-0.000	-0.004	-0.034
0.688	0.077	+0.006	+0.008	+0.006	+0.001	+0.000	+0.000	+0.001	+0.010
	±0.037	-0.016	-0.009	-0.007	-0.005	-0.006	-0.000	-0.004	-0.028
0.721	-0.001	+0.006	+0.007	+0.005	+0.001	+0.000	+0.000	+0.001	+0.012
	±0.032	-0.016	-0.008	-0.006	-0.005	-0.006	-0.000	-0.004	-0.025
0.746	-0.031	+0.006	+0.007	+0.005	+0.001	+0.000	+0.000	+0.001	+0.013
	±0.033	-0.016	-0.008	-0.006	-0.004	-0.005	-0.000	-0.004	-0.023
0.769	0.004	+0.006	+0.006	+0.005	+0.001	+0.000	+0.000	+0.001	+0.014
	±0.026	-0.015	-0.008	-0.006	-0.004	-0.005	-0.000	-0.004	-0.021
0.797	0.028	+0.006	+0.006	+0.004	+0.001	+0.000	+0.000	+0.001	+0.016
	±0.027	-0.015	-0.008	-0.006	-0.003	-0.004	-0.000	-0.004	-0.018
0.838	-0.025	+0.007	+0.005	+0.004	+0.002	+0.000	+0.000	+0.001	+0.018
	±0.019	-0.015	-0.007	-0.006	-0.003	-0.003	-0.000	-0.005	-0.015
0.951	0.070	+0.007	+0.003	+0.002	+0.002	+0.000	+0.000	+0.001	+0.024
	±0.015	-0.013	-0.006	-0.005	-0.001	-0.001	-0.000	-0.005	-0.005

Table C.15: Like table C.12 but in $M_{\pi^+\pi^-}$ bins.

$\langle M_{\pi^+\pi^-} \rangle$ (GeV)	$\Re r_{10}^{04}$	δr_i	δr_{ii}	δr_{iii}	δr_{iv}	δr_v	δr_{vi}	δr_{ix}	δr_x
0.617	0.034	+0.012	+0.010	+0.004	+0.001	+0.001	+0.000	+0.000	+0.050
	±0.014	-0.044	-0.003	-0.002	-0.003	-0.003	-0.000	-0.000	-0.003
0.688	0.013	+0.010	+0.008	+0.003	+0.001	+0.000	+0.000	+0.000	+0.041
	±0.016	-0.036	-0.003	-0.002	-0.003	-0.002	-0.000	-0.000	-0.006
0.721	0.012	+0.009	+0.007	+0.003	+0.001	+0.000	+0.000	+0.000	+0.036
	±0.014	-0.032	-0.002	-0.001	-0.003	-0.002	-0.000	-0.000	-0.006
0.746	-0.018	+0.008	+0.007	+0.003	+0.001	+0.000	+0.000	+0.000	+0.033
	±0.014	-0.029	-0.002	-0.001	-0.002	-0.002	-0.000	-0.001	-0.007
0.769	-0.007	+0.007	+0.006	+0.003	+0.001	+0.000	+0.000	+0.000	+0.030
	±0.015	-0.027	-0.002	-0.001	-0.002	-0.002	-0.000	-0.001	-0.008
0.797	0.062	+0.006	+0.003	+0.003	+0.001	+0.000	+0.000	+0.000	+0.027
	±0.013	-0.024	-0.002	-0.001	-0.002	-0.002	-0.000	-0.001	-0.009
0.838	0.025	+0.005	+0.004	+0.002	+0.001	+0.000	+0.000	+0.000	+0.021
	±0.011	-0.019	-0.001	-0.001	-0.002	-0.001	-0.000	-0.001	-0.010
0.951	0.024	+0.002	+0.001	+0.002	+0.002	+0.000	+0.000	+0.000	+0.007
	±0.008	-0.006	-0.000	-0.001	-0.002	-0.000	-0.000	-0.001	-0.013

Table C.16: Like table C.13 but in $M_{\pi^+\pi^-}$ bins.

$\langle M_{\pi^+\pi^-}\rangle$ (GeV)	r_{1-1}^{04}	δr_1	δr_2	δr_{10}	$\delta r_{1\pi}$	$\delta r_{2\pi}$	δr_{ν_1}	δr_{ν_2}	$\delta r_{1\alpha}$	δr_α
0.617	.008	+0.008	+0.005	+0.001	+0.005	+0.001	+0.000	+0.000	+0.000	+0.011
	±0.016	-0.011	-0.005	-0.000	-0.002	-0.001	-0.001	-0.000	-0.000	-0.001
0.688	.053	+0.007	+0.004	+0.001	+0.005	+0.001	+0.000	+0.000	+0.000	+0.009
	±0.022	-0.009	-0.004	-0.000	-0.002	-0.001	-0.001	-0.000	-0.000	-0.002
0.721	0.017	+0.006	-0.003	+0.001	+0.003	+0.001	+0.000	+0.000	+0.000	+0.008
	±0.024	-0.008	-0.004	-0.000	-0.002	-0.001	-0.001	-0.000	-0.000	-0.002
0.746	0.023	+0.006	-0.003	+0.001	+0.005	+0.001	+0.000	+0.000	+0.000	+0.008
	±0.026	-0.007	-0.003	-0.000	-0.002	-0.001	-0.001	-0.000	-0.000	-0.003
0.789	-0.020	+0.006	+0.003	+0.001	+0.005	+0.001	+0.000	+0.000	+0.000	+0.007
	±0.026	-0.007	-0.003	-0.000	-0.002	-0.001	-0.001	-0.000	-0.000	-0.003
0.797	-0.032	+0.005	+0.003	+0.001	+0.005	+0.001	+0.000	+0.000	+0.000	+0.006
	±0.022	-0.006	-0.003	-0.000	-0.002	-0.001	-0.000	-0.000	-0.000	-0.003
0.838	-0.032	+0.004	+0.002	+0.001	+0.005	+0.001	+0.000	+0.000	+0.000	+0.005
	±0.019	-0.005	-0.002	-0.000	-0.002	-0.001	-0.000	-0.000	-0.000	-0.003
0.951	0.036	+0.002	+0.001	+0.001	+0.006	+0.002	+0.000	+0.000	+0.000	+0.002
	±0.013	-0.002	-0.001	-0.000	-0.003	-0.000	-0.000	-0.000	-0.000	-0.005

$\langle M_{\pi^+\pi^-}\rangle$ (GeV)	r_{1-1}^{04}	δr_1	δr_2	δr_{10}	$\delta r_{1\pi}$	$\delta r_{2\pi}$	δr_{ν_1}	δr_{ν_2}	$\delta r_{1\alpha}$	δr_α
0.617	0.042	+0.139	+0.004	+0.001	+0.005	+0.001	+0.000	+0.000	+0.000	+0.003
	±0.019	-0.024	-0.016	-0.002	-0.002	-0.001	-0.000	-0.001	-0.000	-0.043
0.688	-0.007	+0.114	+0.004	+0.001	+0.004	+0.001	+0.000	+0.000	+0.000	+0.005
	±0.023	-0.020	-0.013	-0.002	-0.001	-0.000	-0.001	-0.000	-0.000	-0.038
0.721	0.034	+0.102	+0.004	+0.001	+0.003	+0.001	+0.000	+0.000	+0.000	+0.006
	±0.023	-0.018	-0.012	-0.002	-0.001	-0.000	-0.001	-0.000	-0.000	-0.036
0.746	0.078	+0.093	+0.004	+0.001	+0.003	+0.001	+0.000	+0.000	+0.000	+0.007
	±0.023	-0.016	-0.011	-0.002	-0.001	-0.000	-0.001	-0.000	-0.000	-0.034
0.789	-0.023	+0.085	+0.003	+0.001	+0.003	+0.001	+0.000	+0.000	+0.000	+0.007
	±0.024	-0.015	-0.010	-0.002	-0.001	-0.000	-0.001	-0.000	-0.000	-0.032
0.797	-0.073	+0.075	+0.003	+0.001	+0.003	+0.001	+0.000	+0.000	+0.000	+0.008
	±0.021	-0.013	-0.009	-0.002	-0.001	-0.000	-0.001	-0.000	-0.000	-0.030
0.838	-0.053	+0.061	+0.003	+0.001	+0.002	+0.001	+0.000	+0.000	+0.000	+0.009
	±0.019	-0.010	-0.007	-0.002	-0.001	-0.000	-0.001	-0.000	-0.000	-0.027
0.951	0.043	+0.021	+0.002	+0.001	+0.001	+0.001	+0.000	+0.000	+0.000	+0.013
	±0.013	-0.003	-0.002	-0.001	-0.001	-0.001	-0.000	-0.000	-0.000	-0.019

Table C.17: Like table C.14 but in $M_{\pi^+\pi^-}$ bins.

Bibliography

[1] ABBHHM Collab., R. Erbe et al.: Photoproduction of Meson and Baryon Resonances at Energies up to 5.8 GeV. *Phys. Rev.* 175 (1968) 1669

[2] K. Abe et al.: Study of the $\rho'(1600)$ Mass Region Using $\gamma p \to \pi^+\pi^- p$ at 20 GeV. *Phys. Rev. Lett.* 53 (1984) 751

[3] H. Abramowicz, E.M. Levin, A. Levy, and U. Maor: A Parameterization of $\sigma_T(\gamma^* p)$ Above the Resonance Region for $Q^2 \geq 0$. *Phys. Lett.* B 269 (1991) 465

[4] G. Alexander et al.: A Comparative Study of ρ^0 Photoproduced on d, n and p at 7.5 GeV. *Nucl. Phys.* B 104 (1976) 397

[5] C. Alvisi et al.: The ZEUS Vertex Detector: Design and Prototype. *Nucl. Inst. Meth.* A 305 (1991) 30

[6] A. Andresen et al.: Construction and Beam Test of the ZEUS Forward and Rear Calorimeter. *Nucl. Inst. Meth.* A 309 (1991) 101

[7] J. Andruszkow et al.: First Measurement of HERA Luminosity by ZEUS Lumi Monitor. *DESY* 92-066 (1992)

[8] M. Arneodo, L. Lamberti, and M. Ryskin: DIPSI: a Monte Carlo Generator for Elastic Vector Meson Production in Charged Lepton-Proton Scattering. *Comput. Phys. Commun.* 100 (1997) 195

[9] J. Ballam et al.: Production of Vector Mesons by Muons in a Hybrid Bubble-Chamber Experiment. *Phys. Rev.* D 10 (1974) 765

[10] T.H. Bauer, R.D. Spital, D.R. Yennie, and F.M. Pipkin: The Hadronic Properties of the Photon in High-Energy Interactions. *Rev. Mod. Phys.* 50 (1978) 261

[11] H. Beier: *Diffractive Production of ρ^0 Mesons in Deep Inelastic Scattering at HERA*, DESY F35D-97-06, University of Hamburg, PhD thesis, 1997

[12] F. Benard, R.S. Orr, S. Polenz, and D. Simmons: The 1995 TLT Filter Software. ZEUS-Note 95-164. Internal report. 1995

[13] C. Berger et al.: "Elastic" Photoproduction of ρ^0 and ϕ^0 Mesons from Hydrogen. *Phys. Lett.* 39 B (1972) 659

[14] A. Bernstein et al.: Beam Tests of the ZEUS Barrel Calorimeter. *Nucl. Inst. Meth.* A 336 (1993) 23

[15] B. Bock et al.: Design, Construction and Test Results of the ZEUS Forward Tracking Detector. *Nucl. Inst. Meth.* A 344 (1994) 335

[16] F.W. Bopp. *Kerne, Hadronen und Elementarteilchen* Teubner Studienbücher: Physik, Stuttgart. 1989

[17] B.D. Burow: *A Measurement of the Total Photon-Proton Cross Section in the Center of Mass Energy Range 167 to 194 GeV*, DESY F35D-94-01, University of Toronto, PhD thesis, 1994

[18] D.G. Cassel et al.: Exclusive ρ^0, ω, and ϕ Electroproduction. *Phys. Rev.* D 24 (1981) 2787

[19] CDF Collab., F. Abe et al.: Measurement of $\bar{p}p$ Single Diffraction Dissociation at $\sqrt{s}$ = 546 and 1800 GeV. *Phys. Rev.* D 50 (1994) 5535

[20] CDF Collab., F. Abe et al.: Measurement of the Antiproton-Proton Total Cross Section at $\sqrt{s}$ = 546 and 1800 GeV. *Phys. Rev.* D 50 (1994) 5550

[21] CHIO Collab., W.D. Shambroom et al.: Diffractive Production of Vector Mesons in Muon-Proton Scattering at 150 and 100 GeV. *Phys. Rev.* D 26 (1982) 1

[22] F. Chlebana: Description of the ZEUS Global Second Level Trigger in 1994. ZEUS-Note 94-102. Internal report. 1994

[23] P.D.B. Collins. *An Introduction to Regge Theory and High Energy Physics* Cambridge University Press, Cambridge. 1977

[24] P.D.B. Collins and A.D. Martin. *Hadron Interactions*. Graduate Student Series in Physics Adam Hilger LTD, Bristol. 1984

[25] R.J.M. Covolan, J. Montanha, and K. Goulianos: A new Determination of the Soft Pomeron Intercept. *Phys. Lett.* B 389 (1996) 176

[26] J.R. Cudell, K. Kang, and K.K. Sung: Bounds on the Soft Pomeron Intercept. *hep-ph 9601336* (1996)

[27] T.J. Dakin et al.: Measurement of ρ^0 and ϕ-Meson Electroproduction. *Phys. Rev.* D 8 (1973) 687

[28] M. Davier et al.: Multibody Photoproduction Between 2 and 16 GeV. *Phys. Rev.* D 1 (1970) 790

[29] C. del Papa et al.: Exclusive Vector-Meson Production in Muon-Proton Scattering. *Phys. Rev.* D 19 (1979) 1303

[30] M. Derrick et al.: Design and Construction of the ZEUS Barrel Calorimeter. *Nucl. Inst. Meth.* A 309 (1991) 77

[31] K. Desler and U. Schneekloth: The Hardware of the Proton Remnant Tagger (PRT) in 1994. ZEUS-Note 95-061. Internal report. 1995

[32] A. Donnachie and G. Shaw, editors. *Electromagnetic Interactions of Hadrons*. Volume 1 and 2 Plenum Press, New York. 1978

[33] A. Donnachie and P.V. Landshoff: pp and $\bar{p}p$ Elastic Scattering. *Nucl. Phys.* B 231 (1984) 189

[34] A. Donnachie and P.V. Landshoff: Dynamics of Elastic Scattering. *Nucl. Phys.* B 267 (1986) 690

[35] A. Donnachie and P.V. Landshoff: Gluon Condensate and Pomeron Structure. *Nucl. Phys.* B 311 (1989) 509

[36] A. Donnachie and P.V. Landshoff: Total Cross Sections. *Phys. Lett.* B 296 (1992) 227

[37] A. Donnachie and P.V. Landshoff: Exclusive Vector Meson Production at HERA. *Phys. Lett.* B 348 (1995) 213

[38] S.D. Drell: Production of Particle Beams at Very High Energies. *Phys. Rev. Lett.* 5 (1960) 278

[39] E665 Collab., M.R. Adams et al.: Diffractive Production of $\rho^0(770)$ Mesons in Muon-Proton Interactions at 470 GeV. submitted to Z. Phys. C. 1997

[40] E710 Collab., N.A. Amos et al.: A Luminosity-Independent Measurement of the $\bar{p}p$ Total Cross Section at $\sqrt{s}$ = 1.8 TeV. *Phys. Lett.* B 243 (1990) 158

[41] V. Eckardt et al.: Electroproduction of ρ^0 Mesons at $0.3 < Q^2 < 1.5$ GeV^2 and $1.7 < W < 2.8$ GeV. *Phys. Lett.* 43 B (1973) 240

[42] R.M. Egloff: Measurements of Elastic ρ and ϕ-Meson Photoproduction Cross Sections on Protons from 30 to 180 GeV. *Phys. Rev. Lett.* 43 (1979) 657

[43] EMC Collab., J. Ashmann et al.: Exclusive ρ^0 and ϕ Production in Deep Inelastic Muon Scattering. *Z. Phys.* C 39 (1988) 169

[44] B. Foster et al.: The Design and Construction of the ZEUS Central Tracking Detector. *Nucl. Inst. Meth.* A 338 (1994) 254

[45] A. Fürtjes: Verhalten des ZEUS Uran-Szintillator-Kalorimeters für niederenergetische Teilchen mit Energien von 0.2 - 10.0 GeV. DESY F35-90-02, University of Münster, Diplomarbeit (in German). 1990

[46] F.J. Gilman, J. Pumplin, A. Schwimmer, and L. Stodolsky: Helicity Conservation in Diffractive Scattering. *Phys. Lett.* B 31 (1970) 387

[47] G.E. Gladding et al.: Measurement of Photoproduction of ω^0 and ρ^0 Mesons in Hydrogen. *Phys. Rev.* D 8 (1973) 3721

[48] K. Goulianos: Diffractive Interactions of Hadrons at High Energies. *Phys. Rep.* 101 (1983) 170

[49] J. Grosse-Knetter: *Measurement of Elastic ω Photoproduction at HERA*, DESY F35D-97-02, University of Hamburg, PhD thesis, 1997

[50] H1 Collab., S. Aid et al.: Measurement of the Total Photon Proton Cross Section and its Decomposition at 200 GeV Centre of Mass Energy. *Z. Phys.* C 69 (1995) 27

[51] H1 Collab., S. Aid et al.: Elastic Photoproduction of ρ^0 Mesons at HERA. *Nucl. Phys.* B 463 (1996) 3

[52] H1 Collab., S. Aid et al.: Elastic Electroproduction of ρ^0 and J/ψ Mesons at large Q^2 at HERA. *Nucl. Phys.* B 468 (1996) 3

[53] H1 Collab., S. Aid et al.: Elastic and Inelastic Photoproduction of J/ψ Mesons at HERA. *Nucl. Phys.* B 472 (1996) 3

[54] F. Halzen and A. Martin. *Quarks and Leptons* John Wiley and Sons, Inc. 1984

[55] L.N. Hand: Experimental Investigation of Pion Electroproduction. *Phys. Rev.* 129 (1963) 1834

[56] G.F. Hartner, Y. Iga, J.B. Lane, and N.A. McCubbin: VCTRAK(3.06/11): Offline Output Information. ZEUS-Note 95-004. Internal report. 1995

[57] H. Holtmann et al.: On the Determination of Double Diffraction Dissociation Cross Section at HERA. *Z. Phys.* C 69 (1996) 297

[58] J.D. Jackson: Remarks on the Phenomenological Analysis of Resonances. *Nuovo Cimento* 34 (1964) 1644

[59] W.G. Jones et al.: Forward Photoproduction of Vector Mesons from Hydrogen at Energies from 6.5 to 17.8 GeV. *Phys. Rev. Lett.* 21 (1968) 586

[60] P. Joos et al.: Rho Production by Virtual Photons. *Nucl. Phys.* B 113 (1976) 53

[61] M. Kamran: A Review of Elastic Hadronic Scattering at High Energies and Small Momentum Transfers. *Phys. Rep.* 108 (1984) 275

[62] M. Kasprzak: *Inclusive Properties of Diffractive and Non-Diffractive Photoproduction at HERA*, DESY F35D-96-16, Warsaw University, PhD thesis, 1996

[63] G. Kramer and H.R. Quinn: A Diffraction-Dissociation Model for High-Energy Rho Photoproduction. *Nucl. Phys.* B 27 (1971) 77

[64] G. Kramer and H.R. Quinn: A Diffraction-Dissociation Model for High-Energy Electroproduction. *Nucl. Phys.* B 55 (1973) 222

[65] A.S. Krass: Interference Effects in Photoproduction of ρ^0 Mesons. *Phys. Rev.* 159 (1967) 1496

[66] K. Kurek: QED Radiative Corrections in Exclusive ρ^0 Leptoproduction. *DESY* 96-209 (1996)

[67] P.V. Landshoff: Soft Hadron Physics. In S. Hegarty, K. Potter, and E. Quercigh, editors, *Proc. of Joint LP Symposium and Europhysics Conference on HEP*. Volume 2. 365. Geneva 1991

[68] E.M. Levin, L.L. Frankfurt, and A.F. Ioffe: The Quark Hypothesis and Relations Between Cross Sections at High Energies. *JETP* 2 (1965) 65

[69] H.J. Lipkin and F. Scheck: Quark Model for Forward Scattering Amplitudes. *Phys. Rev. Lett.* 16 (1966) 71

[70] H.J. Lipkin: The Levin-Frankfurt Additive Quark Model Revisited-New Insight into QCD ? *Phys. Lett.* B 335 (1994) 500

[71] M. Löwe: *Measurement of Positron-Proton Scattering at Q^2 = 0.25 GeV^2*, DESY F35D-96-03, University of Hamburg, PhD thesis, 1996

[72] E. Lohrmann. *Hochenergiephysik* Teubner Studienbücher: Physik, Stuttgart. 1986

[73] J. Mainusch: *Measurement of the Total Photon-Proton Cross-Section at HERA Energies*, DESY F35D-95-14, University of Hamburg, PhD thesis, 1995

[74] G. Marchesini et al.: HERWIG 5.1-a Monte Carlo Event Generator for Simulating Hadron Emission Reactions with Interfering Gluons. *Comput. Phys. Commun.* 67 (1992) 465

[75] G. McClellan et al.: Photoproduction of Neutral ρ Mesons. *Phys. Rev.* D 4 (1971) 2683

[76] N.A. McCubbin: Tracking Summary. Talk given during the ZEUS Meeting at DESY on 4.4.1995

[77] G. Nieseler, G. Piller, and W. Wiese: Diffractive ρ^0 Photo- and Leptoproduction at High Energies. *hep-ph 9610302* (1996)

[78] NMC Collab., M. Arneodo et al.: Exclusive ρ^0 and ϕ Muonproduction at large Q^2. *Nucl. Phys.* B 429 (1994) 503

[79] K. Ohrenberg: *Measurement of the Proton Structure Function F_2 Using the Hadron Electron Separator of the ZEUS Detector at HERA*, DESY F35D-96-17, University of Hamburg, PhD thesis, 1996

[80] OMEGA Collab., D. Aston et al.: Photoproduction of ρ^0 and ω on Hydrogen at Photon Energies of 20 to 70 GeV. *Nucl. Phys.* B 209 (1982) 56

[81] J. Park et al.: The Reaction $\gamma p \to \rho^0 p$ at 5.5 to 18 GeV. *Nucl. Phys.* B 36 (1972) 404

[82] Particle Data Group: Review of Particle Properties. *Phys. Rev.* D 50 (1994) 1

[83] E. Paul: Status FDET. Talk given during the ZEUS Meeting at DESY on 4.4.1995

[84] K. Piotrźkowski and M. Zachara: Determination of the ZEUS Luminosity in 1994. ZEUS-Note 95-138. Internal report. 1995

[85] A. Proskuryakov: private communication

[86] J. Pumplin: Diffraction Dissociation and the Reaction $\gamma p \to \pi^+\pi^- p$. *Phys. Rev.* D 2 (1970) 1859

[87] M. Ross and L. Stodolsky: Photon Dissociation Model for Vector-Meson Photoproduction. *Phys. Rev.* 149 (1966) 1172

[88] M.G. Ryskin and Yu.M. Shabelski: Role of the Non-Resonant Background in the ρ^0-Meson Diffractive Electro- and Photoproduction. *hep-ph 9701407* (1997)

[89] M.G. Ryskin and Yu.M. Shabelski: σ_L/σ_T in the ρ^0-Meson Diffractive Electroproduction. *hep-ph 9704279* (1997)

[90] R. Sacchi: *Studio di eventi diffrattivi con uno spettrometro per protoni a ZEUS*, University of Torino, PhD thesis, 1996. – unpublished (in Italian)

[91] J.J. Sakurai: Vector-Meson Dominance and High-Energy Electron-Proton Inelastic Scattering. *Phys. Rev. Lett.* 22 (1969) 981

[92] SBT Collab., H.H. Bingham et al.: Reaction $\gamma p \to p\rho^0$ with Linearly Polarized Photons at 2.8 and 4.7 GeV: Cross Sections and the ρ^0 Mass Shift. *Phys. Rev. Lett.* 24 (1970) 955

[93] SBT Collab., J. Ballam et al.: Conservation of s-Channel Helicity in ρ^0 Photoproduction. *Phys. Rev. Lett.* 24 (1970) 960

[94] SBT Collab., J. Ballam et al.: Bubble-Chamber Study of Photoproduction by 2.8 and 4.7 GeV Polarized Photons. *Phys. Rev.* D 5 (1972) 545

[95] SBT Collab., J. Ballam et al.: Vector-Meson Production by Polarized Photons at 2.8, 4.7, and 9.3 GeV. *Phys. Rev.* D 7 (1973) 3150

[96] K. Schilling and G. Wolf: How to Analyze Vector-Meson Production in Inelastic Lepton Scattering. *Nucl. Phys.* B 61 (1973) 381

[97] G.A. Schuler and T. Sjöstrand: Towards a Complete Description of High-Energy Photoproduction. *Nucl. Phys.* B 407 (1993) 539

[98] T. Sjöstrand: PYTHIA 5.7 and JETSET 7.4. *CERN-TH.7112/93* (1993)

[99] T. Sjöstrand: High-Energy Physics Event Generation with PYTHIA 5.7 and JETSET 7.4. *Comput. Phys. Commun.* 82 (1994) 74

[100] W.H. Smith et al.: The ZEUS Calorimeter First Level Trigger. *Nucl. Inst. Meth.* A 355 (1995) 278

[101] P. Söding: On the Apparent Shift of the Rho Meson Mass in Photoproduction. *Phys. Lett.* 19 (1966) 702

[102] R. Spital and D.R. Yennie: ρ^0 Shape in Photoproduction. *Phys. Rev.* D 9 (1974) 126

[103] W. Struczinski et al.: Study of Photoproduction on Hydrogen in a Streamer Chamber with Tagged Photons for 1.6 GeV $< E_\gamma <$ 6.3 GeV. *Nucl. Phys.* B 108 (1976) 45

[104] SWT Collab., Y. Eisenberg et al.: Study of High-Energy Photoproduction with Positron-Annihilation Radiation. *Phys. Rev.* D 5 (1972) 15

[105] D. Westphal: Polarisationsmessungen am HERA Elektronenstrahl. DESY F35D-93-04, University of Hamburg, Diplomarbeit (in German). 1993

[106] G. Zech: Comparing Statistical Data to Monte Carlo Simulation - Parameter Fitting and Unfolding. *DESY* 95-113 (1995)

[107] ZEUS Collaboration: The ZEUS Detector, Status Report 1993. DESY. 1993

[108] ZEUS Collab., M. Derrick et al.: Measurement of Total and Partial Photon Proton Cross Sections at 180 GeV Center of Mass Energy. *Z. Phys.* C 63 (1994) 391

[109] ZEUS Collab., M. Derrick et al.: Exclusive ρ^0 Production in Deep Inelastic Electron-Proton Scattering at HERA. *Phys. Lett.* B 356 (1995) 601

[110] ZEUS Collab., M. Derrick et al.: Measurement of Elastic ρ^0 Photoproduction at HERA. *Z. Phys.* C 69 (1995) 39

[111] ZEUS Collab., M. Derrick et al.: Measurement of Elastic ϕ Photoproduction at HERA. *Phys. Lett.* B 377 (1996) 259

[112] ZEUS Collab., M. Derrick et al.: Measurement of Elastic ω Photoproduction at HERA. *Z. Phys.* C 73 (1996) 73

[113] ZEUS Collab., M. Derrick et al.: Elastic Electroproduction of ρ^0 Mesons for $0.25 < Q^2 < 0.85$ GeV^2 at HERA. Paper submitted to XVIIIth International Conference on High Energy Physics, Warsaw, July 1996

[114] ZEUS Collab., M. Derrick et al.: The ZEUS Leading Proton Spectrometer and its Use in the Measurement of Elastic ρ^0 Photoproduction at HERA. *Z. Phys.* C 73 (1997) 253

[115] ZEUS Collab., J. Breitweg et al.: Measurement of Elastic J/ψ Photoproduction at HERA. *Z. Phys.* C 75 (1997) 215

[116] ZEUS Collaboration: Elastic and Proton-Dissociative ρ^0 Photoproduction at HERA. 1997, paper in preparation

Danksagung

Es war eine interessante Erfahrung eine Doktorarbeit im Rahmen einer großen internationalen Kollaboration anzufertigen. Während dieser Zeit habe ich sehr viel Unterstützung erfahren, die zum Gelingen der vorliegenden Dissertation beitragen hat. An dieser Stelle möchte ich mich für diese Unterstützung bedanken. Besonders danke ich:

Meinem Betreuer Robert Klanner für die Möglichkeit in der ZEUS Kollaboration mitzuarbeiten und für seien Einsatz bei der Absicherung meiner wirtschaftlichen Lage über die lange Zeit. Darüberhinaus habe ich in zahlreichen Diskusionen und durch viele, meißt nützliche, Anregungen zur Analyse viel von Ihm gelernt.

Heiko Beier, Jörn Grosse-Knetter, Alexander Proskuryakov, Michal Kasprzak, Luciano Lamberti und Roberto Sacchi danke ich für die gute Zusammenarbeit. Ich habe an verschiedenen Stellen in meiner Analyse von Ihren Arbeiten profitiert und Ihre Diskusionsbereitschaft oft und gerne genutzt.

Allen Koordinatoren der *Soft Photoproduction* und *Diffraction working group* danke ich für die zahlreichen Anregungen. Insbesondere Burkhard Burow und Michele Arneodo haben die Entwicklung dieser Arbeit kritisch begleitet und unterstützt.

Für die Durchsicht des Manuskripts und die konstruktiven Anregungen danke ich Prof. Lohrmann. Sampa Bhadra und Burkhard Burow haben durch ihre kritische Durchsicht des Manuskripts dafür gesorgt, daß der englischen Sprache kein allzu großer Schaden zugefügt wurde.

Schließlich danke ich allen Doktoranden und Diplomanden die mir meine Zeit bei DESY durch allerlei kurzweilige Gespräche, nicht nur über Physik, verkürzt haben. Besonders hervorheben möchte ich: Martin Löwe, Heiko Beier, Kars Ohrenberg, Kai Desler, Teresa Monteiro, Jörn Grosse-Knetter, Song Ming Wang, Jason McFall, Olaf Deppe, Bernd Surrow und Joachim Stamm.

Abschließend möchte ich meiner Frau Ute und meiner Familie für die Geduld danken die Sie aufgebracht haben. Ihnen und meinen Freunden und Bekannten habe ich dafür zu danken, daß Sie mir immer wieder vor Augen gehalten haben, daß es ein Leben außerhalb des DESY gibt.